Influence of Calcium and Magnesium Ions and their Carbonate Scales on CO_2 Corrosion of Mild Steel

A dissertation presented to

the faculty of

the Russ College of Engineering and Technology of Ohio University

In partial fulfillment

of the requirements for the degree

Doctor of Philosophy

Hamed Mansoori

May 2020

.

This dissertation titled

Influence of Calcium and Magnesium Ions and their Carbonate Scales on CO_2 Corrosion of Mild Steel

by

HAMED MANSOORI

has been approved for

the Department of Chemical and Biomolecular Engineering

and the Russ College of Engineering and Technology by

Marc Singer

Associate Professor of Chemical and Biomolecular Engineering

Mei Wei

Dean, Russ College of Engineering and Technology

ABSTRACT

MANSOORI, HAMED., Ph.D., May 2020, Chemical Engineering

Influence of Calcium and Magnesium Ions and their Carbonate Scales on CO_2 Corrosion of Mild Steel

Director of Dissertation: Marc Singer

The produced fluids from oil and gas wells usually contain a considerable amount of carbon dioxide (CO_2). Although CO_2 itself is not a corrosive agent, its hydrated form, carbonic acid (H_2CO_3) is involved in corrosion processes. CO_2 corrosion, also known as "sweet corrosion", is by far the most common type of corrosion encountered in upstream pipelines of the oil and gas industry. Despite its susceptibility to corrosion, low carbon steel (mild steel) is widely used in the oil industry because of its availability and cost-effectiveness. Understanding the corrosion behavior of mild steel in oilfield conditions and applying appropriate mitigation programs are crucial to enhance the lifespan of upstream infrastructures.

Iron (II) carbonate ($FeCO_3$) is the main corrosion product in CO_2 corrosion of mild steel. An $FeCO_3$ layer can protect the steel from rapid corrosion by acting as a diffusion barrier to relevant species for cathodic reactions and by covering portions of the steel surface and retarding the iron dissolution (anodic) reaction. The aqueous phase co-produced with the hydrocarbon phase, known as "brine", usually contains a high concentration of calcium ions (Ca^{2+}) and magnesium ions (Mg^{2+}). Ca^{2+} and Mg^{2+} can incorporate into the $FeCO_3$ lattice and form a substitutional solid solution with different physiochemical characteristics compared to pure $FeCO_3$. This phenomenon happens

because $FeCO_3$ (siderite), $CaCO_3$ (calcite), and $MgCO_3$ (magnesite) share the same hexagonal crystal structure.

Over the past decades, mechanisms of CO_2 corrosion of mild steel and the characteristics of its corrosion products ($FeCO_3$ and Fe_3C) have been intensively studied and documented by different researchers. However, most of these studies have been performed in various dilute solutions of sodium chloride (NaCl), while Ca^{2+} and Mg^{2+} are also present in most geological formations. Additionally, the limited available literature is contradictory about the true effect of Ca^{2+} and Mg^{2+} on the CO_2 corrosion mechanism of mild steel, in some cases linking Ca^{2+} to localized corrosion initiation, in other cases attributing corrosion mitigation properties to Ca^{2+}. One very important experimental parameter, that is the main cause of discrepancies in the open literature, is the saturation degree of carbonates in the bulk solution. This parameter controls the precipitation of scales but is naturally transient if not controlled carefully. However, this parameter is typically not even measured in most published experimental works. In addition, the flow characteristics of most of the experimental setups are also not appropriately studied and/or reported.

The current research has broadened the mechanistic understanding of CO_2 corrosion of mild steel in the presence of Ca^{2+} and Mg^{2+} in experimental scenarios resembling oil and gas pipelines. Special efforts were made to maintain and report the water chemistry (pH, saturation degree in carbonates, Fe^{2+} concentration) and flow characteristics of a glass cell test system over the course of long-term experiments in order to ensure reproducibility and reliability of the data. A novel experimental

methodology and apparatus were utilized to investigate CO_2 corrosion of mild steel in the presence of Ca^{2+}, Mg^{2+}, and simultaneous presence of these cations.

The main conclusions are outlined below:

- The $CaCO_3$ and $MgCO_3$ saturation degree of the electrolyte, $[Ca^{2+}]$ and $[Mg^{2+}]$, and bulk pH are crucial parameters in studying the effect of Ca^{2+} and Mg^{2+} on CO_2 corrosion. Ignoring the influence of such parameter(s) is one of the main reasons for the existing discrepancies in the available literature on this topic.
- The development of Fe_3C on the carbon steel surface played a critical role in precipitation of corrosion products. The mole fraction of Ca and Mg in the surface corrosion products mainly depended on calcium and magnesium concentration in bulk solution.
- The protective behavior of the surface layers was mainly due to the formation of $FeCO_3$ adjacent to the steel surface (inner layer) rather than the outer layer corrosion product/scale ($Fe_xCa_yMg_zCO_3$, $x+y+z=1$) in the presence of Ca^{2+} and/or Mg^{2+} in the electrolyte. However, the presence of the outer layers facilitated $FeCO_3$ precipitation and enhanced its protectiveness by acting as a mass transfer barrier for Fe^{2+} outwards from the steel and H^+ towards the steel
- Although $CaCO_3$ is isomorphous with $FeCO_3$, $CaCO_3$ scale was not protective against further corrosion. No localized corrosion was observed in the presence of Ca^{2+} and/or $CaCO_3$ scale (if uniform surface coverage is conferred). Patchy precipitation of $CaCO_3$ scale could lead to localized corrosion. In addition, pitting

corrosion reported in the literature could be attributed to uncontrolled experimental conditions (mainly pH swings due to scale precipitation).

- Unlike $CaCO_3$, the formation of $MgCO_3$ was not possible in the current experimental conditions due its extremely slow precipitation kinetics.
- The presence of Mg^{2+} in test electrolytes increased the corrosion rate during the active corrosion period while possibly hindering precipitation of $FeCO_3$, compared to Ca^{2+}-containing electrolytes.
- A high concentration of Mg^{2+} (4,200 ppm) at pH 5.5 promoted formation of a thicker Fe_3C layer, compared to its baseline condition, leading to its occasional rupture and/or detachment from the steel surface. Preferential corrosion was observed at such locations but did not qualify as localized corrosion.

DEDICATION

To:

My beloved wife, Mehrnaz Razavi, whom without her support I would not be able to accomplish my academic ambitions.

My kids, Daniel and Melody who accompanied me during this unbelievable journey.

My parents who have supported and prayed for me in every stage of my life.

ACKNOWLEDGMENTS

I would like to express sincere gratitude to Dr. Marc Singer, my Ph.D. advisor, for his support, dedication and mentorship during my academic journey at the Institute for Corrosion and Multiphase Technology (ICMT), Ohio University. I am also grateful to Dr. Bruce Brown, my project leader, for his sincere leadership and help towards my Ph.D. research. Whenever I needed help, he was there! I cannot appreciate enough Dr. David Young for what he has put into my academic and personal life. I learned a lot from him in each communication with him. Special thanks go to Dr. Srdjan Nesic for his leadership and academic help during my Ph.D.

I give my special thanks to Alexis Barxias, Cody Shafer, Al Schubert, Dr. Zineb Belarbi, Dr. Fernando Farelas, Juan Dominguez Olivo, Saba Navabzadeh Esmaeely, and any ICMT family member who contributed in some way to my work.

The members of my graduate committee including Dr. Jason Trembly, Dr. Lauren McMills, and Dr. Travis White are greatly appreciated for their hard work to help and review this dissertation.

I also would like to appreciate the financial and technical support from the sponsoring companies and their invaluable agents throughout my research.

Last but not least, my special thanks go to my family member including my beloved wife and my two lovely kids for allowing me not to act as a normal husband and father but to be a Ph.D. student. I apologize for the time they needed me, and I was not there. My Ph.D. journey would not be accomplished without the dedication of my family.

It should be acknowledged that Any figures reproduced from other sources have been done so after permission was received from the relevant publishers.

TABLE OF CONTENTS

Page

Abstract 3
Acknowledgments 8
List of Tables 13
List of Figures 14
Nomenclature 24
Chapter 1: Introduction 26
Chapter 2: Literature Review 30
2.1 CO_2 Corrosion of Mild Steel in Brief 30
2.1.1 Electrochemistry of Mild Steel Corrosion in CO_2 Environments 31
2.1.2 Corrosion Product ($FeCO_3$) 33
2.2 Carbonate Scales ($CaCO_3$ and $MgCO_3$) 36
2.2.1 Solubility in Water 36
2.2.2 Isostructurality of Calcite and Magnesite with Siderite 38
2.3 A Critical Literature Review: Effect of Ca^{2+} and Mg^{2+} on CO_2 Corrosion 42
Chapter 3: Research Gap, Objectives, and Hypotheses 57
3.1 Research Gaps and Objectives 57
3.2 Hypotheses 59
Chapter 4: Experimental Setup and Mass Transfer Characterization 60
4.1 Controlled Water Chemistry Glass Cell Setup 60
4.2 Mass Transfer Characterization of the Glass Cell with Impeller 65
Chapter 5: Experimental Procedure 73
5.1 Experiment Scenarios 73
5.2 Specimens (chemical composition, microstructure, preparation) 74
5.3 Electrochemical Measurements 75
5.4 Weight Loss Measurement 77
5.5 Pitting Ratio Measurement 78
5.6 Surface Layer Characterization 78
Chapter 6: CO_2 Corrosion Experiments in Ca^{2+} - Containing Electrolytes 81

6.1 Effect of Ca^{2+} on Morphology and Protectiveness of Corrosion Product Layers ($CaCO_3$-saturated solutions) 81
6.1.1 Experiments with 160 ppm Ca^{2+} at pH 6.2 and 0.18 M ionic strength 82
6.1.1.1 Methodology and Test Matrix 82
6.1.1.2 Results and Discussion 84
6.1.1.3 Summary 104
6.1.2 Experiments with 6000 ppm Ca^{2+} at pH 5.5, and 0.6 M ionic strength 105
6.1.2.1 Methodology and Test Matrix 105
6.1.2.2 Results and Discussion 107
6.1.2.3 Descriptive Model for the Effect of high [Ca^{2+}] on Uniform Corrosion 122
6.1.2.4 Summary 125
6.2 Effect of $CaCO_3$ Scale on CO_2 Corrosion Mechanism 125
6.2.1 $CaCO_3$ Precipitation: Electrochemically Driven 126
6.2.1.1 Methodology and Test Matrix 126
6.2.1.2 Results and Discussion 128
6.2.2 $CaCO_3$ Precipitation: Chemically Driven 136
6.2.2.1 Methodology and Test Matrix 137
6.2.2.2 Results and Discussion 142
6.2.2.3 Summary 170
Chapter 7: CO_2 Corrosion Experiments in Mg^{2+} - Containing Electrolytes 172
7.1 Methodology and Test Matrix 172
7.2 Results and Discussion 174
7.2.1 Experiments with 100 ppm Mg^{2+} at pH 6.2 and 0.18 M ionic strength 175
7.2.2 Experiments with 4,200 ppm Mg^{2+} at pH 5.5 and 0.6 M ionic strength 183
7.2.3 Descriptive Model for the Effect of High [Mg^{2+}] on Localized Corrosion 189
7.3 Summary 194
Chapter 8: CO_2 Corrosion in Electrolytes with the Simultaneous Presence of Ca^{2+} and Mg^{2+} 195
8.1 Methodology and Test Matrix 195
8.2 Results and Discussion 196

8.3 Inhibiting Effect of Mg^{2+} on Carbonate Precipitation.....199
8.4 Summary.....201
Chapter 9: Conclusions.....202
Chapter 10: Future Work.....204
References.....206
Appendix I: XRD Data Processing.....214
Appendix II: Effect of Non-Ideality On $FeCO_3$ Saturation Calculation.....217
Appendix III: EIS Data Interpretation.....222
Appendix IV: Electrochemical Investigation on the Influence of Ca^{2+} and Mg^{2+} on CO_2 Corrosion of Mild Steel in Scale Free Conditions.....241

LIST OF TABLES

Page

Table 1. Example of ion concentrations from an oilfield brine 29
Table 2. Key structural parameters for magnesite, siderite, and calcite 39
Table 3. Experimental condition for mass transfer characterization 70
Table 4. Chemical composition of the UNS G10180 mild steel used in this work 75
Table 5. Electrochemical parameters used for LPR and EIS measurements 77
Table 6. Text matrix to investigate the effect of Ca^{2+} at pH 6.2 84
Table 7. Text matrix to investigate the effect of Ca^{2+} at pH 5.5 107
Table 8. Experimental conditions employed to evaluate protectiveness of $CaCO_3$ scale 128
Table 9. Test matrix for different $CaCO_3$ saturation levels at pH 6.2 and 160 ppm $[Ca^{2+}]$ 139
Table 10. Test matrix for different $CaCO_3$ saturation levels at pH 5.5 and 6000 ppm $[Ca^{2+}]$ 140
Table 11. Test matrix for experiments saturated with $MgCO_3$ at pH 6.2 and pH 5.5 174
Table 12. Evolution of localized attacks on specimens exposed to 4,200 ppm Mg^{2+} at pH 5.5 191
Table 13. Experimental condition to study the effect of simultaneous presence of $[Mg^{2+}]$ and $[Ca^{2+}]$ on CO_2 corrosion at pH 5.5 196
Table 14. List of semi-empirical activity coefficient model and their validity depending on ionic strength of solution 218
Table 15. Comparison of timeline for corrosion periods and final LPR corrosion with and without presence of 6000 ppm Ca^{2+} 240
Table 16. Comparison of EIS Nyquist response in different corrosion periods for experiments with and without presence of 6000 ppm Ca^{2+} 240
Table 17. Test matrix for conducting electrochemical measurements in presence of equimolar Mg^{2+} and Ca^{2+} 242
Table 18. Mean value of ionic strength, pH, LPR CR, and OCP for three different solutions 243

LIST OF FIGURES

Page

Figure 1. Solubility products of siderite, calcite, and magnesite *versus* temperature 38

Figure 2. Hexagonal crystal structure of calcite ($CaCO_3$; blue = Ca, red = O, black =C), four-unit cells 40

Figure 3. Hexagonal single unit cell of siderite ($FeCO_3$; tan = Fe, red = O, black =C) 40

Figure 4. Hexagonal single unit cell of calcite ($CaCO_3$; blue = Ca, red = O, black =C)...41

Figure 5. Hexagonal single unit cell of magnesite ($MgCO_3$; yellow = Mg, red = O, black =C) 41

Figure 6. Orthorhombic crystal structure of aragonite ($CaCO_3$; blue = Ca, red = O, black =C), four unit cells.....42

Figure 7. XRD patterns of the layers formed on X65 carbon steel specimens at various pCO_2 values, quiescent condition, 65°C, 64 ppm Ca^{2+}, and 72 ppm Mg^{2+} [46].....45

Figure 8. Nyquist plots *versus* time for API CT5 N80 materials in 3 wt.% NaCl + 1.5 wt.% $CaCl_2$ electrolyte at 57°C [47].....47

Figure 9. Corrosion rate *versus* different concentrations of Ca^{2+} for X65 specimens at 75°C and 10 bar pCO_2 after 10 days of exposure [43].....48

Figure 10. Elemental analysis for calcium in the bilayers formed on the steel surface. Note the higher concentration of calcium in the outer layer ("surface scale") compared to the inner layer ("inner scale") when the test solution contained 512 ppm Ca^{2+} [43].....49

Figure 11. Corrosion rate over time measured by LPR for different initial concentration of calcium ions at 80°C, pCO_2 0.53 bar, 1wt. % NaCl, and 10 ppm Fe^{2+} [44].....50

Figure 12. Variation of pH over time for different concentrations of Ca^{2+} at 80°C, pCO_2 0.53 bar, 1wt. % NaCl, and 10 ppm Fe^{2+} [44] (note the difference in the electrolytes' pH caused by precipitation of $CaCO_3$ in high concentration of calcium ions).....51

Figure 13. SEM images of surface layers' morphology formed on low carbon steel after 72, 336, 672 hours of exposure in CO_2-saturated solutions (a, b, and c) without and (d, e, and f) with $CaCO_3$ [50].....53

Figure 14. Corrosion rate, by weight loss, *versus* exposure time for test electrolytes with and without $CaCO_3$ at 80°C, pCO_2 15 MPa , solution saturated with CO_2 and NaCl [50] 55

Figure 15. Schematic view of the system equipped with impeller and $[Fe^{2+}]/[H^+]$ control loops. The impeller diameter was 4.5″, the distance between the impeller blades and the specimen surface was 0.4″, and the glass cell had an 8″ internal diameter. (All drawings courtesy of Cody Shafer, ICMT, OU.) 62

Figure 16. Schematic view of removeable specimen holder, electrochemical sample configuration, and the experimental setup. 63

Figure 17. Limiting currents obtained at 50°C and varying rotational speeds using ferri-ferrocyanide coupled reactions....68

Figure 18. A straight-line fit of the mass transfer correlation developed for the experimental setup with impeller based on the relation between Sherwood (Sh), Reynolds (Re), and Schmidt (Sc) numbers 69

Figure 19. The relation between impeller rotational speed in the glass cell and velocity of the fluid in single-phase flow through a 0.1m ID pipe obtained by matching mass transfer coefficients. 72

Figure 20. Ferritic-pearlitic microstructure of the UNS G10180 mild steel specimens....75

Figure 21. Change in LPR corrosion rate and open circuit potential with time explained by three different periods: active corrosion, nucleation/growth of $FeCO_3$, and pseudo-passivation (UNS G10180, 80 °C, pCO_2 0.53 bar, pH 6.2, NaCl 1wt%, $4 < SFeCO3 < 14$, $SCaCO3 = 0$, velocity 0.58 m/s) 85

Figure 22. Time-averaged (cumulative) corrosion rate obtained by LPR and WL techniques (UNS G10180, 80 °C, pCO_2 0.53 bar, pH 6.2, NaCl 1wt%, $4 < SFeCO3 < 14$, $SCaCO3 = 0$, velocity 0.58 m/s) 86

Figure 23. SEM images of top view and cross-sectional morphology of surface layers exposed to solution in the absence of $CaCO_3$ at pH 6.2 (note: the CR-WL provided here is specific for the experiment in which the surface characterization is presented here) 90

Figure 24. Corrosion rate by WL and cementite thickness *versus* time in the active (2 days), nucleation/growth of $FeCO_3$ (4 days), and pseudo-passive (7 days) periods, baseline experiment at pH 6.2. 91

Figure 25. EDS analysis (line scan) of cross-sectioned corrosion products formed on a specimen exposed to the baseline solution for 7 days at pH 6.2.....93

Figure 26. SEM/EDS analysis (top view) of the corrosion products developed on the surface of UNS G10180 specimens exposed to the baseline solution for 7 days at pH 6.2 93

Figure 27. pH profiles for both baseline and $CaCO_3$-saturated solution over time (pH 6.2 ± 0.1).....94

Figure 28. Variation of $FeCO_3$ saturation degree over time for experiment with and without $CaCO_3$ at pH 6.2 (the average values of $SFeCO3$were controlled between 4 and 14).....95

Figure 29. Comparison of LPR corrosion behavior of UNS G10180 exposed to $CaCO_3$-saturated and baseline ($CaCO_3$-free) aqueous conditions at pH 6.2.....96

Figure 30. Comparison of cumulative corrosion rate obtained by LPR and WL methods with and without $CaCO_3$ after 2, 4, and 7 days of exposure at pH 6.2 98

Figure 31. Comparison of OCP over time for UNS G10180 exposed to solutions with and without $CaCO_3$ at pH 6.2 99

Figure 32. Top and cross-sectional views of specimens retrieved from the test condition with $CaCO_3$ present after 2, 4 and 7 days of exposure at pH 6.2 101

Figure 33. SEM/EDS analysis (top view) of the surface layers on UNS G10180 developed from a solution saturated with $CaCO_3$ after 7 days of exposure at pH 6.2 101

Figure 34. XRD patterns of surface layers detected on the steel surface after 2, 4, and 7 days of exposure with/without the presence of Ca^{2+} at pH 6.2 103

Figure 35. Elemental analysis (line scan) of cross-sectioned corrosion products formed on a specimen exposed to $CaCO_3$-saturated solution for 7 days at pH 6.2 104

Figure 36. Variation of bulk solution pH over time for experiments with and without 6000 ppm Ca^{2+} ($SCaCO3 = 1$) at 80°C, pCO_2 0.53 bar, 0.60 M ionic strength, and 20 rpm 109

Figure 37. Variation of $FeCO_3$ saturation degree over time for the experiments with and without 6000 ppm Ca^{2+} ($SCaCO3 = 1$) at 80°C, pCO_2 0.53 bar, bulk solution pH 5.5, 0.60 M ionic strength, and 20 rpm 109

Figure 38. Comparison of LPR corrosion rates of UNS G10180 exposed to solutions without and with 6000 ppm Ca^{2+} ($SCaCO3 = 1$) at 80°C, pCO_2 0.53 bar, bulk solution pH 5.5, 0.60 M ionic strength, and 20 rpm..... 110

Figure 39. WL and LPR cumulative corrosion rate over time for solutions without and with 6000 ppm Ca^{2+} ($SCaCO3 = 1$) at 80°C, pCO_2 0.53 bar, bulk solution pH 5.5, 0.60 M ionic strength, and 20 rpm 113

Figure 40. 5 Comparison of OCP over time for UNS G10180 exposed to solutions without and with 6000 ppm Ca^{2+} ($SCaCO3 = 1$) at 80°C, pCO_2 0.53 bar, bulk solution pH 5.5, 0.60 M ionic strength, and 20 rpm..... 114

Figure 41. SEM images (top and cross-section view) of the development of surface layers over time for the experiment without Ca^{2+} at 80°C, pCO_2 0.53 bar, bulk solution pH 5.5, 0.60 M ionic strength, and 20 rpm 115

Figure 42. Cross-section SEM/EDS analysis of the corrosion products after 7 days of exposure to the experiment without Ca^{2+} at 80°C, pCO_2 0.53 bar, bulk solution pH 5.5, 0.60 M ionic strength, and 20 rpm 116

Figure 43. EDS line scan analysis of the surface layers developed after 7 after 7 days of exposure to the experiment without Ca^{2+} at 80°C, pCO_2 0.53 bar, bulk solution pH 5.5, 0.60 M ionic strength, and 20 rpm 116

Figure 44. SEM images (top and cross-section view) of the development of surface layers over time for the experiments conducted in the presence of 6000 ppm Ca^{2+} ($SCaCO3 = 1$) at 80°C, pCO_2 0.53 bar, bulk solution pH 5.5, 0.60 M ionic strength, and 20 rpm 118

Figure 45. EDS analysis (line scan) of the surface layers formed on carbon steel after 7 days of exposure to a solution with the presence of 6000 ppm Ca^{2+} ($SCaCO3 = 1$) at 80°C, pCO_2 0.53 bar, bulk solution pH 5.5, 0.60 M ionic strength, and 20 rpm 119

Figure 46. EDS analysis (map mode) of a cross-section UNS G10180 specimen after 7 days of exposure to a $CaCO_3$-saturated solution at 80°C, bulk solution pH 5.5, pCO_2 0.53 bar, 0.60 M ionic strength, and 6000 ppm Ca^{2+} 121

Figure 47. XRD pattern of the surface layers formed on UNS G10180 specimen after 7 days of exposure to a $CaCO_3$-saturated solution (6000 ppm Ca^{2+}) at 80°C, bulk solution pH 5.5, pCO_2 0.53 bar, 0.60 M ionic strength, and 20 rpm 122

Figure 48. A descriptive model for CO_2 corrosion mechanism of mild steel exposed to the $CaCO_3$-saturated solution at 80°C, bulk solution pH 5.5, pCO_2 0.53 bar, 6000 ppm Ca^{2+}, 0.60 M ionic strength, and 20 rpm 124

Figure 49. Top and cross-section view SEM of the surface layers formed on the steel during 5 days of cathodic polarization; $CaCO_3$-saturated solution (6000 ppm Ca^{2+}), 80°C, bulk solution pH 5.5, pCO_2 0.53 bar, 0.60 M ionic strength, 20 rpm 129

Figure 50. SEM and EDS mapping analysis of the surface layers formed during 5 days of cathodic polarization; Fe is absent in the precipitated crystalline phases (80°C, bulk solution pH 5.5, pCO_2 0.53 bar, 6000 ppm Ca^{2+}, 0.60 M ionic strength, and 20 rpm) ... 129

Figure 51. EDS line scan results showing distribution of Ca, C, O, and Fe within the surface layers; formation of $CaCO_3$ scale (80°C, bulk solution pH 5.5, pCO_2 0.53 bar, 6000 ppm Ca^{2+}, 0.60 M ionic strength, and 20 rpm) 130

Figure 52. LPR Corrosion rate (a) and potential variations (b) over time during cathodic polarization of the specimens (80°C, bulk solution pH 5.5, pCO_2 0.53 bar, 6000 ppm Ca^{2+}, 0.60 M ionic strength, and 20 rpm) 131

Figure 53. pH (a) and Fe^{2+} concentration (b) variation over time during and without cathodic protection (80°C, bulk solution pH 5.5, pCO_2 0.53 bar, 6000 ppm Ca^{2+}, 0.60 M ionic strength, and 20 rpm) 132

Figure 54. Corrosion rate (a) and potential (b) variation over time during and without cathodic protection (80°C, bulk solution pH 5.5, pCO_2 0.53 bar, 6000 ppm Ca^{2+}, 0.60 M ionic strength, and 20 rpm) 133

Figure 55. Comparison of surface layers morphology and thickness at the end of the polarization period (5 days exposure) and after exposure to the corrosive medium without cathodic protection (7 days exposure) at 80°C, bulk solution pH 5.5, pCO_2 0.53 bar, 6000 ppm Ca^{2+}, 0.60 M ionic strength, and 20 rpm..... 134

Figure 56. Chemical composition of the layers at the steel surface after 7 days of exposure to a $CaCO_3$-saturated solution without cathodic protection of specimen at pH 5.5, 80°C, 0.53 bar pCO_2, ionic strength 0.6M, 6000 ppm Ca^{2+}, 20 rpm..... 135

Figure 57. Comparison of corrosion behavior of mild steel with and without $CaCO_3$ scale at bulk solution pH 5.5, 80°C, 0.53 bar pCO_2, ionic strength 0.6M, 6000 ppm Ca^{2+} ($SCaCO3 = 1$), and 20 rpm 136

Figure 58. Schematic of experimental design of three different $CaCO_3$ saturation levels in various solution pH and [Ca^{2+}] at 80°C, pCO_2 0.53 bar, 1wt% NaCl, and 20 rpm 138

Figure 59. Variation of bulk solution pH over time for the experiments with different $CaCO_3$ saturation levels (80˚C, pCO_2 0.53 bar, 20 rpm, ionic strength 0.18 M, $[Ca^{2+}]$ ~160 ppm) 143

Figure 60. Variation of $[Fe^{2+}]$ over time for the experiments with different $CaCO_3$ saturation levels (80˚C, pCO_2 0.53 bar, 20 rpm, pH 6.2, ionic strength 0.18 M, $[Ca^{2+}]$ ~160 ppm) 144

Figure 61. Comparison of LPR corrosion behavior of UNS G10180 exposed to solutions with different $CaCO_3$ saturation levels (80˚C, pCO_2 0.53 bar, 20 rpm, pH 6.2, ionic strength 0.18 M, $[Ca^{2+}]$ ~160 ppm) 146

Figure 62. Cumulative corrosion rate by weight loss techniques over time for solution with different $CaCO_3$ saturation levels (80˚C, pCO_2 0.53 bar, 20 rpm, pH 6.2, ionic strength 0.18 M, $[Ca^{2+}]$ ~160 ppm) 147

Figure 63. Comparison of OCP over time for UNS G10180 exposed to solutions with different $CaCO_3$ saturation levels (80˚C, pCO_2 0.53 bar, 20 rpm, pH 6.2, ionic strength 0.18 M, $[Ca^{2+}]$ ~160 ppm) 148

Figure 64. SEM images (top and cross-section view) of the development of surface layers over time for the experiment with different $CaCO_3$-saturation level at 80˚C, pCO_2 0.53 bar, 20rpm, pH 6.2, ionic strength 0.18 M 151

Figure 65. Fe_3C growth on mild steel over time exposed to solution with different $CaCO_3$ saturation levels at 80˚C, pCO_2 0.53 bar, 20rpm, pH 6.2, ionic strength 0.18 M, $[Ca^{2+}]$ ~160 ppm 152

Figure 66. EDS line scan analysis of the surface layers developed on the specimens after 7 days of exposure to electrolytes with different $CaCO_3$ saturation level at 80˚C, pCO_2 0.53 bar, 0.58 m/s, pH 6.2, ionic strength 0.18 M, $[Ca^{2+}]$ ~160 ppm 153

Figure 67. XRD patterns of surface layers detected on the steel surface after 2, 4, and 7 days of exposure to electrolytes with different $CaCO_3$ saturation level at 80˚C, pCO_2 0.53 bar, 0.58 m/s, pH 6.2, ionic strength 0.18 M, $[Ca^{2+}]$ ~160 ppm 155

Figure 68. Example of profilometry of the specimen after removing the surface layer (7 days of exposure, initially $CaCO_3$ supersaturated solution at pH 6.2, 80˚C, pCO_2 0.53 bar, 20 rpm, and ionic strength 0.18 M) 156

Figure 69. Variation of bulk solution pH over time for the experiments with different $CaCO_3$ saturation levels (80˚C, pCO_2 0.53 bar, 20 rpm, pH 5.5, ionic strength 0.6 M, $[Ca^{2+}]$ ~6000 ppm) 158

Figure 70. Variation of $[Fe^{2+}]$ over time for the experiments with different $CaCO_3$ saturation level at 80˚C, pCO_2 0.53 bar, 20 rpm, pH 5.5, ionic strength 0.6 M, $[Ca^{2+}]$ ~6000 ppm 158

Figure 71. Comparison of LPR corrosion behavior of UNS G10180 exposed to solutions with different $CaCO_3$ saturation level at 80˚C, pCO_2 0.53 bar, 0.58 m/s, pH 5.5, ionic strength 0.6 M, $[Ca^{2+}]$ ~6000 ppm 160

Figure 72. Cumulative corrosion rate by weight loss technique over time for solutions with different $CaCO_3$ saturation level at 80˚C, pCO_2 0.53 bar, 20 rpm, pH 5.5, ionic strength 0.6 M, [Ca^{2+}] ~6000 ppm 161

Figure 73. Comparison of OCP over time for UNS G10180 exposed to solutions with different $CaCO_3$ saturation level at 80˚C, pCO_2 0.53 bar, 20 rpm, pH 5.5, ionic strength 0.6 M, [Ca^{2+}] ~6000 ppm.....162

Figure 74. SEM images (top and cross-section view) of the development of surface layers over time for the experiment with different $CaCO_3$-saturation level at 80˚C, pCO_2 0.53 bar, 20 rpm, pH 5.5, ionic strength 0.6 M.....165

Figure 75. Fe_3C growth on mild steel over time exposed to solutions with different $CaCO_3$ saturation levels at 80˚C, pCO_2 0.53 bar, 20 rpm, pH 5.5, ionic strength 0.6 M, [Ca^{2+}] ~6000 ppm.....166

Figure 76. EDS line scan analysis of the surface layers developed on the specimen after 7 days of exposure to electrolytes with different $CaCO_3$ saturation level at 80˚C, pCO_2 0.53 bar, 20 rpm, pH 5.5, ionic strength 0.6 M, [Ca^{2+}] ~6000 ppm.....168

Figure 77. EDS mapping analysis of the cross-sectioned surface layers after 7 days of exposure to different $CaCO_3$ saturation levels at 80˚C, pCO_2 0.53 bar, 0.58 m/s, pH 5.5, ionic strength 0.6 M, [Ca^{2+}] ~6000 ppm.....169

Figure 78. X-ray diffraction patterns of surface layers detected on the steel surface after 7 days of exposure to electrolytes with $SCaCO3 = 1$ and initially $SCaCO3 \gg 1000$ at 80˚C, pCO_2 0.53 bar, 20 rpm, pH 5.5, ionic strength 0.6 M, [Ca^{2+}] ~6000 ppm. 170

Figure 79. Trend of corrosion rate obtained by LPR over time with and without the presence of 100 ppm Mg^{2+} at pH 6.2.....176

Figure 80. Cumulative corrosion rate by WL (bar chart) and LPR (line chart) techniques over time for solution with and without 100 ppm Mg^{2+} (80˚C, pCO_2 0.53 bar, 0.58 m/s, pH 6.2, ionic strength 0.18 M, 1 wt.% NaCl) 177

Figure 81. Evolution of Fe_3C over time with and without presence of 100 ppm Mg^{2+} (80˚C, pCO_2 0.53 bar, 0.58 m/s, pH 6.2, ionic strength 0.18 M, 1 wt.% NaCl) 177

Figure 82. Comparison of OCP over time for UNS G10180 exposed to solutions with and without 100 ppm Mg^{2+} (80˚C, pCO_2 0.53 bar, 0.58 m/s, pH 6.2, ionic strength 0.18 M, 1 wt.% NaCl).....178

Figure 83. SEM images (top and cross-section view) of the development of surface layers over time for the experiment with presence of 100 ppm Mg^{2+} ($SMgCO3 = 1$) at 80˚C, pCO_2 0.53 bar, 0.58 m/s, pH 6.2, ionic strength 0.18 M, 1wt% NaCl 179

Figure 84. EDS line scan analysis of the surface layers developed on the specimens after 7 days of exposure to electrolytes without (a) and with (b) 100 ppm Mg^{2+} at 80˚C, pCO_2 0.53 bar, 0.58 m/s, pH 6.2, ionic strength 0.18 M, 1wt% NaCl.....180

Figure 85. XRD patterns of surface layers detected on the steel surface after 2, 4, and 7 days of exposure to an electrolyte saturated with $MgCO_3$ at 80˚C, pCO_2 0.53 bar, 100 ppm Mg^{2+}, 0.58 m/s, pH 6.2, ionic strength 0.18 M, 1wt% NaCl 182

Figure 86. Example of profilometry of the specimen after removing the corrosion products (7 days of exposure to solution saturated with $MgCO_3$ at pH 6.2, 80˚C, pCO_2 0.53 bar, 100 ppm Mg^{2+}, ionic strength 0.18 M, 1 wt.% NaCl, 100 ppm Mg^{2+} 183

Figure 87. Trend of corrosion rate obtained by LPR over time with and without presence of 4,200 ppm Mg^{2+} at pH 5.5 185

Figure 88. Cumulative corrosion rate by WL (bar chart) and LPR (line chart) techniques over time for solution with and without 4,200 ppm Mg^{2+} (80˚C, pCO_2 0.53 bar, 0.58 m/s, pH 5.5, ionic strength 0.6 M, 1 wt.% NaCl) 185

Figure 89. Evolution of Fe_3C over time with and without presence of 4,200 Mg^{2+} (80˚C, pCO_2 0.53 bar, 0.58 m/s, pH 5.5, ionic strength 0.6 M, 1 wt.% NaCl) 186

Figure 90. Comparison of OCP over time for UNS G10180 exposed to solutions with and without 4,200 ppm Mg^{2+} (80˚C, pCO_2 0.53 bar, 0.58 m/s, pH 5.5, ionic strength 0.6 M, 1 wt.% NaCl).....186

Figure 91. SEM images (top and cross-section view) of the development of surface layers over time for the experiment with presence of 4,200 ppm Mg^{2+} ($SMgCO3 = 1$) at 80˚C, pCO_2 0.53 bar, 0.58 m/s, pH 5.5, ionic strength 0.6M, 1 wt.% NaCl 188

Figure 92. EDS line scan analysis of the surface layers developed on the specimens after 7 days of exposure to electrolytes without (a) and with (b) 4,200 ppm Mg^{2+} at 80˚C, pCO_2 0.53 bar, 0.58 m/s, pH 5.5, ionic strength 0.6 M, 1 wt.% NaCl 189

Figure 93. SEM images (top and cross section view) of ruptured corrosion products observed on specimens exposed to $MgCO_3$-satuarted solution with 4,200 ppm Mg^{2+} at 80˚C, pCO_2 0.53 bar, 0.58 m/s, pH 5.5, ionic strength 0.6 M, 1 wt.% NaCl.....190

Figure 94. Profilometry of specimens after removing of corrosion product layers ($MgCO_3$-satuarted solution with 4,200 ppm Mg^{2+} at 80˚C, pCO_2 0.53 bar, 0.58 m/s, pH 5.5, ionic strength 0.6M, 1 wt.% NaCl).....191

Figure 95. Proposed mechanism for the localized corrosion observed in presence of high [Mg^{2+}] for mild steel at4,200 ppm Mg^{2+}, 80˚C, pCO_2 0.53 bar, 0.58 m/s, pH 5.5, ionic strength 0.6M, 1 wt.% NaCl 193

Figure 96. Trend of corrosion rate obtained by LPR over time at 80˚C, pCO_2 0.53 bar, 0.58 m/s, pH 5.5, ionic strength 0.6M [baseline (red), 6000 ppm Ca^{2+} (dark blue), Ca^{2+}/Mg^{2+}=7 (yellow), and 4200 ppm Mg^{2+} (light blue)] 197

Figure 97. Cumulative corrosion rate obtained by WL over time at 80˚C, pCO_2 0.53 bar, 0.58 m/s, pH 5.5, ionic strength 0.6M [baseline (red), 6000 ppm Ca^{2+} (dark blue), Ca^{2+}/Mg^{2+}=7 (yellow), and 4200 ppm Mg^{2+} (light blue)] 198

Figure 98. Comparison of OCP over time for UNS G10180 exposed to various solutions at 80˚C, pCO_2 0.53 bar, 0.58 m/s, pH 5.5, ionic strength 0.68 M [baseline (red), 6000 ppm Ca^{2+} (dark blue), Ca^{2+}/Mg^{2+}=7 (yellow), and 4200 ppm Mg^{2+} (light blue)] 198

Figure 99. Comparison of SEM/EDS results for two solutions at 80˚C, pCO_2 0.53 bar, 0.58 m/s, pH 5.5, ionic strength 0.68 M [(a); Ca^{2+}/Mg^{2+}=7, $SCaCO_3$=1 and (b) Ca^{2+}= 6000 ppm, $SCaCO_3$=1] 200

Figure 100. EDS line scan analysis of the surface layers developed on a specimen after 7 days of exposure to a $CaCO_3$-saturated electrolyte with 857 ppm Mg^{2+} at 80˚C, pCO_2 0.53 bar, 0.58 m/s, pH 5.5, ionic strength 0.6M.....201

Figure 101. Bravais lattice of a hexagonal unit cell for $FeCO_3$, $CaCO_3$, and $Fe_xCa_yCO_3$ (x+y=1) [42] 214

Figure 102. Unit cell parameter “c” versus the Ca mole fraction in the lattice of mixed $Fe_xCa_yCO_3$ for the $CaCO_3$-saturated solutions with 160 and 6000 ppm dissolved Ca^{2+} at pH 6.2 and 5.5, respectively.....216

Figure 103. Effect of non-ideality: comparison of iron carbonate saturation ($SFeCO3$) calculation using Equation 17, Equation 51, and GWB simulation package at 80°C, pCO_2 0.53 bar, bulk solution pH 6.2, 0.18 M ionic strength.....220

Figure 104. Effect of non-ideality: comparison of iron carbonate saturation ($SFeCO3$) calculation using Equation 17, Equation 51, and GWB simulation at 80°C, pCO_2 0.53 bar, bulk solution pH 5.5, 0.60 M ionic strength 221

Figure 105. LPR corrosion rate and OCP variation over time for a baseline experiment ($SCaCO3 = 0$) conducted at 80°C, pCO_2 0.53 bar, bulk solution pH 5.5, 0.60 M ionic strength, and 20 rpm 223

Figure 106. Nyquist plot. EIS spectra obtained over time from a baseline experiment ($SCaCO3 = 0$) conducted at OCP at 80°C, pCO2 0.53 bar, bulk solution pH 5.5, 0.60 M ionic strength, and 20 rpm 224

Figure 107. Phase angle. EIS spectra obtained over time from a baseline experiment ($SCaCO3 = 0$) conducted at 80°C, pCO_2 0.53 bar, bulk solution pH 5.5, 0.60 M ionic strength, and 20 rpm 225

Figure 108. Impedance modulus. EIS spectra obtained over time from a baseline experiment ($SCaCO3 = 0$) conducted at 80°C, pCO_2 0.53 bar, bulk solution pH 5.5, 0.60 M ionic strength, and 20 rpm 225

Figure 109. EIS results obtained from active corrosion period of a baseline experiment ($SCaCO3 = 0$) conducted at 80°C, pCO_2 0.53 bar, bulk solution pH 5.5, 0.60 M ionic strength, and 20 rpm: (a) Nyquist plots (b) normalized Nyquist plots (c) phase angle, and (d) impedance modulus.....228

Figure 110. EIS results obtained from stable corrosion period of a baseline experiment ($SCaCO3 = 0$) conducted at 80°C, pCO_2 0.53 bar, bulk solution pH 5.5, 0.60 M ionic

strength, and 20 rpm: (a) Nyquist plots (b) normalized Nyquist plots (c) phase angle, and (d) impedance modulus.....230

Figure 111. EIS results obtained from decreasing corrosion period of a baseline experiment ($SCaCO3 = 0$) conducted at 80°C, pCO_2 0.53 bar, bulk solution pH 5.5, 0.60 M ionic strength, and 20 rpm: (a) and (b) Nyquist plots, (c) phase angle, and (d) impedance modulus 232

Figure 112. LPR corrosion rate and OCP variation over time for an experiment with presence of 6000 ppm Ca^{2+} ($SCaCO3 = 1$) conducted at 80°C, pCO_2 0.53 bar, bulk solution pH 5.5, 0.60 M ionic strength, and 20 rpm.....233

Figure 113. EIS spectra obtained over time from an experiment with presence of 6000 ppm Ca^{2+} ($SCaCO3 = 1$) conducted at 80°C, pCO_2 0.53 bar, bulk solution pH 5.5, 0.60 M ionic strength, and 20 rpm: Nyquist plot (a), phase angle (b), and Impedance modulus (c) 234

Figure 114. EIS results obtained from active corrosion period of an experiment with presence of 6000 ppm Ca^{2+} ($SCaCO3 = 1$) conducted at 80°C, pCO_2 0.53 bar, bulk solution pH 5.5, 0.60 M ionic strength, and 20 rpm: (a) Nyquist plots (b) normalized Nyquist plots (c) phase angle, and (d) impedance modulus 236

Figure 115. EIS results obtained from stable corrosion period of an experiment with presence of 6000 ppm Ca^{2+} ($SCaCO3 = 1$) conducted at 80°C, pCO_2 0.53 bar, bulk solution pH 5.5, 0.60 M ionic strength, and 20 rpm: (a) Nyquist plots (b) normalized Nyquist plots (c) phase angle, and (d) impedance modulus 238

Figure 116. EIS results obtained from decreasing corrosion period of an experiment with presence of 6000 ppm Ca^{2+} ($SCaCO3 = 1$) conducted at 80°C, pCO_2 0.53 bar, bulk solution pH 5.5, 0.60 M ionic strength, and 20 rpm: (a) and (b) Nyquist plots, (c) phase angle, and (d) impedance modulus.....239

Figure 117. Nyquist plots obtained from a blank, Ca^{2+}-containing, and Mg^{2+}-containing solution at 40°C, pCO_2 0.93 bar, bulk solution pH 4.64, 0.77 M ionic strength, and 1500 rpm.....244

Figure 118. Phase angle diagrams obtained from a blank, Ca^{2+}-containing, and Mg^{2+}-containing solution at 40°C, pCO_2 0.93 bar, bulk solution pH 4.64, 0.77 M ionic strength, and 1500 rpm.....245

Figure 119. Impedance modulus diagrams obtained from a blank, Ca^{2+}-containing, and Mg^{2+}-containing solution at 40°C, pCO_2 0.93 bar, bulk solution pH 4.64, 0.77 M ionic strength, and 1500 rpm 245

Figure 120. Potentiodynamic polarization of mild steel in presence of a blank, Ca^{2+}-containing, and Mg^{2+}-containing solution at 40°C, pCO_2 0.93 bar, bulk solution pH 4.64, 0.77 M ionic strength, and 1500 rpm.....247

Figure 121. Cathodic polarization of mild steel in presence of a blank, Ca^{2+}-containing, and Mg^{2+}-containing solution at 80°C, pCO_2 0.53 bar, bulk solution pH 6.2, and 250 rpm 247

Figure 122. Cathodic polarization of mild steel in presence of different concentration of Mg^{2+} (0.01, 0.05, and 0.2 M) at 1°C, pCO_2 0.99 bar, bulk solution pH 4.23, ionic strength 0.2M to 0.77M, and 2000 rpm 248

NOMENCLATURE

Symbol/Abbreviation	Definition
$\boldsymbol{a_i}$	Activity of species *i* (M)
B	Proportional constant in Stern-Geary theory (mV)
$\boldsymbol{C_i}$	Concentration of species *i* in the bulk (M)
$\boldsymbol{CRA}$	Corrosion resistant alloy
CR	Corrosion rate (mm/y)
$\boldsymbol{d}$	Diameter of the impeller, (m)
$\boldsymbol{D}$	Diffusion coefficient (m^2/s)
ρ	Density (kg/m^3)
EIS	Electrochemical impedance spectroscopy
EDS	Energy dispersive X-ray spectroscopy
F	Faraday constant (A·s/mol)
$\boldsymbol{I}$	Ionic strength of electrolyte (M)
i_{lim}	Limiting current density (A/m^2)
$\boldsymbol{K_{sp}}$	Solubility product constant (M^2)
k_{m}	Mass transfer coefficient (m/s)
N	Revolutions per second (r/s)
n	Number of electrons transferred (-)
OCP	Open Circuit Potential (V)
$\boldsymbol{P_{CO_2}}$	Partial pressure of CO_2 (bar)
Re	Reynolds number (-)

Symbol/Abbreviation	Definition
R_p	Polarization resistance (ohm)
R_s	Solution resistance (ohm)
Sc	Schmidt number (-)
Sh	Sherwood number (-)
$\boldsymbol{S_{FeCO_3}}$	Saturation degree of $FeCO_3$ (-)
$\boldsymbol{S_{CaCO_3}}$	Saturation degree of $CaCO_3$ (-)
$\boldsymbol{S_{MgCO_3}}$	Saturation degree of $MgCO_3$ (-)
SEM	Scanning electron microscope
TDS	Total dissolved solids by electrical conductivity (μS/cm)
$\boldsymbol{T_k}$	Temperature (K)
XRD	X-ray diffraction
$\boldsymbol{z_i}$	Charge of ion *i*
$\boldsymbol{\gamma_i}$	Activity coefficient of species *i* (-)
$\boldsymbol{\varepsilon}$	Dielectric constant (-)
ν	Kinematic viscosity (m^2/s)

CHAPTER 1: INTRODUCTION[1]

Oil and gas extraction from geologic reservoirs will continue as long as fossil fuels are the dominant and economical energy source in the world. Corrosion is a destructive and cost-bearing phenomenon for every industry utilizing metallic infrastructure. Oil and gas production has been suffering from corrosion issues since the early history of the industry. Corrosion imposes significant economic costs associated with repair and replacement of infrastructures [1, 2]. Indeed, it also forces unplanned shutdowns and causes catastrophic incidents that result in environmental contamination and, potentially, human casualties. In 2016, the National Association of Corrosion Engineers (NACE) estimated the total costs associated with all types of corrosion at 3.4% of the Gross Domestic Product (GDP) of the United States [3]. However, the costs associated with corrosion can be reduced significantly if appropriate corrosion mitigation programs are applied [4, 5].

Oil and gas production involve the transmission of large quantities of fluids – hydrocarbons (liquid and gaseous), aqueous phase, CO_2 (carbon dioxide), H_2S (hydrogen sulfide) gases – in carbon steel pipelines. In this environment, corrosion occurs naturally and so does and the deposition of solids precipitating on the metal surface from the aqueous phase (scaling) – these two processes occur simultaneously [6]. The aqueous

[1] A version of this chapter has been published as "Influence of Calcium and Magnesium Ions on CO_2 Corrosion of Carbon Steel in Oil and Gas Production Systems-A Review," J. Nat. Gas Sci. Eng., vol. 59, pp. 287–296, 2018."

phase, also called brine, is a by-product of almost every hydrocarbon production system, and contains significant concentrations of dissolved cations such as Ca^{2+} (calcium ion) and Mg^{2+} (magnesium ion) as well as dominant Na^{+} (sodium ion) and Cl^{-} (chloride ion) [7, 8], among others. Depending on the conditions, scales in the form of $CaCO_3$ (calcium carbonate), $MgCO_3$ (magnesium carbonate) or a mixture of both can precipitate. The main concern with excessive scaling is typically related to flow restriction which can diminish production rates. These scales are different from other common precipitates such as iron (II) carbonate, $FeCO_3$, and iron (II) sulfide, FeS, where the constituent cation, Fe^{2+} (ferrous ion), comes from the corroding surface steel. In this dissertation, $FeCO_3$ and FeS are defined as corrosion products since the constituent cation comes from the corrosion process, whereas $CaCO_3$ and $MgCO_3$ are defined as scales since the constituent cation comes from the bulk solution. Distinct bodies of research have been conducted that separately address scaling and corrosion in the oil and gas industry. The understanding of the effects of the presence of scales and/or corrosion products on the extent of corrosion of steel is essential, as these precipitates can provide protection in certain conditions but can also lead to localized corrosion [9]. However, there is minimal information in the literature that addresses situations where corrosion and scaling simultaneously occur, despite there being indications that heavy scaling can lead to pitting and loss of facility integrity [6, 10]. Consequently, there is a need to explore the potential relationships between brine-formed scale deposits and encountered corrosion phenomena.

CO_2 corrosion and scaling processes are both highly dependent on the gas composition and the brine chemistry. Brines encountered in oil and gas production environments typically have complex chemistries. However, most laboratory corrosion studies have only been performed in various dilute NaCl (sodium chloride) electrolytes[2] while, in reality, many other ions are present in the produced brine. Divalent cations that form various carbonate layers have the potential to play a major role in the corrosion behavior of mild steel, especially in downhole conditions for oil and gas wells at high temperature and high pressure. Among these cations, Ca^{2+} and Mg^{2+} are usually present at the highest concentrations in reservoir fluids. Table 1 shows a representative example of these high ion concentrations from wells in Western Pennsylvania [11]. In terms of corrosion products, it is widely accepted that $FeCO_3$ can form a protective layer and play a significant role in CO_2 corrosion of mild steel [2]. The presence of Ca^{2+} and Mg^{2+} can change the composition of the corrosion product layer since their carbonate crystal structures, calcite (one of the mineral names for $CaCO_3$) and magnesite (the mineral name for $MgCO_3$), are isomorphous with siderite (the mineral name for $FeCO_3$) possessing a hexagonal unit cell [12, 13]. However, the effect of Ca^{2+}/Mg^{2+}-containing solutions on the properties of the $FeCO_3$ layer and subsequent effect on CO_2 corrosion mechanisms are insufficiently documented. Because of this lack of knowledge, current mechanistic models do not account for the presence of Ca^{2+} and Mg^{2+} in their corrosion predictions. In most corrosion prediction models, Ca^{2+} and Mg^{2+} are only considered to

[2] Within this manuscript, the terms “solution” and “electrolyte” are used interchangeably.

account for the ionic strength of the aqueous solution but, as mentioned above, this will not be their only role [14].

In this research project, the development of surface layers and the influence of the presence of Ca^{2+} and Mg^{2+} and their carbonate scales ($CaCO_3$ and $MgCO_3$, respectively) on CO_2 corrosion mechanisms are thoroughly investigated. To reach these goals, a new experimental apparatus was developed to generate reliable and reproducible electrochemical corrosion data, as well as specimens for surface layer characterizations, in conditions representative of oilfields.

Table 1. Example of ion concentrations from an oilfield brine [11]

TDS (g/L)	Conductivity (μS/cm)	Na^+ (mg/L)	K^+ (mg/L)	Mg^{2+} (mg/L)	Ca^{2+} (mg/L)	Sr^{2+} (mg/L)	Ba^{2+} (mg/L)	Cl^- (mg/L)
213	190,000	56700	190	2520	18000	691	171	122000

CHAPTER 2: LITERATURE REVIEW

This chapter presents the fundamentals of CO_2 corrosion and relevant corrosion products and scales encountered in CO_2 environments. Furthermore, a critical review of the available literature related to the effect of Ca^{2+} and Mg^{2+} on CO_2 corrosion is provided.

2.1 CO_2 Corrosion of Mild Steel in Brief

Despite its vulnerability to CO_2 corrosion, carbon steel is the most used material for pipelines in the oil and gas industry, considering its cost-effectiveness. CO_2 corrosion, also known as sweet corrosion, is one of the major concerns in the oil and gas industry [15, 16]. CO_2 corrosion of carbon steel represents a phenomenon occurring when CO_2 dissolves in water and hydrates to form carbonic acid (H_2CO_3), which influences solution pH and provides cathodic species for reaction with the surface of the metallic pipe. CO_2 corrosion has been investigated for more than four decades, with the purpose of understanding its mechanisms and preventing or mitigating metal degradation. Modeling of the CO_2 corrosion mechanisms began with de Waard and Milliams in 1975 [17] and continues to this day with fully mechanistic models [18, 19].

CO_2 corrosion of carbon steel is an electrochemical process that involves the anodic dissolution of iron and the cathodic evolution of hydrogen. The overall reaction can be expressed as:

$$Fe_{(s)} + CO_{2_{(aq)}} + H_2O_{(l)} \rightarrow Fe^{2+}_{(aq)} + CO^{2-}_{3_{(aq)}} + H_{2(g)} \qquad \text{Equation 1}$$

A number of chemical, electrochemical, and transport processes occur simultaneously in aqueous CO_2 corrosion of mild steel. The first step is the dissolution of gaseous carbon dioxide in water, as described in Reaction (2). The second step is the hydration of aqueous CO_2, which results in the formation of carbonic acid (H_2CO_3) as shown in Reaction (3). This process is relatively slow and is often the rate-determining step in CO_2 corrosion [20]. The sequence of reactions associated with the presence of CO_2 in H_2O is as follows:

$$CO_{2(g)} \rightleftharpoons CO_{2(aq)} \qquad \text{Equation 2}$$

$$CO_{2(aq)} + H_2O_{(l)} \rightleftharpoons H_2CO_{3(aq)} \qquad \text{Equation 3}$$

$$H_2CO_{3(aq)} \rightleftharpoons H^+_{(aq)} + HCO^-_{3\,(aq)} \qquad \text{Equation 4}$$

$$HCO^-_{3\,(aq)} \rightleftharpoons H^+_{(aq)} + CO^{2-}_{3\,(aq)} \qquad \text{Equation 5}$$

The hydration and dissociation constants for CO_2 and carbonic species have been intensively investigated over the past several decades [20]. In CO_2-H_2O systems, the pH of a CO_2 saturated solution typically increases with temperature at fixed CO_2 partial pressure because of the decrease in the solubility of CO_2 in water [21].

2.1.1 Electrochemistry of Mild Steel Corrosion in CO_2 Environments

The anodic reaction for oxidative iron dissolution is a key element in CO_2 corrosion, which takes place at the steel surface. The mechanism of iron dissolution in a CO_2 environment is complex and still not well understood [22]. A number of multi-step

mechanisms have been proposed by researchers for the anodic reaction of mild steel in CO_2 saturated aqueous media, which is outside the scope of this paper [23-25]. However, anodic dissolution of iron can be simplified to the following Reaction (6):

$$Fe_{(s)} \rightarrow Fe^{2+}_{(aq)} + 2e^- \qquad \text{Equation 6}$$

The possible cathodic reactions in CO_2 environments in the absence of oxygen are listed below:

$$2H^+_{(aq)} + 2e^- \rightarrow H_{2(g)} \qquad \text{Equation 7}$$

$$2H_2CO_{3(aq)} + 2e^- \rightarrow H_{2(g)} + 2HCO^-_{3\,(aq)} \qquad \text{Equation 8}$$

$$2HCO^-_{3\,(aq)} + 2e^- \rightarrow H_{2(g)} + 2CO^{2-}_{3\,(aq)} \qquad \text{Equation 9}$$

$$2H_2O_{(l)} + 2e^- \rightarrow H_{2(g)} + 2OH^-_{(aq)} \qquad \text{Equation 10}$$

Past research mainly focused on the cathodic reactions to describe and model observed corrosion mechanisms [26]. First, de Waard and Milliams proposed that the direct reduction of carbonic acid, Reaction (8), should be dominant if the solution pH is greater than 4 [17]. Ogundele and White also proposed that the direct reduction of bicarbonate ion, Reaction (9), is important when the pH is higher than 5 [27]. Nesic, *et al.*, later proposed that hydrogen ion reduction expressed by Reaction (7) is dominant when the solution pH is less than 4 [28]. However, recent work by Tran, *et al.*, and Kayarian, *et al.*, have cast some doubts on the previous understanding of the role of

different cathodic reactions in CO_2 corrosion [29, 30]. Carbonic acid is a weak acid; it partially dissociates and serves as a hydrogen ion reservoir for the so-called "buffering effect" governing CO_2 corrosion. The authors demonstrated that for pH values below 6, at moderate partial pressures of CO_2 (less than 10 bar) and moderate temperatures (less than 80˚C), the dominant cathodic reaction is governed by hydrogen ion reduction, Reaction (7), where the dissociation of carbonic acid, Reaction (4), and dissociation of bicarbonate, Reaction (5), provide H^+ through a buffering mechanism. This demonstrates that the mechanisms related to direct reduction reactions by carbonic acid and bicarbonate ion were negligible in their test conditions. To complete the list of cathodic reactions in sweet conditions, it can also be observed that water reduction, Reaction (10), plays an important role when the pH is higher than 6 for low partial pressures of CO_2 [28].

2.1.2 Corrosion Product ($FeCO_3$)

$FeCO_3$ is the main corrosion product from mild steel corrosion in CO_2 environments and has been proven to be protective against further corrosion under certain conditions [9]. $FeCO_3$ is considered as a corrosion product rather than scale since its constituent cations (Fe^{2+}) are derived from the corroding surface steel. The corrosion protection conferred by $FeCO_3$ is highly dependent on its growth rate, if the rate of corrosion is higher than the rate of $FeCO_3$ formation then it will not be protective; the ratio of precipitation rate to corrosion rate, labeled scaling tendency, can be used to qualify layer protectiveness [31]. $FeCO_3$ is formed from ferrous ions in solution that originate from corrosion and carbonate ions that are present due to CO_2 dissolution in

water. Reaction (11) describes precipitation (forward reaction) and dissolution (backward reaction) of $FeCO_3$ in aqueous solutions.

$$Fe^{2+}_{(aq)} + CO_3^{2-}{}_{(aq)} \rightleftharpoons FeCO_{3(s)} \qquad \text{Equation 11}$$

Precipitation occurs when the product of the ferrous ion and carbonate ion activities exceeds the solubility limit (K_{sp}) of $FeCO_3$ at equilibrium condition, Equation (12).

$$K_{sp,FeCO_3} = C_{Fe^{2+}} * C_{CO_3^{2-}} \qquad \text{Equation 12}$$

where $a_{Fe^{2+}}$ is the ferrous ion activity (known as effective concentration), $a_{CO_3^{2-}}$ is the carbonate ion activity, and $K_{sp,FeCO_3}$ is the solubility product of $FeCO_3$ in equilibrium conditions. Ionic activity is related to concentration *via* Equation (13):

$$a_i = \gamma_i C_i \qquad \text{Equation 13}$$

where γ_i is the appropriate activity coefficient of species *i*. Activity coefficients can be calculated by a semi-empirical model proposed by Davies, Equation 14, which was derived using Debye-Hückel theory [32]. The Davies model is valid for solutions with ionic strength up to 0.5M [33]. For complicated systems with higher ionic strength, the Debye-Hückel theory is no longer accurate. In such aqueous systems, advanced models such utilizing Pitzer equations can provide more realistic activity coefficients [34]:

$$log\,\gamma_i = -Az_i^2\left(\frac{\sqrt{I}}{1+\sqrt{I}} - 0.3 * I\right) \qquad \text{Equation 14}$$

The parameters associated with the above equations are:

a_i: activity of species i (mol/L)

C_i: concentration of species i (mol/L)

γ_i: activity coefficient of species i (-)

A=$1.82 \times 10^6\ (\varepsilon T)^{-3/2}$; $A \approx 0.5\ M^{-1/2}$ at 25 ˚C [35]

ε: dielectric constant

T: solution temperature (K)

z_i: charge of the species i (-)

I: ionic strength of the solution, mol/L, as described by Equation (16)

Sun, *et al.*, proposed Equation (15) for calculation of $K_{sp,FeCO_3}$ at different temperatures and ionic strengths [36]:

$$logK_{SP,FeCO_3} = -59.3498 - 0.041377 * T_k - \frac{2.1963}{T_k} + 24.5724 * Log(T_k) + 2.518 * I^{0.5} - 0.657 * I$$

Equation 15

where T_k is the temperature (in Kelvin) and I is the ionic strength (in mol/L), as determined by Equation (16):

$$I = \frac{1}{2}\sum_i c_i z_i^2 \qquad \text{Equation 16}$$

where c_i is the concentration of each species in solution and z_i is the charge of the species.

Saturation degree (S) is a key parameter in scale or corrosion product forming situations. Equation (17) expresses the saturation degree with respect to $FeCO_3$:

$$S_{FeCO_3} = \frac{C_{Fe^{2+}} * C_{CO_3^{2-}}}{K_{sp,FeCO_3}} \qquad \text{Equation 17}$$

where $C_{Fe^{2+}}$ and $C_{CO_3^{2-}}$ are ferrous ion and carbonate ion concentrations.

The $FeCO_3$ saturation degree greatly affects the corrosion behavior since it is the main driving force for $FeCO_3$ precipitation kinetics. When the saturation degree is less than unity (*i.e.*, unsaturated condition), a high corrosion rate is expected since a protective layer of $FeCO_3$ is not thermodynamically favored and is not expected to form on the steel substrate. When the saturation degree is greater than unity (*i.e.*, supersaturated solution), formation of $FeCO_3$ layer is expected. This can result in lowering of the uniform corrosion rate as the $FeCO_3$ crystals can cover the metal surface and hinder mass transfer of relevant species and affect the rates of the anodic and cathodic reactions [9].

2.2 Carbonate Scales ($CaCO_3$ and $MgCO_3$)

2.2.1 Solubility in Water

$CaCO_3$ and, to a lesser extent, $MgCO_3$ are amongst the most observed scales in oil production systems, and often exist as mixed carbonates; other examples of scales include $BaSO_4$ and $SrSO_4$. Precipitation happens when their saturation degree is greater than unity. Similarly to $FeCO_3$, the solubilities of $CaCO_3$ (calcite in this paper) and

$MgCO_3$ decrease with increasing temperature. The available correlations for calculation of K_{sp} of $CaCO_3$ and $MgCO_3$ do not take into account the effect of ionic strength, unlike siderite, as shown in Equations (18) and (19), respectively [37, 38]. Therefore, for calculation of the saturation degree of these carbonates, the activity of ions should be considered rather than concentration. Equation (20) and (21) express how to calculate saturation degree for $CaCO_3$ and $MgCO_3$, accordingly.

$$logK_{sp,CaCO_3} = -171.9065 - 0.077993 * T_k + \frac{2839.319}{T_k} + 71.595 * LogT_k$$

Equation 18

$$logK_{sp,MgCO_3} = 7.267 - \frac{1476.604}{T_k} - 0.033918 * T_k$$ Equation 19

$$S_{CaCO_3} = \frac{a_{Ca^{2+}} * a_{CO_3^{2-}}}{K_{sp,CaCO_3}}$$ Equation 20

$$S_{MgCO_3} = \frac{a_{Mg^{2+}} * a_{CO_3^{2-}}}{K_{sp,MgCO_3}}$$ Equation 21

$FeCO_3$ has the lowest solubility compared to $CaCO_3$ and $MgCO_3$. It means that in the same environmental condition, $FeCO_3$ reaches saturation prior to $CaCO_3$ and $MgCO_3$.

Figure 1 depicts how the solubility product constant (K_{sp}) of such carbonates change with temperature based on Equations 15, 18, and 19 (for consistency of the results, ionic strength is set to zero for Equation 15). Earlier studies on $MgCO_3$ solubility have been conducted at specific temperatures and then the results were extrapolated to other conditions. This approach has led to discrepancies in the reported solubility for

$MgCO_3$ at different temperatures [39, 40]. Bénézeth, *et al.*, recently proposed Equation (19) for $MgCO_3$ (magnesite) solubility, which was derived from extensive experimental solubility data conducted on synthetic magnesite at temperatures from 50 to 200°C in 0.1 mol kg^{-1} NaCl solutions with CO_2 partial pressure of 4 to 30 bars [38].

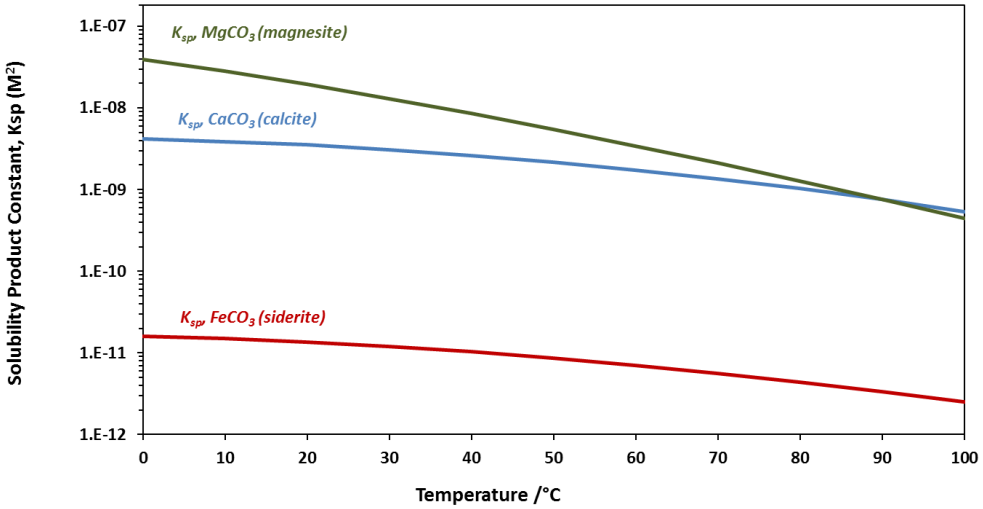

Figure 1. Solubility products of siderite, calcite, and magnesite *versus* temperature

2.2.2 Isostructurality of Calcite and Magnesite with Siderite

Being the main constituent of limestone, calcite ($CaCO_3$) is one of the most commonly observed minerals in sedimentary systems including oil reservoirs. Calcite crystallizes with a hexagonal unit cell as shown in Figure 2.

Calcite ($CaCO_3$) and magnesite ($MgCO_3$) are isostructural with siderite ($FeCO_3$) meaning that they share the same crystal structure; note the trigonal carbonate anions packed between the calcium cations in Figure 2. Each calcium is shielded by six oxygens from six different carbonates (Ca-O distance *ca.* 2.4 Å). Single unit cells of these

minerals are shown in Figure 3 through Figure 5. Each unit cell is shown perpendicular to their *xy*-plane. Note the maintenance of isostructurality for each phase, with metal cations at apices and within the unit cell. All the images related to crystal structure are generated by CrystalMaker® software.

A less common orthorhombic $CaCO_3$ is aragonite as shown in Figure 6. Heavier alkaline earth elements, as well as lead, crystallize carbonates with this structure, such as strontianite ($SrCO_3$), witherite ($BaCO_3$) and cerussite ($PbCO_3$) [12]. The key difference of aragonite-type calcium carbonate from the calcite-type is that each calcium is shielded by nine oxygens from five different carbonate ions (Ca-O distance 2.4-2.6 Å). Consequently, the pseudo-octahedral geometry around each metal cation no longer applies. In addition, aragonite-type calcium carbonate is likely metastable, readily converting to calcite.

Magnesite, siderite, and calcite have the same unit cell type and similar cation radii and can co-exist in a solid solution [12]. Ca^{2+} and Mg^{2+} can replace Fe^{2+} in the crystal structure of $FeCO_3$ and form a mixed substitutional solid solution. These substitutions have the potential to change the protective properties of $FeCO_3$ against further corrosion, as reported by various researchers [41-43]. Table 2 shows key structural parameters of these carbonates.

Table 2. Key structural parameters for magnesite, siderite, and calcite

Formula and Name	Cation Radius (Å)	Unit Cell Type	a (Å)	c (Å)	Density (g/cm^3)
$MgCO_3$ (magnesite)	0.72	hexagonal	4.59	14.87	3.01
$FeCO_3$ (siderite)	0.78	hexagonal	4.72	15.46	3.94
$CaCO_3$ (calcite)	1.00	hexagonal	4.99	17.04	2.71

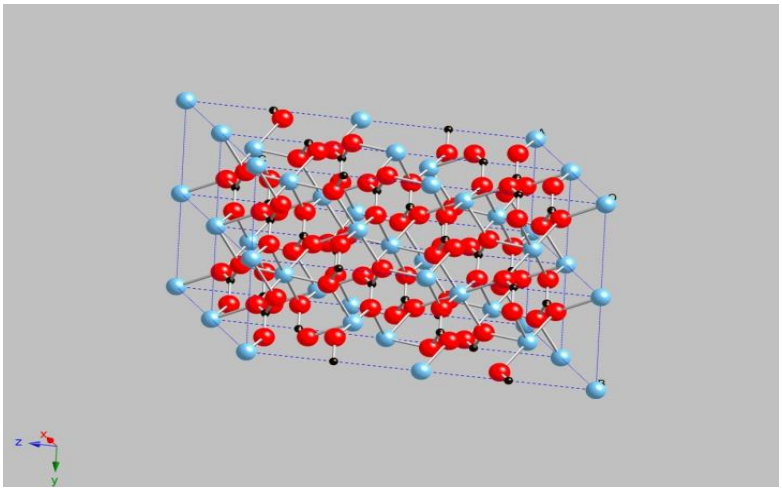

Figure 2. Hexagonal crystal structure of calcite ($CaCO_3$; blue = Ca, red = O, black =C), four-unit cells

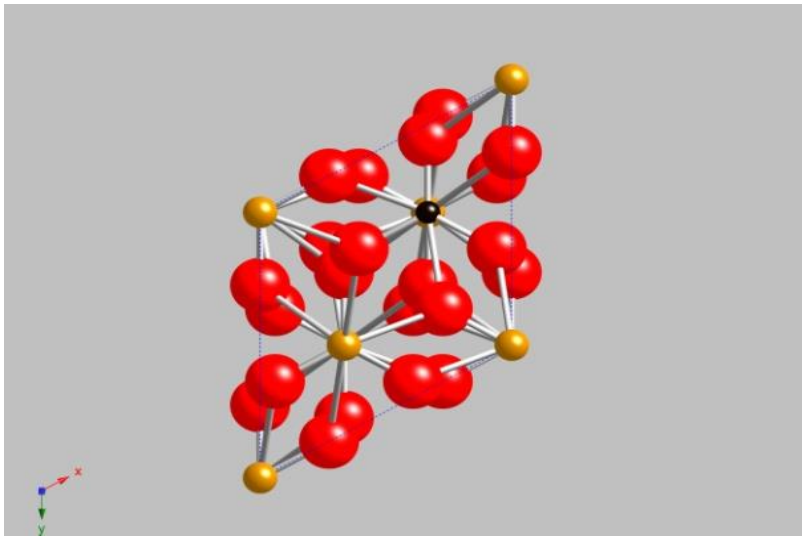

Figure 3. Hexagonal single unit cell of siderite ($FeCO_3$; tan = Fe, red = O, black =C)

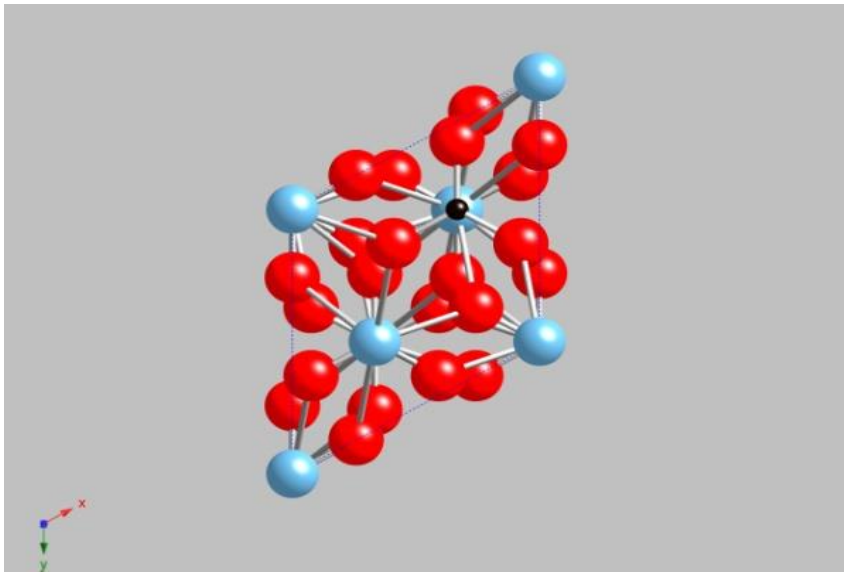

Figure 4. Hexagonal single unit cell of calcite ($CaCO_3$; blue = Ca, red = O, black =C)

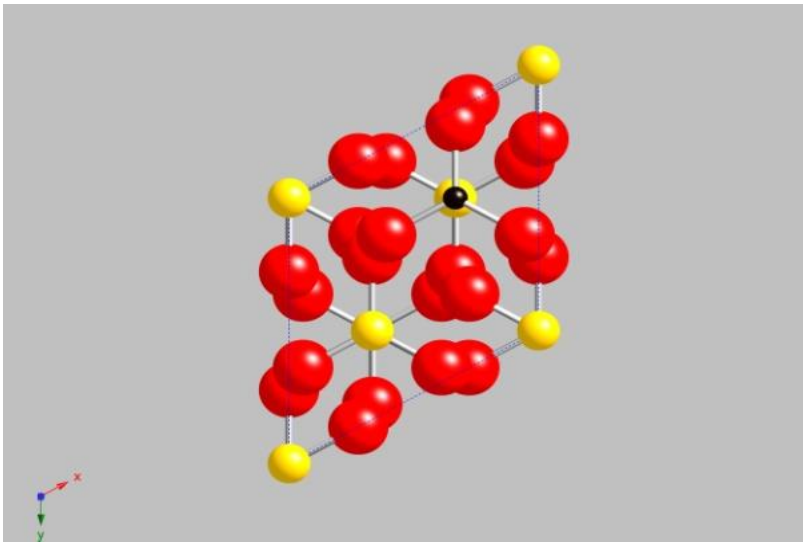

Figure 5. Hexagonal single unit cell of magnesite ($MgCO_3$; yellow = Mg, red = O, black =C)

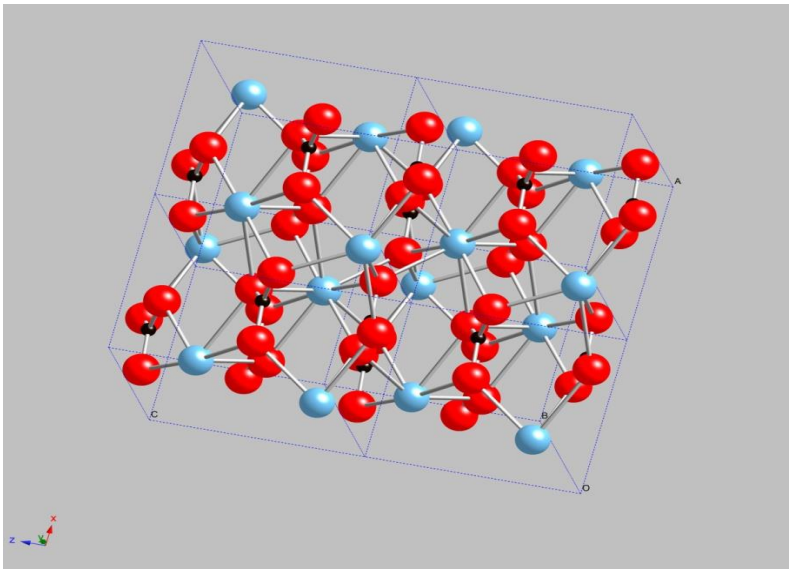

Figure 6. Orthorhombic crystal structure of aragonite ($CaCO_3$; blue = Ca, red = O, black =C), four unit cells

2.3 A Critical Literature Review: Effect of Ca^{2+} and Mg^{2+} on CO_2 Corrosion

Since a limited number of corrosion studies have been conducted using Ca^{2+} and Mg^{2+}, the corrosion mechanisms have not been methodically characterized. However, the few experimental studies conducted on this topic have shed some lights on some aspects of CO_2 corrosion in the presence of these alkaline earth cations. A review of the available literature is provided below, which covers the main messages of each paper and their shortcomings. The methodology of the current research project is based on the findings and conclusions obtained throughout the critical review of the literature provided in this section.

Eriksrud and Sontvedt conducted one of the earliest studies to evaluate the effect of Ca^{2+} and Mg^{2+} along with other ions on CO_2 corrosion behavior of API 5L X52 specimens [44]. Potentiodynamic sweeps were conducted for three different brines with

0, 400 and 1200 ppm of Ca^{2+} at 20°C, 1 bar partial pressure of CO_2 and over a pH range of 5.80 to 7.39. They concluded that formation of protective $FeCO_3$ layers enriched with Ca^{2+} resulted in a drop in corrosion rate of mild steel while the effect of Mg^{2+} on the general corrosion rate was reported to be negligible. One of the shortcomings of this research was that experimental durations were relatively short (2 days); therefore, possible phase transformation of the precipitated carbonates has not been taken into account. $CaCO_3$ has three polymorphs, mineralogically named calcite, aragonite, and vaterite. Calcite is the most stable form of these $CaCO_3$ polymorphs [45]. There have been reports in the literature that aragonite can transform to calcite after several days during corrosion experiments, resulting in possible change of mechanical properties [44].

Zhao, *et al.*, claimed that the corrosion rate decreased in the "short term" in the presence of Ca^{2+} and Mg^{2+}, but that there was no special difference for "long-term exposure" [41]. They postulated that the availability of Ca^{2+} and Mg^{2+} promoted the rapid formation of a protective layer in the short-term (before 72 hours), which resulted in lower general corrosion rates. On the other hand, without Ca^{2+} and Mg^{2+}, a protective layer could form only with longer exposure time when Fe^{2+} concentration was sufficient for precipitation of corrosion products. They conducted experiments at 90°C and CO_2 pressure of 25 bars, with 1000 ppm Mg^{2+} and 6000 ppm Ca^{2+} in solution. In addition to the corrosion behavior, the corrosion product morphology and composition were changed by the presence of Ca^{2+} and Mg^{2+} in the aqueous electrolyte. Inspection of the XRD data indicated that the most intense peak occurred at a position of less than 30° 2θ, which would be consistent with the larger Ca^{2+} being the major cation within the formed metal

carbonate lattice. Peak broadening also seems to have occurred, consistent with inhomogeneity within the corrosion product-scale hybrid surface layers. The authors described the primary corrosion product as "amorphous $Fe(Ca,Mg)(CO_3)_2$" which was thicker than " crystalline $FeCO_3$". Although pH plays a dominant role in corrosion and scaling processes, it was not reported in this work.

Gao, *et al.*, conducted autoclave corrosion experiments with a simulated brine from an oilfield to investigate the formation of surface layers at different test conditions and their effect on CO_2 corrosion of mild steel [46]. The experimental conditions included different flow rates (0, 0.5 and 1 m/s) and partial pressures of CO_2 (0.1, 0.3 and 1 MPa) while the temperature was set to 65°C, with 64 ppm Ca^{2+}, and 72 ppm Mg^{2+}. Based on energy dispersive X-ray spectroscopy (EDS) and X-ray diffraction (XRD) patterns, they suggested the formation of distinct phases of $FeCO_3$, $CaCO_3$, and $MgCO_3$ at 0.1 MPa pCO_2, a solid solution of "$(Fe,Ca,Mg)CO_3$" at 0.3 MPa CO_2 partial pressure, and a solid solution of "$(Fe,Ca)CO_3$" at 1 MPa CO_2 partial pressure. Figure 7 shows an example of X-ray diffraction patterns of the surface layers formed on X65 carbon steel specimens at their quiescent condition. According to their work, at higher CO_2 pressure both general and localized corrosion increased. However, in these experiments, the authors also did not report solution pH.

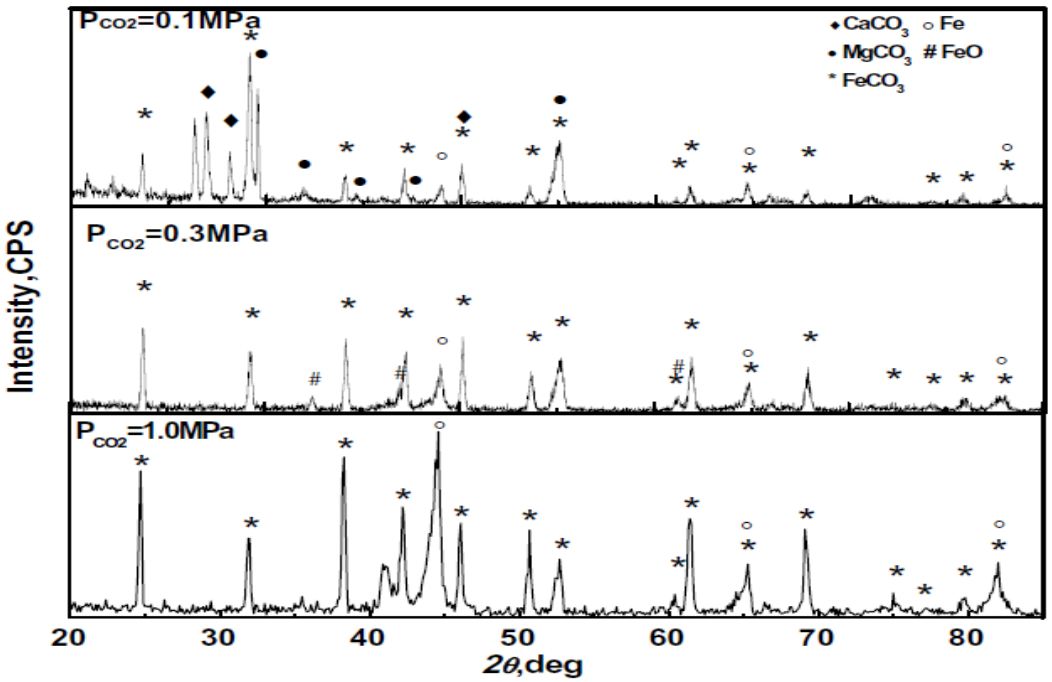

Figure 7. XRD patterns of the layers formed on X65 carbon steel specimens at various pCO_2 values, quiescent condition, 65°C, 64 ppm Ca^{2+}, and 72 ppm Mg^{2+} (reproduced with permission [46])

X. Jiang, *et al.*, conducted experiments in a glass cell at 57 °C, in the presence of 1000 ppm Ca^{2+} and at different concentrations of Cl^- to distinguish the effect of Cl^- and Ca^{2+} on pitting phenomena [47]. They carried out three experiments with different electrolytes, specifically 3 wt.% NaCl, 3 wt.% NaCl + 1.5 wt.% $CaCl_2$, and 4.6 wt.% NaCl. Based on electrochemical impedance spectroscopy (EIS), they reported pitting initiation times were 70 hours for the experiment with 3 wt. % NaCl, 41 hours for the 3 wt.% NaCl + 1.5 wt.% $CaCl_2$ electrolyte, and 23 hours for 4.6% wt.% NaCl. Figure 8 illustrates Nyquist plots over time for the experiment with 3 wt.% NaCl + 1.5 wt.% $CaCl_2$; the specimens were made of API N80 steel. The diameter of the Nyquist semicircles increase over time up to 41 hours. The authors attributed this behavior to the

formation of protective layers on the steel surface and improvement of the protectiveness of the formed surface precipitates over time. However, the impedance noticeably decreased as the immersion time reached 49 hours. According to Figure 8, the impedance, again, gradually increased over the course of the experiment up to 96 hours. The author related this phenomenon to propagation and "repassivation", which the authors of this review interpret associated with pit death (stoppage of pitting corrosion). They also claimed that, while Cl^- caused pitting, the presence of Ca^{2+} delayed pitting initiation. While the authors did not propose a mechanism for pitting attack by Cl^-, their claim is in contrast with some other studies that suggest Cl^- has no effect on pitting corrosion of carbon steels [48, 49]. Another shortcoming of this work is that the authors did not measure the depth and width of pits; therefore, the magnitude of pitting rate was unquantified. In addition, the general corrosion rate for the different electrolytes was not reported.

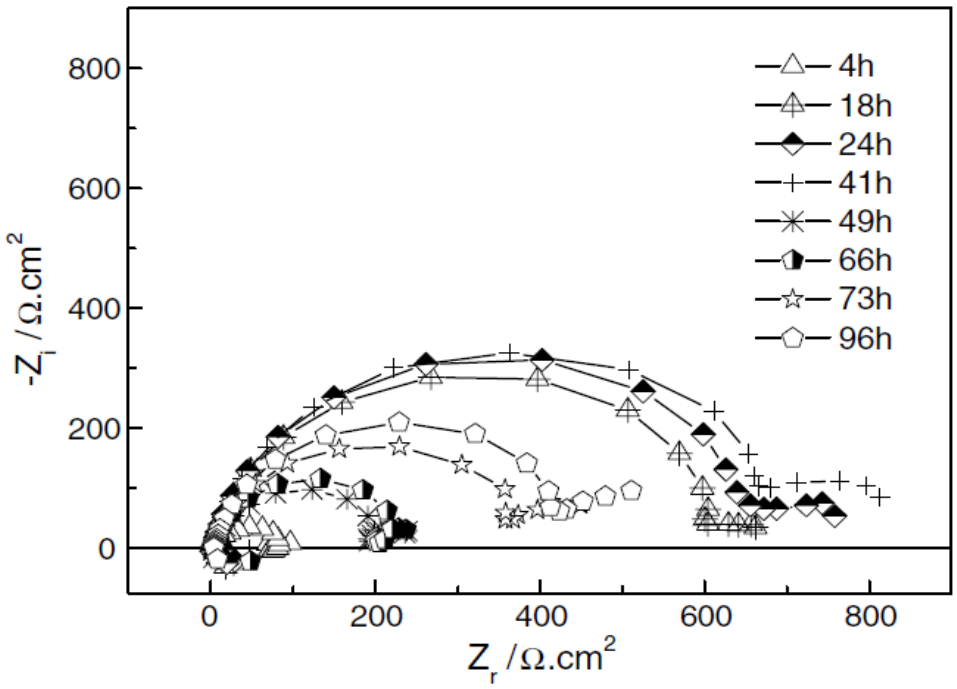

Figure 8. Nyquist plots *versus* time for API CT5 N80 materials in 3 wt.% NaCl + 1.5 wt.% $CaCl_2$ electrolyte at 57°C (reproduced with permission [47])

Ding, *et al.*, conducted 10-day autoclave experiments with X65 specimens at 75°C and 10 bar pCO_2 with up to 512 ppm of Ca^{2+} and 78 ppm Mg^{2+} to study the effect of Ca^{2+} concentration on corrosion behavior [43]. They reported that the corrosion rate increased as the concentration of Ca^{2+} increased, as shown in Figure 9. They also reported that the presence of calcium ions changed the corrosion product layer's crystal size. The authors concluded that the addition of Ca^{2+} forced the corrosion product layer crystals into morphological features that were "bigger" and "looser"; therefore, they did not act as a sufficiently protective barrier and, consequently, allowed corrosive species to more readily diffuse to the metal surface. They also showed XRD data, with shifted peaks from the $FeCO_3$ peak position with increasing Ca^{2+} concentration in the electrolyte. This shift is the result of the change in the unit cell of the corrosion products with the formation of

mixed carbonate layers ($Fe_{1-x}Ca_xCO_3$). It is noteworthy that magnesium was undetected in their corrosion product. However, this is unsurprising as Mg^{2+} was present at a concentration close to its equilibrium concentration in relation to the solubility of $MgCO_3$ in water at the applied physicochemical conditions at the beginning of the experiment. The authors also reported formation of a bilayer on the steel surface. The concentration of calcium in the surface outer layer was higher than the inner layer, as confirmed by EDS and shown in Figure 10.

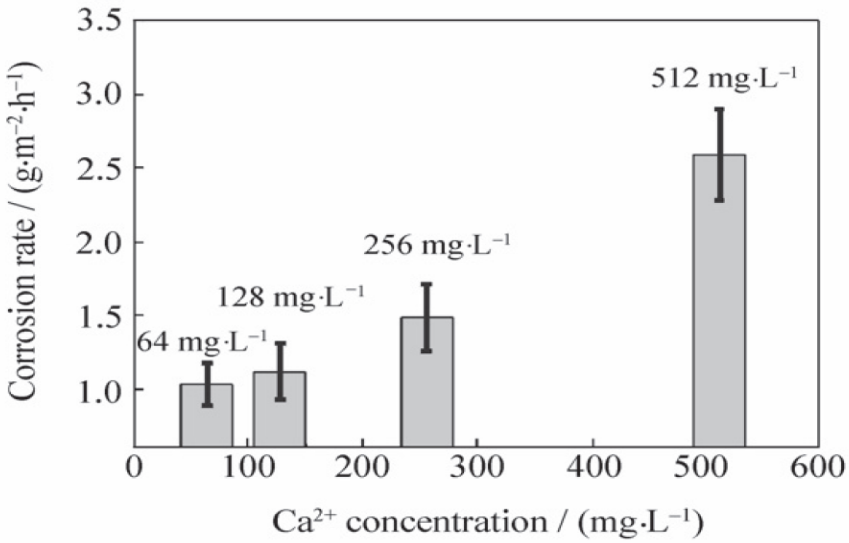

Figure 9. Corrosion rate *versus* different concentrations of Ca^{2+} for X65 specimens at 75°C and 10 bar pCO_2 after 10 days of exposure (reproduced with permission [43])

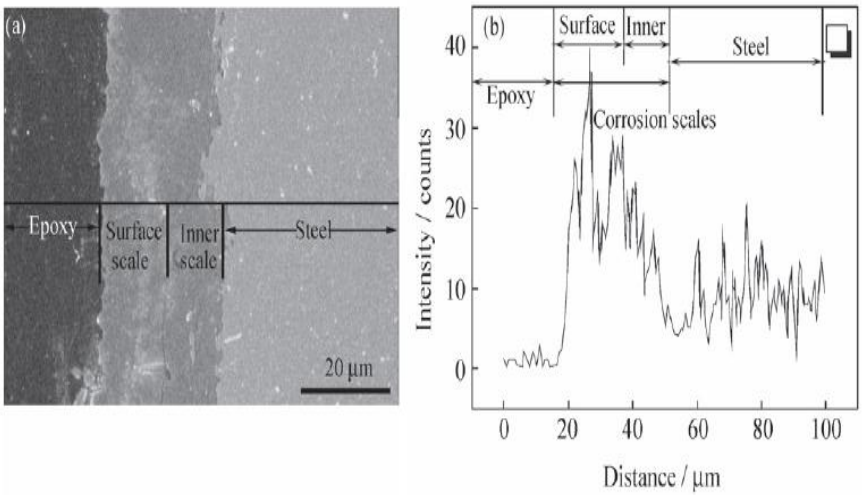

Figure 10. Elemental analysis for calcium in the bilayers formed on the steel surface. Note the higher concentration of calcium in the outer layer ("surface scale") compared to the inner layer ("inner scale") when the test solution contained 512 ppm Ca^{2+} (reproduced with permission [43])

Esmaeely, *et al*., studied the effect of Ca^{2+} on CO_2 corrosion at low and high concentrations of Ca^{2+} in 7-day glass cell experiments at 80°C and pCO_2 0.53 bar [44]. They reported that for a low concentration of Ca^{2+} (up to 100 ppm) a protective layer formed and the corrosion rate decreased with time. However, for the electrolyte with a high initial concentration of Ca^{2+} (1,000 and 10,000 ppm), the formed layers were non-protective and corrosion rate did not drop throughout the experiments; see Figure 11. The authors also observed that the use of the electrolyte with 10,000 ppm Ca^{2+} led to severe pitting corrosion. In this research, the pH for the baseline test and the test with the presence of high concentration of Ca^{2+} were not identical. Upon adding such a high initial concentration of calcium ions (added as $CaCl_2.2H_2O$), massive precipitation of $CaCO_3$ acidified the electrolyte according to Reaction (22). Therefore, it can be postulated that the increase in the corrosion rate was due to the lowered solution pH values rather than

increased calcium ion concentration. pH behavior of electrolyte with different concentrations of Ca^{2+} is depicted in Figure 12. It is worth noting that [Fe^{2+}], [Ca^{2+}], and pH were not kept constant over the course of experiments.

$$Ca^{2+}(aq) + H_2CO_3(aq) \rightarrow CaCO_3(s) + 2H^+(aq) \qquad \text{Equation 22}$$

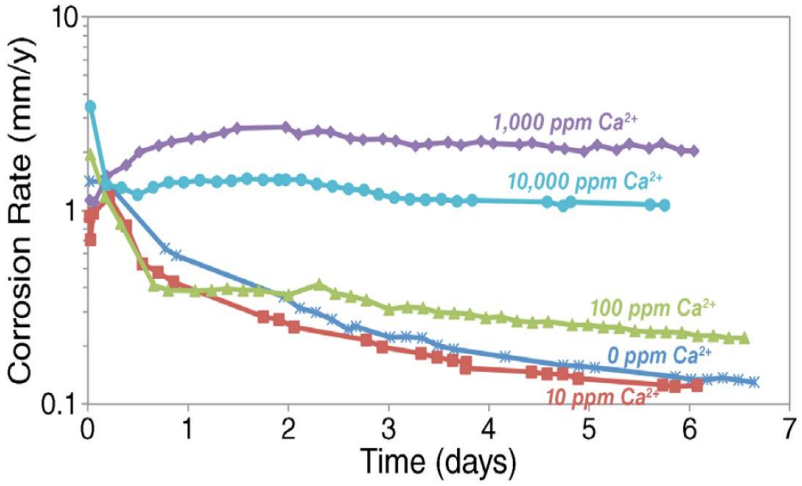

Figure 11. Corrosion rate over time measured by LPR for different initial concentration of calcium ions at 80°C, pCO_2 0.53 bar, 1wt. % NaCl, and 10 ppm Fe^{2+} (reproduced with permission [44])

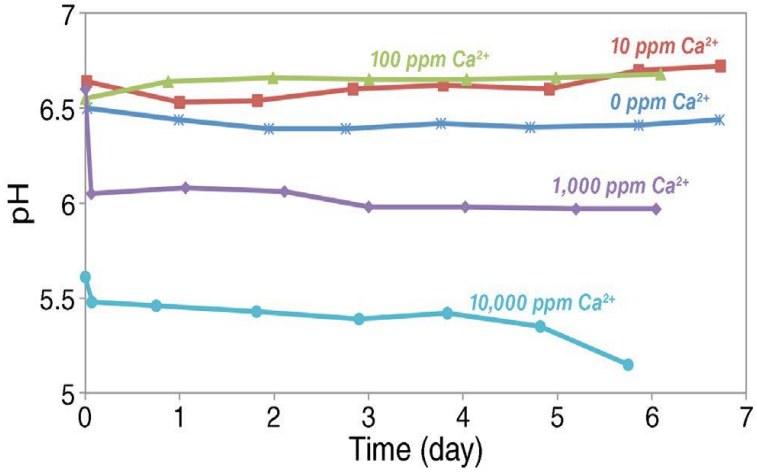

Figure 12. Variation of pH over time for different concentrations of Ca^{2+} at 80°C, pCO_2 0.53 bar, 1wt. % NaCl, and 10 ppm Fe^{2+} (note the difference in the electrolytes' pH caused by precipitation of $CaCO_3$ in high concentration of calcium ions). reproduced with permission [44]

Tavares, *et al.*, conducted long-term (28 days) autoclave experiments to study the effect of $CaCO_3$ on the corrosion behavior of low carbon steel in high partial pressures of CO_2 [50]. The test electrolytes were saturated with CO_2 and NaCl at 80°C, the pCO_2 was 15 MPa. They designed two series of experiments, namely baseline and $CaCO_3$-saturated tests. The baseline test was carried out in the absence of $CaCO_3$. The $CaCO_3$-saturated test was conducted in the presence of a significant excess amount of solid $CaCO_3$ in the electrolyte (0.5 mol/kg; 10 times higher than its solubility limit), ensuring the solution was saturated with respect to $CaCO_3$ over the course of experiments. They claimed that general corrosion was predominant for both test series rather than pitting corrosion. Indeed, they reported a decline in the corrosion rate over time, as determined by mass loss. This behavior was observed for both tests, the authors related their findings to the formation of protective "corrosion scales". Figure 13 shows SEM images of their "corrosion scale" morphologies after 72, 336, and 672 hours of exposure to electrolytes

with and without $CaCO_3$. For the $CaCO_3$-saturated electrolyte, they reported the formation of a carbonate solid solution with an average chemical composition of $Fe_{0.79}Ca_{0.21}CO_3$, concluded from EDS data. The corrosion product from the baseline condition was reported to be pure $FeCO_3$, with apparently larger crystal size compared to the "corrosion scales" formed in the presence of $CaCO_3$ (more evident after 72 and 336 hours; see Figure 13). It is interesting that even at such low initial pH values (2.71 and 4.7, respectively, for electrolyte without/with $CaCO_3$) carbonate layers precipitated. The authors did not measure or calculate pH at the end of their experiments. However, the solution water chemistry would have dramatically changed in the 1-liter autoclave over the course of experiments and resulted in final pH values significantly higher than for the initial conditions [51]. Therefore, high pH and Fe^{2+} concentration (introduced to the solution from the corroding surface) has favored precipitation of $FeCO_3$ and $Fe_xCa_{1-x}CO_3$ over time in these experiments.

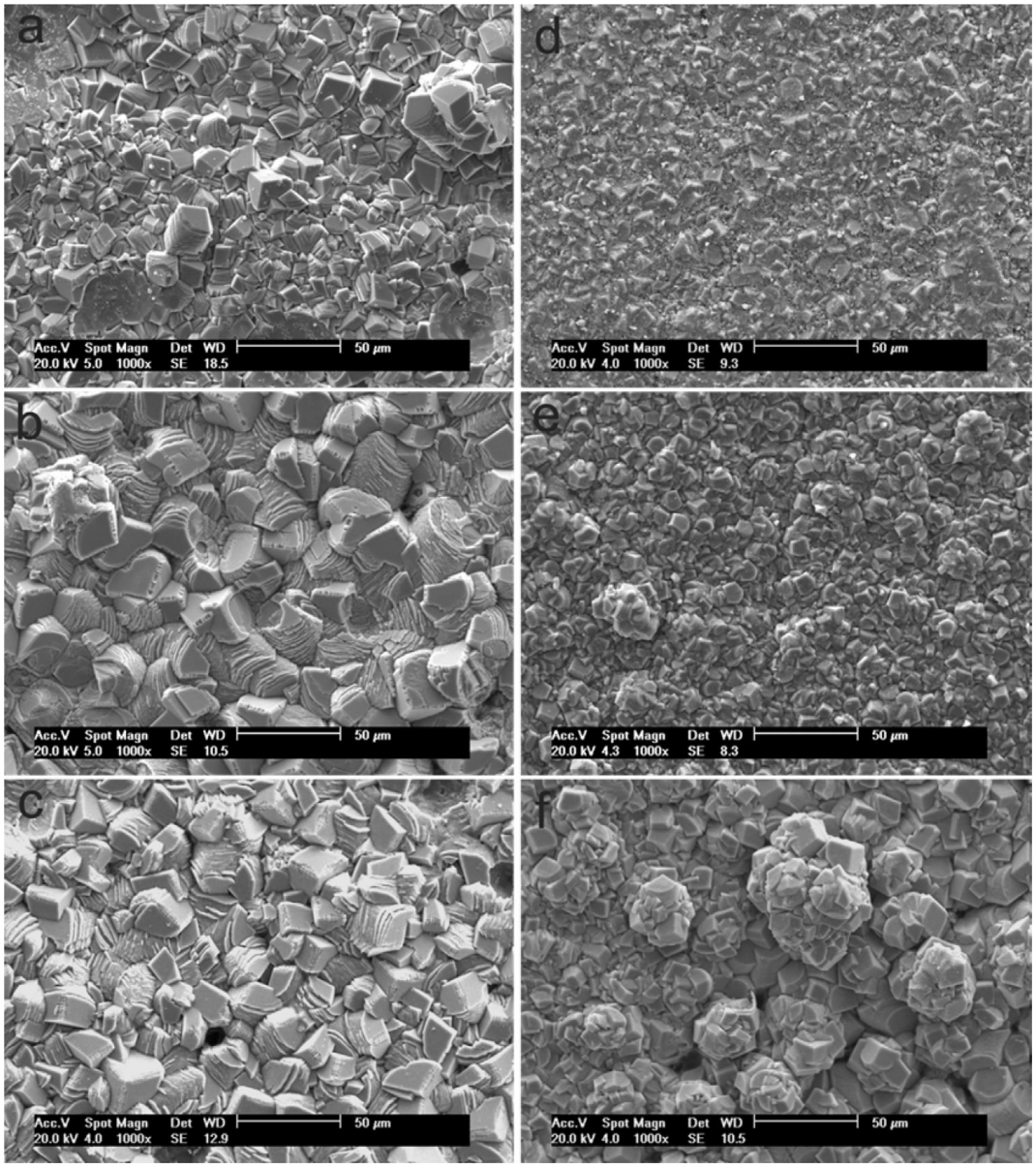

Figure 13. SEM images of surface layers' morphology formed on low carbon steel after 72, 336, 672 hours of exposure in CO_2-saturated solutions (a, b, and c) without and (d, e, and f) with $CaCO_3$ (reproduced with permission [50])

The authors also reported that the average corrosion rate in the presence of $CaCO_3$ was lower when compared to the solution without $CaCO_3$, as shown in Figure 14. This was mainly due to a different initial pH of the two electrolytes rather than a direct effect

of $CaCO_3$ on surface layer protectiveness against corrosion. Indeed, the corrosion rates after 336 and 672 hours of exposure were almost identical for experiments with and without $CaCO_3$, meaning that water chemistry of the system was unchanged after 336 hours. This work was one of the few corrosion studies conducted in electrolytes saturated with $CaCO_3$ and NaCl at a high partial pressure of CO_2. However, the main shortcoming of this research is that comparison of the two tests, with and without $CaCO_3$, are problematic due to the considerable difference in the initial solution pH for each case; pH 4.7 for the solution with $CaCO_3$ and pH 2.71 for the solution without $CaCO_3$. However, this work showed that even in high concentrations of Ca^{2+} (around 2000 ppm; calculated from data provided by the authors), if the solution was saturated with respect to $CaCO_3$, a protective layer formed on the steel surface, similarly to the experiment conducted in the absence of $CaCO_3$. This is in contrast with other studies, as described earlier, reporting that with roughly similar Ca^{2+} concentrations, but different water chemistry conditions, a protective layer could not form [43, 44]. What can be concluded from this study is that the saturation degree of the carbonates is a critical parameter, rather than calcium and magnesium ion concentration. In evaluating the effect of Ca/Mg-containing aqueous solutions on CO_2 corrosion, solution pH measurements before and after the experiments are necessary.

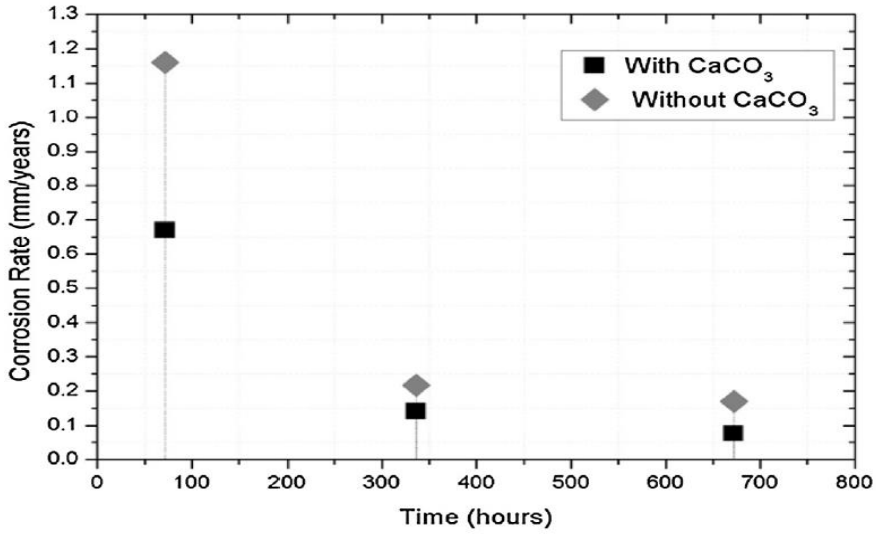

Figure 14. Corrosion rate, by weight loss, *versus* exposure time for test electrolytes with and without $CaCO_3$ at 80°C, pCO_2 15 MPa , solution saturated with CO_2 and NaCl (reproduced with permission [50])

Bekhrad *et al.,* have conducted electrochemical experiments to evaluate the fate of general and localized corrosion of carbon steel covered with $CaCO_3$ scale in CO_2 environments [52]. The API 5L X52 specimen was covered with a $CaCO_3$ scale layer decapitated from a separate supersaturated solution and then transferred to the main corrosion test cell. They concluded that the presence of $CaCO_3$ scale on the carbon steel resulted in lowering the general corrosion rate and that specimens were not susceptible to localized corrosion in presence of $CaCO_3$ scale. In oilfield pipelines, after precipitation of $CaCO_3$ scale from a supersaturated condition, the brine would still have dissolved Ca^{2+} (now in unity saturation with respect to $CaCO_3$). Although the work by Bekhrad *et al.,* is one of the few works to evaluate protectiveness of $CaCO_3$ scale, the employed methodology is not resembling oil pipelines since the CO_2 corrosion experiment with the "calcite-covered carbon steel" was performed in solution without presence of Ca^{2+}. There

has been other research works in the context of external corrosion of buried pipelines, under cathodic protection, where $CaCO_3$ scale precipitated on the steel from soils rich with calcium ions. For example, Ghanbari, *et al.*, conducted experiments to evaluate the effect of $CaCO_3$ scale formation on alternating current (AC) induced corrosion rates (corrosion due to stray alternating current is common in external corrosion of oil pipelines) of X65 carbon steel at atmospheric pressure (open air) and room temperature [53]. They concluded that $CaCO_3$ deposits did not have any effect on AC corrosion rates other than by decreasing the exposed surface area of the steel. The experimental conditions of these tests were designed to add more understanding to the influence of external AC corrosion of a carbon steel pipeline under cathodic protection and in $CaCO_3$ scaling conditions. With so few references available that address the influence of pure $CaCO_3$ scale on CO_2 corrosion mechanisms, a true gap in the knowledge related to the internal corrosion of oil and gas pipelines has been identified.

CHAPTER 3: RESEARCH GAP, OBJECTIVES, AND HYPOTHESES

3.1 Research Gaps and Objectives

From a general literature review on this topic, one cannot conclusively describe the true effect of Ca^{2+} and Mg^{2+} on CO_2 corrosion for different water chemistries and operating conditions. There are studies claiming that the general corrosion rate is higher in the presence of calcium ions [43, 44]. Conversely, some researchers reported the exact opposite conclusions [50, 54]. In addition, there are also experiments suggesting magnesium ions have no effect on CO_2 corrosion processes [54]. Some researchers claimed that calcium ions initiate pitting corrosion attack [44], while others stated that the presence of Ca^{2+} would postpone the pitting tendency on carbon steel [47]. These discrepancies about the true effect of Ca^{2+} and Mg^{2+} on CO_2 corrosion necessitate development of systematic and well-designed procedures in corrosion testing for understanding the relevant issues surrounding CO_2 corrosion in the presence of these ubiquitous alkaline earth cations.

One of the important parameters that has caused discrepancies in the open literature is the uncertainty related to the saturation degree of carbonates in the bulk solutions of autoclave and glass cell experiments. This parameter is not straight forward to measure, especially in autoclave settings, and is changing with time as corrosion and precipitation occur. Saturation degree of the bulk solution is as important a parameter as the individual ion concentrations when studying the effect of Ca^{2+} and Mg^{2+} on corrosion mechanisms. Precipitation kinetics of carbonates is greatly influenced by the bulk saturation degree as the main driving force [55, 56]. Most researchers have disregarded

this important environmental characteristic, solely relying on initial ion concentration as the core influencing parameter. Furthermore, the majority of available research on this topic has been conducted in conditions where the water chemistry of the systems was unstable (uncontrolled) and, in some cases, completely ignored (e.g., pH is unreported) [41, 43]. In addition, the flow characteristics of most of the experimental setups were not appropriately studied and/or reported. Corrosion processes and formation of corrosion products/scales are influenced by the mass transfer of the relevant ions between the bulk solution and the metal surface [57]. These important operating details can significantly affect results, making experiments impossible to reproduce independently, and making any conclusions about the mechanisms highly dependent on the experimental procedure.

The objective of the current research is to systematically study the effect of water chemistry of the electrolyte on the CO_2 corrosion mechanism in the presence of Ca^{2+} and Mg^{2+} and their carbonate scales ($CaCO_3$ and $MgCO_3$), with focus on carbonate saturation, ion concentrations, and pH. Particular efforts are made to control and report the water chemistry (pH, $[Fe^{2+}]$, $[Ca^{2+}]$, and $[Mg^{2+}]$) and flow characteristics of the designed glass cell test system over the course of experiments. For a precise and clear study of the effect of Ca^{2+} and Mg^{2+} on CO_2 corrosion, experiments are conducted in relation to two distinct saturation scenarios with respect to $CaCO_3$ and $MgCO_3$:

1) Non-scaling conditions: when the solution is undersaturated, or at the saturation point, with respect to the $CaCO_3$ and $MgCO_3$ which can thermodynamically form but which precipitation is not kinetically favored.

2) Scaling conditions: when the solution is supersaturated with respect to $CaCO_3$ and $MgCO_3$ which are expected to precipitate.

It is worth mentioning that in corrosion studies the test solution, usually made of a small volume, eventually becomes saturated with respect to $FeCO_3$ due to the corrosion process and production of Fe^{2+}. At such a condition, precipitation of $FeCO_3$ as the corrosion product is expected.

3.2 Hypotheses

In non-scaling bulk solution condition:

If the solution is undersaturated and/or saturated with respect to $CaCO_3$ and/or $MgCO_3$, Ca^{2+} and/or Mg^{2+} can incorporate in the $FeCO_3$ crystal structure, forming a substitutional solid solution which would not change the corrosion products protectiveness.

In scaling bulk solution condition:

If the solution is supersaturated with respect to $CaCO_3$ and/or $MgCO_3$, carbonates with distinct boundaries can form affecting the homogeneity and porosity of corrosion products, compromising their protectiveness and leading to localized corrosion.

CHAPTER 4: EXPERIMENTAL SETUP AND MASS TRANSFER CHARACTERIZATION

4.1 Controlled Water Chemistry Glass Cell Setup

As mentioned in the introduction, the discrepancies seen in the literature regarding the effect of Ca^{2+} and Mg^{2+} on CO_2 corrosion are in part due to poorly controlled water chemistry, resulting in unknown bulk saturation degree of metal carbonates, and poorly defined mass transfer conditions. Therefore, one main objective in this research was to overcome these issues using an improved glass cell setup enabling control of the water chemistry, of the flow conditions, and measurements of corrosion rate with electrochemical and weight loss techniques.

In the newly designed glass cell, seven mild steel specimens, identical in size (1.5 cm^2 x 1.5 cm^2), were held in place using cylindrical PEEK rods as specimen holders (Figure 15 and Figure 16). One of the specimen holders was specially built with an electrical connection for *in situ* electrochemical measurements, while the other holders held specimens for weight loss and cross-section surface analysis; see Figure 16. All seven steel specimens experienced identical flow (*i.e.*, the same shear stress and mass transfer conditions) as they were all located at the same radial distance from the center of the glass cell (see Figure 15). An impeller was used to create uniform mass transfer characteristics and shear stress across the specimen surfaces. This improvement eliminated the non-uniformity of the flow and mass transfer characteristics experienced by the unstable hanging specimens in the conventional glass cell setup used in a previous study relating to this topic [44]. In the current study, the solution to surface area ratio is

almost 5 times larger than recommended [58], in order to avoid any significant changes in water chemistry. However, the effect of any increased concentration of ferrous ions released by the seven specimens corroding in 3-liters of solution was also addressed by the new cell design, as described below.

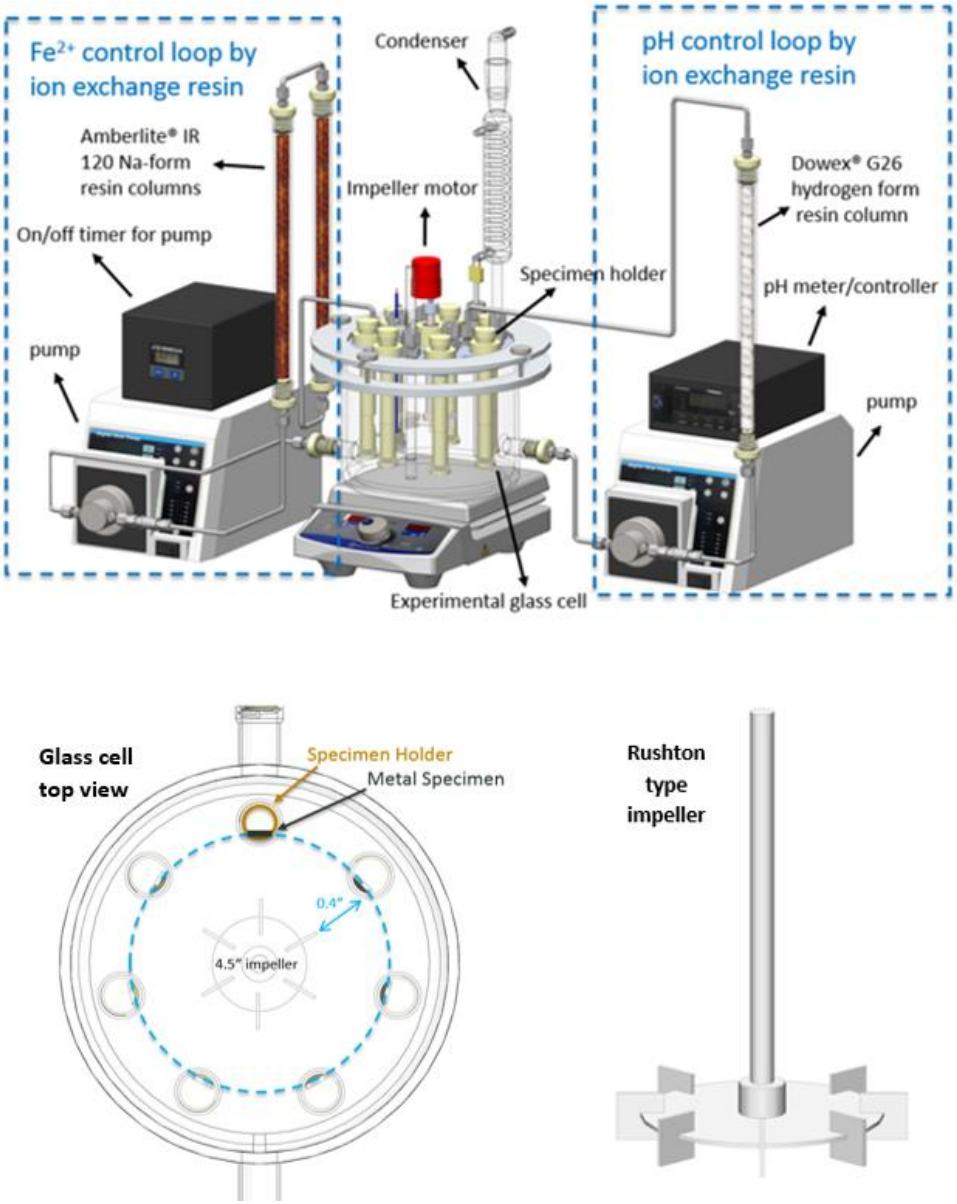

Figure 15. Schematic view of the system equipped with impeller and $[Fe^{2+}]/[H^{+}]$ control loops. The impeller diameter was 4.5″, the distance between the impeller blades and the specimen surface was 0.4″, and the glass cell had an 8″ internal diameter. (All drawings courtesy of Cody Shafer, ICMT, OU.)

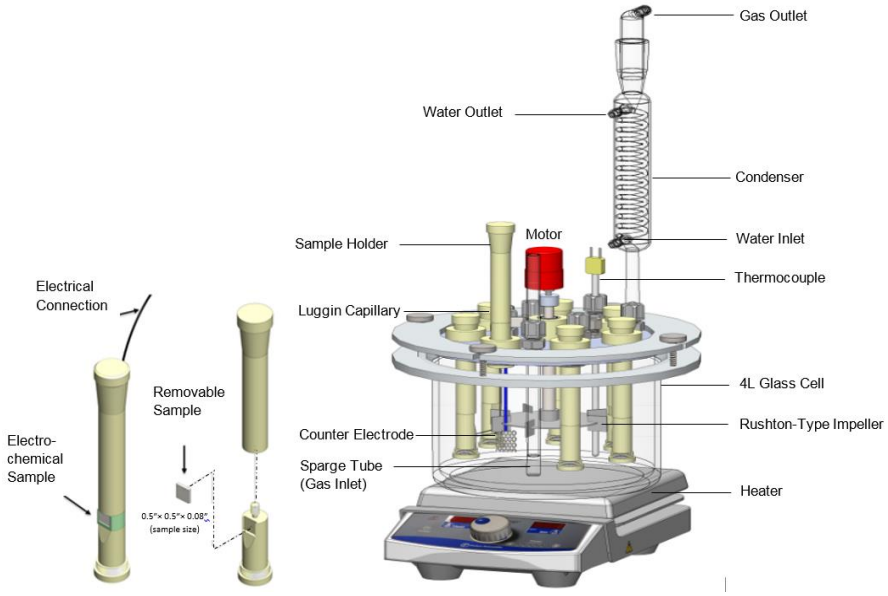

Figure 16. Schematic view of removeable specimen holder, electrochemical sample configuration, and the experimental setup.

The partial pressure of CO_2 was maintained by a continuous sparging of CO_2 into solution and the temperature was controlled by using a hot plate with thermocouple feedback, as it is traditionally done. However, specific improvements were made to control the water chemistry of the system (pH, $[Fe^{2+}]$, $[Ca^{2+}]$, $[Mg^{2+}]$). The pH and $[Fe^{2+}]$ controlled by using H-form and Na-form ion-exchange resins installed in two independent control loops attached to the main glass cell. Both types of ion exchange resin interchange ions by accepting cations from the solution and releasing either hydrogen ions (from the H-form resin) or sodium ions (from the Na-form resin) back to the solution to maintain a charge balance. To maintain the $[Fe^{2+}]$, a sample of the solution was collected and externally analyzed twice daily with a spectrophotometer (Thermo Scientific GENESIS 10 Vis) using phenanthroline as the colorimetric reagent [59]. When the measured $[Fe^{2+}]$ reached or exceeded the target value (for instance ~10 ppm for an

experiment conducted at pH 6.2), the pump moving the solution through the Na-form ion-exchange column was manually turned on to decrease the [Fe^{2+}]. An on/off timer was used to control the amount of time the pump would move the solution through the Na-form ion-exchange resin. The pH of the solution was maintained automatically using a pH controller to turn on or turn off the positive displacement pump moving the solution through the H-form ion-exchange column.

The ion-exchange resins employed to control the water chemistry of the solutions were polymeric compounds (cross-linked) with exchangeable cations based off the cations' affinity. The capability of such resins to proficiently trade cations in solution brands them advantageous for controlling water chemistry. Classically, ions with greater valence (bigger in size) have greater affinity compared to smaller ions with less valence. Affinity order of the typical cations used in resins are as following [60]:

$Hg^{2+} < Li^{+} < H^{+} < Na^{+} < K^{+} \approx < NH_4^{+} < Cd^{2+} < Cs^{+} < Ag^{+} << Mn^{2+} < Fe^{2+} < Cu^{2+} < Ni^{2+} < Co^{2+} < Ca^{2+} < Sr^{2+} < Pb^{2+} < Al^{3+} < Fe^{3+}$

The hydrogen-form resin (Dowex® G26 used in the current work) compensates the hydrogen cation in the solution by releasing its hydrogen and subsequently substituting it with Na^{+} cations present in the bulk solution, as described in Equation 23.

$$Na^{+} + R - H \rightarrow H^{+} + R - Na \qquad \text{Equation 23}$$

Likewise, the extra ferrous ions in the solution (introduced by corrosion processes) are removed by attaching to the polymeric backbone, freeing Na^+ that is released to the solution (see Equation 24).

$$Fe^{2+} + 2R - Na \rightarrow 2Na^+ + 2R - Fe \qquad \text{Equation 24}$$

More explanations about the efficiency of ion-exchange resins in corrosion studies are presented in a recent publication by Zhong, *et al.* [60].

In some experiments, the test solutions were kept saturated with respect to calcium carbonate over the course of 7-day experiments, corresponding to a constant $[Ca^{2+}]$ of approximately 160 ppm or 6000 ppm at pH 6.2 and 5.5, respectfully. This goal was achieved by maintaining a layer of solid calcium carbonate at the bottom of the glass cell. For $MgCO_3$ saturated experiments, $MgCl_2$ was used as the source of Mg^{2+}. The $[Ca^{2+}]$ and $[Mg^{2+}]$ were measured at the beginning and end of experiments using the Inductively Coupled Plasma (ICP) technique [61]. The results were in agreement with concentration values calculated using The Geochemist's Workbench software (using PHREEQC as the thermodynamic database) considering the non-ideality of the solution. The procedure for solution preparation in the presence of Ca^{2+} and/or Mg^{2+} will be explained in each experiment category.

4.2 Mass Transfer Characterization of the Glass Cell with Impeller

Defining the hydrodynamic and mass transfer conditions of any new experimental corrosion setup is essential when studying the influence of flow on corrosion, and helps ensure reproducibly of the results [62]. An equimolar ferri-ferrocyanide aqueous solution

is typically employed to define the mass transfer conditions for various flow geometries and related hydrodynamics [63]. The ferri-ferrocyanide coupled electrochemical reaction, Equation 25, displays very clear limiting currents that can be used to define the mass transfer coefficients of the ionic species. In the current experimental setup, a nickel specimen was used as the working electrode.

$$Fe(CN)_6^{3-} + e^- \leftrightharpoons Fe(CN)_6^{4-} \qquad \text{Equation 25}$$

Table 3 shows the experimental conditions for the mass transfer characterization experiments. Measurements were conducted at 40°C and 50°C to prove repeatability and to extend the applicability of the mass transfer correlation. Rotational speeds for measurements at each temperature ranged from 50 rpm to 200 rpm. Figure 17 depicts an example of potentiodynamic sweeps performed on a Ni electrode in 0.5 M KOH + 0.01 M $K_3Fe(CN)_6$ + 0.01 M $K_4Fe(CN)_6 \cdot 3H_2O$ solution at 50°C for each rotational speed. The limiting current in the cathodic region was then recorded and used to calculate the mass transfer coefficient k_m (m/s) as expressed in Equation (26) [64]. Finally, the dependence of the Sherwood (Sh) number on the Reynolds (Re) and Schmidt (Sc) numbers was defined by performing multiple regression to calculate the unknown constants pertaining to the specific geometry of the glass cell setup with this impeller.

$$k_m = \frac{i_{lim}}{nFC_b} \qquad \text{Equation 26}$$

$$Sh = \frac{k_m d}{D} \qquad \text{Equation 27}$$

$$Re = \frac{d^2 N}{\upsilon} \qquad \text{Equation 28}$$

$$Sc = \frac{\upsilon}{D} \qquad \text{Equation 29}$$

The obtained data was then used to fit the following classical correlation:

$$Sh = a\, Re^b\, S\, c^c \qquad \text{Equation 30}$$

This is expressed logarithmically as equation (31):

$$Sh = log\, a + b\, log\, Re + c\, log\, S\, c \qquad \text{Equation 31}$$

Parameter a, b, and c can be fitted by performing a multiple linear regression. The final coefficients are shown in Equation 32.

$$Sh = 0.47\, Re^{0.62} Sc^{0.33} \qquad \text{Equation 32}$$

Figure 18 shows the fitted results based on equation (32), a good agreement is observed.

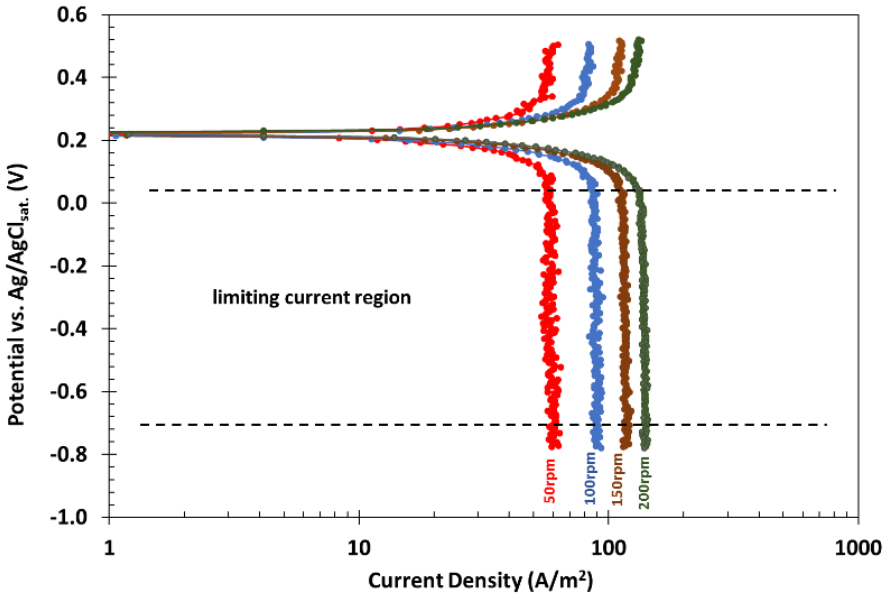

Figure 17. Limiting currents obtained at 50°C and varying rotational speeds using ferri-ferrocyanide coupled reactions

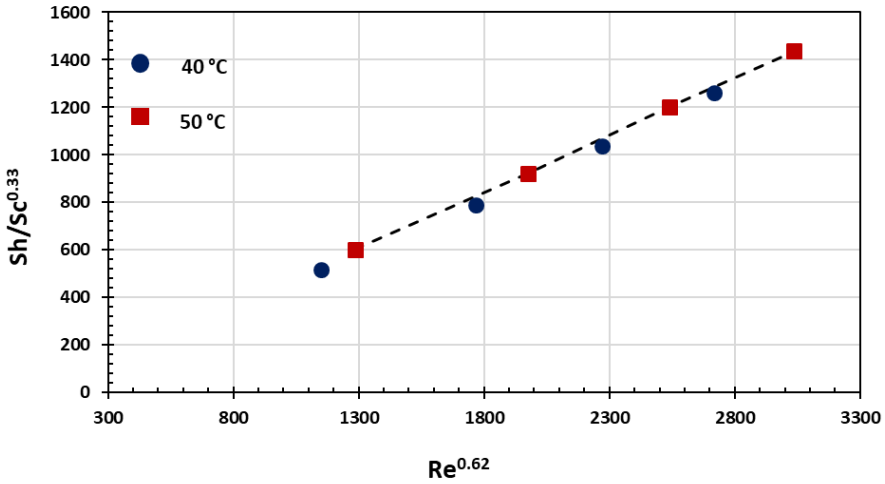

Figure 18. A straight-line fit of the mass transfer correlation developed for the experimental setup with impeller based on the relation between Sherwood (Sh), Reynolds (Re), and Schmidt (Sc) numbers

Table 3. Experimental condition for mass transfer characterization

Parameter	Description
Material	Nickel (Ni) Flat Square Specimen (A = 1.58 cm^2)
Temperature	40°C, 50°C
Total Pressure (N_2 as dominant gas)	1 bar
Reference Electrode	Saturated Ag/AgCl
Electrolyte	0.5 M NaOH 0.01 M of $K_3Fe(CN)_6$ 0.01 M of $K_4Fe(CN)_6.3H_2O$
Rotational Speed Range	50, 100, 150 rpm
Electrochemical Technique	Potentiodynamic Sweep 0.4 V above (anodic) and 1 V below (cathodic) OCP 5 mV/s Polarization Scan Rate
Dissolved O_2	<5 ppb

The exponent for Sc number in Equation 30 was set at 0.33 following the original correlation for a single-phase pipe geometry proposed by Berger and Hau (Equation 31) [65]. This exponent was not part of the regression analysis since the Sc number varied only very slightly over the experimental conditions tested.

$$Sh = 0.0165\, Re^{0.86} Sc^{0.33} \qquad \text{Equation 33}$$

With the goal of relating the conditions in this glass cell with single-phase pipe flow conditions in the field, the equivalent fluid velocity in a pipe corresponding to selected rotational speed of the impeller in the glass cell setup can be determined by equating the mass transfer coefficients in the pipe and the glass cell, as expressed in Equation 34 [66].

$$V = \left(28.48 \times N^{0.62} \times d_{pipe}^{0.14} \times d_{imp.}^{0.24} \times \upsilon^{0.24}\right)^{1.162}$$ Equation 34

where:

d_{pipe} = diameter of pipe (m)

$d_{imp.}$ = diameter of impeller (m)

N = impeller rotational speed (radian per second)

$\boldsymbol{\upsilon}$ = kinematic viscosity (m^2/s)

Figure 19 shows the near linear relationship between the flow velocity in a 0.1 m ID pipe (a typical pipe internal diameter) and the rotational speed in the glass cell with impeller, based on Equation 28. The actual impeller speed used in the current experiments (20 rpm) corresponds to approximately 0.58 m/s in a pipe flow, which is a reasonably representative condition to simulate.

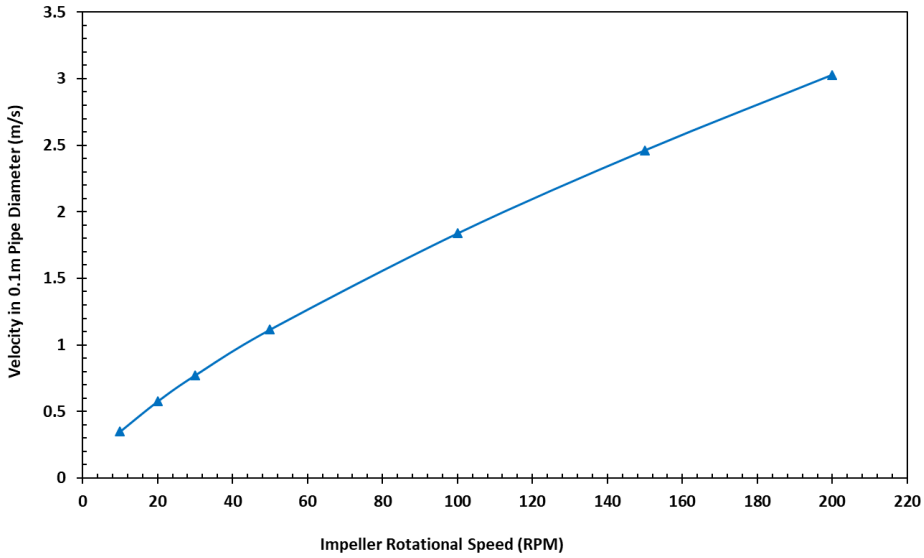

Figure 19. The relation between impeller rotational speed in the glass cell and velocity of the fluid in single-phase flow through a 0.1m ID pipe obtained by matching mass transfer coefficients.

CHAPTER 5: EXPERIMENTAL PROCEDURE

5.1 Experiment Scenarios

In order to investigate the hypotheses articulated in Section 3.2, the following experiments were designed and conducted at pH 6.2 and 5.5; these values of pH were selected to allow for particular dissolved Ca^{2+} and Mg^{2+} concentrations which better reflect typical field conditions.

1) Study performed with different saturation levels with respect to $CaCO_3$ (saturated and supersaturated), to investigate the effect of $[Ca^{2+}]$ and $CaCO_3$ scale on CO_2 corrosion mechanism (Chapter 6 of this dissertation).
2) Study performed with saturated solution with respect to $MgCO_3$, to investigate the influence of low and high $[Mg^{2+}]$ on CO_2 corrosion. Unlike for $CaCO_3$ scale, the formation of $MgCO_3$ scale was not possible due to the slow kinetics of $MgCO_3$ precipitation (Chapter 7 of this dissertation).
3) Study performed with saturated solution with respect to $CaCO_3$ with simultaneous presence of Mg^{2+}, this scenario is chosen to resemble oilfield realities where Ca^{2+} and Mg^{2+} are simultaneously present in encountered brines (Chapter 8 of this dissertation).

The experimental conditions and the associated test matrix of each of the aforementioned scenarios are thoroughly explained in the appropriate chapters/sections of this dissertation.

5.2 Specimens (chemical composition, microstructure, preparation)

The specimens were made of a UNS G10180[3] mild steel displaying a ferritic-pearlitic microstructure, as shown in Figure 20 with a chemical composition described in Table 4. The specimens were machined to have a square shape with dimensions of ~ 12.3 mm × 12.3 mm × 2.5 mm. The four side edges and one face of the weight loss specimens were coated with a thin layer of XYLAN® (fluoropolymer composite manufactured by Whitford™) before immersion in the test solutions. Therefore, the exposed surface area of the specimens was approximately 1.5 cm^2. A conductive wire was soldered to the electrochemical specimen that was then embedded in a waterproof epoxy resin (MarineWeld™), this left to cure overnight to ensure complete solidification. The electrochemical and weight loss specimens were wet-polished with silicon carbide papers up to 600 grit. Following the polishing process, the specimens were rinsed with isopropanol and placed in an ultrasonic cleaner for at least 2 minutes to remove any possible debris from the steel surface. Finally, they were dried by cold air and weighed prior to immersion into the test solutions. A schematic of how the weight loss and electrochemical specimens are introduced into the specimen holders is shown in Figure 16, *vide supra*.

---

[3] UNS numbers are listed in *Metals and Alloys in the Unified Numbering System*, published by the Society of Automotive Engineers (SAE International) and cosponsored by ASTM International

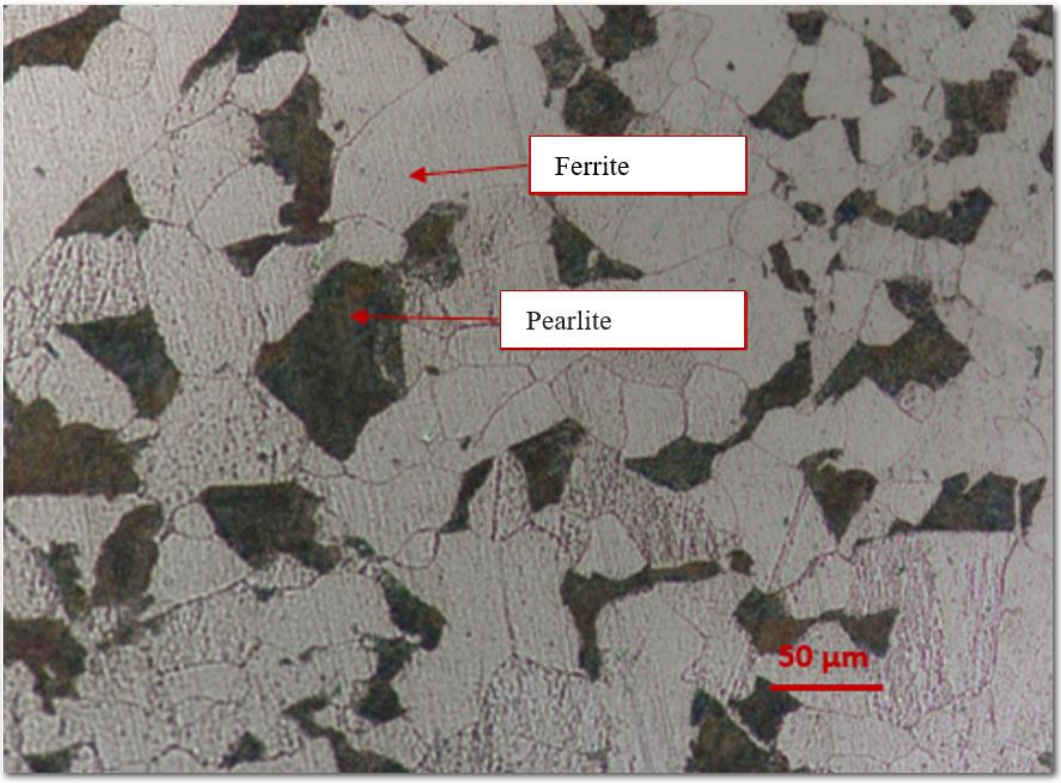

Figure 20. Ferritic-pearlitic microstructure of the UNS G10180 mild steel specimens

Table 4. Chemical composition of the UNS G10180 mild steel used in this work

Elem.	Al	C	Cu	Cr	Mn	Mo	Ni	P	S	Si	Fe
wt.%	0.008	0.18	0.18	0.12	0.75	0.02	0.065	0.011	0.021	0.016	Bal.

5.3 Electrochemical Measurements

A three-electrode system, including working, counter, and reference electrodes along with a Gamry Reference600™ potentiostat, was used to conduct electrochemical measurements. For all experiments discussed within this dissertation, the corrosion rate was measured at least twice per day using the linear polarization resistance (LPR) method, open circuit potential (OCP) was also recorded. The duration of each experiment was seven days. The polarization resistance measurements obtained by LPR included

determination of solution resistance. Electrochemical impedance spectroscopy (EIS) was used to measure the solution resistance (R_s) and the polarization resistance at the metal/solution interface was thereby compensated. The corrected polarization resistance (R_p-R_s) was used to calculate the current density (i_{corr}) by employing the Stern-Geary equation, shown in (35) [67]:

$$i_{corr} = \frac{B}{R_{p-R_S}} \qquad \text{Equation 35}$$

The parameters used for the electrochemical measurements are described in Table 5 (other experimental conditions will be described in the appropriate sections based on the experiment scenarios). In this study, a *B* value of 26 mV was used in the Stern-Geary equation to convert the experimental polarization resistance to corrosion rate. This value is commonly accepted in CO_2 environments but is not based on any specific Tafel slopes since the corrosion mechanism is not strictly charge transfer controlled. Instead, this *B* value was determined by best fit comparison between current densities and weight loss measurements [68-70]. It is understood that the value selected be dependent on the specific testing conditions and even change slightly during the experiments. However, LPR data are used herein to establish trends rather than for obtaining values of corrosion rates, which are measured more accurately by the WL method. Consequently, the approach adopted in this study was to select a reasonable B value and to keep it constant for all test conditions.

Table 5. Electrochemical parameters used for LPR and EIS measurements

Technique	Parameters
LPR	Potential range (± 5 mV vs. OCP), scan rate (0.125 mV/s), B[4] (26 mV)
EIS	Frequency range (5000-0.01 Hz), DC voltage (zero vs. OCP), peak to peak amplitude (10 mV), sampling rate (8 points/decade)

5.4 Weight Loss Measurement

Weight loss specimens were weighed prior to immersion into the test solutions. At day 2, 4, and 7 of exposure, the specimens were recovered from the solutions, washed with deionized water, rinsed with isopropyl alcohol, and dried. Corrosion products/scales were removed by use of Clarke solution (comprised of 1000 ml concentrated HCl (37%, 12 M), 20 g Sb_2O_3, and 50 g $SnCl_2$) according to the ASTM G1 procedure [71]. The weight of specimens (with and without corrosion products) were measured using an electronic scale. To remove corrosion products, the specimens were immersed and kept in Clarke solution for interval of 20-30 seconds. After immersion the specimens were rinsed with deionized water and alcohol (isopropyl), separately. Finally, they were dried with cold air blower and reweighed. The repetition of this process was continued until the subsequent weight loss change was less than 0.001 g. The total metal loss was used to calculated corrosion rate based on Equation (36):

$$CR_{wl} = \frac{W}{DAt} \qquad \text{Equation 36}$$

[4] The B value used in the Stern-Geary equation for corrosion rate calculation

where CR_{wl} is the corrosion rate expressed in mm/y, "87.6 value" is a constant to yield CR_{wl} in a unit of "mm/y", W is the metal mass loss in milligram, D is the density of metal in g/cm^3, A is the specimen surface area in cm^2, and t is the exposure time in hours [72].

5.5 Pitting Ratio Measurement

After removing the corrosion product/scale by Clarke solution, optical profilometry was performed by infinite focus microscopy (IFM) to investigate the magnitude of non-uniform (localized) corrosion. In the case of localized attack, the maximum depth of the pit is measured by IFM and then converted to penetration rate, reported in mm/y, according to Equation (37):

$$CR_{pr} = \frac{max.\ pit\ dept\ (\mu m) * 0.001 * 365}{exposure\ time\ (day)} \qquad \text{Equation 37}$$

The pitting ratio defined by equation (38) is used to evaluate the magnitude of pitting (localized) corrosion compared to the uniform corrosion. Within this dissertation, the occurrence of localized corrosion is characterized by a pitting ratio greater than 5.

$$Pitting\ Ratio = \frac{CR_{pr}}{CR_{wl}} \qquad \text{Equation 38}$$

5.6 Surface Layer Characterization

Surface layer characterization including morphology, chemical composition, compound identification, and thickness measurement were accomplished using scanning electron microscopy (SEM), energy dispersive X-ray spectroscopy (EDS), X-ray

diffraction (XRD), and infinite focus microscopy (IFM). The specimens were washed with deionized (DI) water, rinsed with isopropanol alcohol, dried with cold air, and finally stored in desiccator (free from oxygen contamination) prior to surface characterization. Surface characterization is essential to investigate the effect of Ca^{2+} and Mg^{2+} on the morphology and chemical composition of corrosion product/scale and the magnitude of localized attack, if it happens. This assists interpretation of the corrosion data obtained by electrochemical measurements.

SEM characterization of the surface layers were performed using a JEOL[5] JSM-6390LV. The chemical composition of the corrosion products and scales was analyzed by a Bruker QUANTAX/XFlash EDS detector attached to the SEM as well as by XRD using a Rigaku Ultima[6] IV diffractometer (CuK_α radiation, $\lambda = 1.5406$ Å). The procedure for XRD experiments and successive analysis is provided in Appendix I.

SEM/EDS provides secondary and backscatter imaging, elemental mapping and line scans analysis. SEM/EDS was used to analyze both top and cross-section views of specimens. For the cross-section analysis, the specimens were immersed in an epoxy resin to retain the corrosion products/scale formed during corrosion processes. The epoxy resin was left overnight to completely cure and solidify before cutting the specimen, typically in half. Once the specimen had been cut, it was wet ground using silicon carbide abrasive paper up to 600 grit using a rotating polishing table. The cross-section specimen

---

[5] Trade Name

[6] Trade Name

was then rinsed with DI water, isopropanol and dried with cold air. All the cross-sectioned specimens were palladium coated using a sputtering machine (HUMMER® 6.2) to eliminate any potential surface charging before conducting SEM/EDS analysis. It should be mentioned that for the top view analysis in the presence of $CaCO_3$ scale and $Fe_xCa_yCO_3$ (y>x), the specimens were sputtered to reduce inadvertent effects of surface charging.

It is worth mentioning that calculation of the porosity of the corrosion product layers was attempted, with the initial goal of correlating this parameter with the extent of corrosion and the presence of Ca^{2+} and/or Mg^{2+}. However, this effort proved to be unsuccessful as the composition of the layer, and its density, could not be determined precisely. This was due to the nature of the corrosion products which were usually made of a mixture of $Fe_xCa_yMg_zCO_3$ and Fe_3C (the value of x, y, and z differing depending on experimental condition, x+y+z=1).

CHAPTER 6: CO_2 CORROSION EXPERIMENTS IN Ca^{2+} - CONTAINING ELECTROLYTES

In this chapter, the experimental results related to the presence of Ca^{2+} in the electrolyte, considering varying $CaCO_3$ saturation levels, [Ca^{2+}], pH and ionic strengths are presented. The discussion follows two main steps. Firstly, the effect of Ca^{2+} on CO_2 corrosion while the electrolyte is saturated with $CaCO_3$ is discussed. Secondly, results related to experiments where the solution is temporarily supersaturated with respect to $CaCO_3$ are presented (precipitation of $CaCO_3$ scale).

6.1 Effect of Ca^{2+} on Morphology and Protectiveness of Corrosion Product Layers ($CaCO_3$-saturated solutions)

Effect of $CaCO_3$ saturated solutions on CO_2 corrosion were investigated at pH 6.2 and 5.5. In this section, the experiments conducted at pH 6.2, 160 ppm Ca^{2+} and 0.18 M ionic strength are initially discussed. This is followed by presentation of experimental data for corrosion tests conducted with more aggressive water chemistry at pH 5.5, 6000 ppm Ca^{2+} and 0.6 M ionic strength.

6.1.1 Experiments with 160 ppm Ca^{2+} at pH 6.2 and 0.18 M ionic strength[7]

6.1.1.1 Methodology and Test Matrix

Two series of corrosion experiments were performed and repeated, one without Ca^{2+} ions (as a baseline) and one in a $CaCO_3$ saturated solution (with approximately 160 ppm aqueous Ca^{2+}). Other than that, both tests were conducted under the same experimental conditions, as described in Table 6. The experiments were conducted at atmospheric pressure, 80°C and 0.53 bar pCO_2. After preparation of each 1 wt.% NaCl electrolyte, $CaCO_3$ reagent (for the electrolyte containing Ca^{2+}) and $NaHCO_3$ (to the baseline electrolyte) was added to adjust the pH and the $CaCO_3$ saturation level. The electrolytes were deoxygenated by sparging with CO_2 for at least two hours prior to each experiment as they were heated to 80°C. At 80°C, the water vapor pressure was 0.47 bar with the balance gas being CO_2. In these conditions, the autogenous initial pH for the electrolyte in the presence of $CaCO_3$ reagent, when the system was at equilibrium, was pH 6.2. Therefore, to have a similar testing environment, the pH of the baseline electrolyte was initially adjusted to 6.2 (using $NaHCO_3$). CO_2 gas was continuously bubbled into the solutions to maintain saturation with CO_2 during corrosion experiments. The pH was maintained at 6.2 ± 0.1 by the means of H-form ion-exchange resin (Dowex® G26). The $[Fe^{2+}]$ was controlled to be no greater than 10 ppm using Na-form ion-

---

[7] A version of this section in under review for published as "Effect of $CaCO_3$-Saturated Solution on CO_2 Corrosion of Mild Steel Explored in a System with Controlled Water Chemistry and Well-Defined Mass Transfer Conditions," Corros. Sci., 2019.

exchange resin (Amberlite® IR 120). The $CaCO_3$-saturated solution initially contained 1.2 g/L powdered $CaCO_3$ reagent with 99% purity (ACROS Organics™). This excess amount of $CaCO_3$ in the solution was calculated to be three times higher than what was needed in order for the solution to remain saturated with respect to $CaCO_3$ over the course of the long-term experiments. The excess $CaCO_3$ reagent guaranteed that the solution remained saturated with respect to $CaCO_3$ with a stable [Ca^{2+}] due to the relatively fast kinetics of $CaCO_3$ precipitation/dissolution [56].

$FeCO_3$ saturation degree (S_{FeCO_3}) is an important parameter in CO_2 corrosion studies, influencing precipitation rate of $FeCO_3$ and thus the corrosion mechanism [73], [74]. Release of Fe^{2+} ions in solution is also an unavoidable consequence of the corrosion of steel, and the potential precipitation of $FeCO_3$ cannot consequently be ignored. The S_{FeCO_3} values were calculated over time for experiments with and without Ca^{2+} using Equation (15) and (17). Equation (15) was developed to take into account the non-ideality of the solution through the "$2.518 \cdot I^{0.5} - 0.657 \cdot I$" term [36]. The $FeCO_3$ saturation value was also calculated using an approach solely based on activity coefficients. The results, shown in Appendix II, yielded very similar results, at least in the range of conditions tested (Table 6). It is acknowledged that more severe deviations exist, especially considering higher S_{FeCO3} and that the activity coefficient approach would generate more accurate predictions. For each [Fe^{2+}] measured, the operating temperature and pH were used to calculate [CO_3^{2-}] from an equilibrium model for CO_2 speciation in aqueous environments [75], enabling the determination of S_{FeCO_3}. As explained earlier,

the $CaCO_3$ saturation degree (S_{CaCO_3}) was unity for the experiment with the presence of Ca^{2+}.

Table 6. Text matrix to investigate the effect of Ca^{2+} at pH 6.2

Parameter	Description	
Temperature	80°C	
pCO_2	0.53 bar	
pH	Baseline (without Ca^{2+})	With Ca^{2+}
	6.2 (adjusted with $NaHCO_3$)	6.2 (autogenous in presence of excess amount of $CaCO_3$ reagent)
Electrolyte	1 wt.% NaCl + $NaHCO_3$ (Ionic Strength ~ 0.18 M)	1 wt.% NaCl + $CaCO_3$ (Ionic Strength ~ 0.18 M)
Calcium carbonate saturation ($\mathbf{S_{CaCO_3}}$)	0 (without Ca^{2+})	Unity (Ca^{2+} ~ 160 ppm)
Iron carbonate saturation ($\mathbf{S_{FeCO_3}}$)	$4 < S_{FeCO_3} < 14$ (using correction for ionic strength) $2 < S_{FeCO_3} < 8$ (using activity model, see Appendix II)	
Dissolved O_2	<5 ppb	
Reference electrode	Saturated Ag/AgCl	
Impeller rotation speed	20 rpm	
Mass transfer conditions	Equivalent to 0.58 m/s in a 0.1m ID pipe	
Test duration	7 days	

6.1.1.2 Results and Discussion

In this section, the results of the baseline CO_2 corrosion experiments without Ca^{2+} at pH 6.2 are presented and discussed. Then, the results of the experiments conducted in $CaCO_3$-saturated electrolyte are presented and compared with the results of baseline experiments conducted with an otherwise identical water chemistry.

Baseline Experiments at pH 6.2:

Figure 21 shows the corrosion rate obtained by LPR and the open circuit potential values over the course of experiments without the presence of Ca^{2+} in the electrolyte. The

reproducibility of results was indicated by the error bars displayed in Figure 21, representing the maximum and minimum values from two different experiments (the same is true for other error bars shown in various graphs throughout this dissertation). The corrosion rate trend can be divided into three different periods that correspond to active corrosion, nucleation/growth of $FeCO_3$, and pseudo-passivation. Each period is discussed separately. Figure 22 shows the comparison of the time-averaged (cumulative) corrosion rate obtained by LPR and WL techniques. There is a reasonable agreement between the corrosion rate obtained by LPR and WL given the error of measurement. Although LPR shows a higher corrosion rate than WL at each measuring point, both methods indicate a decreasing corrosion rate over time.

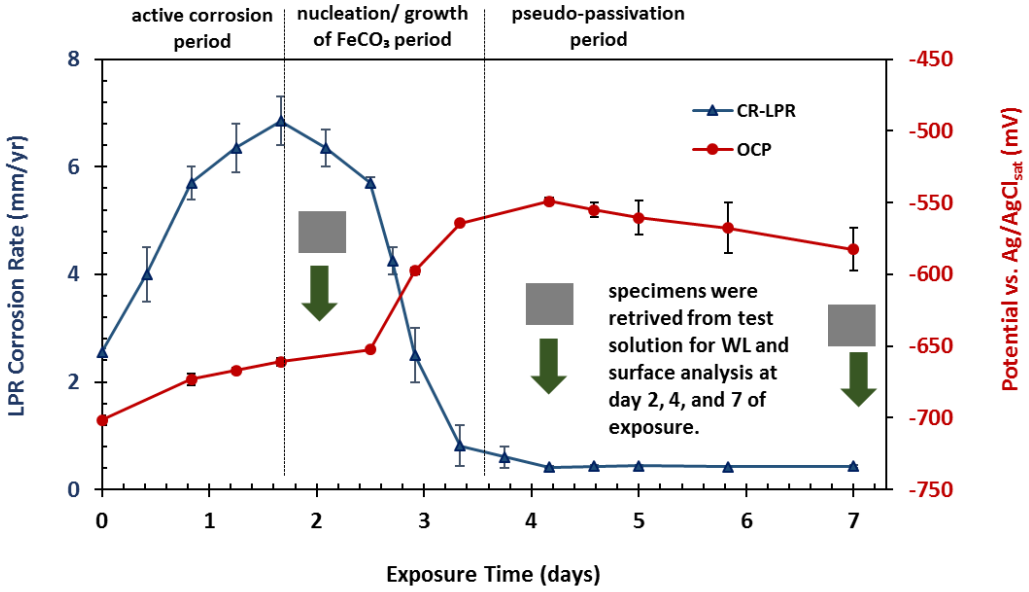

Figure 21. Change in LPR corrosion rate and open circuit potential with time explained by three different periods: active corrosion, nucleation/growth of $FeCO_3$, and pseudo-passivation (UNS G10180, 80 °C, pCO_2 0.53 bar, pH 6.2, NaCl 1wt%, $4 < S_{FeCO_3} < 14$, $S_{CaCO_3} = 0$, velocity 0.58 m/s)

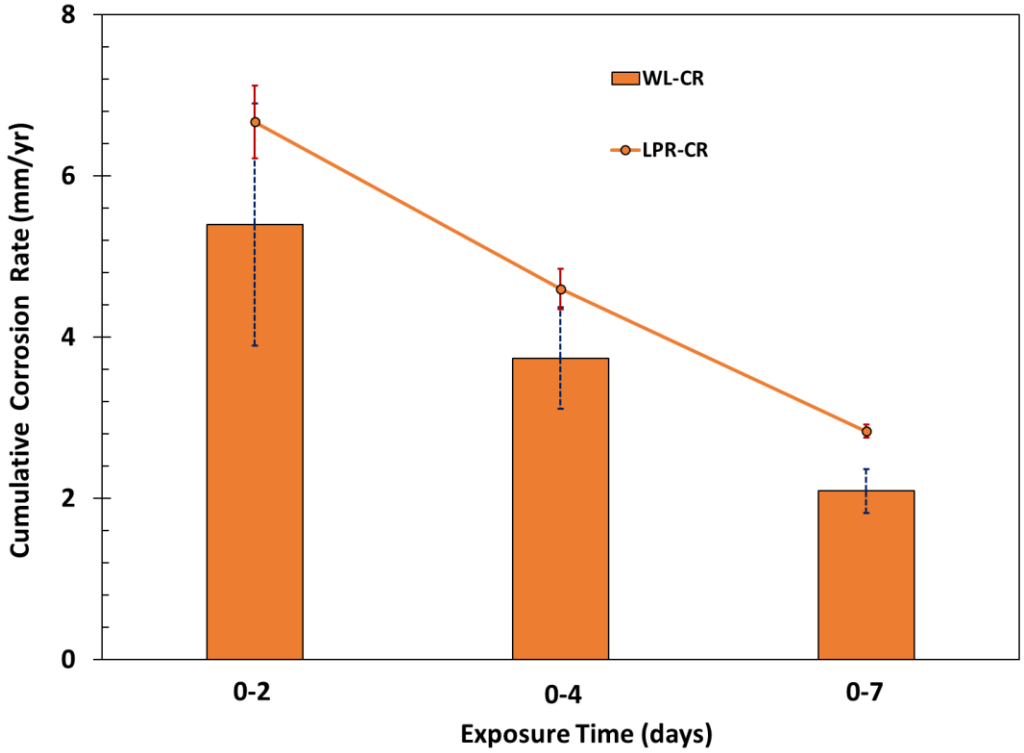

Figure 22. Time-averaged (cumulative) corrosion rate obtained by LPR and WL techniques (UNS G10180, 80 °C, pCO_2 0.53 bar, pH 6.2, NaCl 1wt%, $4 < S_{FeCO_3} < 14$, $S_{CaCO_3} = 0$, velocity 0.58 m/s)

Active Corrosion Period:

The increase in the corrosion rate, shown in Figure 21, in the first two days is characterized as the active corrosion period. In this period, the starting corrosion rate (average) was around 2.5 mm/y and this value reached 6.8 mm/y after 40 hours. The increase in corrosion rate is attributed to the ferritic-pearlitic microstructure of the UNS G10180 steel. Preferential corrosion of the ferrite (α-Fe) phase over cementite (Fe_3C) phase leaves behind a porous, high surface area Fe_3C structure on the steel surface. It has been reported that the development of this residual Fe_3C network, which is electrically conductive, accelerates the corrosion rate by providing more surface area for cathodic

reactions (e.g., hydrogen evolution reaction) within its porous structure, leading to a galvanic effect between Fe_3C and α-Fe phases [74, 76]. It should be pointed out that while this increase of the corrosion rate as measured by LPR is valid, the actual magnitude of the elevated corrosion rate may be exaggerated. This is due to the inability of the LPR technique settings to cope with the change in cathodic surface area (LPR technique measures total current and not current density).

At the end of this period, two steel specimens were retrieved from the electrolyte for WL measurements and surface characterization. The top view and cross-section morphology of the surface layers developed in this period are shown in Figure 23. The porous structure of surface layers is obvious from the cross-section SEM image. The color of the corrosion product layer was gray to black, which is a typical characteristic of Fe_3C residue [77]. The average thickness of the surface layer at this time period was around 15 μm. The yellow arrow on the cross-section specimen indicates the calculated metal loss thickness based on WL corrosion rate, which gives a value of 21.3 μm. This value is slightly greater than the measured thickness indicating a possibility that the shear stress created by flow could have removed some of the residual Fe_3C.

Nucleation and Growth of $FeCO_3$ Period:

In the second period, shown in Figure 21, the corrosion rate continuously decreased from 6.8 mm/y at day 2 to approximately 0.8 mm/y on day 4. At the end of this period, two of the specimens were retrieved from the glass cell for surface analysis and WL measurements. Figure 23 shows representative SEM images of the top and cross-sectional view of these specimens. The cross-section view revealed that the surface layer

adjacent to the steel surface was denser than previously observed during the active corrosion period. EDS and XRD confirmed that these layers were made of $FeCO_3$ which precipitated within the Fe_3C structure (EDS and XRD results will be discussed in detail, *vide infra*).

$FeCO_3$ can potentially act as a protective layer against corrosion when its precipitation rate is higher than the corrosion rate, measured in the same units [9]. In the current work, the bulk saturation degree of $FeCO_3$ was kept at a relatively low level, between 4 and 14, which would explain why relatively few $FeCO_3$ crystals can be observed in the top view (on the outer edge of the corrosion product layer). However, inside the porous Fe_3C layer, quiescent conditions were achieved and the water chemistry of the solution in contact with the metal surface was significantly different from the bulk solution. The development of Fe_3C layers restricted the transport of corrosion reactants and products through the surface layer. This resulted in a higher pH (due to hydrogen reduction reactions at the metal surface that consumed H^+) and accumulation of Fe^{2+} (generated from the corrosion process). Therefore, a significantly higher $FeCO_3$ saturation degree was achieved close to the metal surface. Such local conditions accelerated the precipitation of a relatively protective $FeCO_3$ layer, resulting in a decrease in the corrosion rate and an increase in the corrosion potential over time during this period.

Pseudo-Passivation Period:

Within this manuscript, the term pseudo-passivation refers to a situation when two phenomenon are observed simultaneously: a decrease in corrosion rate along with an

increase in corrosion potential due to the formation of iron carbonate at the steel surface [78]. During the pseudo-passivation period, the experimental corrosion rate was typically stable, but significantly lower than the corrosion rate in the two previous periods. This was due to further growth of $FeCO_3$ within the other parts of the Fe_3C layers (in addition to the locations close to the steel surface).The formation of $FeCO_3$ has been reported to mainly retard the anodic reaction, which can result in an increase in OCP [79]. Consequently, the layer became progressively less porous. It is noteworthy that the thickness of the corrosion product layer was almost the same as observed in the second period. The main reason for this observation was that the corrosion rate in the third period was considerably lower, therefore, the Fe_3C layer could not appreciably be further developed. Another characteristic of this period is the steep increase in OCP reflected by a decrease in anodic reaction rate due to the precipitation of corrosion product layers on the steel surface. SEM images of the top and cross-section view of the corrosion product layer after 7 days of exposure are shown in Figure 23. Just like previously discussed for the nucleation and growth period, $FeCO_3$ crystals did not form on the outer edge of the Fe_3C layer since the bulk solution was not highly supersaturated with respect to $FeCO_3$, as shown from top view images in Figure 23. However, precipitation of $FeCO_3$ adjacent to the steel surface and within the Fe_3C occurred, regardless of the water chemistry in the bulk solution. This is obvious from the cross-section images after 4 days and 7 days of specimen exposure.

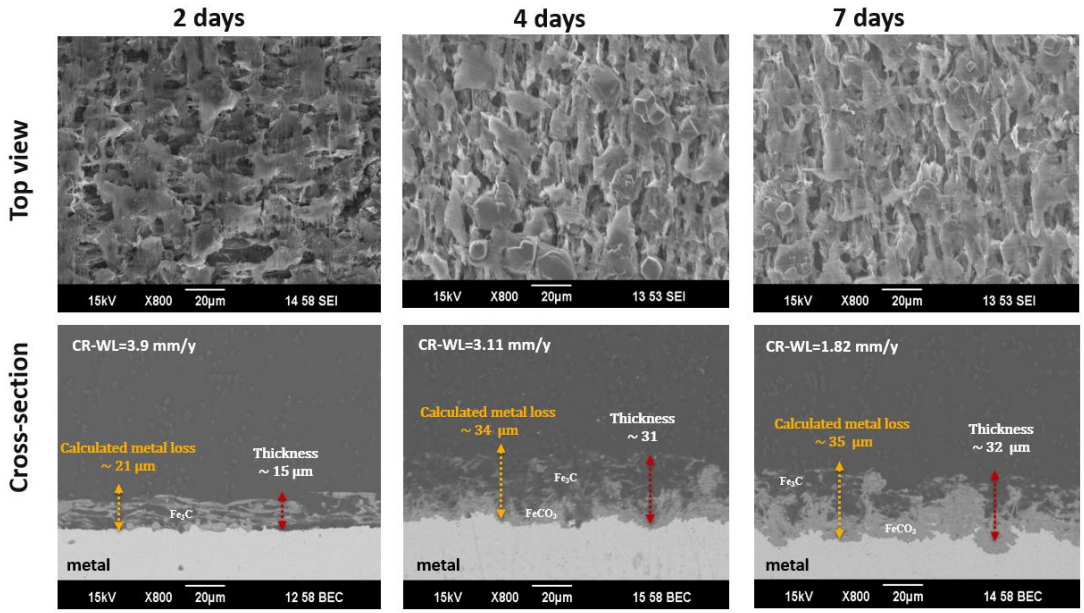

Figure 23. SEM images of top view and cross-sectional morphology of surface layers exposed to solution in the absence of $CaCO_3$ at pH 6.2 (note: the CR-WL provided here is specific for the experiment in which the surface characterization is presented here)

In summary, the development of the porous and conductive Fe_3C layer accelerated the corrosion rate in the "active corrosion" period by providing additional cathodic surface area for hydrogen reduction reactions. Then, the Fe_3C layer acted as an anchoring site and facilitated the precipitation of $FeCO_3$ in the second "growth and nucleation of $FeCO_3$" and third "pseudo-passivation" periods. Based on the corrosion rate *versus* time trend and the SEM cross-section images, it seems that there was a critical thickness of Fe_3C layer required for nucleation and subsequent growth of $FeCO_3$ crystals. In the experiments presented above, the cross-section SEM image of specimens at the end of day 2 (active corrosion period) presented a Fe_3C layer 15 µm thick. Therefore, precipitation was likely favored when the thickness of the porous Fe_3C residual layer was greater than this value. It is fully understood that this critical thickness is highly

dependent on several operating parameters such as the mass transfer characteristics, the chemistry of the bulk electrolyte, the steel microstructure and composition; consequently, it is only relevant to the experimental conditions of the current research. Figure 24 shows the corrosion rate measured by WL methods and thickness of Fe_3C at different exposure times. The corrosion rate clearly decreased after 4 days when the Fe_3C layer reached this critical thickness.

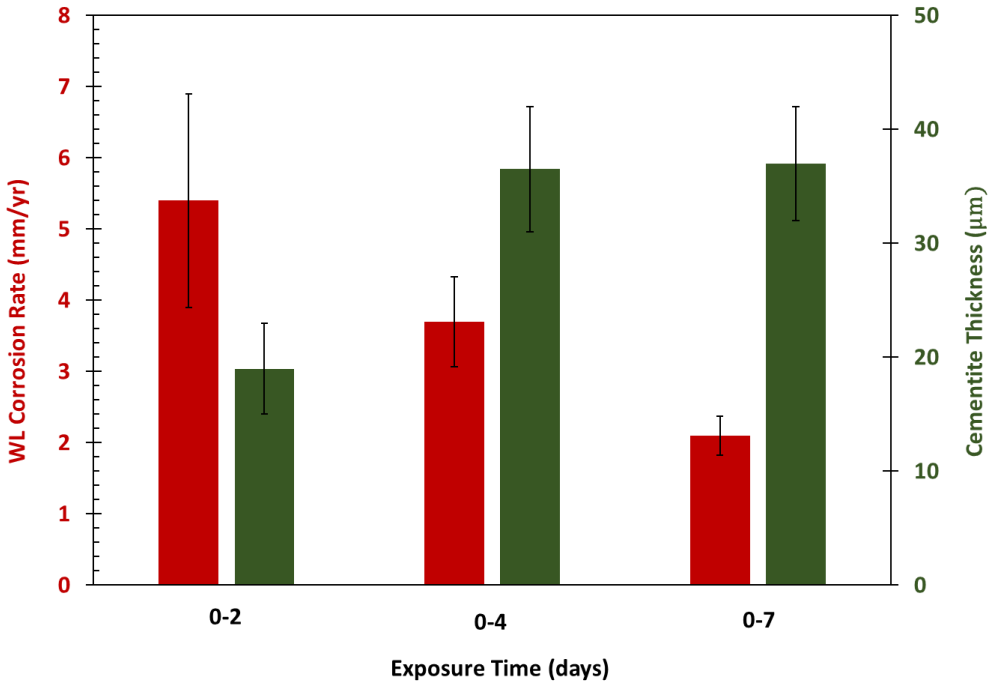

Figure 24. Corrosion rate by WL and cementite thickness *versus* time in the active (2 days), nucleation/growth of $FeCO_3$ (4 days), and pseudo-passive (7 days) periods, baseline experiment at pH 6.2.

The results of EDS analysis (line scan) from the cross-section specimens showed that (close to the steel surface) Fe, C, and O elements were present for specimens

retrieved at 4 and 7 days of exposure. An example of such EDS analyses for a specimen exposed to the baseline solution for 7 days is illustrated in Figure 25. The presence of the atomic oxygen in the EDS analysis is consistent with the formation of $FeCO_3$ adjacent to the steel surface and no other compound containing oxygen was expected to form under these experimental conditions. Also, the EDS analysis confirmed the presence of Ni, Cu, Cr, Si, Mn and Mo as residual alloying elements often associated with the presence of the Fe_3C network as shown in Figure 26, Table (a). These elements are part of the chemical composition of the UNS G10180 steel. Furthermore, a typical composition of $FeCO_3$ crystal, formed on the top of Fe_3C network, is provided in Table (b), Figure 26. A trace of Mn was present in such crystals along with Fe, C, and O elements. The presence of a trace amount of Mn, coming from the corroding specimens, in the carbonate crystals is not surprising since $MnCO_3$ (rhodochrosite) shares the same calcite-type crystal structure as $FeCO_3$ and $CaCO_3$, therefore, they can coexist in a carbonate solid solution [80].

XRD data also confirmed the presence of Fe_3C and $FeCO_3$ as the main corrosion products on the steel surface. These XRD patterns from the top view of the corrosion product layers at different exposure times with and without the presence of Ca^{2+} will be discussed and compared later.

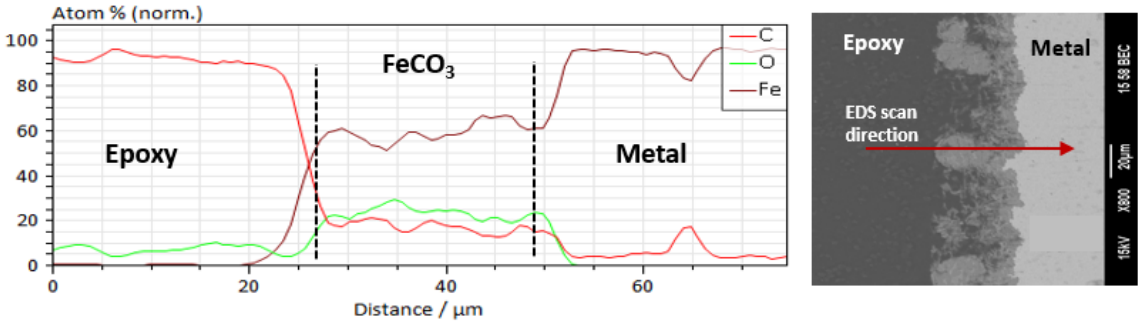

Figure 25. EDS analysis (line scan) of cross-sectioned corrosion products formed on a specimen exposed to the baseline solution for 7 days at pH 6.2

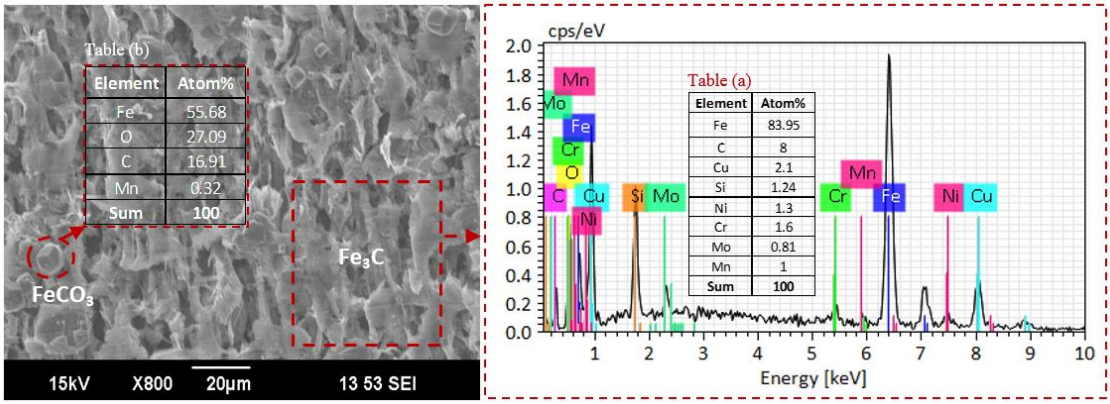

Figure 26. SEM/EDS analysis (top view) of the corrosion products developed on the surface of UNS G10180 specimens exposed to the baseline solution for 7 days at pH 6.2

$CaCO_3$-Saturated Experiments at pH 6.2:

In this part, the results of corrosion experiments performed in a $CaCO_3$-saturated solution are shown, discussed and compared with the results of the baseline experiments presented above. Figure 27 and Figure 28 compare the bulk solution pH and $FeCO_3$ saturation degree values over time, respectively. For both series of experiments, these two important parameters were maintained over the course of each experiment. As shown in Figure 27, the pH values were controlled to pH 6.2 ± 0.1 for both experiments. The

initial target value for $FeCO_3$ saturation degree (S_{FeCO_3}) was 10, calculated using Equation (17); however, it was impossible to strictly maintain this value over the course of experiments. Instead, as indicated in Figure 28, the average values of S_{FeCO_3} were controlled between 4 and 14 which seems acceptable considering the experimental difficulties. The similarity in water chemistry and test conditions of the baseline and $CaCO_3$-saturated electrolytes facilitates the comparison of corrosion results. This constitutes a considerable improvement from previous studies reported in the literature for which the water chemistry of the experiments was not well controlled, rendering any comparisons and conclusions difficult [44, 50].

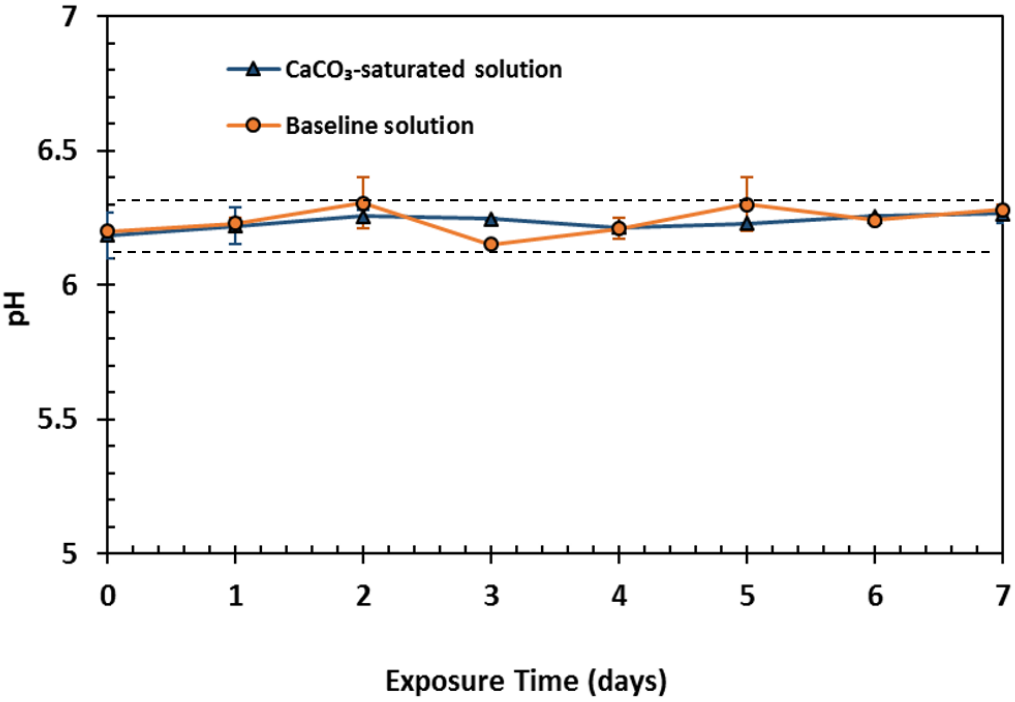

Figure 27. pH profiles for both baseline and $CaCO_3$-saturated solution over time (pH 6.2 ± 0.1)

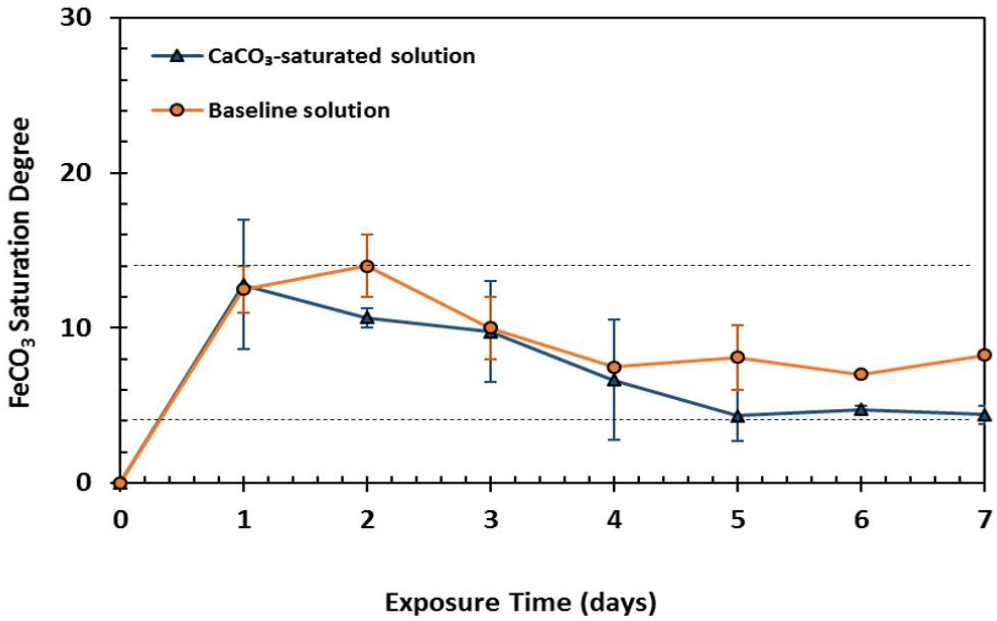

Figure 28. Variation of $FeCO_3$ saturation degree over time for experiment with and without $CaCO_3$ at pH 6.2 (the average values of S_{FeCO_3} were controlled between 4 and 14)

Corrosion rate and open circuit potential with time:

The measured corrosion rates obtained by LPR for the experiments conducted in the presence of $CaCO_3$ are compared with that of the baseline experiments in Figure 29.

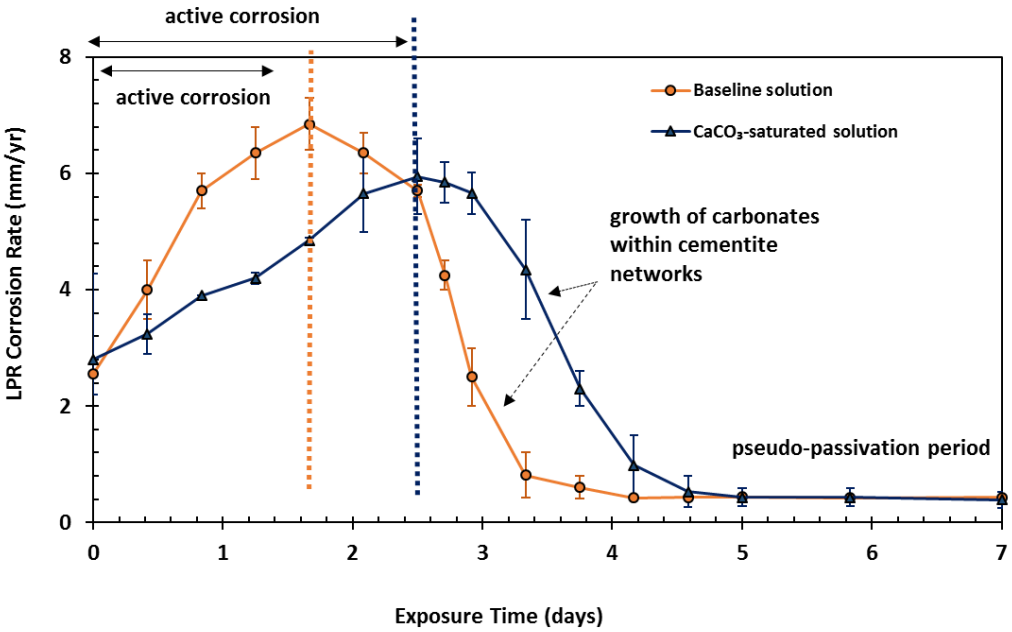

Figure 29. Comparison of LPR corrosion behavior of UNS G10180 exposed to $CaCO_3$-saturated and baseline ($CaCO_3$-free) aqueous conditions at pH 6.2

The three corrosion periods described earlier for the baseline experiments were also observed in the presence of $CaCO_3$, although several differences could be identified. The kinetics of formation of the protective corrosion product layer was lower in the presence of $CaCO_3$. That suggests the presence of Ca^{2+} was interfering with the precipitation of $FeCO_3$, slowing the processes of nucleation and/or growth and leading to a longer active corrosion period. Limited studies in the literature highlight similar findings without proposing any underlying mechanisms: Alsaiari, *et al.*, have reported that calcium ions have an impact on increasing the solubility of $FeCO_3$ and thus decreasing its precipitation rate [81]. According to Figure 29, regardless of the influence of Ca^{2+} on the earlier periods of the corrosion process, the corrosion rate at the end of the experiment with $CaCO_3$ (pseudo-passivation period) is identical to the baseline

experiment in the same corrosion period. This observation suggests that the presence of Ca^{2+} in a solution saturated with $CaCO_3$ would not jeopardize the protectiveness of corrosion product layers when fully developed on the mild steel surface.

Figure 30 shows a comparison of the cumulative corrosion rate obtained by LPR (line chart) and WL (bar chart) methods at day 2, 4, and 7 of the experiment with and without $CaCO_3$. At each measuring point, LPR shows a higher cumulative corrosion rate compared to WL for both series of experiments. This is mainly due to uncertainties around the B value, as stated earlier. Both LPR and WL techniques indicate that the cumulative corrosion rate in the presence of $CaCO_3$ was lower than the baseline experiment at each measuring point. Another observation is that the difference of cumulative corrosion rate for experiments with and without $CaCO_3$ is decreasing over time, captured by both LPR and WL methods.

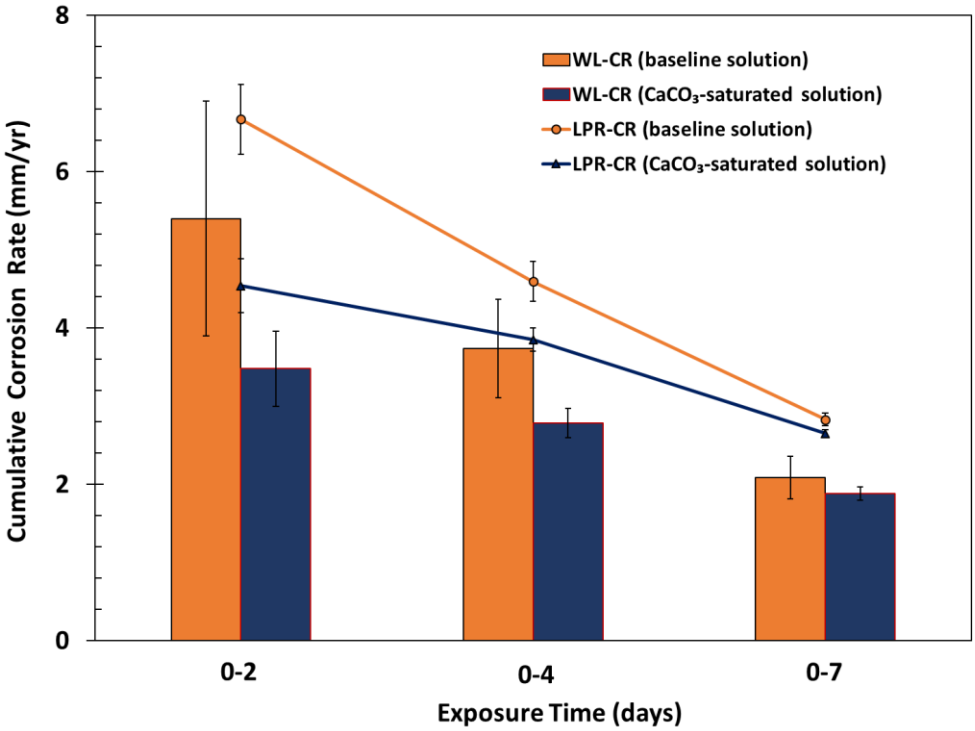

Figure 30. Comparison of cumulative corrosion rate obtained by LPR and WL methods with and without $CaCO_3$ after 2, 4, and 7 days of exposure at pH 6.2

The open circuit potential measurements for both test series are shown in Figure 31. The overall behavior of OCP with and without $CaCO_3$ was similar, with more positive potentials at the end of the tests as a result of the formation of a relatively dense layer on the metal surface.

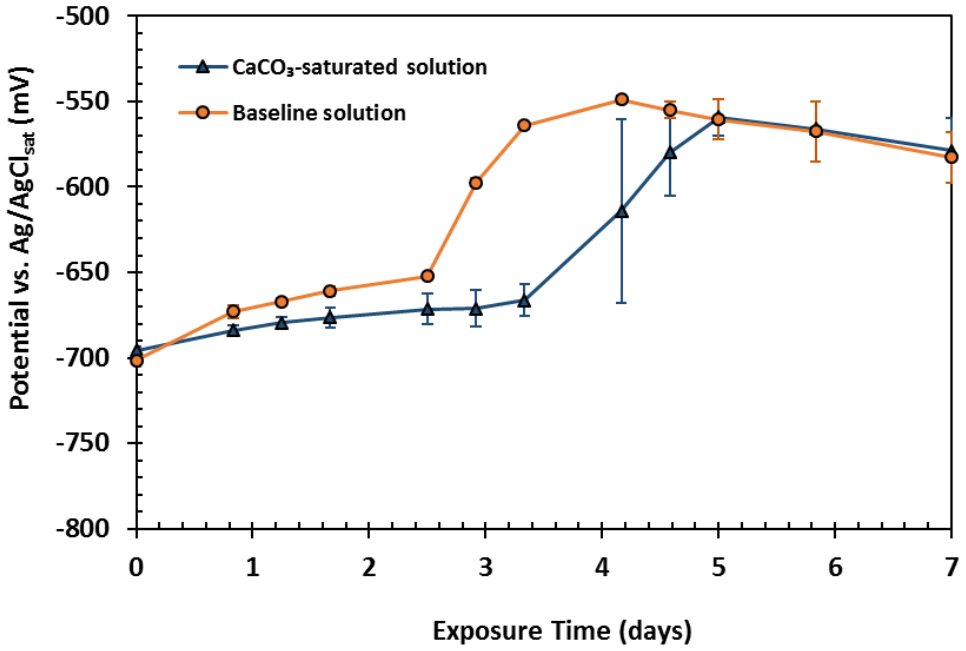

Figure 31. Comparison of OCP over time for UNS G10180 exposed to solutions with and without $CaCO_3$ at pH 6.2

Surface layer characteristics:

Figure 32 shows the SEM images of top and cross-sectional views of the specimens at different exposure times in the presence of $CaCO_3$. The top view images show the typical morphology of Fe_3C for all specimens. A small quantity of carbonate crystals is present on the top of the developed Fe_3C networks; the presence of such crystals is more obvious after 4 and 7 days of exposure. The cross-sectional images show that the surface layer thickness grew steadily up to day 4, at which point its growth was hindered due to the formation of carbonates within the Fe_3C porous structure; this resulted in a rapid decrease in the corrosion rate marking the end of the active corrosion period. The yellow arrows on the cross-sectional images indicate the calculated metal

loss thickness, which were obtained from the WL corrosion rate. Similar to the baseline experiments, these calculated values are slightly higher than the measured thickness in the cross-sectional SEM images, suggesting that some of the surface layers have been removed by flow effects. It is worth mentioning that Fe_3C is fragile and vulnerable to removal by flow [70]. However, precipitation of $FeCO_3$ within the pores of Fe_3C would increase its mechanical strength. The author believes that the slight difference in the measured and calculated corrosion product thickness could be due to partial removal of Fe_3C in the active corrosion period while the Fe_3C was building up on the steel surface (before precipitation of $FeCO_3$).

The same conclusions related to the baseline experiments on the effect of Fe_3C layers on precipitation of carbonate crystals are also valid for experiments conducted in the presence of $CaCO_3$. In addition, EDS and XRD confirmed the presence of calcium within the carbonate crystals and, to some extent, within the Fe_3C layer. Figure 33 shows a top view EDS analysis of the corrosion products after 7 days of exposure for an experiment conducted in the presence of $CaCO_3$. Such EDS analysis along with XRD confirmed the formation of solid solutions of iron-calcium carbonate with a trace of manganese (Mn) incorporated into the lattice of such crystals (see Table (a) in Figure 33). Furthermore, the elemental analysis of the Fe_3C layer in Figure 33, Table (b), shows residual alloying elements along with Ca are present in the Fe_3C network.

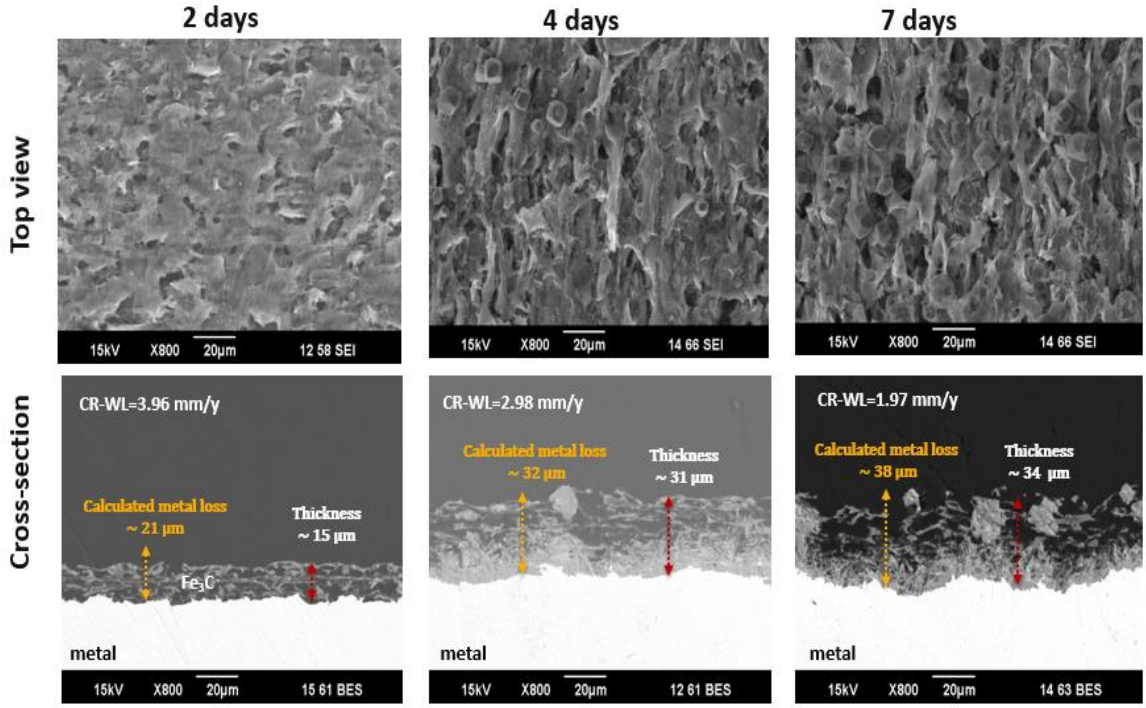

Figure 32. Top and cross-sectional views of specimens retrieved from the test condition with $CaCO_3$ present after 2, 4 and 7 days of exposure at pH 6.2

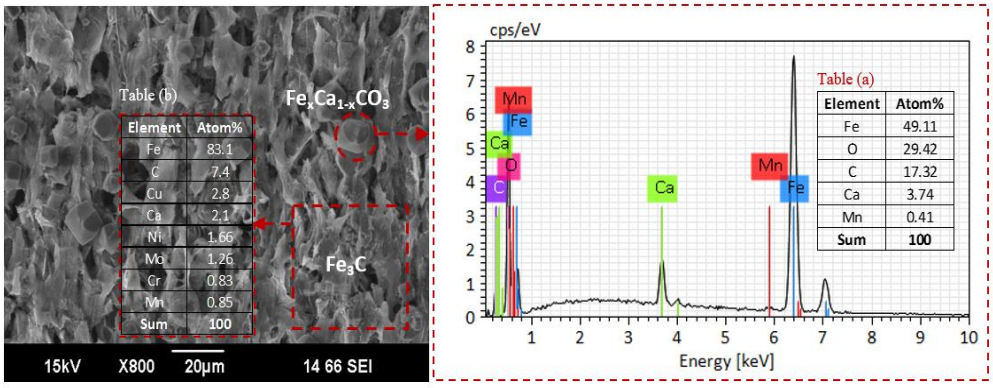

Figure 33. SEM/EDS analysis (top view) of the surface layers on UNS G10180 developed from a solution saturated with $CaCO_3$ after 7 days of exposure at pH 6.2

Figure 34 shows the XRD data obtained for the specimens recovered after different exposure times in $CaCO_3$-saturated electrolytes (solid blue lines) and in

electrolytes without $CaCO_3$ (dashed red lines). $FeCO_3$ was the only crystalline phase detected on the steel surface in the absence of Ca^{2+} ions. However, in the presence of Ca^{2+} ions, XRD data confirmed that a substitutional solid solution of $Fe_xCa_{1-x}CO_3$ was formed after 7 days of exposure. The most intense diffraction peak, corresponding to the *hkl* (104) Bragg reflection, for siderite ($FeCO_3$) and calcite ($CaCO_3$) occurs at 32.07 and 29.42 2θ, respectively (CuK_α radiation). The effect of Ca^{2+} on the corrosion product layers can be seen by comparing the XRD data of experiments with and without $CaCO_3$ at days 4 and 7. The XRD data are almost identical with/without $CaCO_3$ for the first 2 days when the Fe_3C layers are developing. However, $FeCO_3$ peaks for the experiment in the presence of Ca^{2+} are broadened and shifted toward the reference peaks for $CaCO_3$, indicating heterogeneous substitution of Fe^{2+} by Ca^{2+} in the lattice of $FeCO_3$. This phenomenon is more obvious for XRD data at day 7 of the experiment, which revealed a substitutional solid solution with a formula of $Fe_{0.898}Ca_{0.102}CO_3$; this analysis was achieved by determining the mole fraction of Ca incorporated into the $FeCO_3$ lattice using Bragg's law [42]. Although all of the $FeCO_3$ peaks are slightly shifted towards the left in the presence of Ca^{2+} ions, the more intense peaks associated with (104) and (116) Miller planes located at 32.07 and 52.7 degrees are more easily recognizable after 7 days of exposure. Another observation is that the intensity of peaks related to α-Fe is decreasing over time for both series of experiments. This indicates that surface layers were increasing in depth and, as a result, incident X-rays could not reach the steel substrate as easily.

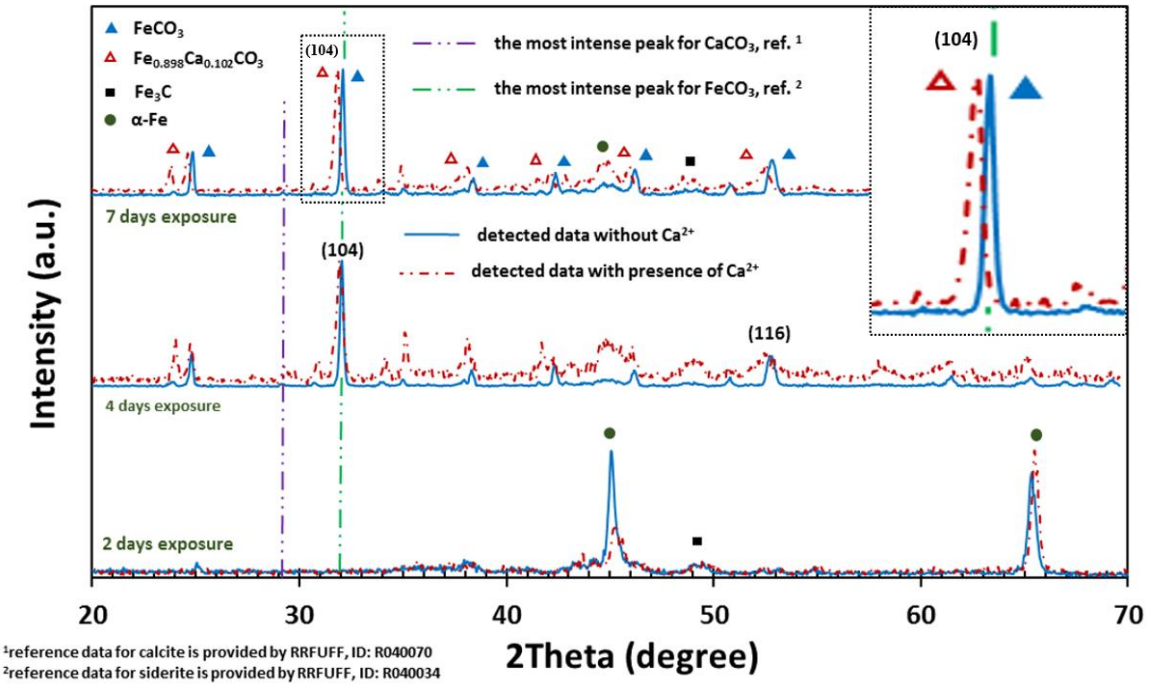

Figure 34. XRD patterns of surface layers detected on the steel surface after 2, 4, and 7 days of exposure with/without the presence of Ca^{2+} at pH 6.2

Figure 35 illustrates the EDS line scan analysis (left-hand graph) of a cross-sectioned specimen exposed to $CaCO_3$-saturated solution for 7 days shown by SEM (right-hand image). Such analysis proves a pure $FeCO_3$ layer was formed as an inner layer adjacent to the steel surface, whereas the outer corrosion product layer was $Fe_xCa_yCO_3$ (x+y=1) with an atomic percentage of Fe being dominant over Ca within this solid solution (x>y). The EDS results are in accordance with XRD observations in the presence of Ca^{2+}.

The vulnerability of the specimens to localized corrosion was also. Profilometry of the specimen surfaces was performed after removing corrosion product layers by Clarke solution [71] and no localized corrosion was observed for any of the above

experiments with or without $CaCO_3$. This is in stark contrast with other studies in the literature [42, 47].

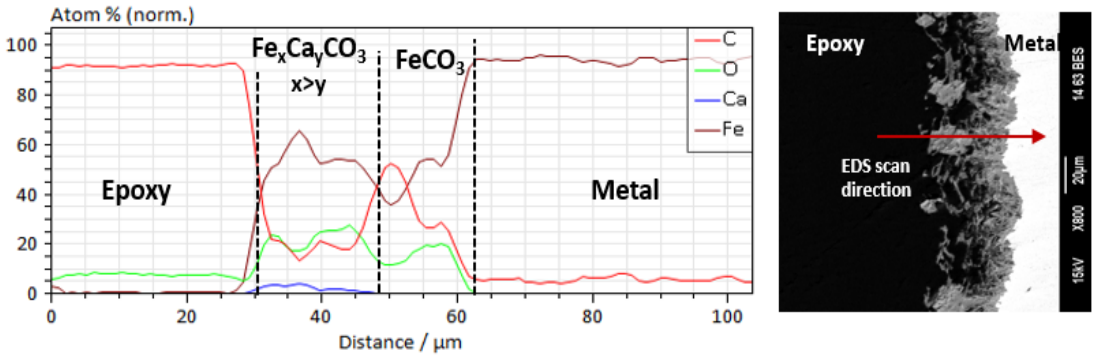

Figure 35. Elemental analysis (line scan) of cross-sectioned corrosion products formed on a specimen exposed to $CaCO_3$-saturated solution for 7 days at pH 6.2

6.1.1.3 Summary

- The development of Fe_3C acted as anchoring sites for precipitation of $Fe_xCa_{1-x}CO_3$ and $FeCO_3$ within its porous structure in solutions with and without $CaCO_3$, respectively. This was due to different water chemistry within the Fe_3C compared to the bulk solution, *i.e.*, higher pH and $FeCO_3$ saturation.
- A critical thickness for the Fe_3C network favoring the precipitation of carbonate crystals could be identified.
- The formation of a substitutional solid solution, $Fe_{0.9}Ca_{0.1}CO_3$ (outer layer) along with $FeCO_3$ (inner layer) lowered the general corrosion at the end of the exposure with no localized corrosion. There was no difference in this behavior when compared to what was seen in the experiments without Ca^{2+}, where only $FeCO_3$ precipitated.

- The protectiveness of the corrosion product was not jeopardized in the presence of Ca^{2+} ions when the solution was saturated with respect to $CaCO_3$ at pH 6.2.
- Overall, CO_2 corrosion mechanisms were not altered in $CaCO_3$ saturated solutions (with Ca^{2+} ~ 160 ppm) after full development of corrosion products (pseudo-passivation period).

6.1.2 Experiments with 6000 ppm Ca^{2+} at pH 5.5, and 0.6 M ionic strength[8]

In previous section, the effect of $CaCO_3$-saturtaed solution at pH 6.2, 160 ppm Ca^{2+}, and 0.18 M ionic strength was investigated. In this section, the effect of Ca^{2+} on CO_2 at more extreme, yet more representative, conditions are investigated, *i.e.*, lower pH, and higher [Ca^{2+}] and higher ionic strength as seen in oilfield conditions.

6.1.2.1 Methodology and Test Matrix

Similarly to the experiment performed at pH 6.2, two series of experiments were conducted (and repeated) at pH 5.5. One was performed in a $CaCO_3$-saturated solution ([Ca^{2+}] ≈ 6000 ppm) and one without Ca^{2+} (baseline experiment); other than that, both test series were conducted under the same conditions based on the test matrix presented in Table 7. The solutions, with and without Ca^{2+}, contained 1 wt.% NaCl in the presence of 0.53 bar pCO_2 at 80°C (1 bar total pressure of the glass cell). An excess amount of

[8] A version of this section has been published as "Effect of Calcium Ions and $CaCO_3$ Scale on the CO_2 Corrosion Mechanism of Mild Steel," presented at the NACE, Paper No. 13000, 2019.

powdered $CaCO_3$ reagent (15 g/L) was initially added to the solution in order to keep it saturated with respect to $CaCO_3$ over the course of the 7-day experiments. After adding $CaCO_3$, the pH was adjusted with 1.0 M HCl to a value of 5.50. For the tests without $CaCO_3$, the pH was adjusted to 5.50 by adding $NaHCO_3$ to the solution. For the experiments conducted in the absence of Ca^{2+}, sodium perchlorate salt ($NaClO_4$) was used to achieve the same ionic strength as the experiment with the presence of Ca^{2+}. $NaClO_4$ is highly soluble in water and has been used to adjust ionic strength as it does not react with common anions and cations, perchlorate has excellent ion stability in aqueous environments akin to those encountered in CO_2 corrosion [82]. Although no specific effects of Cl^- on the corrosion processes discussed herein are presented in this dissertation, many literature works have linked the presence of chloride ions with enhanced localized corrosion [83-85] and governance of adsorption properties [86-88]. No such characteristics has been reported about $NaClO_4$ and, since $NaClO_4$ does not yield free Cl^- when it dissociates in water, the two series of experiments had the same Cl^- ions concentration while maintaining identical ionic strength of 0.60 M. Using this approach, any observed difference in the experimental results would be due to the change in calcium concentration and would not be related to a change in chloride ions concentration. The solutions were deoxygenated by sparging with CO_2 for two hours prior to insertion of the specimen. In addition, CO_2 was continuously bubbled into solution to maintain CO_2 saturation during the 7-day corrosion experiments. The measured dissolved oxygen concentration was less than 5 ppb.

Table 7. Text matrix to investigate the effect of Ca^{2+} at pH 5.5

Parameter	Description	
	Baseline (without Ca^{2+})	With Ca^{2+}
Temperature	80°C	
pCO_2	0.53 bar	
pH	5.5 ± 0.2 (adjusted by $NaHCO_3$)	5.5 ± 0.1 (adjusted by HCl)
Electrolyte	1 wt.% NaCl +$NaHCO_3$+$NaClO_4$ (ionic strength=0.6 M)	1 wt.% NaCl +HCl+$CaCO_3$ (ionic strength=0.6 M)
$CaCO_3$ saturation degree (S_{CaCO_3})	0	Unity ([Ca^{2+}] ≈ 6000 ppm)
$FeCO_3$ saturation degree (S_{FeCO_3})	0 to 10.8 0 to 8.1 (using activity model, see Appendix II)	0 to 1.2 0 to 0.9 (using activity model, see Appendix II)
Dissolved O_2	<5 ppb	
Impeller rotation speed	20 rpm	
Mass transfer conditions	Equivalent to 0.58 m/s in a 0.1m ID pipe	
Experiment duration	7 days	

6.1.2.2 Results and Discussion

A special effort was made to maintain a very similar water chemistry for experiments based on the test matrix presented in Table 7. Figure 36 shows the bulk solution pH for experiments with and without Ca^{2+} over time at pH 5.5. Solution pH was maintained at pH 5.5 by adding hydrochloric acid (HCl) as necessary during the experiment without the presence of Ca^{2+}. However, the $CaCO_3$-saturated solution showed a strong buffering capacity over the course of experiments, therefore, for such solutions the pH was self-controlled (autogenous) at its initial value of pH 5.5. Such buffering behavior in the presence of excessive dissolved $CaCO_3$ was also reported by Duan, *et al.* [89]. Figure 37 compares the $FeCO_3$ saturation degree of the bulk solution for

experiments with and without Ca^{2+} over time. S_{FeCO_3} was calculated using Equation (17). Unlike, the experiments conducted at pH 6.2, the ferrous ion concentration ($[Fe^{2+}]$) could not be controlled over time for experiments conducted at pH 5.5 with a higher concentration of Ca^{2+} (6000 ppm). This is because the Na-form ion-exchange resin does not differentiate between Ca^{2+} and Fe^{2+} and adsorbs both divalent cations. Therefore, the resin would decrease the $[Ca^{2+}]$ dramatically without much influence on the $[Fe^{2+}]$, which was not the desired effect. In addition, the ion-exchange resin would become saturated with Ca^{2+} and lose its efficiency in a short time, although the supply of $CaCO_3$ powder at the bottom of the glass cell replenished the adsorbed Ca^{2+}. For consistency, the $[Fe^{2+}]$ was also not controlled, but only measured, in the baseline experiments conducted at pH 5.5.

Fe^{2+} was introduced into the bulk solution by the corrosion process and, as a result, $FeCO_3$ saturation increased over time for all experiments irrespective of Ca^{2+} presence. However, the final value of $FeCO_3$ saturation for the experiments without Ca^{2+} was higher than the experiment with Ca^{2+} due to its higher corrosion rate, leading to a higher Fe^{2+} concentration in the bulk solution. The final $FeCO_3$ saturation value for experiments with and without Ca^{2+} was 1.2 and 10.8, respectively (see Figure 37).

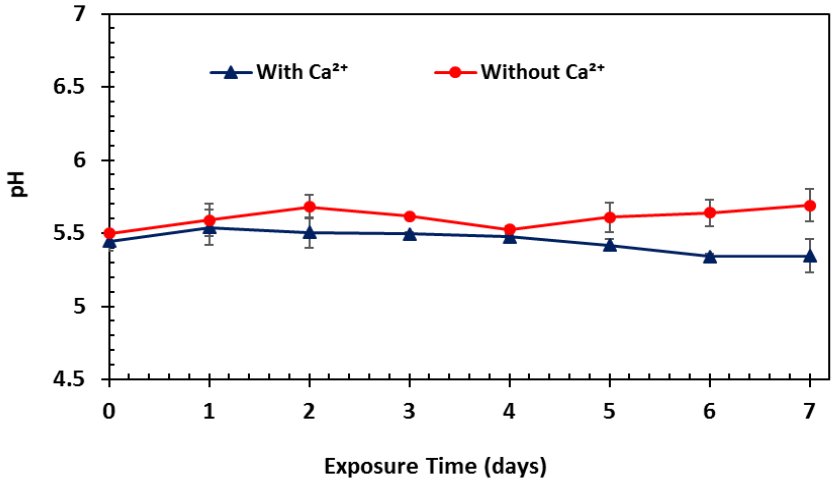

Figure 36. Variation of bulk solution pH over time for experiments with and without 6000 ppm Ca^{2+} ($S_{CaCO_3} = 1$) at 80°C, pCO_2 0.53 bar, 0.60 M ionic strength, and 20 rpm

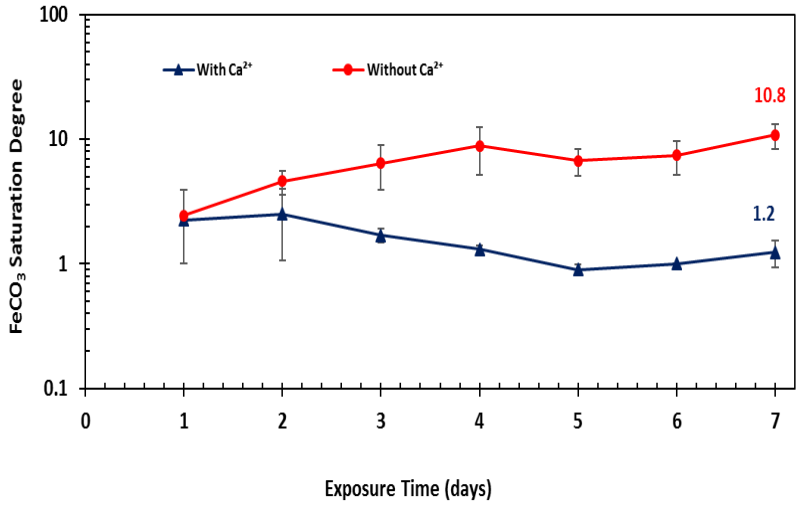

Figure 37. Variation of $FeCO_3$ saturation degree over time for the experiments with and without 6000 ppm Ca^{2+} ($S_{CaCO_3} = 1$) at 80°C, pCO_2 0.53 bar, bulk solution pH 5.5, 0.60 M ionic strength, and 20 rpm

The LPR corrosion rate of the steel specimens for experiments conducted in the presence of 6000 ppm Ca^{2+} (solution was saturated with respect to $CaCO_3$) is compared with that of the baseline conditions (in the absence of Ca^{2+} ions) in Figure 38.

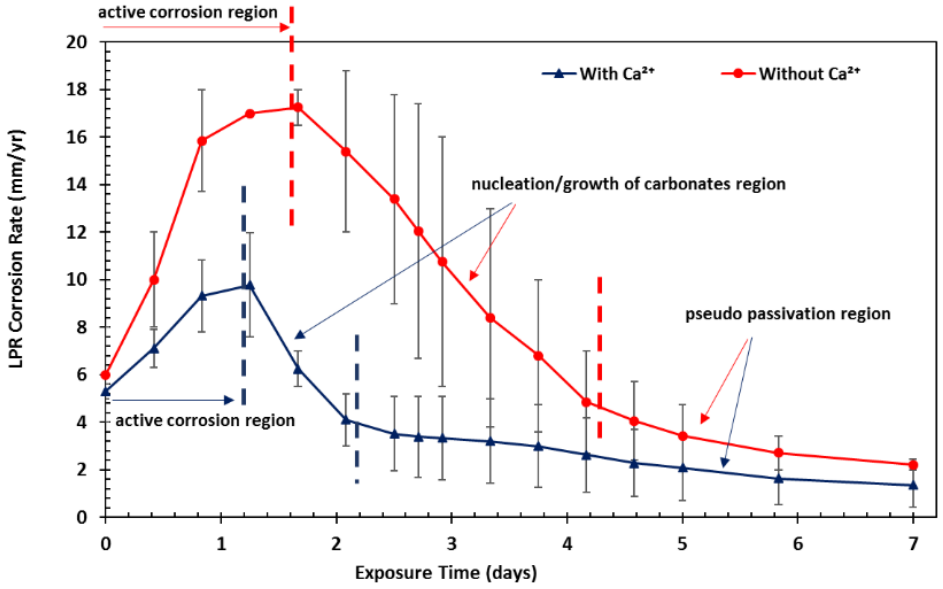

Figure 38. Comparison of LPR corrosion rates of UNS G10180 exposed to solutions without and with 6000 ppm Ca^{2+} ($S_{CaCO_3} = 1$) at 80°C, pCO_2 0.53 bar, bulk solution pH 5.5, 0.60 M ionic strength, and 20 rpm

Three corrosion regions were identified in both experiments (see Figure 38): 1-active corrosion, 2-nucleation, and growth of carbonates, and 3-pseudo passivation (similar to experiments conducted at pH 6.2 but with different timelines). The initial increase in the corrosion rate is related to a semi-conductive cementite phase (Fe_3C) that has been reported as the early-stage corrosion product for a UNS G10180 steel [76]. Fe_3C is often found on the steel surface, derived from the pre-existing ferritic-pearlitic microstructure, due to the preferential dissolution of the ferrite phase (α-Fe) over Fe_3C in

the corrosion process. The presence of Fe_3C increases the steel corrosion rate through a galvanic effect as it provides more cathodic sites for the hydrogen evolution reaction (HER) [90, 91]. The main HER in CO_2 aqueous environments is described as follows:

$$2H^+_{(aq)} + 2e^- \rightarrow H_{2(g)} \qquad \text{Equation 39}$$

As can be seen from Figure 38, the active corrosion region was shorter and the LPR corrosion rate was lower in the presence of Ca^{2+}. However, for both experiments, corrosion rates decrease after reaching a maximum value of 9 mm/y and 19 mm/yr for experiments with and without Ca^{2+}, respectively. As mentioned before, the magnitude of corrosion rate obtained by LPR is exaggerated. This is due to the inability of the LPR technique to cope with the galvanic corrosion effect inherent from the active corrosion region. However, LPR data are here used for trends rather than for obtaining values of corrosion rates, which are measured more accurately by the WL method.

Cross-sectional characterization and SEM/EDS analysis were performed on the specimens retrieved from the test solutions at the different exposure times for both series of experiments. Such investigations revealed that the decrease of corrosion rate was due to nucleation and growth of carbonate layers within the Fe_3C network and adjacent to the steel surface. (Results of surface characterization will be discussed in more detail in the next section.) In the pseudo-passivation region, the corrosion rates with and without Ca^{2+} significantly decreased. This was mainly attributed to the fact that corrosion product layers became denser and more compact during this time. It should be mentioned that the residual corrosion rate in this region remained high for both experiments with and

without Ca^{2+} (see Figure 38). Other researchers have also observed the same results as the corrosion product layer could not offer a good level of protectiveness at low bulk solution pH (*i.e.*, pH 5.5) [92]. However, the final corrosion rate was lower in the presence of Ca^{2+}. This indicated that the corrosion products in the presence of Ca^{2+} were comparatively more protective. At each measuring point, at days 2, 4, and 7 of the experiments, two specimens were retrieved from the test solutions for surface layer characterization and measurement of corrosion rate by weight loss techniques. Figure 39 depicts a comparison of time-averaged, cumulative, corrosion rate by WL (bar chart) and LPR (line chart) at different exposure times. LPR shows a higher corrosion rate than WL at each measuring point regardless of the presence of Ca^{2+}. As explained earlier, it is related to the inability of LPR to cope with the galvanic effect in the presence of Fe_3C at the initial stage of the corrosion process (first two days) and also to uncertainties related the use of the correct B value. Although the exaggeration of LPR values at the initial stage of the corrosion process is reflected in the other cumulative measuring points (0 to 4 and 0 to 7 days), the difference between LPR and WL values diminishes over time based on Figure 39 (with and without Ca^{2+}). This graph also indicates that the corrosion rate without Ca^{2+} is higher than for the experiments with Ca^{2+} at each measuring point, confirmed by both WL and LPR methods. Similarly to the corrosion rates obtained by LPR, WL results showed that the corrosion rate was decreasing over time for both series of experiments due to formation of corrosion products and reduction of active surface area at the steel substrate.

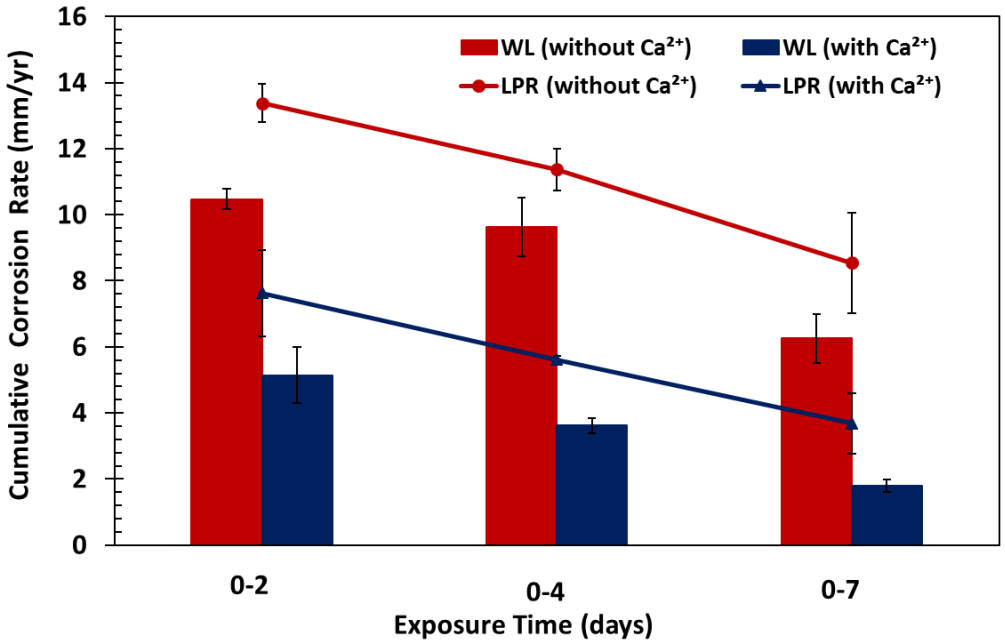

Figure 39. WL and LPR cumulative corrosion rate over time for solutions without and with 6000 ppm Ca^{2+} ($S_{CaCO_3} = 1$) at 80°C, pCO_2 0.53 bar, bulk solution pH 5.5, 0.60 M ionic strength, and 20 rpm

A comparison of OCP in solutions with and without Ca^{2+} is shown in Figure 40. The initial OCP for both experiments was almost the same and it became more positive after the carbonate layers formed on the steel surface. Note that the OCP values at the end of experiments with the presence of Ca^{2+} are greater indicating a better protectiveness offered by the surface layers in the pseudo-passivation region.

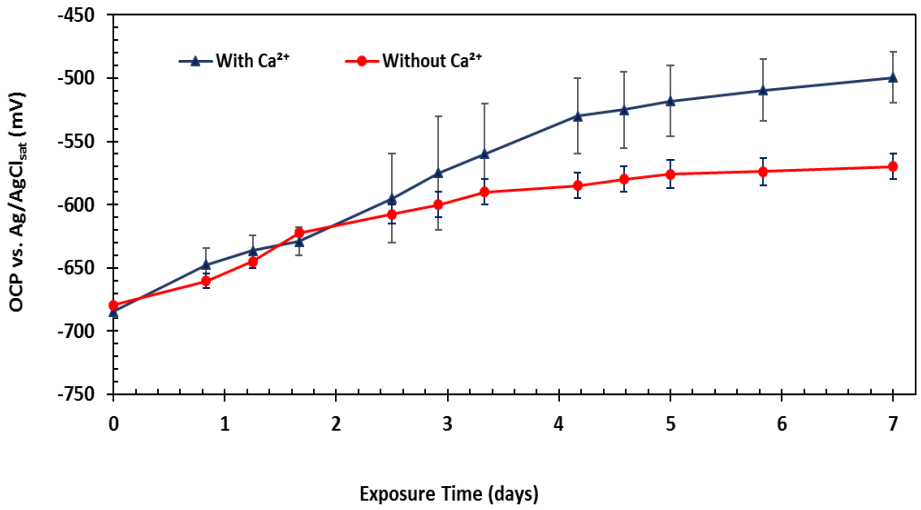

Figure 40. 5 Comparison of OCP over time for UNS G10180 exposed to solutions without and with 6000 ppm Ca^{2+} ($S_{CaCO_3} = 1$) at 80°C, pCO_2 0.53 bar, bulk solution pH 5.5, 0.60 M ionic strength, and 20 rpm

Surface layer characterization (experiments without Ca^{2+} at pH 5.5):

Figure 41 shows SEM cross-sectional and top view images of surface layers developed at different exposure times for experiments conducted in the absence of Ca^{2+}. The yellow arrows on the cross-sectioned specimens indicate the calculated metal loss based on WL corrosion rate. Such values were greater than the measured physical thickness of the Fe_3C layer, indicating that shear stress created by flow could have removed some of the Fe_3C from the steel surface, particularly at the beginning of the experiments.

Top and cross-sectional images taken for the first two days of the experiment confirm the development of a porous Fe_3C layer with an approximate thickness of 24 µm. The cross-section image at the end of day 4 suggests that a second layer precipitated within the Fe_3C network (first phase), adjacent to the steel surface. This phase

composition, as determined by EDS analysis, was consistent with $FeCO_3$ (Figure 42). Upon the precipitation of $FeCO_3$ within the Fe_3C pores, the corrosion rate decreased and so did the layer growth rate from day 4 to day 7. A scan of the top view images at different exposure times suggests that $FeCO_3$ crystals did not precipitate on top of the Fe_3C layer, even though $FeCO_3$ saturation degree for the bulk solution reached a value of 10.8 by the end of the experiment. To provide more proof of such a phenomenon, Figure 43 shows an EDS elemental line scan of the surface layers developed after seven days of exposure that suggests precipitation of $FeCO_3$ adjacent to the steel surface.

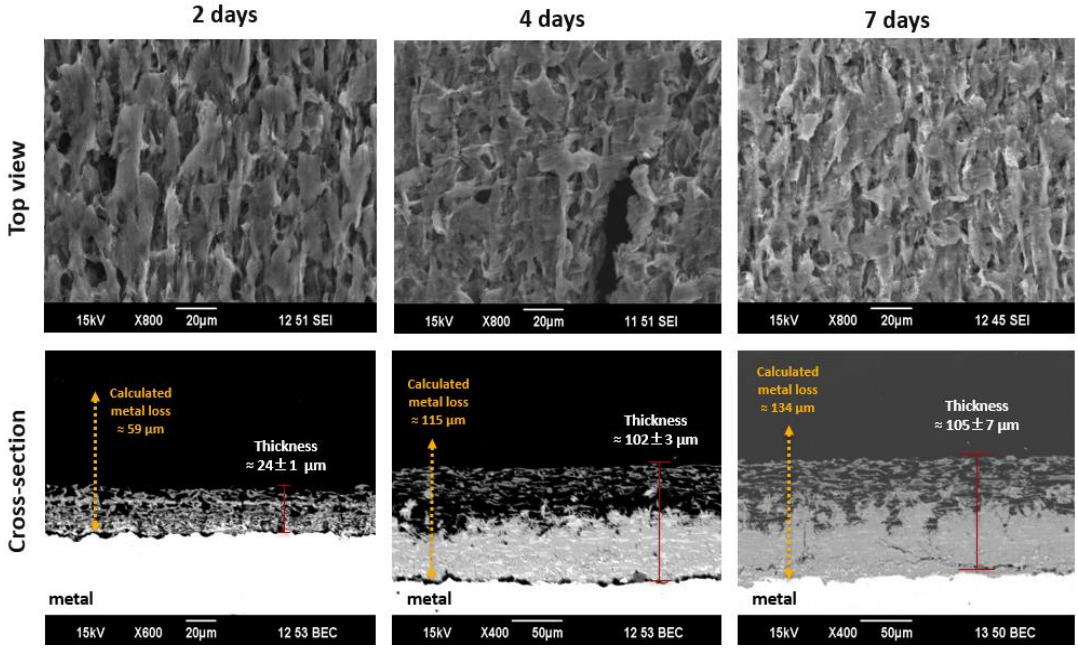

Figure 41. SEM images (top and cross-section view) of the development of surface layers over time for the experiment without Ca^{2+} at 80°C, pCO_2 0.53 bar, bulk solution pH 5.5, 0.60 M ionic strength, and 20 rpm

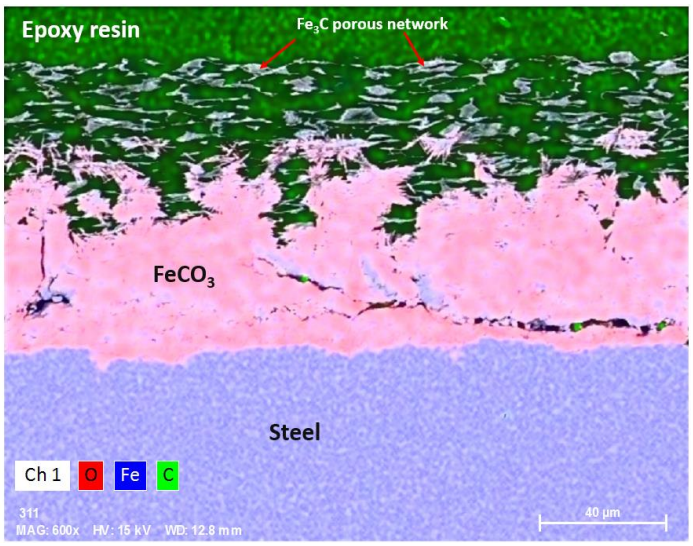

Figure 42. Cross-section SEM/EDS analysis of the corrosion products after 7 days of exposure to the experiment without Ca^{2+} at 80°C, pCO_2 0.53 bar, bulk solution pH 5.5, 0.60 M ionic strength, and 20 rpm

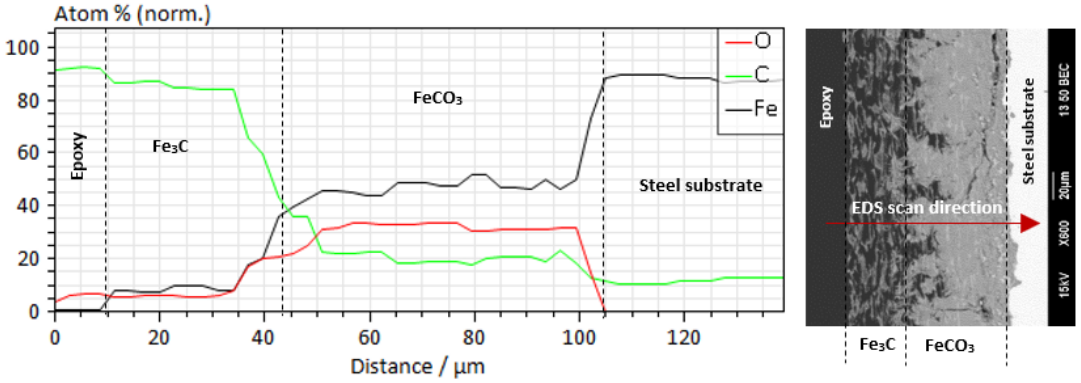

Figure 43. EDS line scan analysis of the surface layers developed after 7 after 7 days of exposure to the experiment without Ca^{2+} at 80°C, pCO_2 0.53 bar, bulk solution pH 5.5, 0.60 M ionic strength, and 20 rpm

Surface layer characterization (experiments with 6000 ppm Ca^{2+} at pH 5.5)

Figure 44 shows SEM images (cross-section and top view) of surface layers developed for the experiment performed with a $CaCO_3$-saturated solution. Unlike the experiment conducted in the absence of Ca^{2+}, SEM images of the top view confirmed

precipitation of crystalline phases on the top of the steel surface after two days of exposure. Such crystals did not cover the entire surface and their quantity and size grew over time (see top view images in Figure 44). EDS analysis and XRD data confirmed that such crystalline phases were a substitutional iron-calcium carbonate solid solution, with calcium being dominant over iron ($Fe_xCa_yCO_3$, $x+y=1$ and $x<y$). The cross-sectional SEM image of the specimen after 2 days of exposure confirmed that $Fe_xCa_yCO_3$ was partially precipitated within the Fe_3C porous structure. As mentioned earlier, the expected increased pH within the Fe_3C network would favor precipitation of $CaCO_3$. However, Fe^{2+} should also be involved in the crystallization process along with Ca^{2+} since it is present close to the steel surface where the nucleation/growth process occurs. Consequently, a substitutional solid solution of iron-calcium carbonate with Ca being dominant over Fe formed at this stage. Precipitation of mixed carbonates first started within the Fe_3C network, however, propagation and growth of such phases continued out of the Fe_3C layers, which in some locations were visible from top view and cross-section images as shown in Figure 44. Based on Figure 38, the corrosion rate was still increasing up to day 2 of the experiment without Ca^{2+}, whereas for the experiment with 6000 ppm Ca^{2+}, the corrosion rate was already decreasing by day 2. This decrease was due to precipitation of the mixed metal carbonates within the Fe_3C and partial blockage of the steel surface, retarding the anodic reaction. Cross-section morphology of the surface layers at the end of day 4 showed that almost the entire Fe_3C layer was filled with $Fe_xCa_yCO_3$. The corrosion rate obtained by LPR showed a high value of 2.3 mm/yr at this stage (Figure 38). An immediate conclusion was that precipitation of $Fe_xCa_yCO_3$ on the

steel surface could not offer an acceptable level of protection against further corrosion, and undermining corrosion was still ongoing. That was why the thickness of surface layers grew from 35 µm at day 4 to 60 µm at day 7 of the experiment.

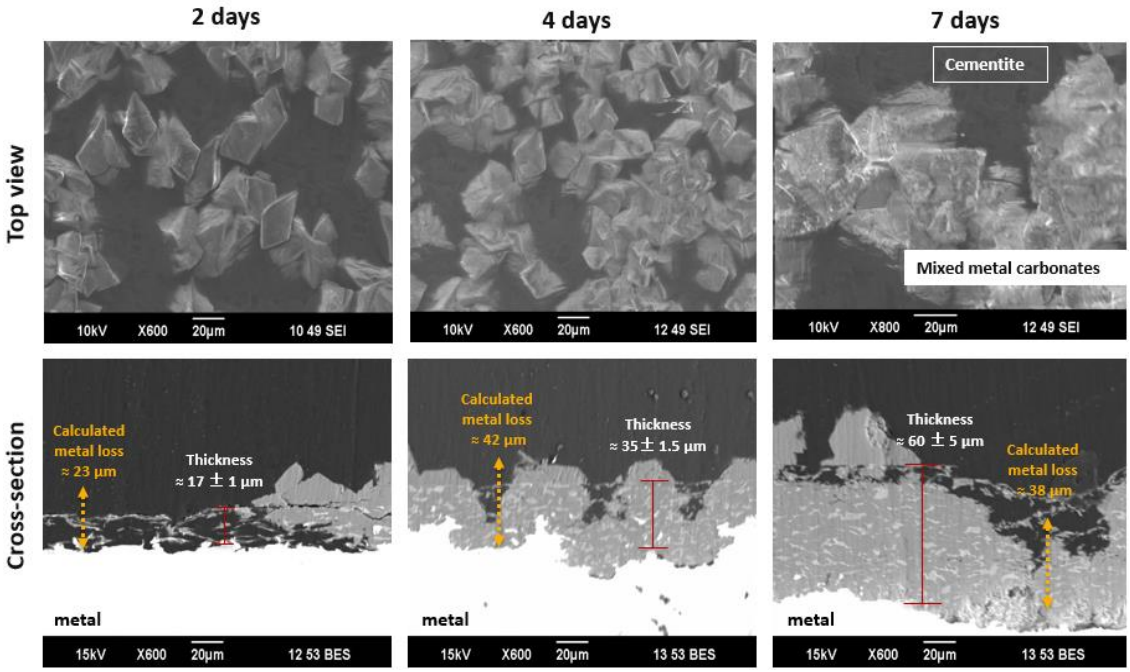

Figure 44. SEM images (top and cross-section view) of the development of surface layers over time for the experiments conducted in the presence of 6000 ppm Ca^{2+} ($S_{CaCO_3} = 1$) at 80°C, pCO_2 0.53 bar, bulk solution pH 5.5, 0.60 M ionic strength, and 20 rpm

Figure 45 illustrates the chemical composition obtained by EDS of the surface layers after 7 days of exposure to the solution saturated with $CaCO_3$. For better visualization, the graph is divided into 6 zones, from (a) to (f), with different colors. Zone (a) corresponds to the epoxy resin, used for the preparation of specimens for cross-sectioning, with carbon and oxygen being the dominant constituent elements. The line scan enters the cementite structure in zone (b), with carbon and iron being the principal

constituent elements. Zone (c) confirms the formation of a mixed metal cation solid solution of $Fe_xCa_yCO_3$ where the mole fraction of Ca is greater than Fe (y>x). Therefore, this compound is named "scale" rather than "corrosion product" since Ca is dominant over Fe. This zone comprises the main portion of surface layers with an approximate thickness of 45 µm. Zone (d) begins at a point where the mole fractions of Ca and Fe are equal within the solid solution of $Fe_xCa_yCO_3$ (x=y). However, closer to the steel surface, the mole fraction of Fe becomes dominant over Ca. Therefore, the surface layer precipitated in this zone is considered a "corrosion product" with partial incorporation of Ca. Zone (e) is located very close to the steel surface. In this zone, Ca is not present and a pure $FeCO_3$ is formed. Eventually, the line scan enters the steel substrate in zone (f). The presence of carbon in this zone is mainly considered to be a contamination from epoxy resin during conservation of the corrosion product layer and the polishing process.

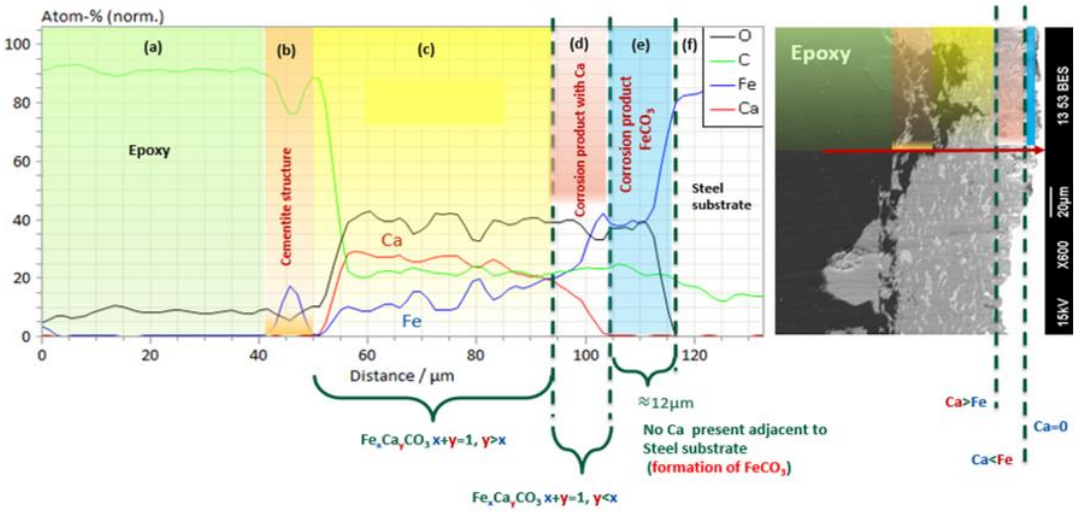

Figure 45. EDS analysis (line scan) of the surface layers formed on carbon steel after 7 days of exposure to a solution with the presence of 6000 ppm Ca^{2+} ($S_{CaCO_3} = 1$) at 80°C, pCO_2 0.53 bar, bulk solution pH 5.5, 0.60 M ionic strength, and 20 rpm

Morphological analysis of SEM images (Figure 44) and chemical composition characterization of surface layers (Figure 45) suggests the formation of a composite layer on the steel surface in the presence of Ca^{2+}. Very close to the steel surface and within the Fe_3C network, a pure $FeCO_3$ phase was formed as the inner layer. The outer layer was comprised of a solid solution of $Fe_xCa_yCO_3$. The mole fraction of Ca was dominant over Fe as this outer layer grew/developed toward the outer border of the Fe_3C network. Figure 46 (EDS mapping) clearly illustrates the formation of $Fe_xCa_yCO_3$ within and outside the Fe_3C network, along with the formation of $FeCO_3$ adjacent to the steel surface.

As mentioned earlier, the change of water chemistry near the steel surface and within the Fe_3C pores was the main driving force for precipitation of the mixed carbonates. Figure 47 shows the XRD patterns of the surface layers after 7 days of exposure to the solution saturated with respect to $CaCO_3$. Although X-ray penetration power is limited and cannot reach the layers close to the steel surface, it is able to provide information relevant to the outer side of the surface layers. As can be seen in Figure 47, the detected carbonate peaks in the presence of Ca^{2+} ions are broadened and located between the reference peaks for $CaCO_3$ and $FeCO_3$. This indicates the formation of a heterogeneous solid solution with a chemical formula of $Fe_xCa_yCO_3$. Peaks associated with α-Fe and Fe_3C are also present in the acquired XRD data. This could mean that the $Fe_xCa_yCO_3$ phase did not cover the entire steel surface.

The vulnerability of the specimens to localized corrosion was also evaluated. Profilometry of the specimen surfaces was performed after removing corrosion product

layers by Clarke solution, according to ASTM G1 standard, [71] and no localized corrosion was observed for experiments with or without Ca^{2+} at the conducted experimental condition.

In general, the EIS data was in accord with the discussions and conclusions provided throughout this manuscript. An example of EIS data related to this section (6.1.2) is presented and interpreted in Appendix III.

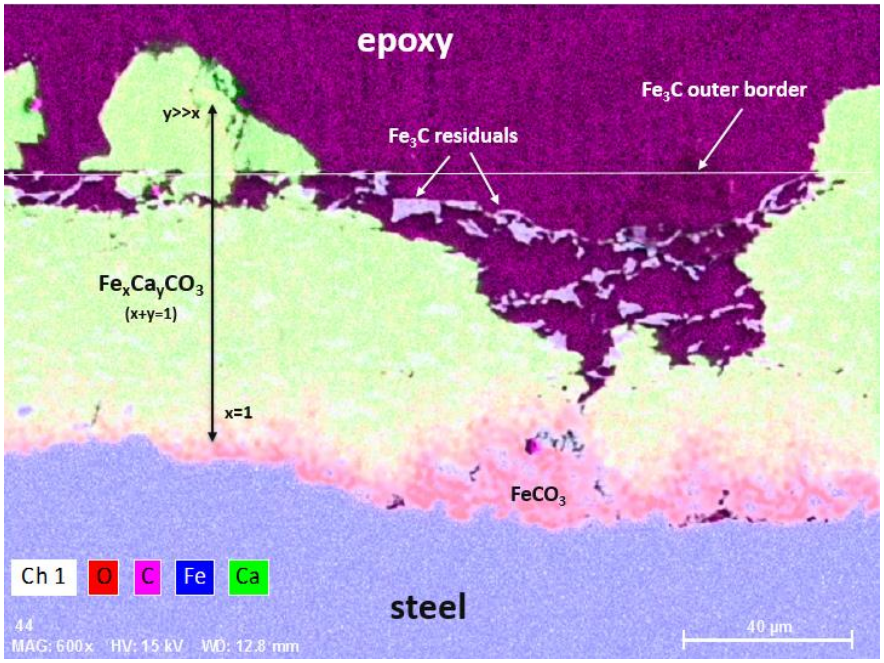

Figure 46. EDS analysis (map mode) of a cross-section UNS G10180 specimen after 7 days of exposure to a $CaCO_3$-saturated solution at 80°C, bulk solution pH 5.5, pCO_2 0.53 bar, 0.60 M ionic strength, and 6000 ppm Ca^{2+}

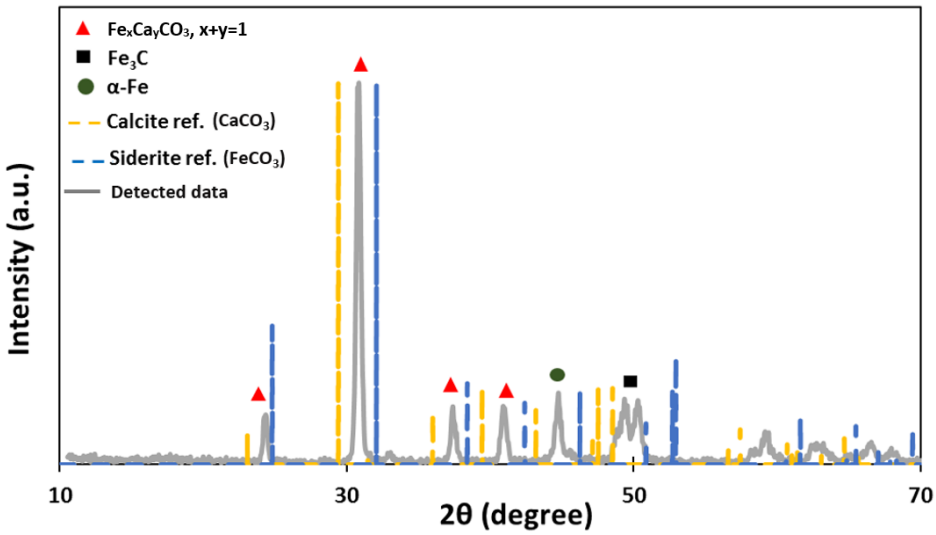

Figure 47. XRD pattern of the surface layers formed on UNS G10180 specimen after 7 days of exposure to a $CaCO_3$-saturated solution (6000 ppm Ca^{2+}) at 80°C, bulk solution pH 5.5, pCO_2 0.53 bar, 0.60 M ionic strength, and 20 rpm

6.1.2.3 Descriptive Model for the Effect of high [Ca^{2+}] on Uniform Corrosion

Based on the experimental results, a descriptive model is proposed for the mechanism of CO_2 corrosion of mild steel (with ferritic-pearlitic microstructure) exposed to a $CaCO_3$-saturated solution with a high concentration of Ca^{2+} at 80˚C, bulk solution pH 5.5, pCO_2 0.53 bar, 0.60 M ionic strength:

(a) UNS G1018 carbon steel is exposed to solution saturated with $CaCO_3$ and CO_2 as shown in Figure 48a;

(b) Fe dissolves and Fe^{2+} is released into solution. Consequently, a porous Fe_3C network is left behind on the steel surface and grows in thickness over time, as shown in Figure 48b;

(c) The Fe_3C layer reaches a critical thickness with a water chemistry very different within its pores ($S_{CaCO_3} \gg 1$) as compared to the bulk solution

($S_{CaCO_3} = 1$). This condition favors nucleation and growth of $CaCO_3$. However, due to the presence of Fe^{2+} and isostructurality of calcite ($CaCO_3$) and siderite ($FeCO_3$), a substitutional carbonate, $Fe_xCa_yCO_3$ (x+y=1), forms within the pores of the Fe_3C network, as shown in Figure 48c;

(d) At this stage, almost the entire Fe_3C network is filled with $Fe_xCa_yCO_3$ (x+y=1) with y>>x for the exterior of the surface layer, as shown in Figure 48d;

(e) Although the corrosion rate decreases upon precipitation and development of $Fe_xCa_yCO_3$ on the steel surface, undermining corrosion is ongoing and, as a result, the thickness of the surface layer grows over time, as shown in Figure 48e;

(f) The presence of mixed carbonates on the steel surface hinders mass transfer of Fe^{2+} outward from the steel, therefore, the solubility limit of $FeCO_3$ is exceeded adjacent to the steel substrate and beneath the mixed carbonate layers. $FeCO_3$ is supersaturated in such conditions and forms on the steel surface as an inner layer, as shown in Figure 48f. Precipitation of $FeCO_3$ and its growth at this stage is responsible for the further decrease in corrosion rate.

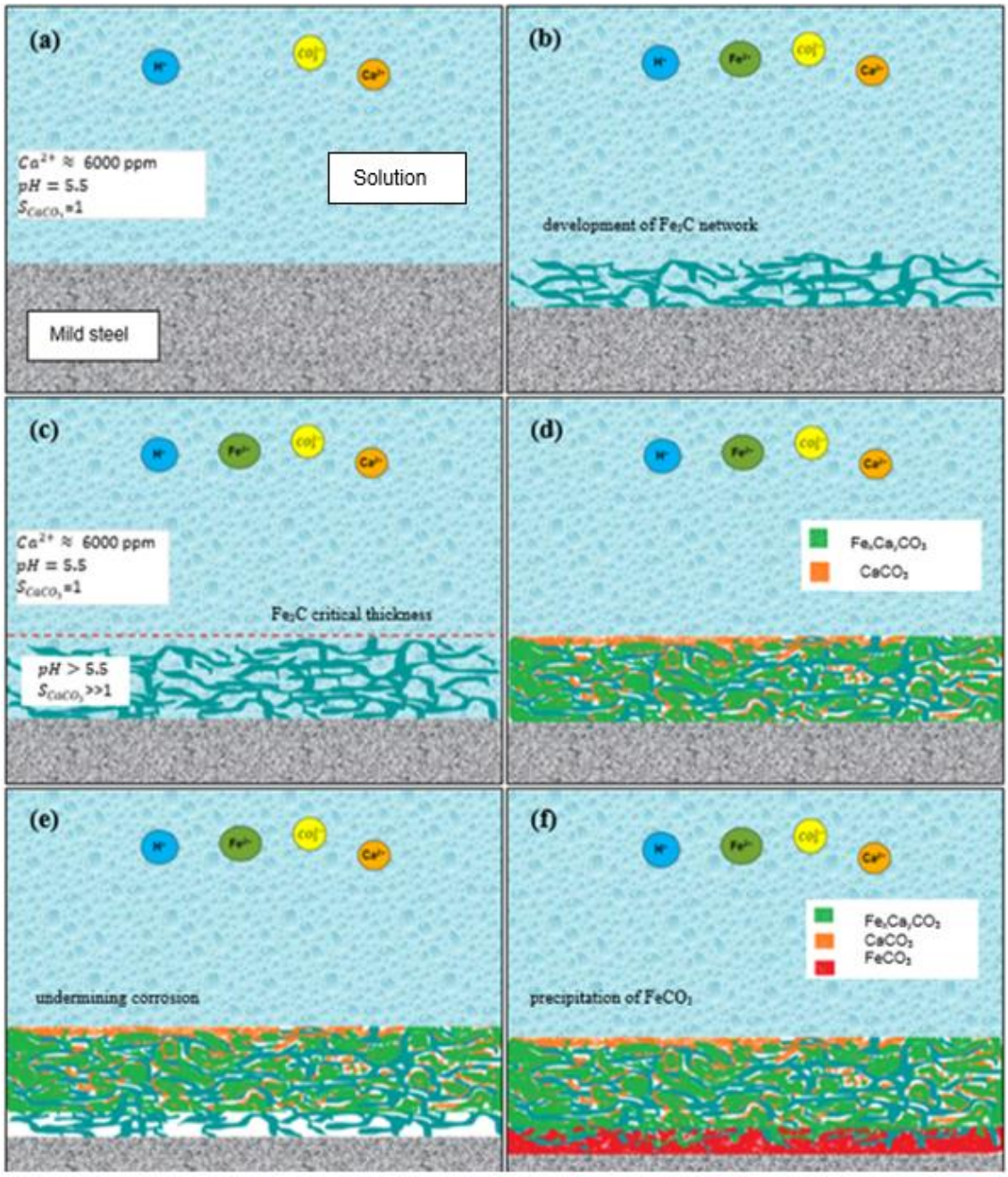

Figure 48. A descriptive model for CO_2 corrosion mechanism of mild steel exposed to the $CaCO_3$-saturated solution at 80°C, bulk solution pH 5.5, pCO_2 0.53 bar, 6000 ppm Ca^{2+}, 0.60 M ionic strength, and 20 rpm

6.1.2.4 Summary

- Fe_3C played a critical role in precipitation of $Fe_xCa_yCO_3$ (x+y=1) and $FeCO_3$. The mole fraction of Ca in $Fe_xCa_yCO_3$ depended on the calcium ion concentration in bulk solution.
- The protective behavior of the surface layers was mainly due to the formation of $FeCO_3$ adjacent to the steel surface and not $Fe_xCa_yCO_3$. However, the presence of $Fe_xCa_yCO_3$ facilitated $FeCO_3$ precipitation and enhanced its protectiveness by acting as a mass transfer barrier of Fe^{2+} outwards from the steel and H^+ towards the steel.
- No localized corrosion was observed in the presence of high concentration of Ca^{2+} while the electrolyte was saturated with respect to $CaCO_3$.
- Based on experiments conducted at low and high Ca^{2+} (pH 6.2 and 5.5, respectively), the presence of Ca^{2+}, regardless of its concentration, does not adversely influence uniform and localized corrosion if the solutions remain in saturated condition with respect to $CaCO_3$.

6.2 Effect of $CaCO_3$ Scale on CO_2 Corrosion Mechanism

In the previous section (section 6.1), the protectiveness of a mixed $Fe_xCa_yCO_3$ in CO_2 environments was evaluated in the presence of different concentrations of Ca^{2+}. To the author's best knowledge, there is limited experimental data related to the protectiveness of a pure $CaCO_3$ scale formed in supersaturated condition with respect to $CaCO_3$. This section presents the results of an experimental test series, performed in $CaCO_3$ supersaturated solutions, and aimed to evaluate the protective properties of

$CaCO_3$ scale in CO_2 corrosion of mild steel. Two methodologies were employed to precipitate $CaCO_3$ scale on the metal substrate, one electrochemically driven and the other chemically driven. Each methodology and its experimental results are discussed in the following sections.

6.2.1 $CaCO_3$ Precipitation: Electrochemically Driven

6.2.1.1 Methodology and Test Matrix

While the properties of "pure" $FeCO_3$ layers have been extensively investigated [20, 93], this is not the case for "pure" $CaCO_3$. The protectiveness of $CaCO_3$ has not been systematically studied since it is difficult to promote $CaCO_3$ precipitation while, at the same time, suppressing $FeCO_3$ formation. However, this was successfully performed in the current research using a novel methodology. The idea was to precipitate a uniform $CaCO_3$ layer on the steel substrate (as opposed to patchy precipitation), without the participation of Fe^{2+} (coming from the corroding steel) in the carbonate formation process. To reach this goal, the working electrodes were cathodically polarized (-200 mV *versus* OCP) to limit Fe dissolution during the entire exposure time (five days). Table 8 shows the experimental conditions used for this series of experiments. The corrosion rate was significantly decreased by cathodic polarization; hence minimizing dramatically Fe^{2+} production (the Fe^{2+} concentration was so low that it was not detectable in the bulk solution by spectrophotometry). The bulk solution was kept saturated with respect to $CaCO_3$ by introducing an excess amount of powdered $CaCO_3$ to the solution at the beginning of the experiments. The experimental conditions used for this series of experiments were identical to those for $CaCO_3$-saturated solutions at pH 5.5 (section

6.1.2) except that here the specimens were cathodically protected in order to form pure $CaCO_3$ scale on the steel surface while suppressing any Fe^{2+} release by corrosion and any formation of $FeCO_3$. During cathodic protection, the surface pH of the specimen was much higher than the bulk solution due to the artificial acceleration of hydrogen evolution reactions and consumption of hydrogen ions. Therefore, the surface water chemistry was favorable for precipitation of $CaCO_3$ scale in the absence of Fe^{2+}. LPR and OCP measurements were performed once a day when the cathodic polarization was temporarily removed (for approximately 5 minutes) in order to observe the effect of $CaCO_3$ scale formation on corrosion rate and OCP. After 5 days, the cathodic protection was permanently removed, and one specimen was retrieved from the test solution for surface characterization while the other specimen (now covered with $CaCO_3$ scale) was exposed to the corrosive solution that was saturated with $CaCO_3$.

Table 8. Experimental conditions employed to evaluate protectiveness of $CaCO_3$ scale

Temperature	80°C
pCO_2	0.53 bar
pH	5.5 ± 0.1
Electrolyte	1 wt.% NaCl+HCl+$CaCO_3$ (ionic strength=0.6 M)
$CaCO_3$ saturation degree in bulk solution	Unity (6000 ppm Ca^{2+})
$CaCO_3$ saturation degree at the steel/solution interface (during cathodic polarization, the solution at the steel surface was temporarily supersaturated with respect to $CaCO_3$)	$S_{CaCO_3}>1$
Impeller rotation speed	20 rpm
Mass transfer conditions	Equivalent to 0.58 m/s in a 0.1m ID pipe
Specimen steel	UNS G10180
Cathodic polarization potential	-200 mV vs. OCP
Methods for monitoring corrosion behavior	LPR, OCP
Dissolved O_2	<5 ppb
Cathodic protection duration (formation of $CaCO_3$)	5 days
Pre-scaled ($CaCO_3$) specimen exposed for active corrosion	7 days

6.2.1.2 Results and Discussion

Formation of artificial $CaCO_3$ scale:

Figure 49 shows the morphology of the surface layer formed on the mild steel surface during 5 days of exposure to the electrolyte and under continuous cathodic polarization. The SEM cross-section image reveals a uniform, thin and compact (5-7 μm) layer. The chemical composition analysis by EDS confirmed that this surface layer is indeed pure $CaCO_3$ without any detectable incorporation of Fe. Figure 50 and Figure 51 shows EDS mapping and line scan analysis of the top and cross-section surface layers,

respectively. Fe did not incorporate into $CaCO_3$ during its crystallization and that pure $CaCO_3$ scale precipitated on the steel surface.

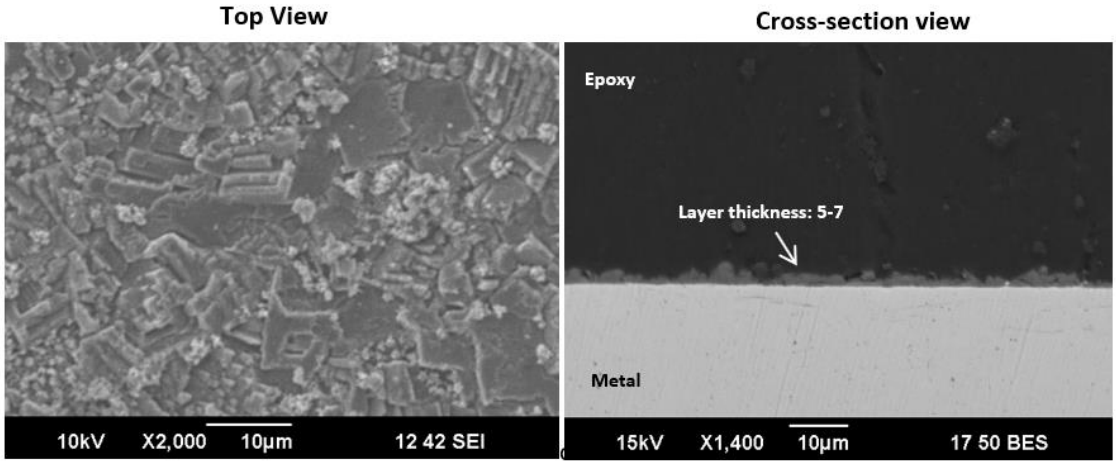

Figure 49. Top and cross-section view SEM of the surface layers formed on the steel during 5 days of cathodic polarization; $CaCO_3$-saturated solution (6000 ppm Ca^{2+}), 80°C, bulk solution pH 5.5, pCO_2 0.53 bar, 0.60 M ionic strength, 20 rpm

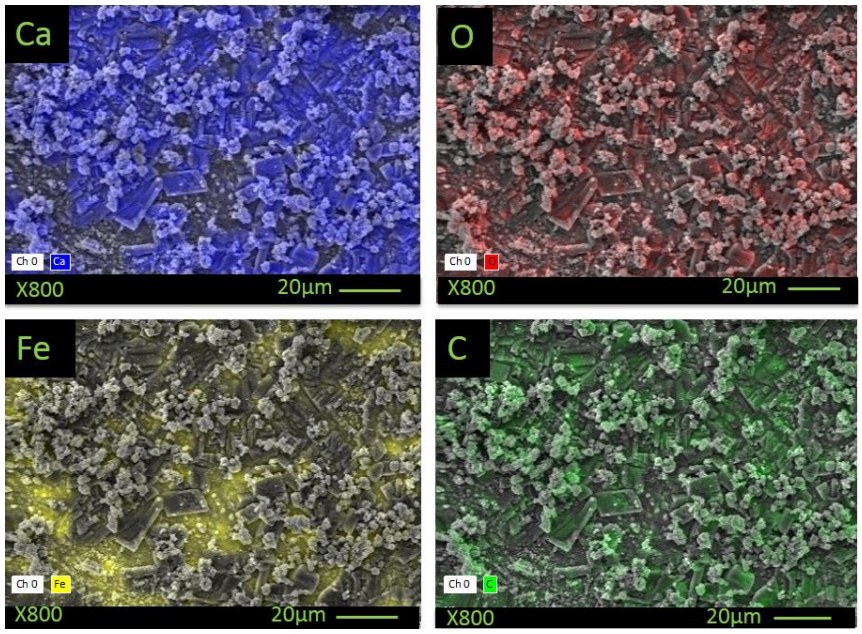

Figure 50. SEM and EDS mapping analysis of the surface layers formed during 5 days of cathodic polarization; Fe is absent in the precipitated crystalline phases (80°C, bulk solution pH 5.5, pCO_2 0.53 bar, 6000 ppm Ca^{2+}, 0.60 M ionic strength, and 20 rpm)

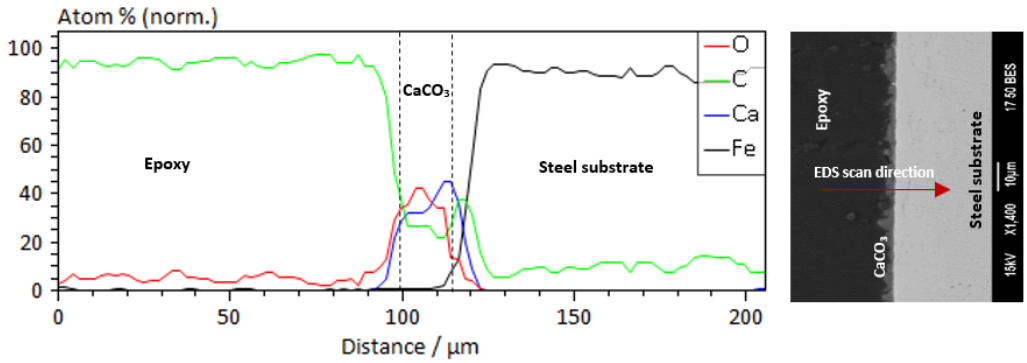

Figure 51. EDS line scan results showing distribution of Ca, C, O, and Fe within the surface layers; formation of $CaCO_3$ scale (80°C, bulk solution pH 5.5, pCO_2 0.53 bar, 6000 ppm Ca^{2+}, 0.60 M ionic strength, and 20 rpm)

During the cathodic polarization of the specimens, the corrosion rate was measured daily at the OCP. To achieve this, the cathodic polarization was temporarily interrupted for about 5 minutes allowing the potential to reach its OCP and then LPR corrosion rate was measured. Figure 52a and Figure 52b depicts corrosion rate and potential trends (average OCP and cathodic potential) during the entire duration (5 days) of the experiment, respectively. The corrosion rate decreased over time upon precipitation of $CaCO_3$ scale on the steel surface. The corrosion rate trend shows that $CaCO_3$ scale can offer some protectiveness against further corrosion. However, this is a premature conclusion since the cathodic polarization prevented any undermining corrosion during the whole 5-day period. The average OCP over time remained almost unchanged and it seemed that formation of $CaCO_3$ scale did not influence the OCP. One explanation for this observation is that $CaCO_3$ scale retarded the anodic and cathodic reactions at the same rate by decreasing the active surface area of the steel. A question

remained whether or not this protectiveness could be retained after permanently removing the cathodic polarization. This issue is addressed in the next section.

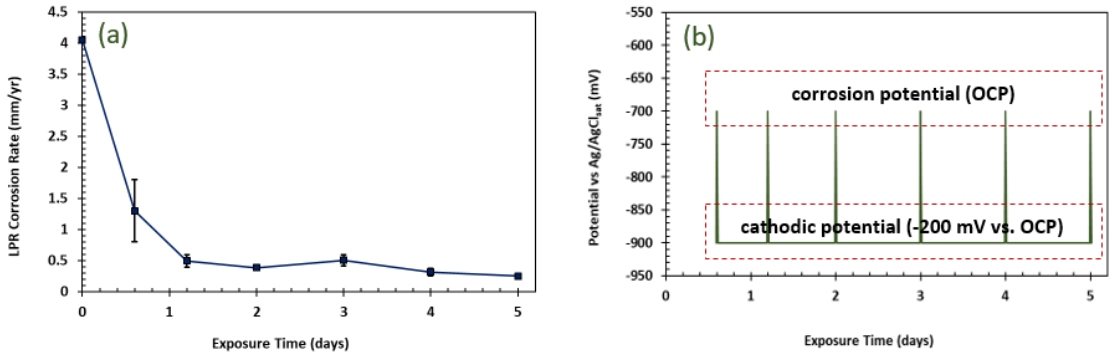

Figure 52. LPR Corrosion rate (a) and potential variations (b) over time during cathodic polarization of the specimens (80°C, bulk solution pH 5.5, pCO_2 0.53 bar, 6000 ppm Ca^{2+}, 0.60 M ionic strength, and 20 rpm)

The $CaCO_3$-covered specimen continued to be exposed to the corrosive solution but this time without cathodic polarization to investigate the protectiveness of the precipitated scale. Figure 53a and Figure 53b show pH and Fe^{2+} variation over time, respectively, with and without cathodic polarization. The bulk solution was always saturated with respect to $CaCO_3$, which acted as a strong buffer at the conducted experimental conditions (Figure 53a). As can be seen from Figure 53b, the corrosion rate was well controlled during the polarization period with no measurable Fe^{2+} in the bulk solution. Upon removal of the cathodic polarization after day 5, Fe^{2+} concentration in the bulk solution increased over the remaining 7 days of the experiment, indicating active corrosion of the steel surface. Figure 54a and Figure 54b compares the corrosion rate, obtained with LPR, and the potential between periods with and without cathodic

protection. As can be seen in Figure 54a, in the first 5 days (during cathodic protection), the corrosion rate decreased over time with the formation of $CaCO_3$ scale. However, after removing the cathodic protection, the corrosion seemed to first increase rapidly, reaching a similar level as that observed at the start of the experiment, and then was observed to decrease over the rest of the experimental duration. The corrosion behavior of the second period essentially similar to the bare steel specimen exposed to the $CaCO_3$-saturated solution (first experimental scenario described above). Figure 54b shows that the OCP was increasing over time after removal of cathodic protection. Such behavior is related to the surface layer development after exposure to the corrosion medium (without cathodic protection).

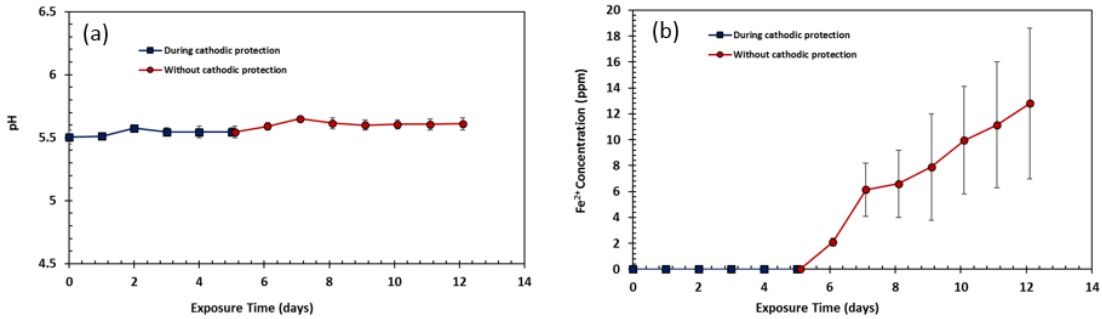

Figure 53. pH (a) and Fe^{2+} concentration (b) variation over time during and without cathodic protection (80°C, bulk solution pH 5.5, pCO_2 0.53 bar, 6000 ppm Ca^{2+}, 0.60 M ionic strength, and 20 rpm)

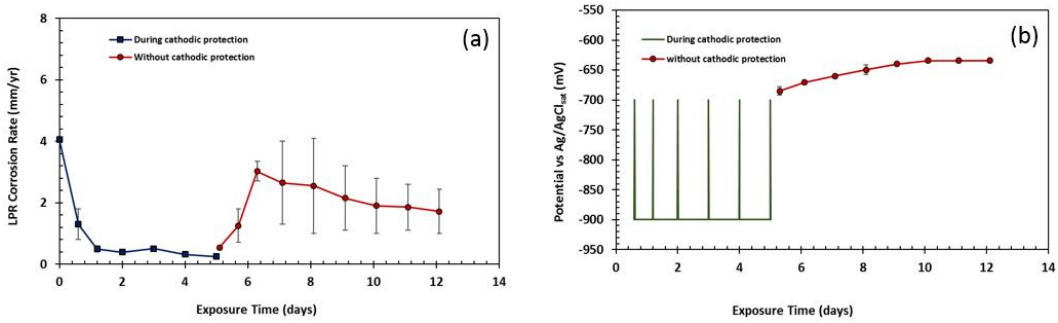

Figure 54. Corrosion rate (a) and potential (b) variation over time during and without cathodic protection (80°C, bulk solution pH 5.5, pCO_2 0.53 bar, 6000 ppm Ca^{2+}, 0.60 M ionic strength, and 20 rpm)

Figure 55 compares the SEM cross-sectional morphology of the specimens obtained with (a) and after removal (b) of the cathodic polarization. The surface layer thickness increased from 5-7 µm at the end of the polarization period to 17-25 µm after 7 days of exposure to the $CaCO_3$-saturated solution without cathodic polarization. The chemical composition analysis of the layers revealed that the $CaCO_3$ scale formed during polarization was still present as the outer layer and that a mixed metal carbonate of $Fe_xCa_yCO_3$ was formed beneath the $CaCO_3$ layer, driven by corrosion processes as shown in Figure 56. Such analysis confirmed that although the corrosion rate decreased upon formation of $CaCO_3$ scale during polarization (by reducing the anodic and cathodic reactions at the same rate), $CaCO_3$ scale did not maintain its protective behavior when exposed to the corrosive medium without cathodic polarization (active corrosion was observed). Such behavior of $CaCO_3$ scale is also reported by Ghanbari, *et al*., in AC corrosion [53] and by Bekhrad, *et al.*, in the absence of dissolved Ca^{2+} ions [52]. It is noteworthy that despite $CaCO_3$ (scale) sharing a similar crystal structure to $FeCO_3$ (corrosion product), $CaCO_3$ did not show sustained protective behavior against further

corrosion while $FeCO_3$ is considered as a protective layer. The main argument is that the constituent cations of $CaCO_3$ scale and $FeCO_3$ have different sources. Ca^{2+} ions come from bulk solution while Fe^{2+} ions come from the corroding steel surface. Therefore, $FeCO_3$ has superior adherence to steel with probably different adherence, and mechanical, properties. This is what makes $FeCO_3$ a more protective layer in comparison to $CaCO_3$.

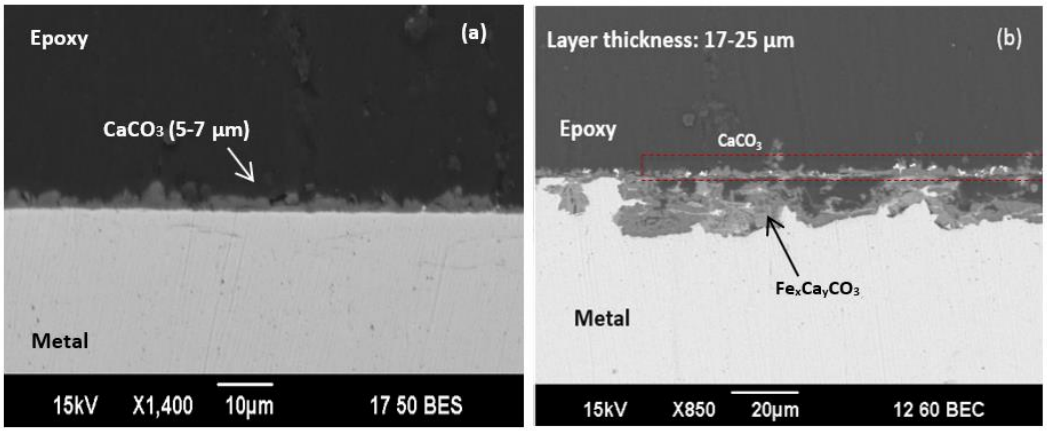

Figure 55. Comparison of surface layers morphology and thickness at the end of the polarization period (5 days exposure) and after exposure to the corrosive medium without cathodic protection (7 days exposure) at 80°C, bulk solution pH 5.5, pCO_2 0.53 bar, 6000 ppm Ca^{2+}, 0.60 M ionic strength, and 20 rpm

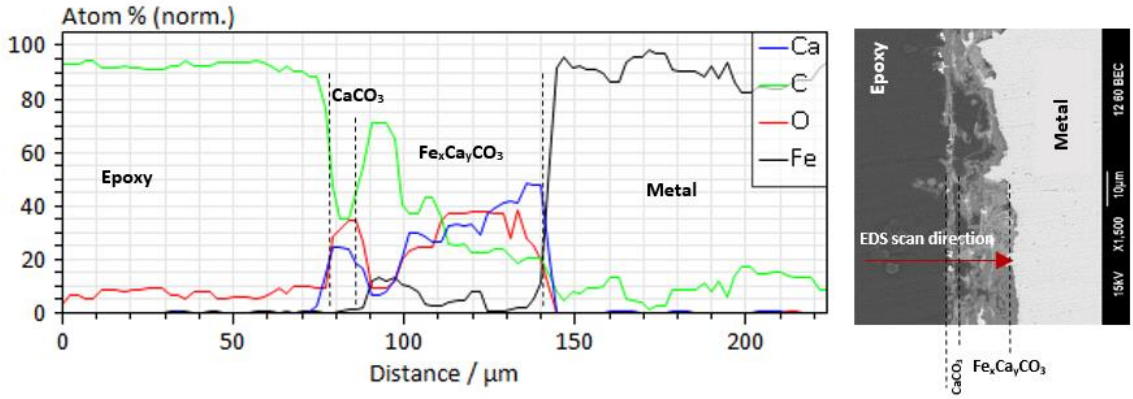

Figure 56. Chemical composition of the layers at the steel surface after 7 days of exposure to a $CaCO_3$-saturated solution without cathodic protection of specimen at pH 5.5, 80°C, 0.53 bar pCO_2, ionic strength 0.6M, 6000 ppm Ca^{2+}, 20 rpm

Figure 57 compiles the results already presented for $CaCO_3$-saturated (initial bare specimen) and $CaCO_3$-supersaturated solution (initial precipitation of $CaCO_3$ scale). Figure 57 compares the corrosion rate trend over time of carbon steel considering two different starting conditions, a bare specimen and of a specimen pre-scaled with $CaCO_3$. The two specimens were exposed to the same experimental conditions described in Table 7, and no cathodic polarization was applied at that point. The purpose of this comparison is to investigate if the presence of $CaCO_3$ scale has any effect on the corrosion trend and on the steady-state corrosion rate. The bare specimen showed a higher initial corrosion rate over the first days of the experiment compared to the pre-scaled specimens. However, the final corrosion rate of both specimens was identical at the end of the experiments. It can be concluded that $CaCO_3$ scale is not protective in the experimental conditions conducted. However, its presence accelerated the formation of $Fe_xCa_yCO_3$ and/or $FeCO_3$ by hindering the mass transfer of Fe^{2+} from the steel surface to the bulk solution. For the bare specimen, the development of Fe_3C was also a mass transfer barrier

for Fe^{2+}, however, the galvanic effect between Fe_3C and α-Fe phases led to a pronounced acceleration of the corrosion rate, as compared to the pre-scaled specimens in the active corrosion zone.

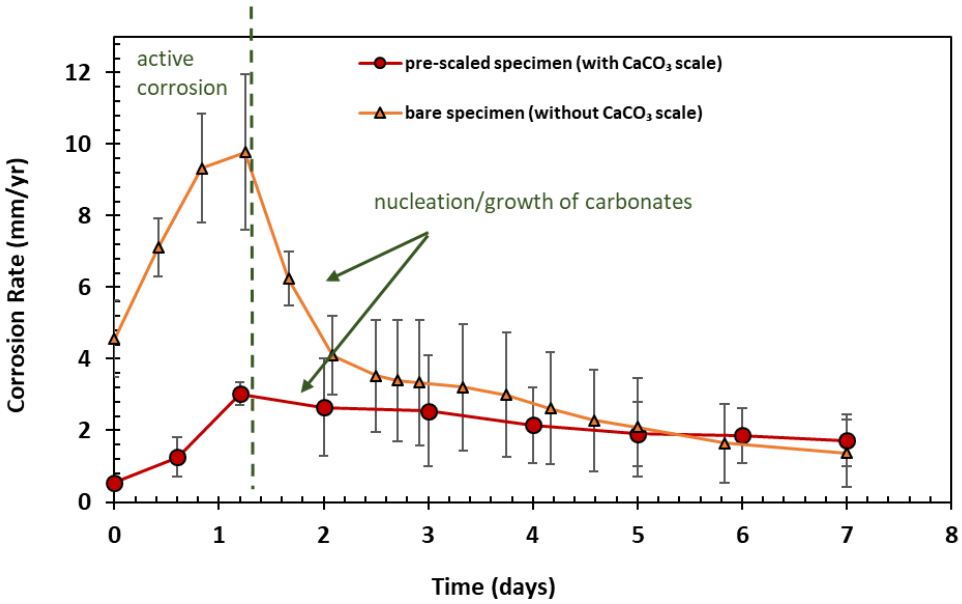

Figure 57. Comparison of corrosion behavior of mild steel with and without $CaCO_3$ scale at bulk solution pH 5.5, 80°C, 0.53 bar pCO_2, ionic strength 0.6M, 6000 ppm Ca^{2+} ($S_{CaCO_3} = 1$), and 20 rpm

6.2.2 $CaCO_3$ Precipitation: Chemically Driven

In section 6.2.1, the protectiveness of $CaCO_3$ scale precipitated from a 5-day cathodic polarization (electrochemically driven) of the specimens was evaluated. In this section, a thorough comparison of different solution's $CaCO_3$ saturation level in CO_2 environment is provided. The $CaCO_3$ scale was precipitated from a temporarily (around 2 hours) supersaturated solution by addition of $Ca(OH)_2$ (chemically driven).

6.2.2.1 Methodology and Test Matrix

Three experiments were designed with different saturation levels with respect to $CaCO_3$: 1-$S_{CaCO_3} = 0$ (baseline solution), 2- $S_{CaCO_3} = 1$ ($CaCO_3$-saturated solution) and 3- $S_{CaCO_3} >> 1000$ (temporarily supersaturated solution with respect to $CaCO_3$). All the experiments were conducted and repeated in two different bulk solution pH values, 6.2 and 5.5. Using different solution pHs permitted having different dissolved Ca^{2+} concentrations while the solution was saturated with respect to $CaCO_3$ for both pHs. The stable $CaCO_3$-saturated solutions were achieved by addition of an excess amount of $CaCO_3$ reagent at the beginning of the Ca^{2+}-containing experiments. A schematic of the experimental design is illustrated in Figure 58. The methodology and experimental results of baseline experiments and $CaCO_3$-saturated experiments in different solution pHs were thoroughly presented in Section 6.1. Here, only the methodology of the third series of experiments when the solution is initially supersaturated (chemically driven) with respect to $CaCO_3$ is presented. However, the experimental results of the new experiments ($S_{CaCO_3} >> 1000$) are compared with experiments of $S_{CaCO_3} = 0$ and $S_{CaCO_3} = 1$.

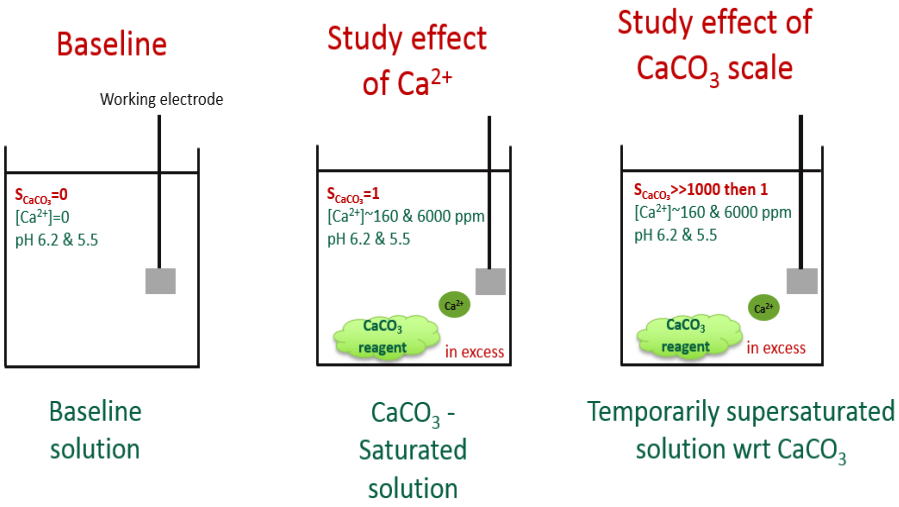

Figure 58. Schematic of experimental design of three different $CaCO_3$ saturation levels in various solution pH and [Ca^{2+}] at 80°C, pCO_2 0.53 bar, 1wt% NaCl, and 20 rpm

As mentioned earlier, the experimental setup can control [Fe^{2+}] and [H^+] by means of two different ion-exchange resins (Na-form and H-form, respectively). It should be pointed that for experiments with lower pH value (5.5) and higher Ca^{2+} concentration (6000 ppm), [Fe^{2+}] has not been controlled due to the fact that Na-form resin does not differentiate between Ca^{2+} and Fe^{2+} and adsorbs both divalent cations. Therefore, after a short period, the resin can become saturated with Ca^{2+} and Fe^{2+} and lose its efficiency. Despite the lack of controlling [Fe^{2+}] at pH 5.5, the $FeCO_3$ saturation level at pH 6.2 and 5.5 are in good agreement (due to the higher solubility of $FeCO_3$ at pH 5.5 as compared to pH 6.2). Therefore, the comparison of the results of the two pHs is still valid. The conditions are presented in Table 9 and Table 10, accordingly. The three sets of experiments have identical water chemistry. At pH 5.5, sodium perchlorate salt ($NaClO_4$) was used in the associated baseline experiments to achieve the same ionic strength as of those for $CaCO_3$-satuated and temporarily supersaturated experiments (0.6 M ionic

strength). $NaClO_4$ does not have free Cl^-, therefore, all the solutions in different $CaCO_3$ saturation levels have the same concentration of free Cl^-. Calcium hydroxide ($Ca(OH)_2$) was used to make the solution temporarily supersaturated with respect to $CaCO_3$.

Table 9. Test matrix for different $CaCO_3$ saturation levels at pH 6.2 and 160 ppm [Ca^{2+}]

Parameter	Description		
Temperature	80°C		
pCO_2	0.53 bar		
pH	6.2 (controlled)		
Electrolyte	Baseline	Study effect of Ca^{2+}	Study effect of $CaCO_3$ scale (chemically driven)
	1 wt.% NaCl +$NaHCO_3$ (Ionic Strength ~0.18 M)	1 wt.% NaCl +$CaCO_3$ (Ionic Strength ~0.18 M)	1 wt.% NaCl +$CaCO_3$ +$Ca(OH)_2$ (Ionic Strength ~ 0.18 M)
[Ca^{2+}]	0	160 ppm	166 ppm (at pH 10.5) then 160 ppm (at pH6.2)
$\mathbf{S_{CaCO_3}}$	0	1	>> 1000 then 1 (caused by addition of $Ca(OH)_2$)
$\mathbf{S_{FeCO_3}}$	0 to 10 0 to 5 (using activity model, see Appendix II)		
Dissolved O_2	<5 ppb		
Reference Electrode	Saturated Ag/AgCl		
Impeller Rotation Speed	20 rpm		
Mass Transfer Conditions	Equivalent to 0.58 m/s in a 0.1m ID pipe		

Table 10. Test matrix for different $CaCO_3$ saturation levels at pH 5.5 and 6000 ppm $[Ca^{2+}]$

Parameter	Description		
Temperature	80°C		
pCO_2	0.53 bar		
pH	5.5 (controlled)		
Electrolyte	Baseline	Study effect of Ca^{2+}	Study effect of $CaCO_3$ scale (chemically driven)
	1 wt.% NaCl +$NaHCO_3$+$NaClO_4$ (Ionic Strength ~0.6 M)	1 wt.% NaCl +$CaCO_3$ (Ionic Strength ~0.6 M)	1 wt.% NaCl +$CaCO_3$+$Ca(OH)_2$ (Ionic Strength ~0.6 M)
$[Ca^{2+}]$	0	6000 ppm	6020 (at pH 11) then 6000 ppm (at pH5.5)
S_{CaCO_3}	0	1	>> 1000 then 1 (caused by addition of $Ca(OH)_2$)
S_{FeCO_3}	0 to 10 0 to 8 (using activity model, see Appendix II)		
Dissolved O_2	<5 ppb		
Reference Electrode	Saturated Ag/AgCl		
Impeller Rotation Speed	20 rpm		
Mass Transfer Conditions	Equivalent to 0.58 m/s in a 0.1m ID pipe		

The methodology used for making the solution temporarily (around 2 hours) supersaturated with respect to $CaCO_3$ was similar to experiments with $CaCO_3$-saturated solution presented in Section 6.1. The only difference was that the deoxygenated slurry of $Ca(OH)_2$ was injected to the system at the very beginning of the experiments to facilitate precipitation of $CaCO_3$ (chemically driven). Before addition of $Ca(OH)_2$, the solution was saturated with respect to $CaCO_3$ at both pH 6.2 and 5.5. Addition of $Ca(OH)_2$ slurry

resulted in large increases in solution pH and [Ca^{2+}] over the first two hours of the experiments. During this relatively short time window the solution became temporarily supersaturated with respect to $CaCO_3$, which allowed precipitation of a uniform $CaCO_3$ scale on the steel surface. The solution pH, [Ca^{2+}], and S_{CaCO_3} naturally returned to initial conditions after two hours and a uniform layer of $CaCO_3$ scale was formed on the steel surface. The pH, [Ca^{2+}], and S_{CaCO_3} of the solution before and during injection of $Ca(OH)_2$ are presented in Table 9 and Table 10. The pH values reached up to 11, therefore; the specimens should experience a very low corrosion rate in such a temporarily high pH. A series of chemical reactions took place by injection of $Ca(OH)_2$ into the solution that temporarily changed the water chemistry:

- First, dissociation of $Ca(OH)_2$ resulted in releasing more Ca^{2+} and OH^- (reaction 40) into the system.
- Second, consumption of hydrogen ions and increasing solution pH (reaction 41). At this stage, the solution became extremely supersaturated with respect to $CaCO_3$ ($S_{CaCO_3} \gg 1000$).
- Third, precipitation of $CaCO_3$ scale resulted in consumption of excess amount of Ca^{2+} and release of hydrogen ion (reaction 42). At the end of this stage, the water chemistry was as identical as before injection of $Ca(OH)_2$. The overall reaction is as expressed in equation (43).

$$Ca(OH)_{2(aq)} \rightleftarrows Ca^{2+}_{(aq)} + 2OH^-_{(aq)} \qquad \text{Equation 40}$$

$$2H^-_{(aq)} + 2H^+_{(aq)} \rightleftarrows 2H_2O_{(l)} \quad \text{Equation 41}$$

$$Ca^{2+}_{(aq)} + H_2CO_{3(aq)} \rightleftarrows CaCO_{3(s)} + 2H^+_{(aq)} \quad \text{Equation 42}$$

$$Ca(OH)_{2(aq)} + H_2CO_{3(aq)} \rightleftarrows CaCO_{3(s)} + 2H_2O_{(l)} \quad \text{Equation 43}$$

This methodology was employed to mimic the oilfield condition when sudden changes in brine production rate and chemistry can lead to the aqueous solution becoming locally supersaturated with respect to $CaCO_3$ and to precipitation of $CaCO_3$ scale. However, after precipitation of $CaCO_3$ scale, the brine returns to the equilibrium state (saturated with respect to $CaCO_3$).

One metal specimen was retrieved from the solution after the first two hours to characterize the $CaCO_3$ scale formation resulted from $Ca(OH)_2$ injection. One specimen was taken out at day 2 and two specimens were retrieved from the glass cell at day 4 and 7 from each experiment to obtain WL and conduct surface characterizations using techniques including scanning SEM, EDS, and XRD.

6.2.2.2 Results and Discussion

Effect of $CaCO_3$ saturation - Experiments conducted at pH 6.2:

Figure 59 shows the bulk solution pH for the three types of experiment over time. Solution pH was maintained at pH 6.2 by means of H-form ion-exchange resin when it was necessary during the experiments. For the experiment initially supersaturated with respect to $CaCO_3$ ($S_{CaCO_3} \gg 1000$), as explained in the methodology section, $Ca(OH)_2$ was used to increase the solution pH in the first two hours in order to facilitate the precipitation of $CaCO_3$ scale on the steel surface. Except for this short time period, the

solution pH for all the experiments with different $CaCO_3$ saturation levels were identical. $[Fe^{2+}]$ was controlled in a way to achieve a $FeCO_3$ saturation level not higher than 10 in all experiments. For experiments with $S_{CaCO_3} = 0$ and $S_{CaCO_3} = 1$, ferrous ion concentration was controlled by means of Na-form ion-exchange resin. However, for the experiments initially at $S_{CaCO_3} \gg 1000$, ferrous ion concentration did not need to be controlled due to the lower general corrosion rate and consequently slower rate of Fe^{2+} generation. Figure 60 shows a comparison of ferrous ion concentration, $[Fe^{2+}]$, over time for solutions with different $CaCO_3$ saturation levels. The average $FeCO_3$ saturation level achieved during experiments with different $CaCO_3$ saturation levels is also indicated in Figure 60. Note that the average S_{FeCO_3} for the experiments, initially supersaturated with respect to $CaCO_3$, is 5.5 which is lower than the other two experiments.

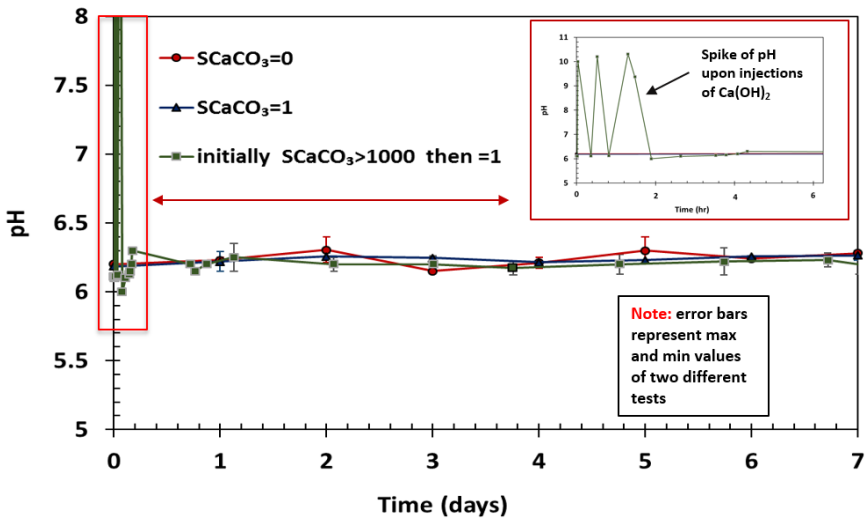

Figure 59. Variation of bulk solution pH over time for the experiments with different $CaCO_3$ saturation levels (80˚C, pCO_2 0.53 bar, 20 rpm, ionic strength 0.18 M, $[Ca^{2+}]$ ~160 ppm)

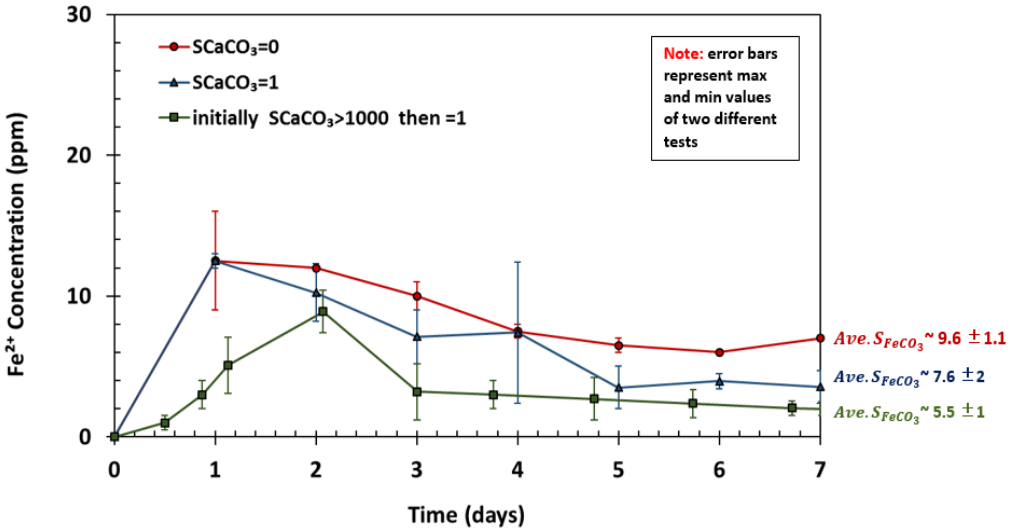

Figure 60. Variation of [Fe^{2+}] over time for the experiments with different $CaCO_3$ saturation levels (80˚C, pCO_2 0.53 bar, 20 rpm, pH 6.2, ionic strength 0.18 M, [Ca^{2+}] ~160 ppm)

Comparison of corrosion rate and open circuit potential at pH 6.2

Figure 61 illustrates a comparison of corrosion rate (CR) by the LPR method over time for experiments with different $CaCO_3$ saturation levels. For each experiment, specimens at day 2, 4 and 7 were also retrieved from the test solution to conduct weight loss characterization. Based on Figure 61, between day 4 and 5, the corrosion rate became very similar for all experiments with lower final CR obtained in the presence of $CaCO_3$ scale on the metal surface (experiments with initially $S_{CaCO_3} \gg 1000$). Another observation is that for experiments with $S_{CaCO_3} = 0$ and $S_{CaCO_3} = 1$, CR was obviously increasing (active corrosion) up to approximately day 2, while for experiments with initially $S_{CaCO_3} \gg 1000$, the active corrosion period was much shorter (less than day 1). The increase of CR in such periods (active corrosion) is attributed to the development of the Fe_3C network on the steel surface as explained in previous sections. In Figure 61, the

three identified corrosion periods (active corrosion, nucleation/growth of $FeCO_3$, and pseudo-passivation) associated to the baseline experiments ($S_{CaCO_3} = 0$) are indicated. For a complete explanation about such corrosion periods and the role of Fe_3C on CO_2 corrosion mechanism of UNS G10180, please refer to section 6.1 of this manuscript. Conclusively, the presence of $CaCO_3$ scale on the steel surface decreased the general CR with a much shorter active corrosion period and lower final CR in comparison to the other experiments. It seems that $CaCO_3$ scale has promoted formation of a protective corrosion product on the steel surface and enhanced its protectiveness based on LPR and WL corrosion behavior over long-term experiments (see Figure 61 and Figure 62). Such behavior was also observed for the $CaCO_3$ scale precipitated by electrochemical methods as discussed in the previous section.

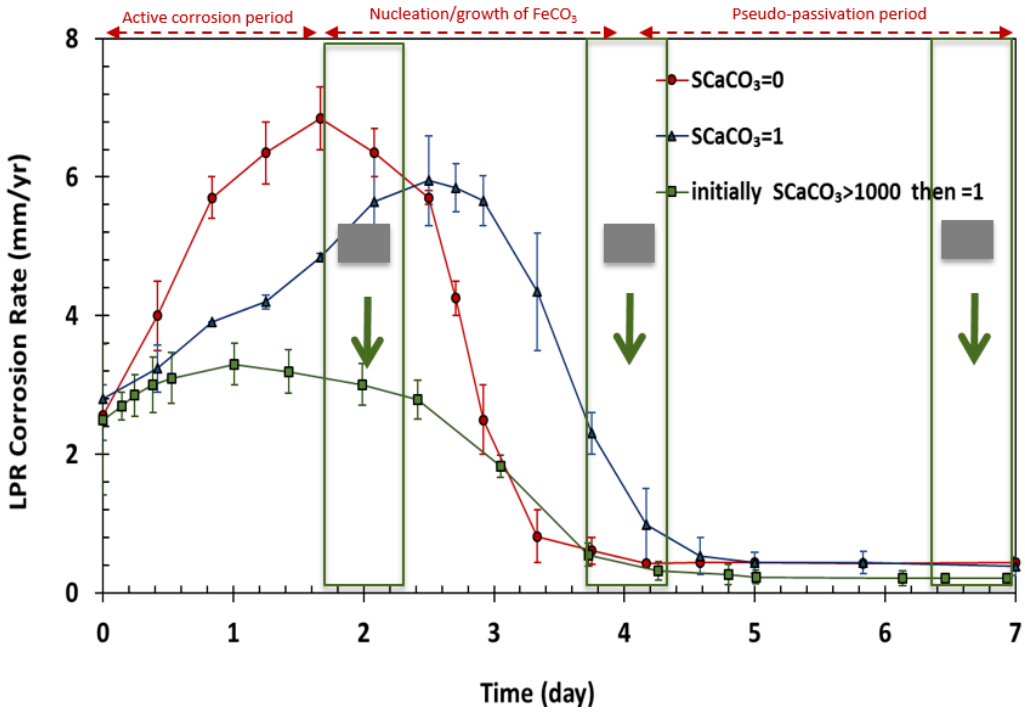

Figure 61. Comparison of LPR corrosion behavior of UNS G10180 exposed to solutions with different $CaCO_3$ saturation levels (80˚C, pCO_2 0.53 bar, 20 rpm, pH 6.2, ionic strength 0.18 M, $[Ca^{2+}]$ ~160 ppm)

Figure 62 shows a comparison of cumulative CR by WL at different exposure times for experiments with different $CaCO_3$ saturation levels. In each measuring point, the general CR in the presence of $CaCO_3$ scale on the steel surface (initially $S_{CaCO_3} \gg 1000$) was noticeably lower than the baseline ($S_{CaCO_3} = 0$) and $CaCO_3$-saturated experiments ($S_{CaCO_3} = 1$). Indeed, for all experiments, the CR was decreasing over time which was due to formation of corrosion products on the surface of mild steel. It is worth mentioning that the WL CR was in accordance with LPR CR results.

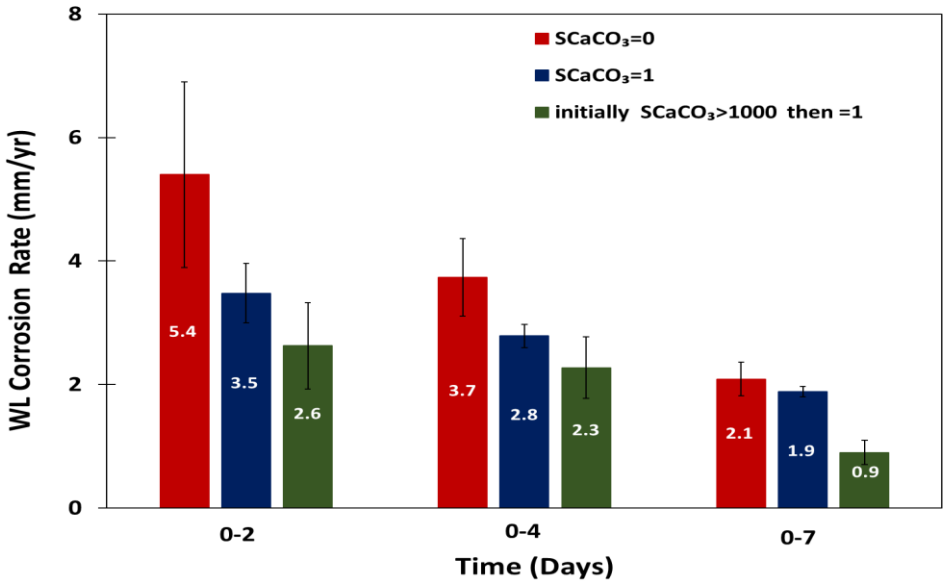

Figure 62. Cumulative corrosion rate by weight loss techniques over time for solution with different $CaCO_3$ saturation levels (80˚C, pCO_2 0.53 bar, 20 rpm, pH 6.2, ionic strength 0.18 M, $[Ca^{2+}]$ ~160 ppm)

A comparison of open circuit potential (OCP) for all experiments is provided in Figure 63. The initial OCP for all experiments was almost the same and it became more positive when the corrosion product layers had formed on the steel surface roughly in the middle of the experiments. OCP values were more positive in the pseudo-passivation period for all experiments with even more positive OCP for experiments with initial $S_{CaCO_3} \gg 1000$. This could be attributed to a better protection offered by the corrosion product layers being formed on the steel surface in the presence of $CaCO_3$ scale.

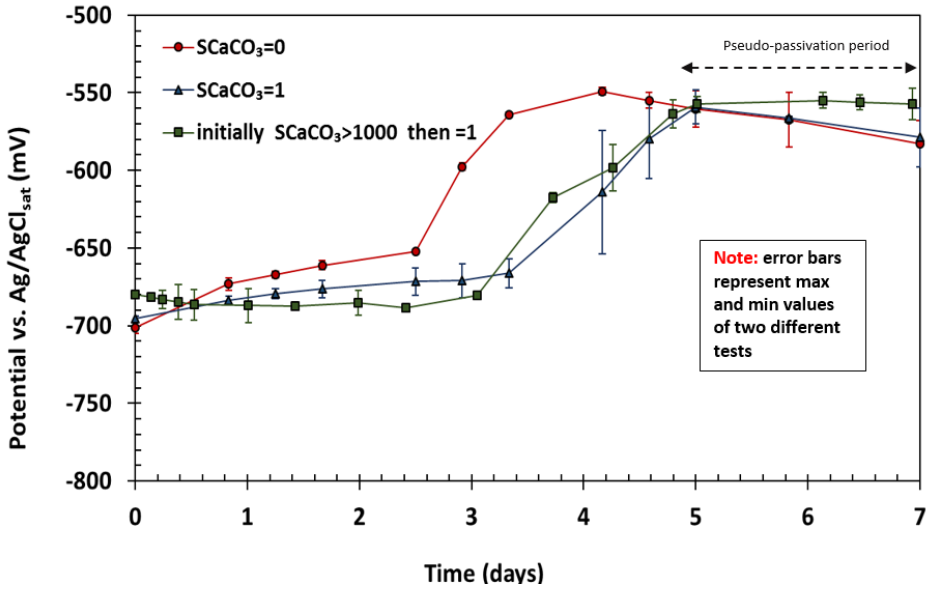

Figure 63. Comparison of OCP over time for UNS G10180 exposed to solutions with different $CaCO_3$ saturation levels (80˚C, pCO_2 0.53 bar, 20 rpm, pH 6.2, ionic strength 0.18 M, $[Ca^{2+}]$ ~160 ppm)

Effect of $CaCO_3$ saturation - Comparison of surface layers at pH 6.2:

SEM cross-sectional and top view images of surface layers developed at different exposure times for experiments with different $CaCO_3$ saturation levels are provided in Figure 64 (a, b, and c). The yellow arrows on the cross-sectioned specimens indicate the calculated thickness for surface layers based on WL corrosion rate. A complete explanation of the surface layer characterization for experiments with $S_{CaCO_3} = 0$ and $S_{CaCO_3} = 1$ at pH 6.2 are in previous sections. Here, focus is given to the experiments in the presence of chemically driven formation of $CaCO_3$ scale on the steel surface from initial $S_{CaCO_3} \gg 1000$. The morphology of the surface layer (top view and cross-sectional view) in the presence of $CaCO_3$ scale (Figure 64(c)) is different than those of the baseline (Figure 64(a)) and the $CaCO_3$-saturated experiments (Figure 64(b)). The

presence of $CaCO_3$ scale decreased the active surface area of the steel which resulted in lowering the corrosion rate. However, corrosion was still active beneath the $CaCO_3$ scale. That is why the thickness of Fe_3C in the presence of $CaCO_3$ was noticeably smaller (at each of the measuring points, specifically days 2, 4, and 7) than that of baseline and $CaCO_3$ saturated experiments. Indeed, the Fe_3C structure at the end of day 2 and beneath the $CaCO_3$ scale was less porous than the other experiments at this moment. This could be attributed to the presence of $CaCO_3$ scale which hindered mass transport of the species towards and away from the steel surface. Therefore, the water chemistry beneath the $CaCO_3$ scale and within the developed Fe_3C structure became favorable for precipitation of $FeCO_3$ and $Fe_xCa_yCO_3$ (x+y =1) because of higher $[Fe^{2+}]$ and higher pH values near the surface as compared to the bulk solution. According to the previous experimental findings with $S_{CaCO_3} = 0$ and $S_{CaCO_3} = 1$, a critical thickness for Fe_3C was required to achieve different water chemistry at the steel surface which would favor precipitation of $FeCO_3$ (consequently decreasing CR). From CR behavior (Figure 61) and surface characterization (Figure 64), it is obvious that in the presence of $CaCO_3$ scale, the required thickness of Fe_3C for precipitation of $FeCO_3$ was much lower than in the other two experiments. To confirm this statement, Figure 65 shows a comparison of Fe_3C thickness over time for UNS G10180 with ferritic-pearlitic microstructure exposed to different $CaCO_3$ saturation levels at bulk pH 6.2.

Figure 66 depicts a comparison of cross-sectional EDS line scan analysis of the surface layers developed on specimens exposed to solutions with different $CaCO_3$ saturation after 7 days. One important takeaway from such analysis is that even in the

presence of Ca^{2+} and $CaCO_3$ scale, $FeCO_3$ was the only corrosion product existing adjacent to the steel surface which was responsible for the final reduction in the corrosion rate. Indeed, formation of a mixed iron-calcium carbonate (solid solutions) was confirmed by these analyses in the presence of Ca^{2+} and $CaCO_3$ scale. However, the mole fractions of Ca and Fe within such solid solutions were dependent on each solution's $CaCO_3$ saturation level. (e.g., the blue lines in Figure 66 represent Ca in the surface layers where Ca was absent in the baseline experiment and are more prominent in the $CaCO_3$ supersaturated solution).

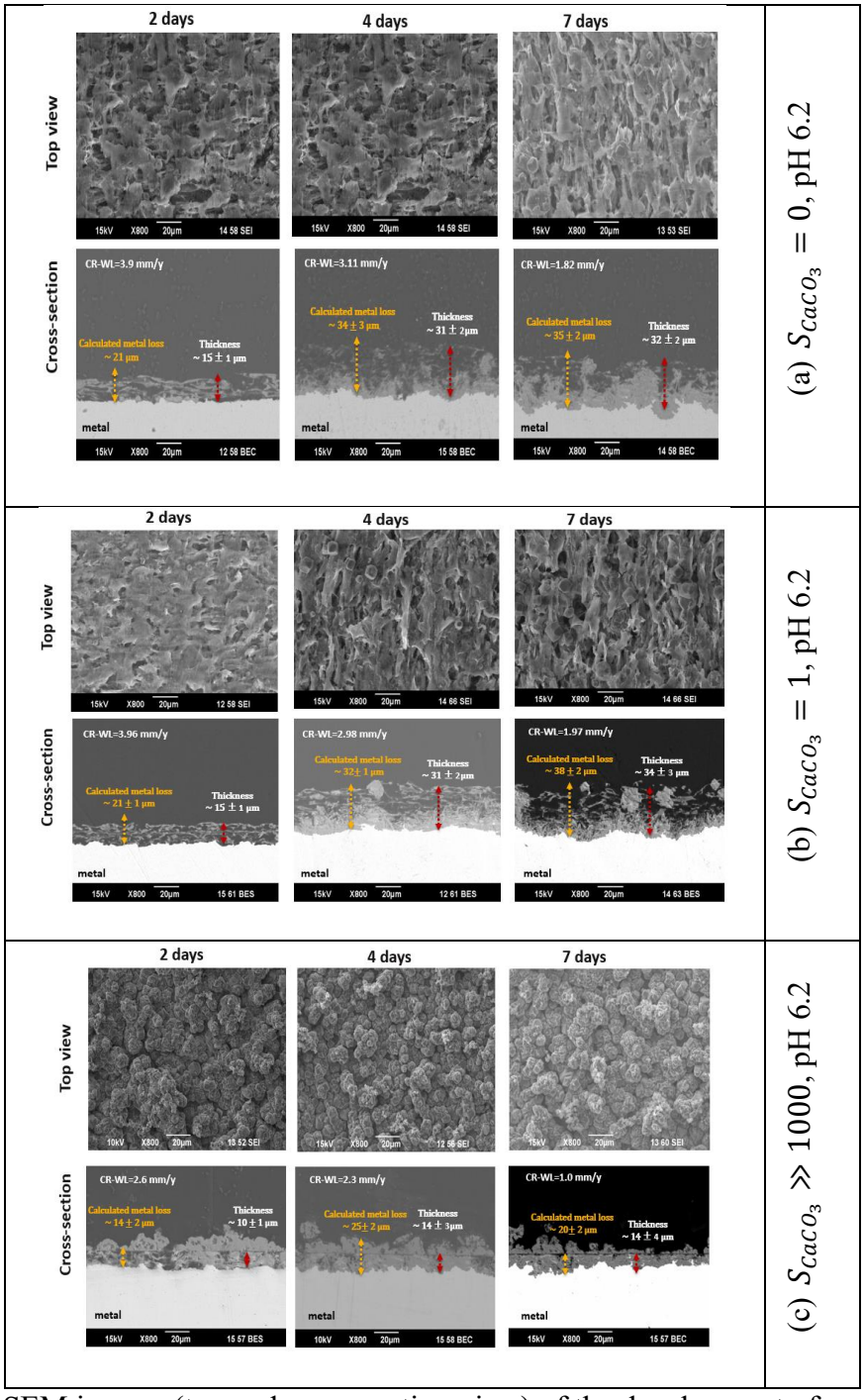

Figure 64. SEM images (top and cross-section view) of the development of surface layers over time for the experiment with different $CaCO_3$-saturation level at 80˚C, pCO_2 0.53 bar, 20rpm, pH 6.2, ionic strength 0.18 M

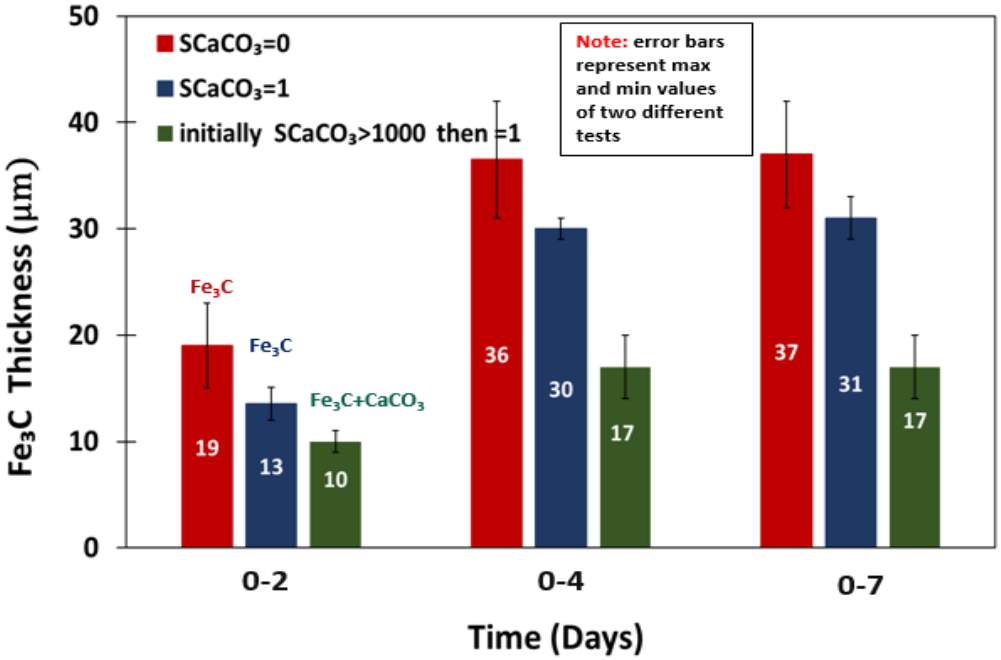

Figure 65. Fe_3C growth on mild steel over time exposed to solution with different $CaCO_3$ saturation levels at 80˚C, pCO_2 0.53 bar, 20rpm, pH 6.2, ionic strength 0.18 M, $[Ca^{2+}]$ ~160 ppm

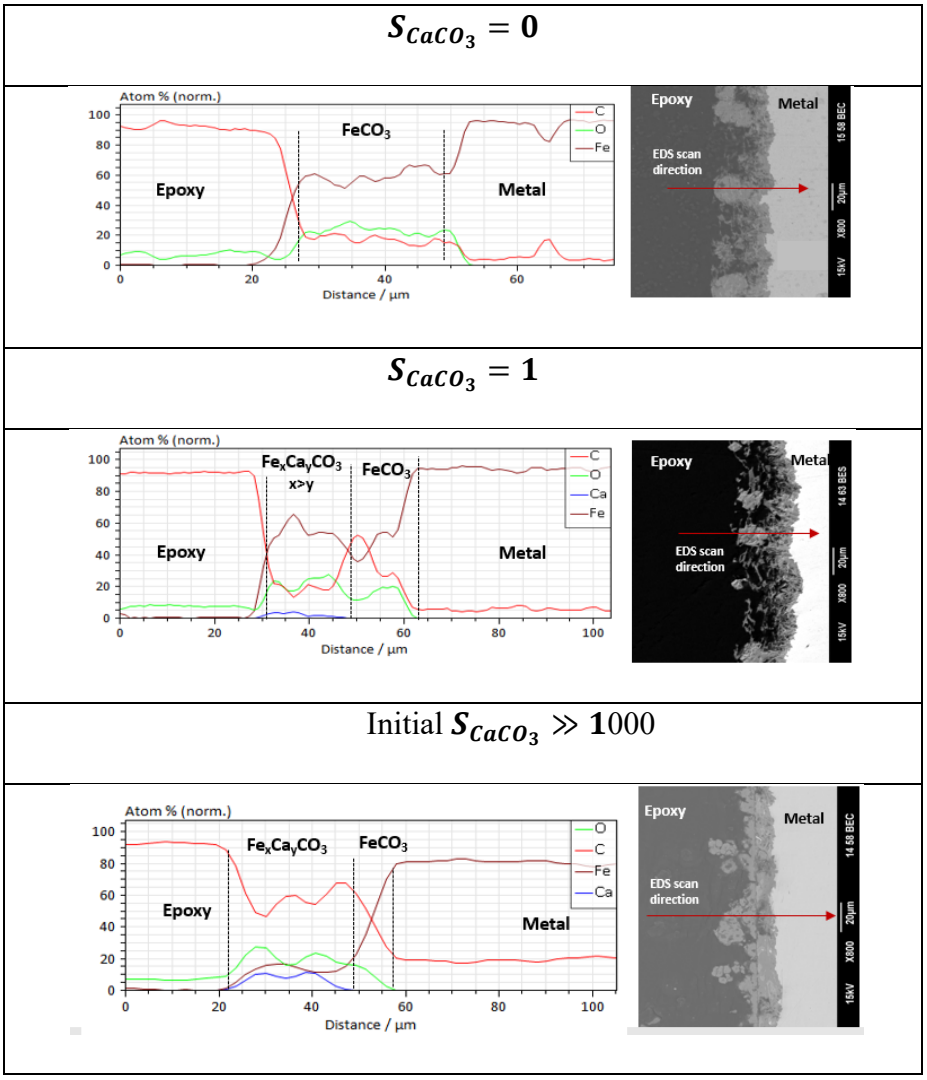

Figure 66. EDS line scan analysis of the surface layers developed on the specimens after 7 days of exposure to electrolytes with different $CaCO_3$ saturation level at 80˚C, pCO_2 0.53 bar, 0.58 m/s, pH 6.2, ionic strength 0.18 M, [Ca^{2+}] ~160 ppm

Figure 67 shows the XRD data obtained for the specimens recovered after different exposure times for varying $CaCO_3$ saturation levels. Solid red lines denote the baseline experiment ($S_{CaCO_3} = 0$), solid blue lines represent the $CaCO_3$-saturated experiment ($S_{CaCO_3} = 1$), and solid green lines characterize the $CaCO_3$ supersaturated experiments (initial $S_{CaCO_3} \gg 1000$). For the $CaCO_3$ supersaturated experiments, a solid

solution of $Fe_{0.47}Ca0_{.53}CO_3$ was detected in all the three measuring points (day 2, 4, and 7). Indeed, the XRD data confirmed that, after 7 days of exposure, a substitutional solid solution of $Fe_{0.90}Ca_{0.10}CO_3$ was formed in the $CaCO_3$-saturated experiment. For the baseline experiments, $FeCO_3$ was the only crystalline phase detected on the steel surface in the absence of Ca^{2+} ions. The XRD data are almost identical for experiments with $S_{CaCO_3} = 0$ and $S_{CaCO_3} = 1$ for the first 2 days when only the Fe_3C structure is present. However, for the $CaCO_3$ supersaturated experiment, additional peaks related to formation of iron-calcium carbonates are revealed even after 2 days. $FeCO_3$ peaks for the experiment in the presence of Ca^{2+} and $CaCO_3$ scale are broadened and shifted toward the reference peaks for $CaCO_3$, indicating heterogeneous substitution of Fe by Ca in the lattice of $FeCO_3$. This phenomenon is more obvious for XRD data at day 7 of the experiments. Although all the $FeCO_3$ peaks are shifted towards the left, in the presence of Ca^{2+} ions, the more intense peak associated with the (104) Miller planes located, at 32.07 degrees, is more easily recognizable after 7 days of exposure. Another observation is that the intensity of peaks related to α-Fe are decreasing over time for all series of experiments. This could indicate that surface layers were growing and, as a result, incident X-rays could not reach the steel substrate as easily.

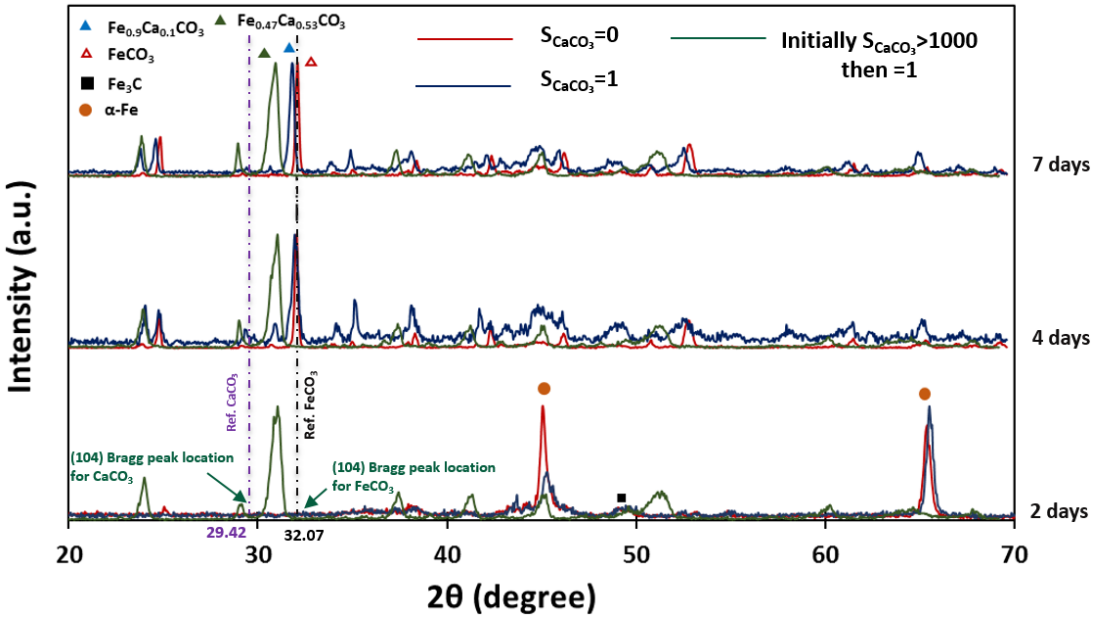

Figure 67. XRD patterns of surface layers detected on the steel surface after 2, 4, and 7 days of exposure to electrolytes with different $CaCO_3$ saturation level at 80˚C, pCO_2 0.53 bar, 0.58 m/s, pH 6.2, ionic strength 0.18 M, [Ca^{2+}] ~160 ppm

The vulnerability of the specimens to localized corrosion exposed to different $CaCO_3$ saturation levels at pH 6.2 was also evaluated. Profilometry of the specimen surfaces was performed after removing corrosion product layers by Clarke solution [71] and no localized corrosion was observed for experiments in different $CaCO_3$ saturation levels at bulk pH 6.2. Figure 68 illustrates an example of profilometry of a specimen exposed for 7 days to a solution initially supersaturated with respect to $CaCO_3$. In this example of surface investigation, the maximum pit depth measured was 10 µm (equal to a penetration rate of 0.2 mm/y) which cannot be considered as localized attack when compared to the 0.75 mm/y of uniform corrosion rate measured by weight loss method (pitting ratio= 0.2/0.75=0.26)

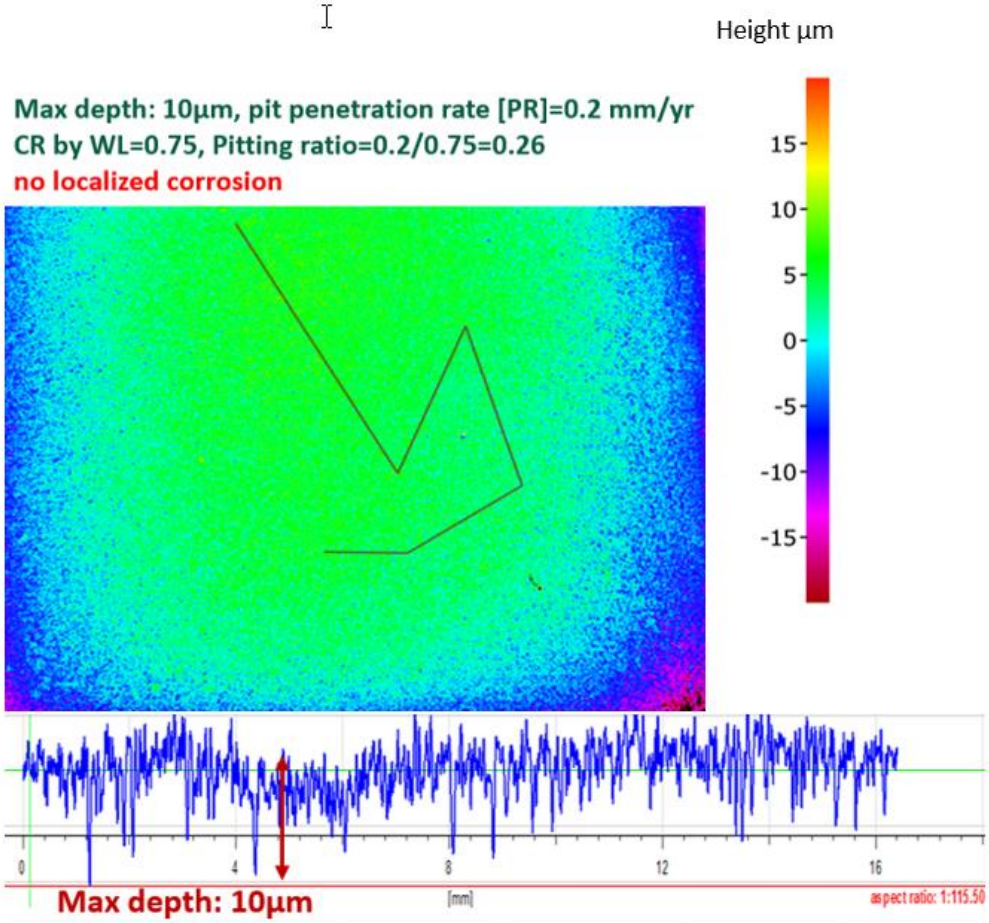

Figure 68. Example of profilometry of the specimen after removing the surface layer (7 days of exposure, initially $CaCO_3$ supersaturated solution at pH 6.2, 80˚C, pCO_2 0.53 bar, 20 rpm, and ionic strength 0.18 M)

Effect of $CaCO_3$ saturation - Experiments conducted at pH 5.5:

In the above discussion, the results of the experiments conducted at pH 6.2 and 160 ppm [Ca^{2+}] were compared to each other based on conditions detailed in Table 9. In this part of the dissertation, the effect of $CaCO_3$ saturation levels on CO_2 corrosion are explored at lower pH (5.5) and higher Ca^{2+} concentration (6000 ppm) according to conditions illustrated in Table 10. Indeed, test solutions hold a higher ionic strength (0.6 M) which is more representative of oilfield conditions.

Figure 69 shows the bulk solution pH for the experiments with different $CaCO_3$ saturation levels over time. Solution pH was maintained at pH 5.5 by adding hydrochloric acid (HCl) when necessary during the experiment without the presence of Ca^{2+} ($S_{CaCO_3} = 0$). However, the $CaCO_3$-saturated and $CaCO_3$-supersaturated conditions, the solution showed a strong buffering capacity over the course of experiments since such solutions contained a significant amount of carbonate species. Consequently, the solution pH was self-controlled at its initial/autogenous value of pH 5.5. Such buffering behavior was also reported by Duan, *et al.* [89]. For the experiments initially supersaturated with respect to $CaCO_3$ ($S_{CaCO_3} \gg 1$), $Ca(OH)_2$ was used to adjust solution pH and Ca^{2+} content in the first two hours in order to accelerate precipitation of $CaCO_3$ scale on the steel surface (likewise for experiments at pH 6.2). Except for this short period, the solution pH values for all experiments with different $CaCO_3$ saturation levels were identical. It is worth mentioning that for the solutions with pH 6.2, the $Ca(OH)_2$ slurry was injected three times into the system while for the experiments with solution pH 5.5, the $Ca(OH)_2$ slurry was injected one time in the same period (two hours). This difference in the response of the two systems to pH change could be related to the different buffering capacity of the systems. As explained earlier, solutions containing a high concentration of Ca^{2+} at pH 5.5 showed a stronger buffering behavior.

Figure 70 shows the trends of uncontrolled [Fe^{2+}] over time for solutions with different $CaCO_3$ saturation levels. The average $FeCO_3$ saturation level achieved during experiments with different $CaCO_3$ saturation levels is also indicated in Figure 70. For all of the experiments at pH 5.5, the average S_{FeCO_3} was less than 10, which is of the same

order of magnitude as for the experiments conducted in electrolytes with pH 6.2 (see Figure 60). As indicated in Figure 70, the lowest average S_{FeCO_3} belongs to the $CaCO_3$ supersaturated experiments.

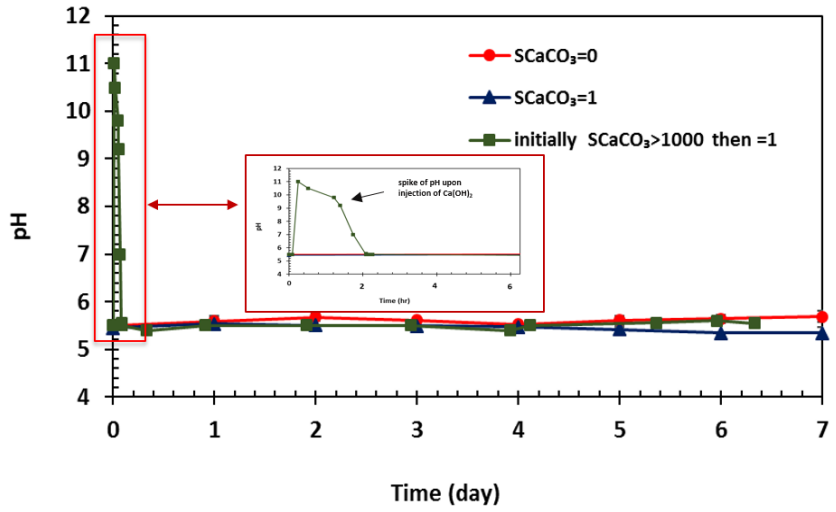

Figure 69. Variation of bulk solution pH over time for the experiments with different $CaCO_3$ saturation levels (80˚C, pCO_2 0.53 bar, 20 rpm, pH 5.5, ionic strength 0.6 M, $[Ca^{2+}]$ ~6000 ppm)

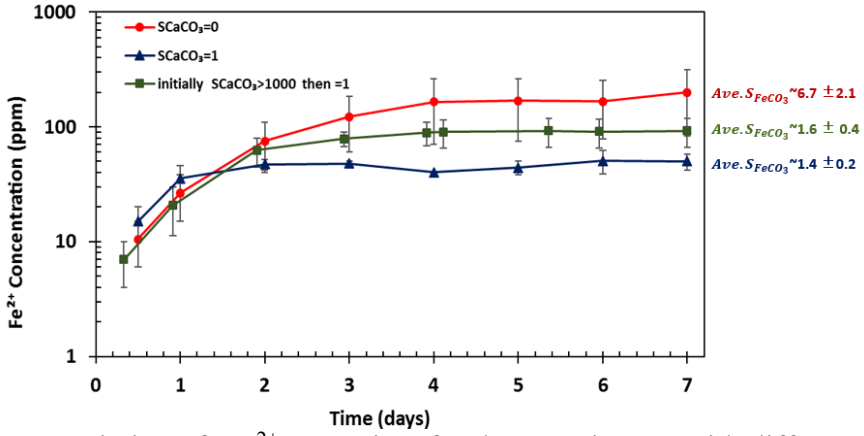

Figure 70. Variation of $[Fe^{2+}]$ over time for the experiments with different $CaCO_3$ saturation level at 80˚C, pCO_2 0.53 bar, 20 rpm, pH 5.5, ionic strength 0.6 M, $[Ca^{2+}]$ ~6000 ppm

Effect of $CaCO_3$ saturation - Comparison of corrosion rate and open circuit potential at pH 5.5:

Figure 71 shows a comparison of LPR corrosion rate over the course of experiments with different $CaCO_3$ saturation levels at pH 5.5. The detailed analysis of the baseline experiments and $CaCO_3$-saturated experiments at pH 5.5 and 6000 ppm Ca^{2+} is provided in Section 6.1. It is obvious from Figure 71 that, at all conditions, there exists an active corrosion period at the early stage of the experiments; even for the experiments with the presence of $CaCO_3$ scale (initial $S_{CaCO_3} \gg 1000$). The CR also dropped in each experiment after the active corrosion period. Such behavior was also observed for the experiments with pH 6.2, however, with different timelines. For example, the active corrosion period at pH 5.5 was shorter than the active corrosion period at pH 6.2 for each identical $CaCO_3$ saturation level (see Figure 61 and Figure 71). Such corrosion behavior with different pH values and $CaCO_3$ saturation levels could be attributed to surface layer characterization. In general, at pH 5.5 higher corrosion rates were obtained in comparison to pH 6.2 due to the more acidic environment which accelerated the overall cathodic reaction rate. As can be seen from Figure 71, for all experiments, the corrosion rate dropped after reaching a maximum value for each condition. Maximum corrosion rates for experiments with $S_{CaCO_3} = 1$ and initial $S_{CaCO_3} \gg 1000$ are noticeably lower than for experiments with $S_{CaCO_3} = 0$. Another observation is that the final corrosion rate in the presence of Ca^{2+} and $CaCO_3$ scale was lower than the baseline experiments. In fact, the presence of Ca^{2+} and $CaCO_3$ scale improved the protective behavior of corrosion product layers at the end of the 7-day exposure. However, the residual corrosion rate was still

high at the end of all experiments. Other researchers have also observed that corrosion product layers formed at low bulk solution pH (*i.e.*, pH 5.5) could not confer a good level of protectiveness [92].

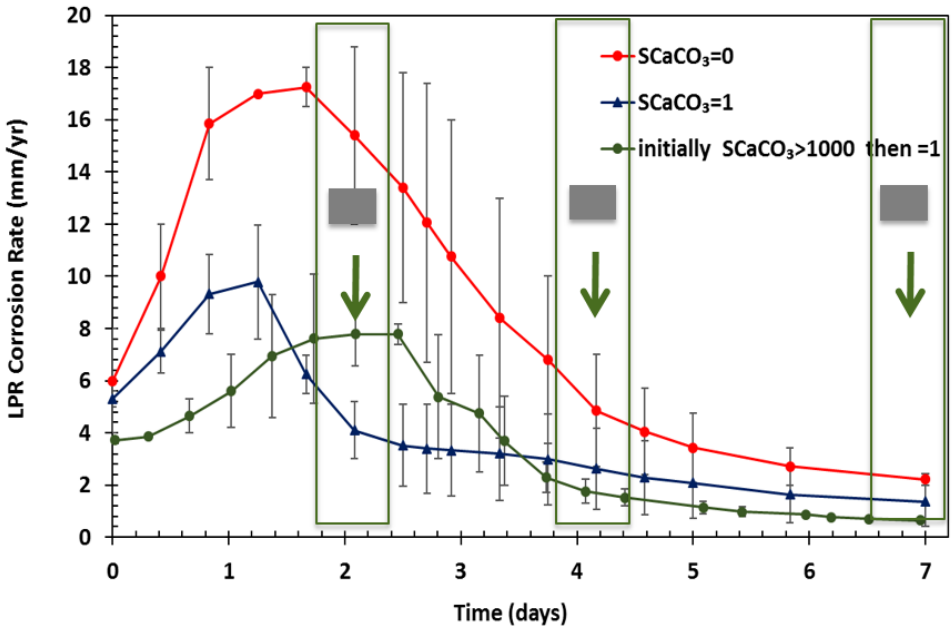

Figure 71. Comparison of LPR corrosion behavior of UNS G10180 exposed to solutions with different $CaCO_3$ saturation level at 80˚C, pCO_2 0.53 bar, 0.58 m/s, pH 5.5, ionic strength 0.6 M, $[Ca^{2+}]$ ~6000 ppm

Figure 72 shows a comparison of cumulative corrosion rate by WL at different exposure times for experiments with different $CaCO_3$ saturation levels at bulk pH 5.5. At each measured point, the general corrosion rate in the presence of Ca^{2+} ($S_{CaCO_3} = 1$) and $CaCO_3$ scale on the steel surface (initial $S_{CaCO_3} \gg 1000$) was noticeably lower than the baseline ($S_{CaCO_3} = 0$). Indeed, for all experiments, the corrosion rate decreased over time which was due to formation of corrosion products on the surface of mild steel. Furthermore, the WL corrosion rate confirmed the accuracy of LPR corrosion rate results.

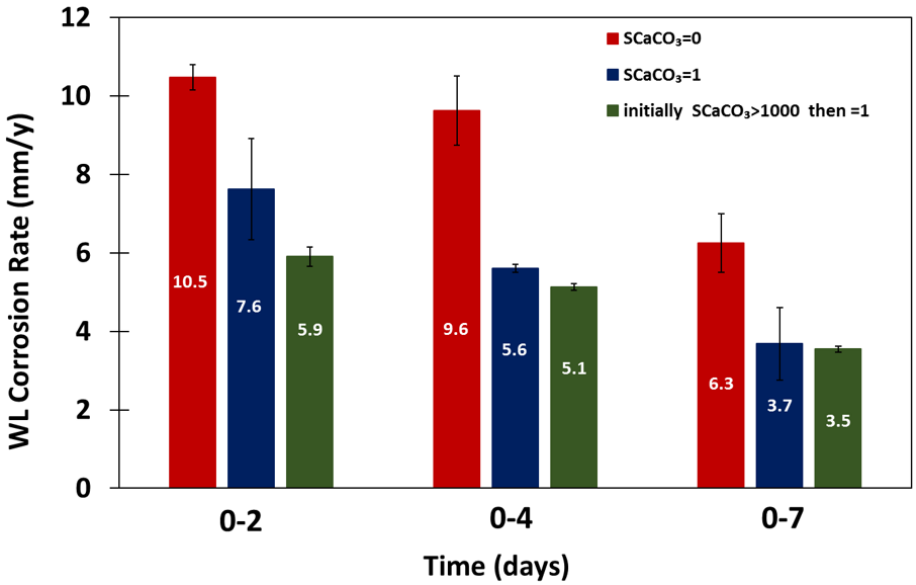

Figure 72. Cumulative corrosion rate by weight loss technique over time for solutions with different $CaCO_3$ saturation level at 80˚C, pCO_2 0.53 bar, 20 rpm, pH 5.5, ionic strength 0.6 M, $[Ca^{2+}]$ ~6000 ppm

A comparison of OCP for all experiments is provided in Figure 73. The initial OCP for all experiments was almost the same, and it became more positive when the corrosion product layers had formed on the steel surface towards the end of each 7-day experiment. One important observation is that the pseudo-passivation period was not as obvious for experiments conducted at pH 6.2 for each identical $CaCO_3$ saturation level. This phenomenon could be related to the better protectiveness of the corrosion product layers formed at pH 6.2 compared to pH 5.5 for each identical $CaCO_3$ saturation level.

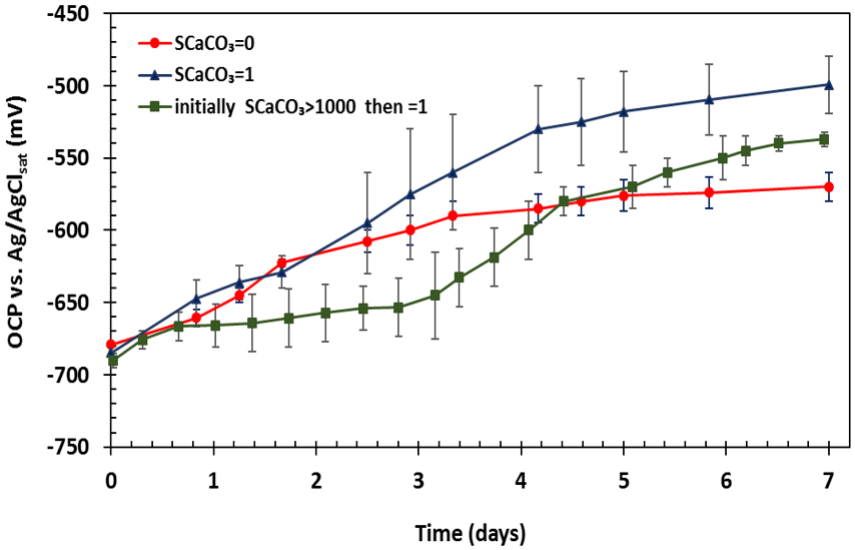

Figure 73. Comparison of OCP over time for UNS G10180 exposed to solutions with different $CaCO_3$ saturation level at 80˚C, pCO_2 0.53 bar, 20 rpm, pH 5.5, ionic strength 0.6 M, [Ca^{2+}] ~6000 ppm

Effect of $CaCO_3$ saturation - Comparison of surface layers at pH 5.5:

SEM cross-sectional and top view images of surface layers developed at different exposure times for experiments with different $CaCO_3$ saturation levels are depicted in Figure 74. A complete analysis of the surface layer characterization for experiments with $S_{CaCO_3} = 0$ and $S_{CaCO_3} = 1$ at pH 5.5 are provided in the previous sections.

The morphology of the surface layer (top view and cross-sectional view) considering $S_{CaCO_3} = 1$ (Figure 74,c) and considering $S_{CaCO_3} \gg 1$ (Figure 74,b) can be compared to the baseline experiment, $S_{CaCO_3} = 0$ (Figure 74,a). The SEM images of the top view confirmed partial precipitation of crystalline phases on the top of the steel surface even after two days of exposure (this was not observed at pH 6.2). Such crystals did not cover the entire surface and their quantity and size grew over time (see top view images in Figure 74,b). EDS analysis and XRD data confirmed that such crystalline

phases were substitutional iron-calcium carbonate solid solutions, with calcium being dominant over iron ($Fe_xCa_yCO_3$, x+y=1 and x<y). The cross-sectional SEM image of the specimen after 2 days of exposure confirmed that $Fe_xCa_yCO_3$ was partially precipitated within the Fe_3C porous structure. The thickness of the Fe_3C layers at this time was around 17μm. A much higher pH would have occurred within the Fe_3C pores in comparison to the pH 5.5 of the bulk solution. The increased pH within the Fe_3C network would favor precipitation of $CaCO_3$. However, due to its presence close to the steel surface, Fe^{2+} would also be involved in the crystallization process along with Ca^{2+} and a substitutional solid solution of iron-calcium carbonate with, calcium being dominant over iron formed at this stage. Precipitation of mixed carbonates first started within the Fe_3C network, however, propagation and growth of such phases continued out of the Fe_3C layers, which in some locations were visible from top view and cross-section images as shown in Figure 74 (b.) Based on Figure 71, the corrosion rate was still increasing approximately up to day 2 for the baseline experiment ($S_{CaCO_3} = 0$), whereas for the experiment with $S_{CaCO_3} = 1$, the corrosion rate was already decreasing well before day 2. This decrease was due to precipitation of the mixed metal carbonate within the Fe_3C matrix which partially blocked the steel surface and retarded the anodic reaction. Cross-section morphology of the surface layers at the end of day 4 showed that almost the entire Fe_3C layer was filled with $Fe_xCa_yCO_3$ (Figure 74,b). The corrosion rate obtained by LPR showed a high value of 2.3 mm/yr at this stage (Figure 71). An immediate conclusion was that precipitation of $Fe_xCa_yCO_3$ on the steel surface could not offer an acceptable level of protection against further corrosion, and undermining corrosion was still

ongoing. That was why the thickness of surface layers grew from 35 μm at day 4 to 60 μm at day 7 for the experiment with $S_{CaCO_3} = 1$ (Figure 74,b).

Bulk solution pH, [Ca^{2+}] and $CaCO_3$ saturation level all played a prominent role on CO_2 corrosion and on $CaCO_3$ formation. In both bulk solution conditions (pH 6.2 and 5.5), precipitation of carbonates was dependent on the development of the Fe_3C network and the inevitable different water chemistry within the pores of Fe_3C compared to bulk solution. However, at pH 5.5, the corrosion rate was much higher than at pH 6.2 which resulted in a thicker Fe_3C on the steel surface for pH 5.5 in the earlier stage of experiments (see Figure 64,b and Figure 74,b). Higher thickness of a conductive and porous Fe_3C network provided more available surface area for hydrogen evolution reactions and more of a diffusion barrier, which consequently would have developed a higher pH within the pores of Fe_3C near the metal. Kinetics of carbonate formation is accelerated at higher pH but also at higher concentration/activity of Ca^{2+}. For experiments at pH 5.5, the high [Ca^{2+}] (~6000 ppm) played a role in the earlier nucleation/growth of $CaCO_3$ and $Fe_xCa_yCO_3$ compared to the 160 ppm [Ca^{2+}] at pH 6.2 which resulted in a shorter active corrosion period for $CaCO_3$-saturated experiments in pH 5.5 bulk solution compared to pH 6.2 bulk solution (see Figure 61 and Figure 71).

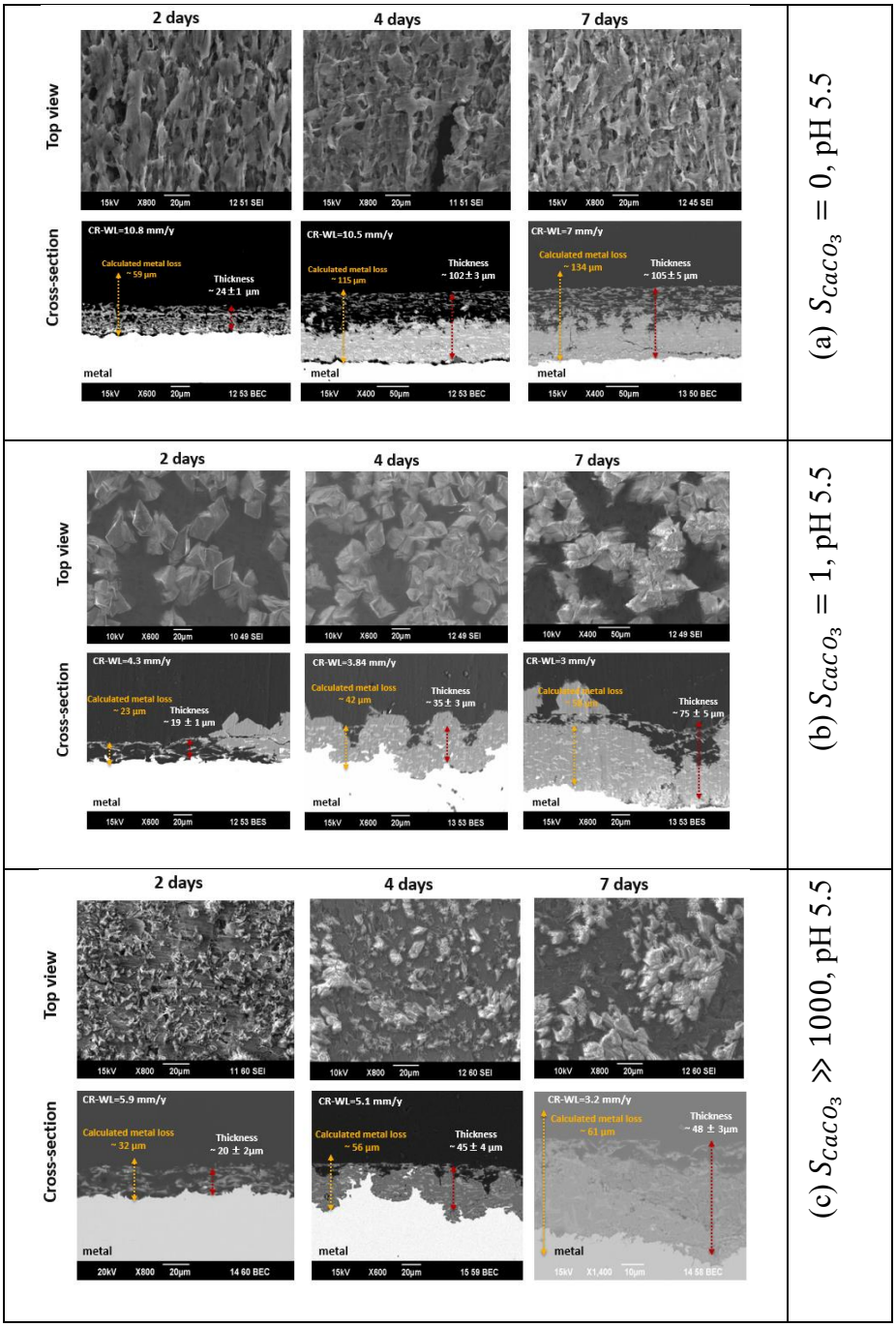

Figure 74. SEM images (top and cross-section view) of the development of surface layers over time for the experiment with different $CaCO_3$-saturation level at 80˚C, pCO_2 0.53 bar, 20 rpm, pH 5.5, ionic strength 0.6 M

For the $S_{CaCO_3} \gg 1000$ experiments, the initial corrosion rate was lower than for the other experiments ($S_{CaCO_3} = 0$ and $S_{CaCO_3} = 1$) at pH 5.5. This was due to the blocking effect of $CaCO_3$ scale and reducing the active surface area of the steel. Yet, previous results have clearly shown that $CaCO_3$ scale by itself does not offer a good level of protectiveness and, as a result, undermining corrosion still occurred, albeit at a lower rate compared to experiments with $S_{CaCO_3} = 0$ and $S_{CaCO_3} = 1$. Figure 75 shows a comparison of Fe_3C thickness over time, which is directly related to undermining corrosion rates, for experiments with different $CaCO_3$ saturation levels. The explanation provided in the previous section on the importance of Fe_3C thickness in the experiments at pH 6.2 is also valid for experiments at pH 5.5.

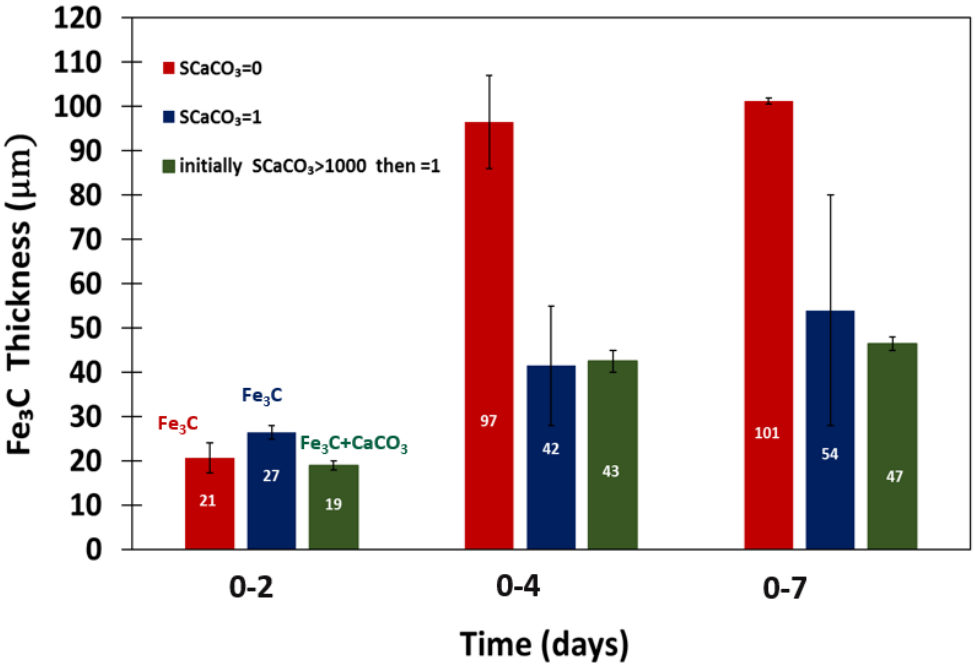

Figure 75. Fe_3C growth on mild steel over time exposed to solutions with different $CaCO_3$ saturation levels at 80˚C, pCO_2 0.53 bar, 20 rpm, pH 5.5, ionic strength 0.6 M, $[Ca^{2+}]$ ~6000 ppm

EDS line scan analysis revealed that the final reduction in the corrosion rate (at the end of 7-day experiments) was due to the precipitation of $FeCO_3$ corrosion products adjacent to the steel surface and not $CaCO_3$ scale, see Figure 76. However, the presence of the $CaCO_3$ scale acted as a barrier and promoted surface conditioning favorable for precipitation of $FeCO_3$ and also enhanced its protectiveness as compared to experiments with $S_{CaCO_3} = 0$ and $S_{CaCO_3} = 1$ (lower final LPR corrosion rate obtained in the presence of $CaCO_3$ scale, see Figure 71). To confirm this claim, Figure 77 shows EDS mapping analysis of the cross-sectioned surface layers after 7 days of exposure to different $CaCO_3$ saturation levels. It also indicates the thickness of each surface layer along with the final LPR corrosion rate. The thickest corrosion product and highest corrosion rate belongs to the baseline experiment with ($S_{CaCO_3} = 0$), while the thinnest corrosion product and lowest corrosion rate is obtained in the presence of initial $CaCO_3$ scale (initial $S_{CaCO_3} \gg 1000$). This observation suggests that the level of protectiveness of the corrosion products was not strictly related to its thickness, but other parameters should be considered in any judgment of a corrosion product's protectiveness. Physiochemical properties including adherence to the steel, porosity, and tortuosity are also influential in establishing the protectiveness of corrosion products.

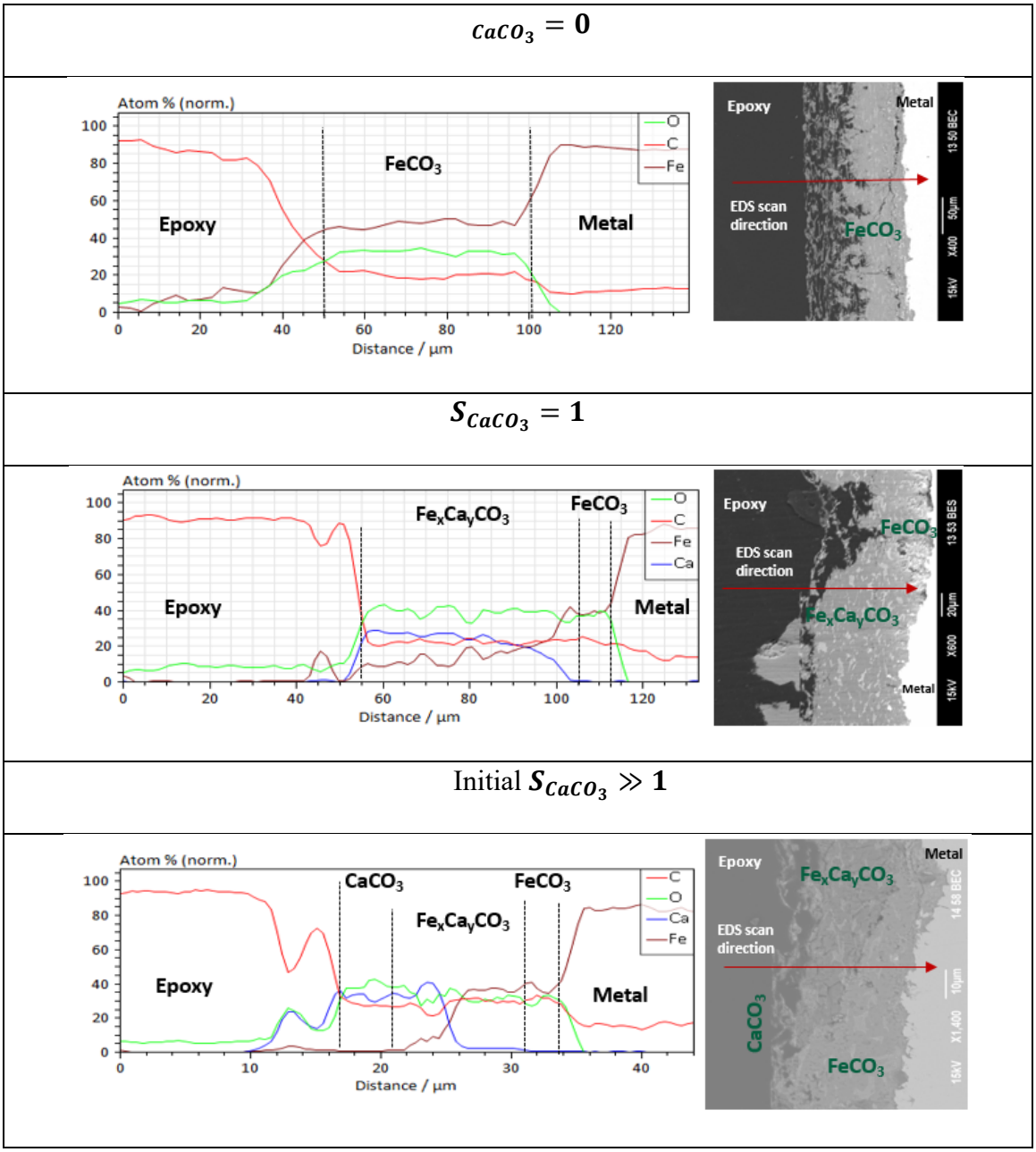

Figure 76. EDS line scan analysis of the surface layers developed on the specimen after 7 days of exposure to electrolytes with different $CaCO_3$ saturation level at 80˚C, pCO_2 0.53 bar, 20 rpm, pH 5.5, ionic strength 0.6 M, [Ca^{2+}] ~6000 ppm.

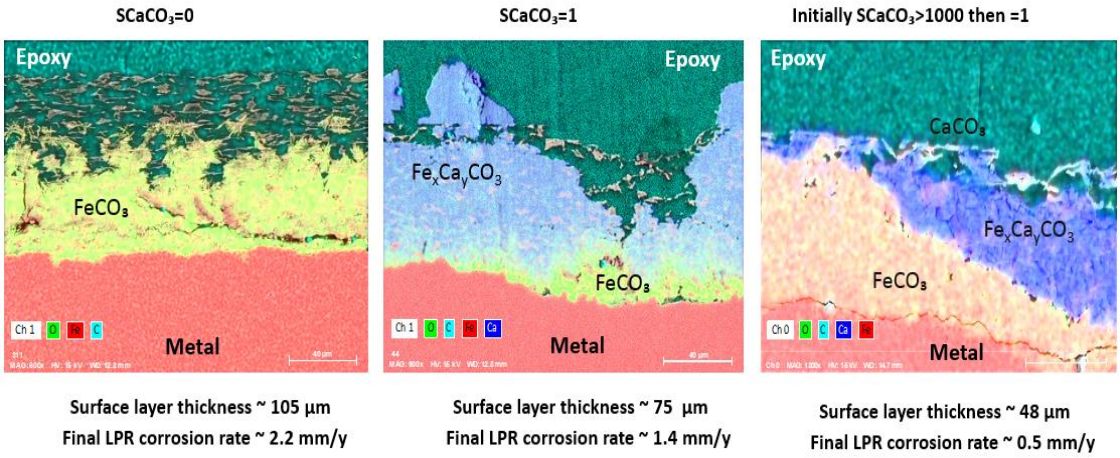

Figure 77. EDS mapping analysis of the cross-sectioned surface layers after 7 days of exposure to different $CaCO_3$ saturation levels at 80˚C, pCO_2 0.53 bar, 0.58 m/s, pH 5.5, ionic strength 0.6 M, [Ca^{2+}] ~6000 ppm

Figure 78 shows the XRD results for the specimens exposed for 7 days to electrolytes with $S_{CaCO_3} = 1$ and initially $S_{CaCO_3} \gg 1000$ at pH 5.5. Fe_3C and $FeCO_3$ are the type of corrosion products expected for UNS G10180 specimens exposed to the baseline solution in the absence of $CaCO_3$ scale and Ca^{2+} (also confirmed with EDS analysis, Figure 76). According to Figure 78, peaks related to Fe_3C, α-Fe, and mixed metal carbonates ($Fe_xCa_yCO_3$, x+y=1) are revealed on the steel. However, the mole fraction of Fe (x) and Ca (y) elements in the mixed metal carbonates was dependent on the solution saturation level with respect to $CaCO_3$. For the experiment with $S_{CaCO_3} = 1$, the mole fraction of Fe and Ca are almost equal (x≈y) while for the experiments with initial $S_{CaCO_3} \gg 1000$, the mole fraction of Ca was much larger (y>>x). It should be mentioned that X-ray penetration power is limited to the surface layers' thickness and cannot reach the steel substrate in the case of a thick corrosion product. Therefore, XRD

was only able to provide information highly influenced by the bulk solution side of the corrosion product layers.

Similarly to the experiments conducted at pH 6.2, the vulnerability of the specimens to localized corrosion exposed to different $CaCO_3$ saturation levels was also evaluated. Localized corrosion attacks were not detected in any experiments at pH 5.5.

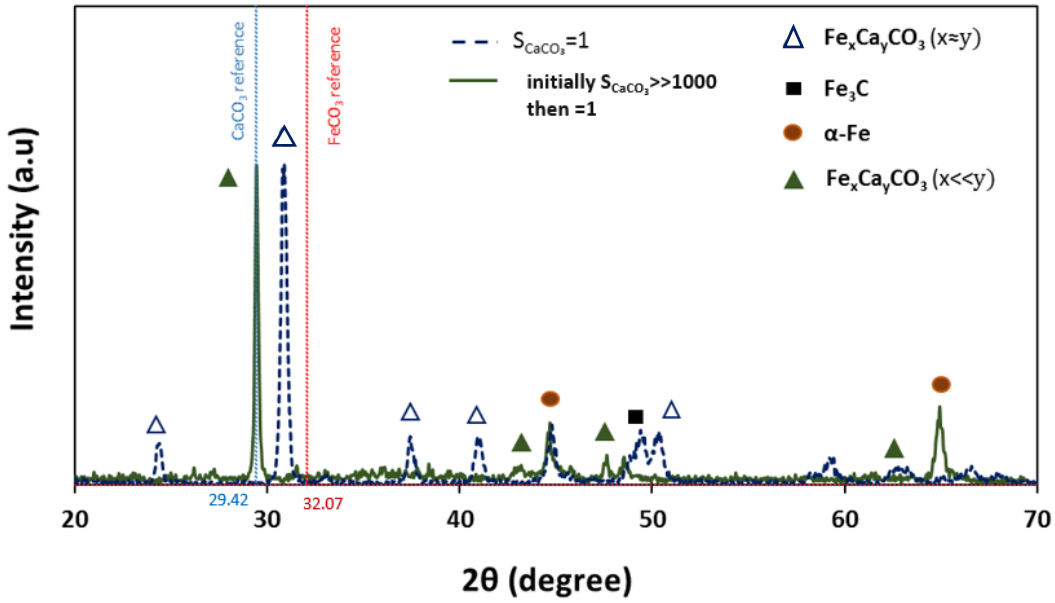

Figure 78. X-ray diffraction patterns of surface layers detected on the steel surface after 7 days of exposure to electrolytes with $S_{CaCO_3} = 1$ and initially $S_{CaCO_3} \gg 1000$ at 80˚C, pCO_2 0.53 bar, 20 rpm, pH 5.5, ionic strength 0.6 M, [Ca^{2+}] ~6000 ppm.

6.2.2.3 Summary

- The electrolyte's $CaCO_3$ saturation level, calcium ion concentration, and bulk pH are crucial parameters in studying the effect of Ca^{2+} on CO_2 corrosion. Ignoring the influence of such parameter(s) is one of the main reasons for the existing discrepancies in the available literature on this topic.

- Fe_3C played a critical role in precipitation of $Fe_xCa_yCO_3$, x+y=1, and $FeCO_3$. The mole fraction of Ca in $Fe_xCa_yCO_3$ depended on the experimental conditions.
- The protective behavior of the surface layers was mainly due to the formation of $FeCO_3$ adjacent to the steel surface and not $Fe_xCa_yCO_3$ nor $CaCO_3$. However, the presence of $Fe_xCa_yCO_3$ and/or $CaCO_3$ facilitated $FeCO_3$ precipitation and enhanced its protectiveness by acting as a mass transfer barrier of Fe^{2+} outwards from the steel and H^+ towards the steel.
- Although $CaCO_3$ is isomorphous with $FeCO_3$, $CaCO_3$ scale was not protective against further corrosion. Ca^{2+} comes from bulk solution while Fe^{2+} comes from the corroding steel surface. Therefore, $FeCO_3$ has superior adherence to steel. This makes $FeCO_3$ protective while $CaCO_3$ is not.
- No localized corrosion was observed in different $CaCO_3$ saturation levels in the conducted experimental conditions.

CHAPTER 7: CO_2 CORROSION EXPERIMENTS IN Mg^{2+} - CONTAINING ELECTROLYTES

Precipitation kinetics of $CaCO_3$ is relatively fast and was successfully achieved experimentally. However, precipitation kinetics of $MgCO_3$ is very slow and can be extremely challenging in the laboratory environments, even from highly supersaturated solutions with respect to $MgCO_3$ or with cathodic polarization. All experimental efforts to precipitate $MgCO_3$ scales were consequently unsuccessful. Conceivably, it is the reason that a pure $MgCO_3$ scale is rarely seen in oilfields. Therefore, this section focuses on the effect of Mg^{2+} on formation of mixed carbonates scales rather than on pure $MgCO_3$ precipitation.

The main objective of such experiments was to further broaden the mechanistic understanding of CO_2 corrosion of mild steel in the presence of Mg^{2+} ions while the solution is saturated with respect to $MgCO_3$ at different pH values.

7.1 Methodology and Test Matrix

$MgCO_3$-saturated experiments were conducted and repeated for two different bulk solution pH values, 6.2 and 5.5. Using different solution pHs permitted having different dissolved Mg^{2+} concentrations while the solution was saturated with respect to $MgCO_3$, for both pHs. For each Mg^{2+}-containing experiment, a baseline experiment was performed, in an identical water chemistry condition, to compare the effect of Mg^{2+} on CO_2 corrosion. A $MgCl_2$ salt (SIGMA-ALDRICH®) was used to prepare Mg^{2+}-containing solutions. Table 11 shows the experimental condition for experiments conducted at pH 6.2 and 5.5. Likewise, for the experiments in the presence of Ca^{2+}, [Fe^{2+}]

and [H^+] were controlled by means of two different ion-exchange resins (Na-form and H-form, respectively) at pH 6.2. However, for the experiments with lower pH value (5.5) and higher Mg^{2+} concentration (4,200 ppm), [Fe^{2+}] could not be controlled due to the Na-form resin being unable to differentiate between Mg^{2+} and Fe^{2+}, adsorbing both dipositive cations. Despite the lack of controlling [Fe^{2+}] at pH 5.5, the $FeCO_3$ saturation levels at pH 6.2 and 5.5 are in good agreement (due to the higher solubility of $FeCO_3$ at pH 5.5 as compared to pH 6.2). Therefore, the comparison of the results for the two pHs is still valid.

Table 11. Test matrix for experiments saturated with $MgCO_3$ at pH 6.2 and pH 5.5

Parameter	Description			
Material and Specimen Type	UNS G10180 with Ferritic-Pearlitic Microstructure Flat Square Sample (A = 1.5 cm^2)			
Temperature	80°C			
pCO_2	0.53 bar			
pH	6.2		5.5	
Electrolyte	Baseline	Effect of Mg^{2+} (low concentration)	Baseline	Effect of Mg^{2+} (high concentration)
	1 wt.% NaCl +$NaHCO_3$ (Ionic Strength ≈0.18 M)	1 wt.% NaCl +$MgCl_2$ (Ionic Strength ≈0.18 M)	1 wt.% NaCl +$NaHCO_3$+ $NaClO_4$ (Ionic Strength ≈ 0.6 M)	1 wt.% NaCl +$MgCl_2$ (Ionic Strength ≈0.6 M)
$[Mg^{2+}]$	0	100 ppm	0	4,200 ppm
S_{MgCO_3}	0	1	0	1
S_{FeCO_3}	0 to 10 0 to 8 (using activity model, see Appendix II)			
Dissolved O_2	<5 ppb			
Reference Electrode	Saturated Ag/AgCl			
Impeller Rotation Speed	20 rpm			
Mass Transfer Conditions	Equivalent to 0.58 m/s in a 0.1m ID pipe			
Experiment Duration	7 days			

7.2 Results and Discussion

In this section, the results of experiments saturated with $MgCO_3$ at two different pHs, Mg^{2+} concentrations and ionic strength are discussed.

7.2.1 Experiments with 100 ppm Mg^{2+} at pH 6.2 and 0.18 M ionic strength[9]

Figure 79 illustrates a comparison of corrosion rate by the LPR method for $MgCO_3$-saturated experiments (Mg^{2+} concentration *ca.* 100 ppm) and the baseline experiments at pH 6.2. For each experiment, specimens at day 2, 4, and 7 were retrieved from the test solution to conduct weight loss and surface characterization (such specimens are indicated with gray squares in Figure 79). Based on Figure 79, it seems that the presence of Mg^{2+} accelerated the CR in the active period compared to its baseline. However, after 4 days of exposure, the corrosion rate became similar for experiments with and without the presence of Mg^{2+}. At this time (pseudo-passivation), the corrosion product layers had fully developed and, as a result, the iron dissolution reaction (anodic reaction) was significantly retarded compared to the initial stage of the corrosion process (active corrosion period). The three corrosion periods indicated in Figure 79 are thoroughly explained in Section 6.1. In conclusion, the presence of 100 ppm Mg^{2+} did not alter the protectiveness of corrosion products when they were fully developed in the pseudo-passivation period. However, the solution saturated with $MgCO_3$ showed a higher CR in the active corrosion period.

---

[9] A version of this section has been presented as "Investigations on the CO_2 Corrosion of Mild Steel in the Presence of Magnesium and Calcium Ions," at the NACE2020 conference.

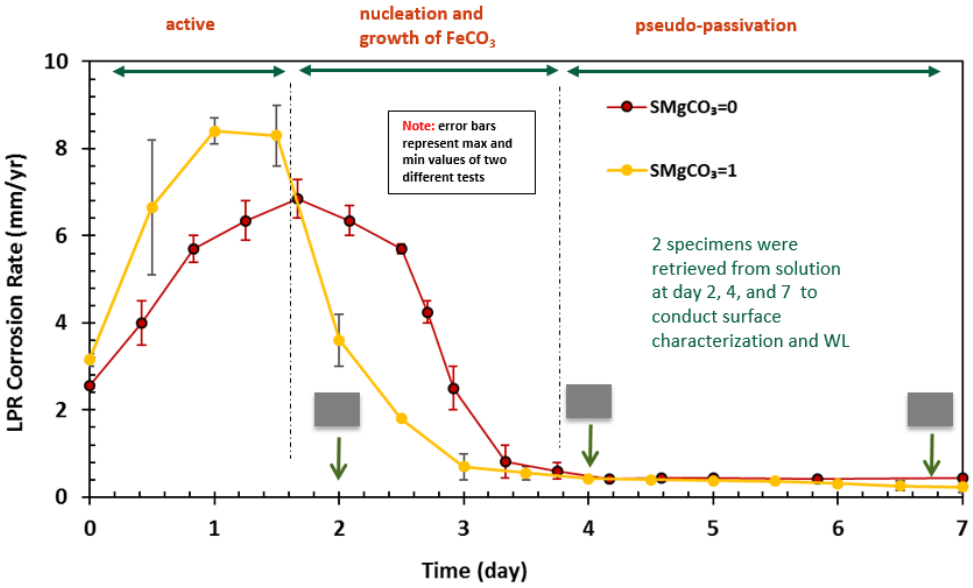

Figure 79. Trend of corrosion rate obtained by LPR over time with and without the presence of 100 ppm Mg^{2+} at pH 6.2

Figure 80 shows a comparison of cumulative CR by WL (bar chart) and LPR (line chart) at different exposure times for experiments with and without Mg^{2+}. Both LPR and WL methods show that CR decreases over time, probably due to formation and development of corrosion product layers. Another observation is that although the initial corrosion rate in the presence of Mg^{2+} seems slightly higher than the baseline experiment (see corrosion rate by LPR in Figure 79), the cumulative corrosion rates for both experiments are similar at the first two days; based on Figure 80. That is probably due to the drop in corrosion rate (end of the active corrosion period) happening earlier in the presence of Mg^{2+}, which is reflected by the thicker Fe_3C layer thickness in the first 2 days of testing (see Figure 81). As mentioned earlier, Fe_3C acts as an anchoring site for precipitation of $FeCO_3$; the thicker the Fe_3C is, the more favorable for precipitation of $FeCO_3$ the water chemistry becomes.

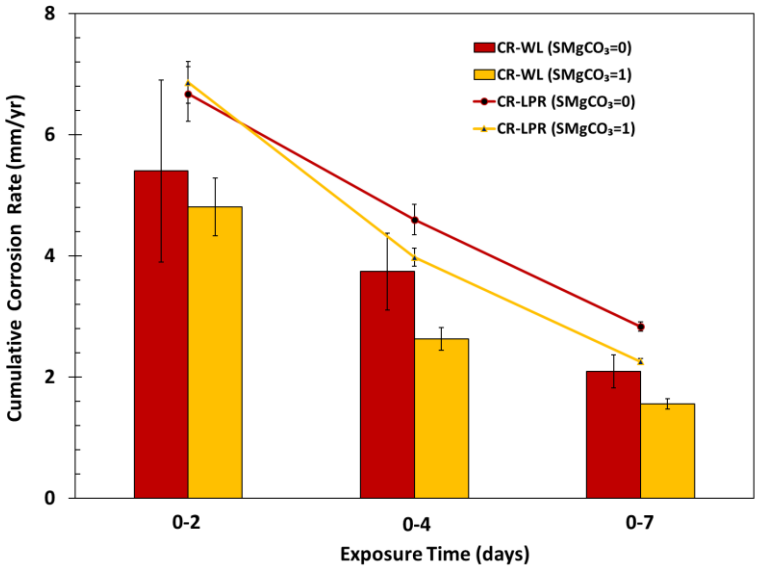

Figure 80. Cumulative corrosion rate by WL (bar chart) and LPR (line chart) techniques over time for solution with and without 100 ppm Mg^{2+} (80˚C, pCO_2 0.53 bar, 0.58 m/s, pH 6.2, ionic strength 0.18 M, 1 wt.% NaCl)

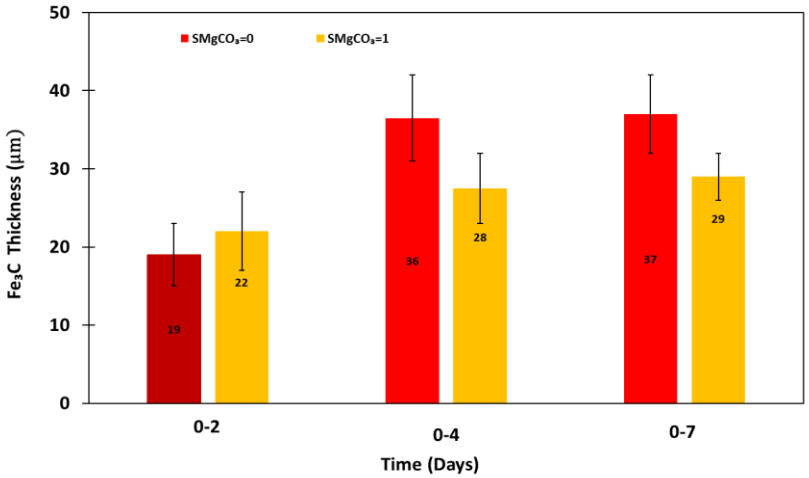

Figure 81. Evolution of Fe_3C over time with and without presence of 100 ppm Mg^{2+} (80˚C, pCO_2 0.53 bar, 0.58 m/s, pH 6.2, ionic strength 0.18 M, 1 wt.% NaCl)

A comparison of open circuit potential (OCP) values for experiments with and without 100 ppm Mg^{2+} is provided in Figure 82. The OCP trends with and without Mg^{2+}

are identical, with more positive OCP achieved at the end of both experiments (pseudo-passivation period) due to a better protectiveness offered by the corrosion products.

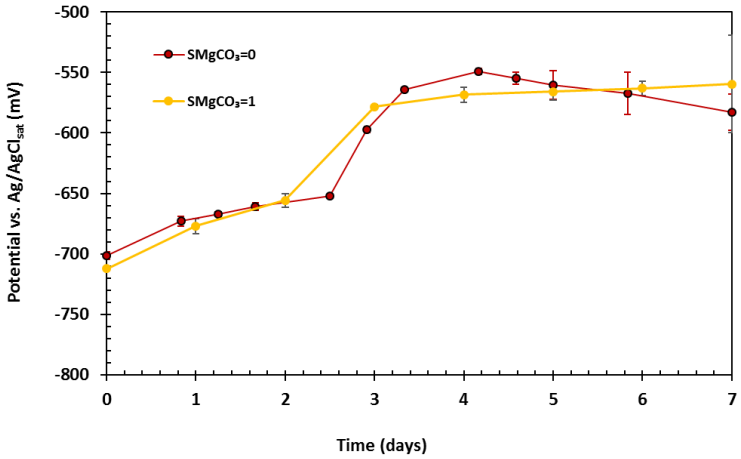

Figure 82. Comparison of OCP over time for UNS G10180 exposed to solutions with and without 100 ppm Mg^{2+} (80˚C, pCO_2 0.53 bar, 0.58 m/s, pH 6.2, ionic strength 0.18 M, 1 wt.% NaCl)

Evolution of surface layers over time at pH 6.2

SEM cross-sectional and top view images of surface layers developed in the presence of 100 ppm Mg^{2+} are provided in Figure 83. The results related to the baseline experiment are presented in section 6.1.1. Therefore, Figure 83 should be compared with Figure 23. The yellow arrows on the cross-sectioned specimens in Figure 83 indicate the calculated thickness for surface layers based on WL corrosion rate. Such values were typically slightly greater than the measured physical thickness indicating that shear stress created by flow could have removed some of the corrosion products at the steel surface, and/or not all of the generated Fe^{2+} ions have participated in the corrosion product formation (some Fe^{2+} dissolved in the solution and some retained in the corrosion

product). Overall, the morphology of surface layers is similar with and without the presence of 100 ppm Mg^{2+} when comparing Figure 83 and Figure 23. One big difference is that the Fe_3C thickness in the presence of 100 ppm Mg^{2+} is higher in the first 2 days (see the cross-sectioned images) because of the higher corrosion rate. A greater thickness of Fe_3C means more favorable water chemistry for precipitation of $FeCO_3$ within its pores. Upon precipitation of $FeCO_3$, the corrosion rate would drop; Figure 79 is indicative of this phenomenon. A complete explanation for the role of Fe_3C in CO_2 corrosion over time is provided in section 6.1.

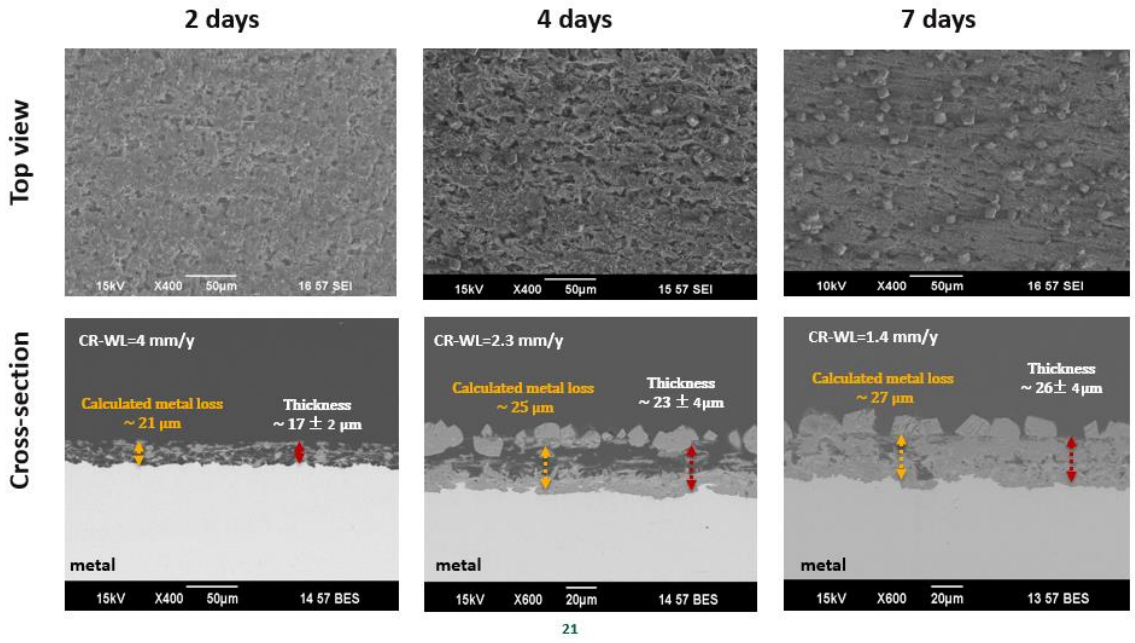

Figure 83. SEM images (top and cross-section view) of the development of surface layers over time for the experiment with presence of 100 ppm Mg^{2+} ($S_{MgCO_3} = 1$) at 80˚C, pCO_2 0.53 bar, 0.58 m/s, pH 6.2, ionic strength 0.18 M, 1wt% NaCl

Figure 84 depicts a comparison of cross-sectional EDS line scan analysis of the surface layers developed on specimens exposed to solutions with and without 100 ppm Mg^{2+} after 7 days. $FeCO_3$ is the only corrosion product in the absence of Mg^{2+} (see Figure 84 (a). One important takeaway from such analysis is that even in the presence of 100 ppm Mg^{2+}, $FeCO_3$ was the only corrosion product existing adjacent to the steel surface, as the inner layer, which was responsible for the final decrease in the corrosion rate; see Figure 84 (b). Indeed, formation of a mixed iron-magnesium carbonate ($Fe_xMg_yCO_3$, x>>y), as the outer layer, was confirmed by these analyses in the presence of 100 Mg^{2+}. However, the mole fraction of Fe is significantly dominant over Mg in such a mixed metal carbonate.

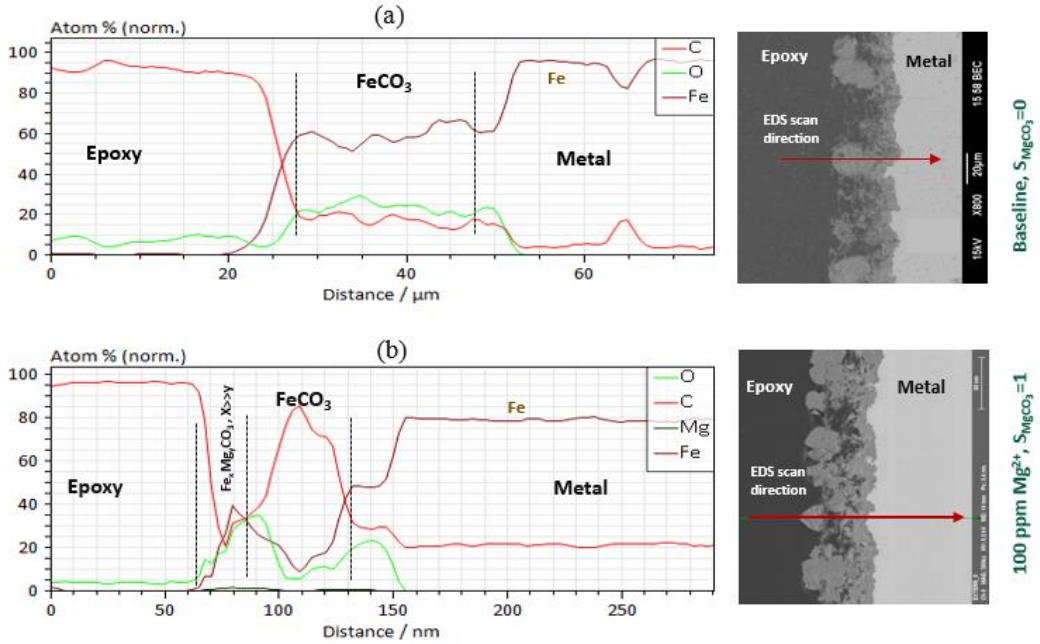

Figure 84. EDS line scan analysis of the surface layers developed on the specimens after 7 days of exposure to electrolytes without (a) and with (b) 100 ppm Mg^{2+} at 80˚C, pCO_2 0.53 bar, 0.58 m/s, pH 6.2, ionic strength 0.18 M, 1wt% NaCl

Figure 85 shows the XRD data obtained for the specimens recovered from a $MgCO_3$-saturated solution with 100 ppm Mg^{2+} after 2 days (black line), 4 days (yellow line), and after 7 days (purple line). XRD data shows that after 2 days of exposure α-Fe and Fe_3C peaks are dominant over weak peaks related to the formation of $FeCO_3$. However, after 4 and 7 days of exposure, the intensity of peaks related to α-Fe and Fe_3C are noticeably diminished and, instead, peaks associated with $FeCO_3$ are intensified. However, $FeCO_3$ peaks are now broadened and shifted slightly towards the $MgCO_3$ reference peaks (green lines). The more intense $FeCO_3$ peaks associated with (104) and (116) Miller planes located at 32.07 and 52.7 degrees 2θ (CuK_α radiation) are more easily recognizable after 4 and 7 days of exposure, although all of the peaks are slightly shifted towards the right ($MgCO_3$ reference peak) in the presence of Mg^{2+} ions. It should be mentioned that the incorporation of Mg^{2+} into the lattice of $FeCO_3$ was very limited compared to similar conditions with the presence of Ca^{2+} (see Figure 34). The XRD detected data is in accordance with the EDS analysis provided in Figure 84.

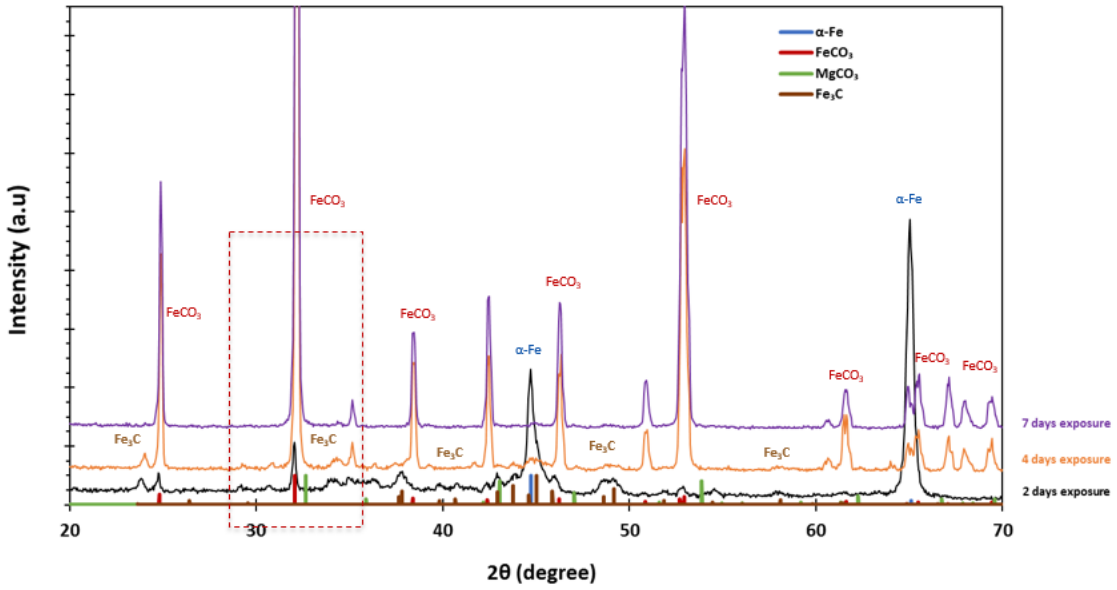

Figure 85. XRD patterns of surface layers detected on the steel surface after 2, 4, and 7 days of exposure to an electrolyte saturated with $MgCO_3$ at 80˚C, pCO_2 0.53 bar, 100 ppm Mg^{2+}, 0.58 m/s, pH 6.2, ionic strength 0.18 M, 1wt% NaCl

The vulnerability of the specimens to localized corrosion exposed to electrolytes with and without Mg^{2+} was also evaluated. Profilometry of the specimen surfaces was performed after removing corrosion product layers by Clarke solution [71], no localized corrosion was observed for experiments conducted at bulk pH 6.2. Figure 86 illustrates an example of profilometry of a specimen exposed for 7 days to a solution saturated with respect to $MgCO_3$.

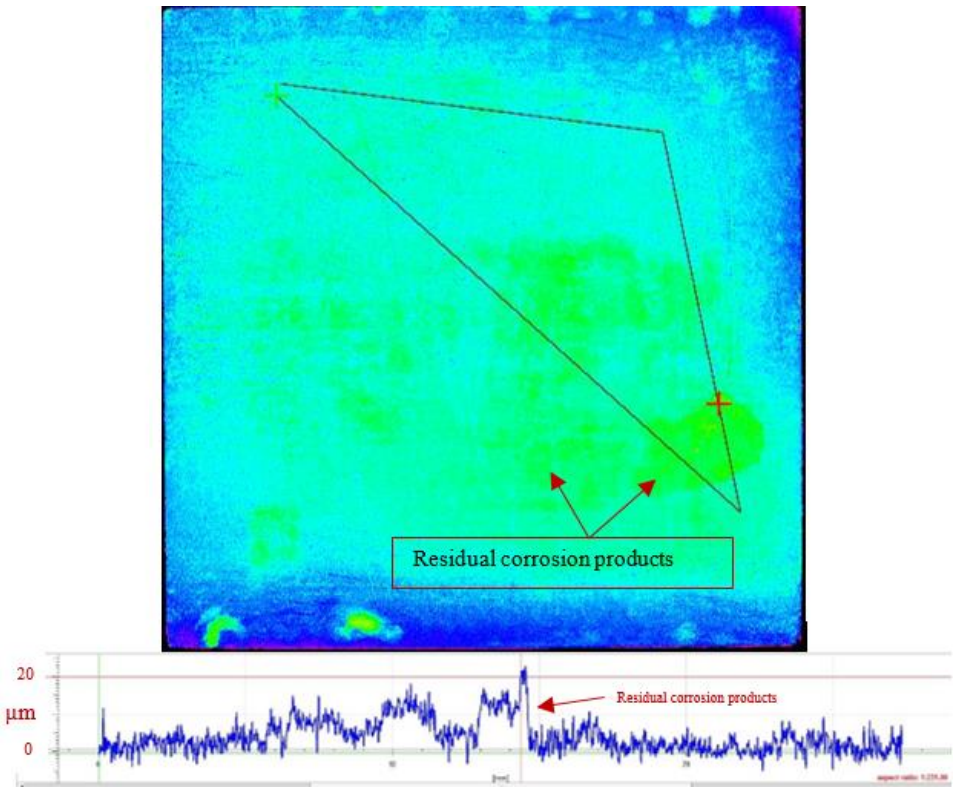

Figure 86. Example of profilometry of the specimen after removing the corrosion products (7 days of exposure to solution saturated with $MgCO_3$ at pH 6.2, 80˚C, pCO_2 0.53 bar, 100 ppm Mg^{2+}, ionic strength 0.18 M, 1 wt.% NaCl, 100 ppm Mg^{2+}

7.2.2 Experiments with 4,200 ppm Mg^{2+} at pH 5.5 and 0.6 M ionic strength

From experiments conducted at pH 6.2, it was observed that the presence of 100 ppm Mg^{2+} did not alter the protectiveness of corrosion products when they were fully developed on the steel surface in the pseudo-passivation period. However, the presence of Mg^{2+} increased corrosion rate in the active corrosion period, which resulted in higher thickness of Fe_3C compared to the baseline experiments. Indeed, localized corrosion was not observed for such experiments. It was necessary to conduct the same type of experiment in higher concentration of Mg^{2+} while the solution is saturated with $MgCO_3$

to better resemble oilfield conditions. In this part of the dissertation, the effect of 4,200 ppm Mg^{2+} in solutions saturated with $MgCO_3$ at pH 5.5 on CO_2 corrosion are discussed.

Basically, the same phenomena discussed for the 100 ppm Mg^{2+} experiments are valid in the presence of 4,200 ppm Mg^{2+}; experimental conditions are expressed in Table 11. Therefore, in order to avoid repetition, only significantly different observations are discussed here, and the appropriate graphs and results are provided. Figure 87 shows the trend of LPR corrosion rate over time with and without the presence of 4,200 ppm Mg^{2+} at pH 5.5. The three corrosion periods are identified similarly to the experiments conducted at pH 6.2. The final corrosion rates are higher compared to pH 6.2 because of the more aggressive solution (lower pH). Figure 88 shows the cumulative corrosion rate with and without 4,200 ppm Mg^{2+}. The presence of 4,200 ppm Mg^{2+} leads to a higher corrosion rate especially at the first two days of experiments, which is reflected in a greater Fe_3C thickness as shown in Figure 89. The OCP variation over time for experiments conducted at pH 5.5 is shown in Figure 90.

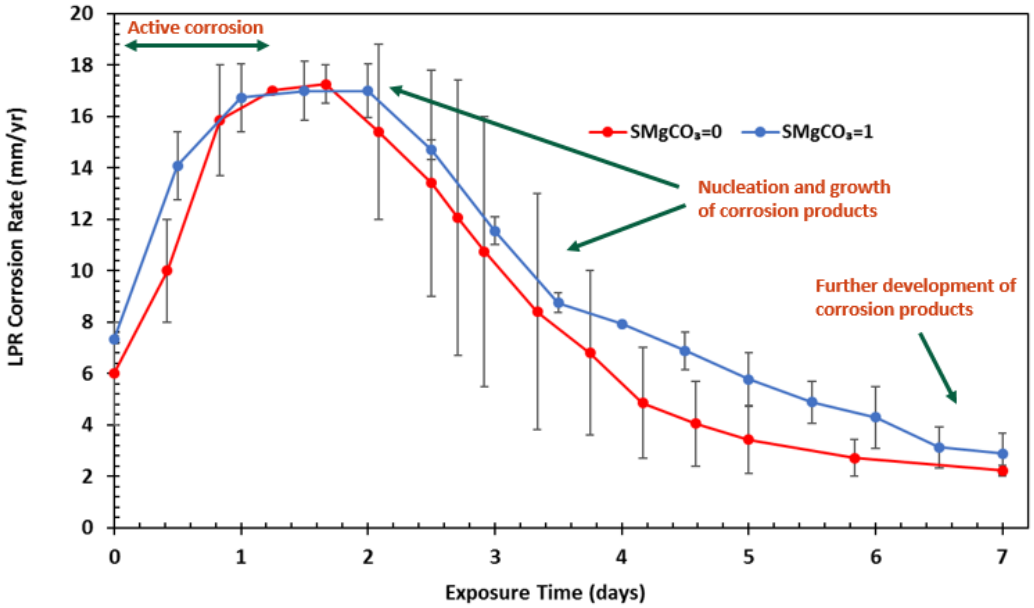

Figure 87. Trend of corrosion rate obtained by LPR over time with and without presence of 4,200 ppm Mg^{2+} at pH 5.5

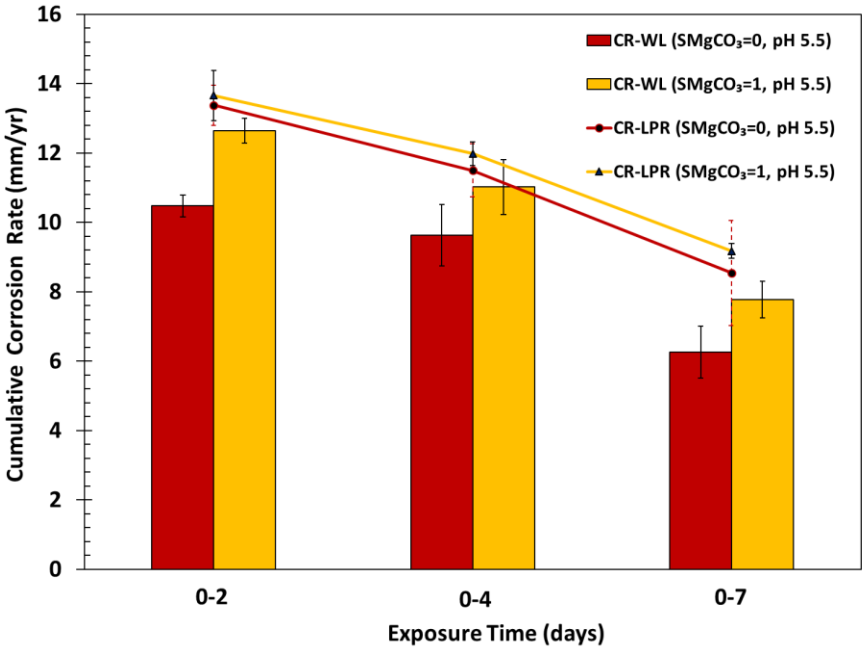

Figure 88. Cumulative corrosion rate by WL (bar chart) and LPR (line chart) techniques over time for solution with and without 4,200 ppm Mg^{2+} (80˚C, pCO_2 0.53 bar, 0.58 m/s, pH 5.5, ionic strength 0.6 M, 1 wt.% NaCl)

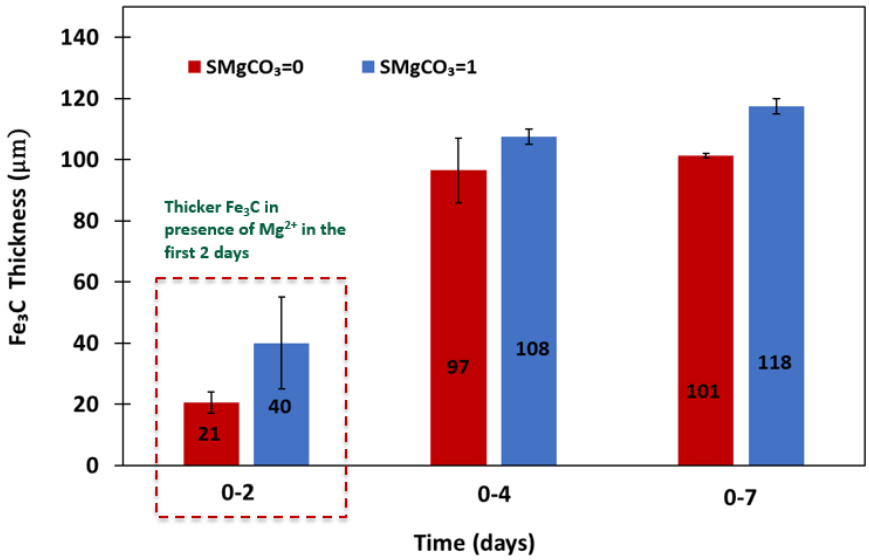

Figure 89. Evolution of Fe_3C over time with and without presence of 4,200 Mg^{2+} (80˚C, pCO_2 0.53 bar, 0.58 m/s, pH 5.5, ionic strength 0.6 M, 1 wt.% NaCl)

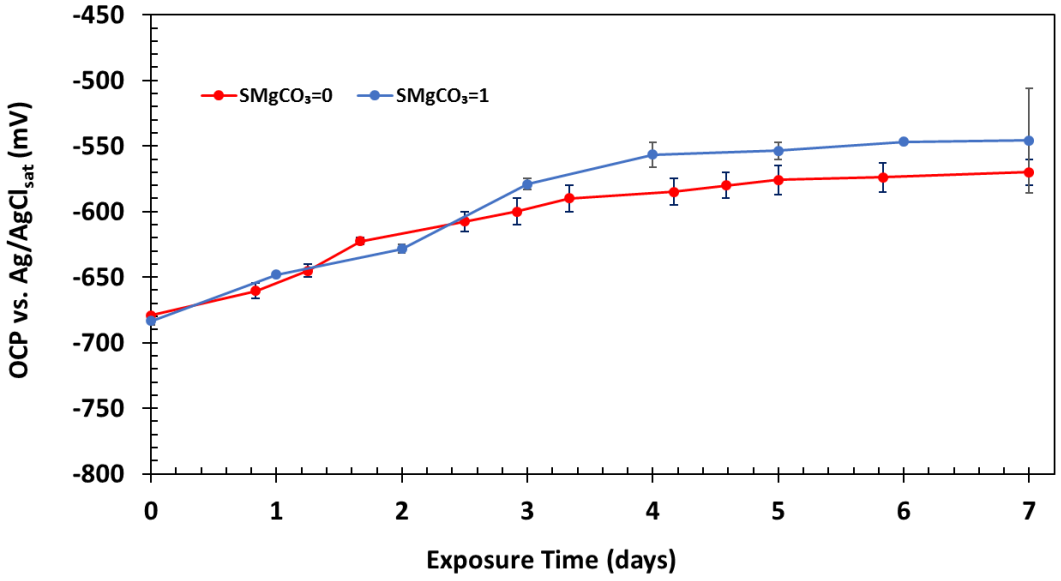

Figure 90. Comparison of OCP over time for UNS G10180 exposed to solutions with and without 4,200 ppm Mg^{2+} (80˚C, pCO_2 0.53 bar, 0.58 m/s, pH 5.5, ionic strength 0.6 M, 1 wt.% NaCl)

SEM cross-sectional and top view images of surface layers developed in the presence 4,200 ppm Mg^{2+} are shown in Figure 91. Morphological characterization of top and cross-section specimen views for the baseline experiment at pH 5.5 is provided in Figure 41. Therefore, Figure 91 and Figure 41 should be compared when investigating the effect of 4,2000 ppm Mg^{2+} on corrosion product characteristics. With 4,200 ppm Mg^{2+}, the morphology and composition of corrosion products were similar to those obtained at pH 6.2 with 100 ppm Mg^{2+}. However, a greater thickness of corrosion products was achieved for experiments at pH 5.5 due to the higher corrosion rate. The $FeCO_3$ saturation degree for experiments conducted at both pH 6.2 and 5.5 was lower than ~10, which explains why a limited quantity of $FeCO_3$ crystals formed on top of the Fe_3C network even after 7 days of exposure (see top view images in Figure 83 and Figure 91).

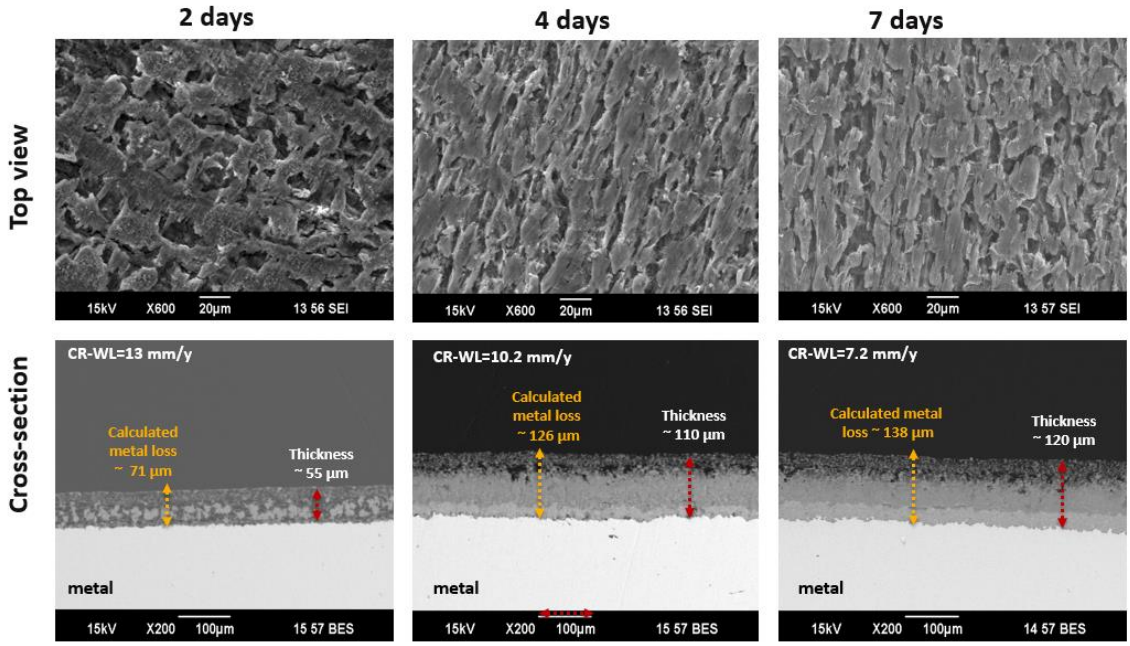

Figure 91. SEM images (top and cross-section view) of the development of surface layers over time for the experiment with presence of 4,200 ppm Mg^{2+} ($S_{MgCO_3} = 1$) at 80˚C, pCO_2 0.53 bar, 0.58 m/s, pH 5.5, ionic strength 0.6M, 1 wt.% NaCl

Figure 92 shows a comparison of cross-sectional EDS line scan analysis of the surface layers developed on specimens exposed to solutions with and without 4,200 ppm Mg^{2+} after 7 days. $FeCO_3$ is the only corrosion product in the absence of Mg^{2+} (see Figure 92 (a)). From Figure 92 (b), it is obvious that even such a high concentration of Mg^{2+} did not significantly incorporate into the lattice of $FeCO_3$. Likewise, for the experiment with lower [Mg^{2+}], a solid solution of $Fe_xMg_yCO_3$ formed on the steel surface with x>>y. Formation of a bi-layer of corrosion product on the specimen is confirmed from Figure 92 (b).

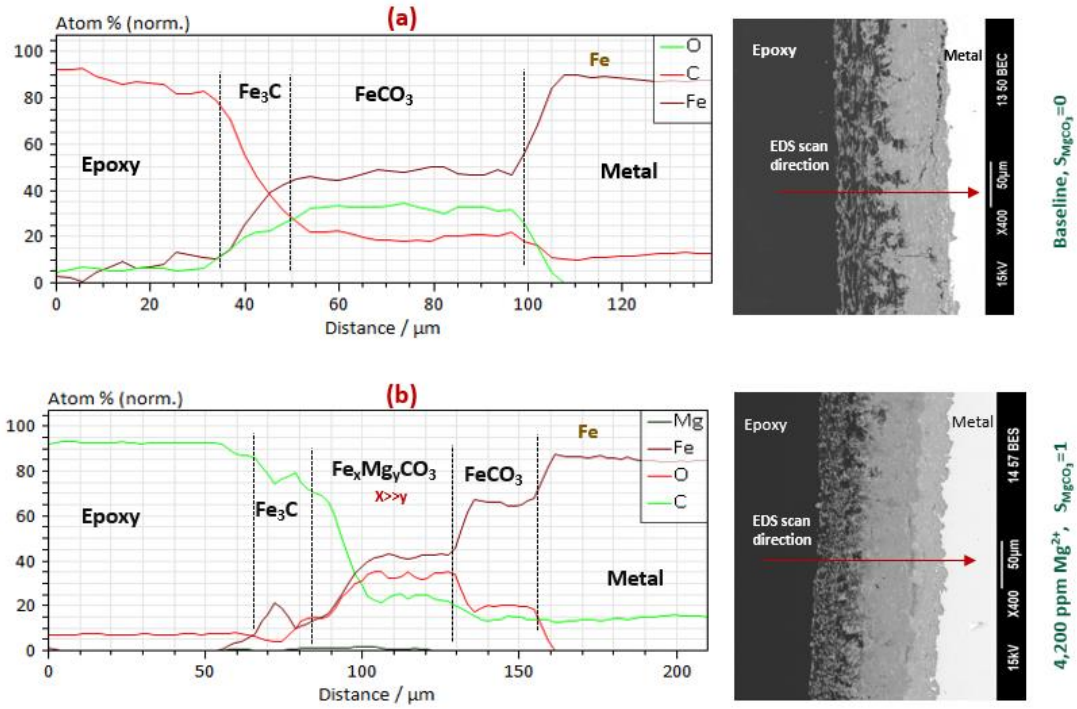

Figure 92. EDS line scan analysis of the surface layers developed on the specimens after 7 days of exposure to electrolytes without (a) and with (b) 4,200 ppm Mg^{2+} at 80˚C, pCO_2 0.53 bar, 0.58 m/s, pH 5.5, ionic strength 0.6 M, 1 wt.% NaCl

7.2.3 Descriptive Model for the Effect of High [Mg^{2+}] on Localized Corrosion

Unlike the experiments conducted at low [Mg^{2+}], localized corrosion was observed with high [Mg^{2+}] at the lower pH of 5.5. Corrosion products were occasionally ruptured on the steel surface after 4 and 7 days of exposure, see Figure 93. Beneath such damaged layers, localized corrosion was observed. It is believed that a thick and fragile layer of Fe_3C, in comparison to the baseline experiment (see Figure 89), was vulnerable to rupture before $FeCO_3$ could precipitate within its pores and confer more mechanical strength. Figure 93 shows a top and cross-section view of such damage in corrosion products influenced by flow and possible internal stresses within the Fe_3C network.

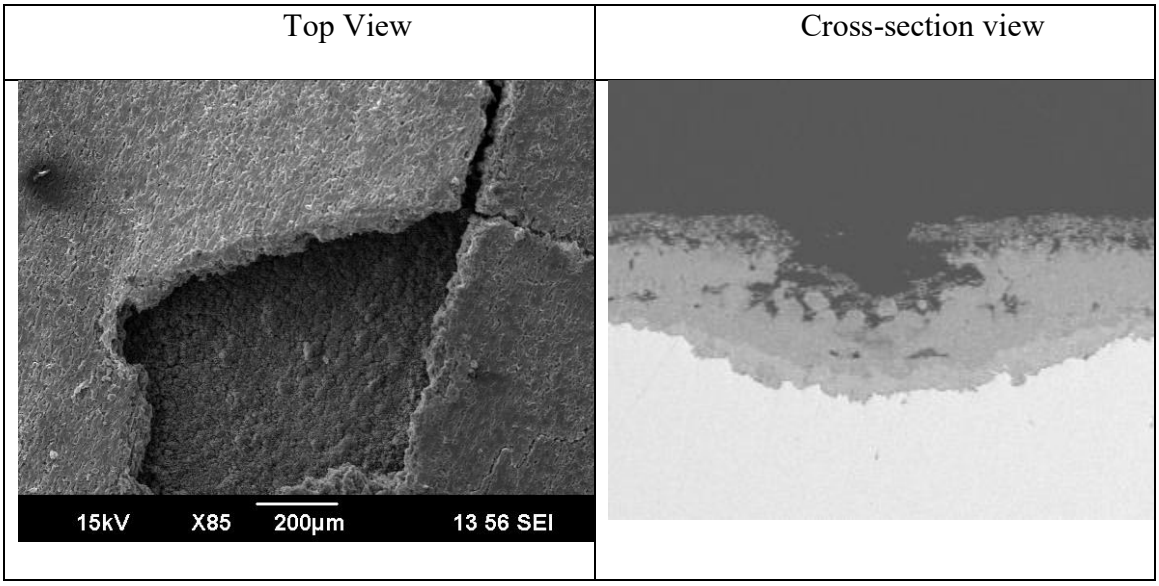

Figure 93. SEM images (top and cross section view) of ruptured corrosion products observed on specimens exposed to $MgCO_3$-satuarted solution with 4,200 ppm Mg^{2+} at 80˚C, pCO_2 0.53 bar, 0.58 m/s, pH 5.5, ionic strength 0.6 M, 1 wt.% NaCl

Figure 94 shows profilometry of specimens after removal of corrosion products by Clarke solution [71]. Localized corrosion was observed at locations where the corrosion product layers were damaged. The number of localized attack sites were limited but were relatively wide. That is why the pitting ratio (maximum penetration over uniform corrosion, Equation 32) of such attacks is small. Such observation of localized corrosion was repeatable in the presence of high concentration of Mg^{2+}. Table 12 provides more information regarding maximum pit depth in µm and pitting ratio for two different specimens exposed to $MgCO_3$-saturated electrolyte with 4,200 ppm Mg^{2+}. The maximum pitting ratio is lower than 2, therefore, such attack does not qualify as “pitting corrosion”. According to the experimental procedure, only a pitting ratio greater than 5 is considered as “pitting corrosion”.

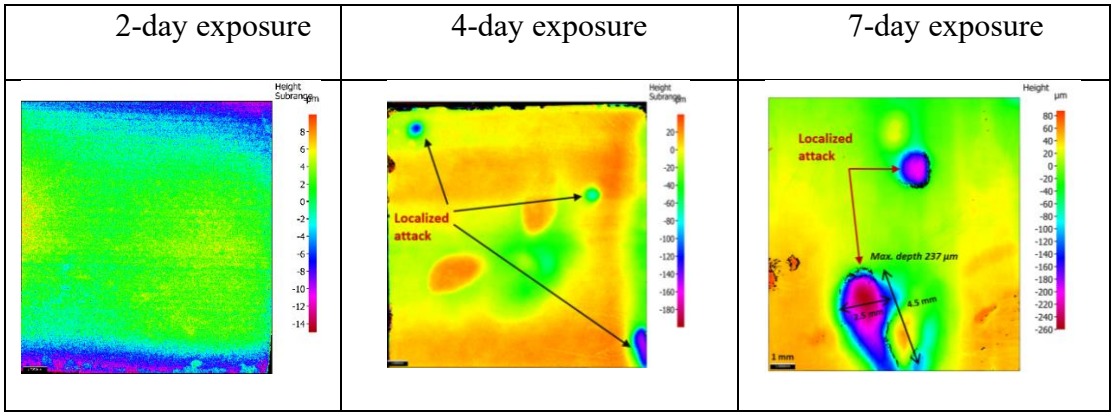

Figure 94. Profilometry of specimens after removing of corrosion product layers ($MgCO_3$-satuarted solution with 4,200 ppm Mg^{2+} at 80˚C, pCO_2 0.53 bar, 0.58 m/s, pH 5.5, ionic strength 0.6M, 1 wt.% NaCl)

Table 12. Evolution of localized attacks on specimens exposed to 4,200 ppm Mg^{2+} at pH 5.5

Repeatability of localized corrosion in presence of high [Mg^{2+}] at pH 5.5				
	Experiment #A			
	Exposure time (day)	Max pit (µm)	Max penetration rate (mm/y)	Pitting ratio
	2	8	1.46	0.12
	4	140	12.78	1.08
	7	237	12.36	1.49
	Experiment #B (Repeat of A)			
	Exposure time day	Max pit (µm)	Max penetration rate (mm/y)	Pitting ratio
	2	12	2.19	0.17
	4.5	200	16.22	1.59
	7	216	11.26	1.56

Based on the experimental results, a mechanism is proposed for the localized corrosion observed in CO_2 corrosion of mild steel (with ferritic-pearlitic microstructure) exposed to $MgCO_3$-saturated solution with high concentration of Mg^{2+} at 80˚C, bulk solution pH 5.5, pCO_2 0.53 bar, 0.6M ionic strength as illustrated in Figure 95 (a-h):

a) UNS G10180 carbon steel is exposed to solution saturated with $MgCO_3$ and CO_2 with bulk pH 5.5.

b) Fe oxidatively dissolves and Fe^{2+} is released into solution. Consequently, a porous Fe_3C network is left behind on the steel surface and is growing over time. It is postulated that presence of Mg^{2+} has hindered nucleation/growth of $FeCO_3$ crystal within Fe_3C pores. Therefore, the corrosion rate is higher compared to Ca^{2+}-containing experiments at this stage of the corrosion process. Other researchers have also reported the inhibition effect of Mg^{2+} on carbonate nucleation in different aqueous systems [94-96].

c) The fragile Fe_3C layers reach a critical thickness. Occasional breakage occurs possibly due to internal stress within the Fe_3C network and due to flow effects.

d) Continuation of corrosion and Fe_3C development.

e) Achievement of favorable water chemistry for nucleation/precipitation of $FeCO_3$ within Fe_3C pores where they are intact. At this stage, the water chemistry is very favorable for precipitation of $FeCO_3$ which counters the inhibiting effect of Mg^{2+}. As a result, the general corrosion rate reduced.

f) Occurrence of localized corrosion where the steel is not covered with $FeCO_3$ (locations with damaged Fe_3C).

g) Retardation of localized corrosion rate due to precipitation of $FeCO_3$.

h) Further development of $FeCO_3$ (inner layer) and $Fe_xMg_yCO_3$, x>>y (outer layer)

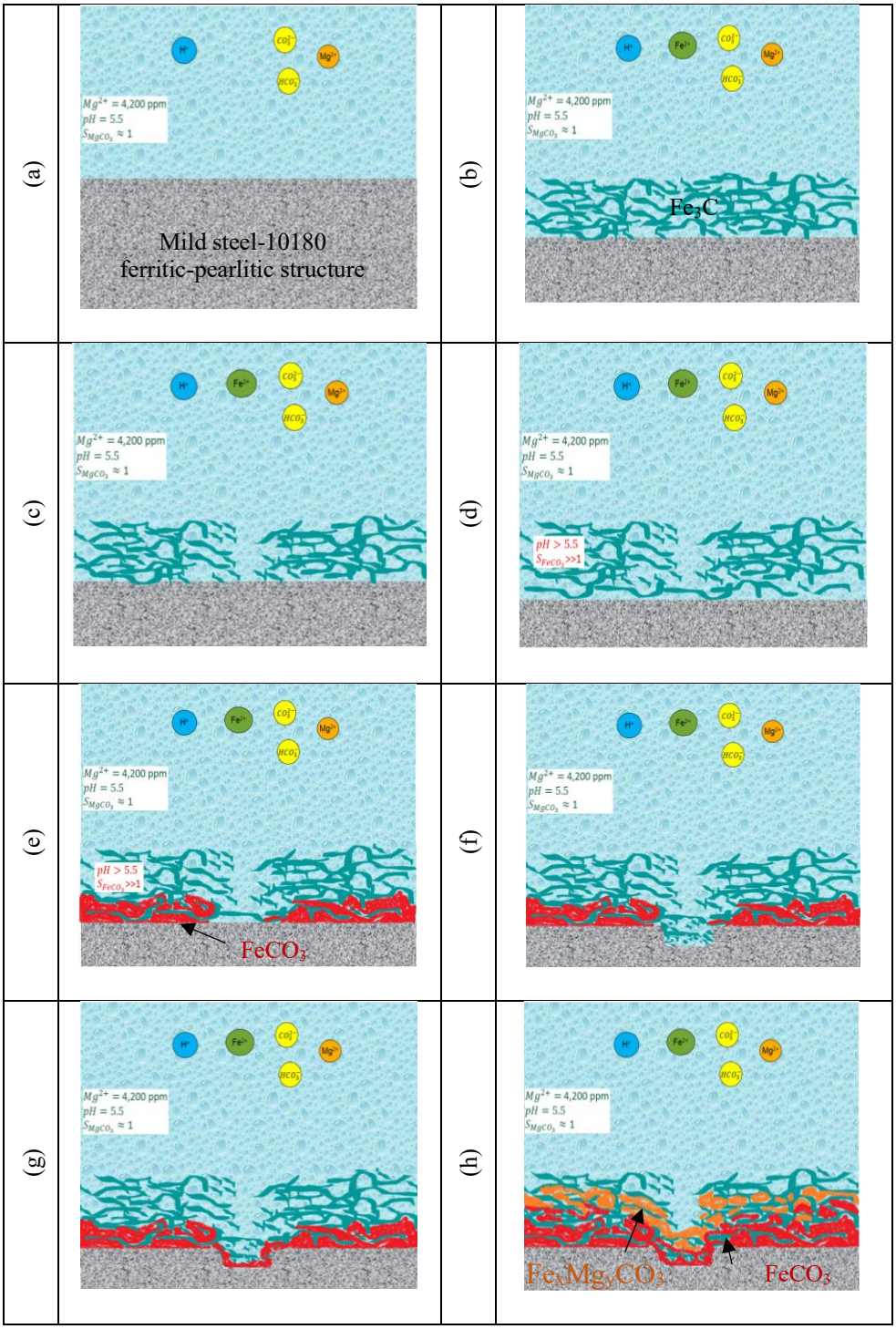

Figure 95. Proposed mechanism for the localized corrosion observed in presence of high [Mg^{2+}] for mild steel at4,200 ppm Mg^{2+}, 80˚C, pCO_2 0.53 bar, 0.58 m/s, pH 5.5, ionic strength 0.6M, 1 wt.% NaCl

7.3 Summary

- The presence of Mg^{2+} (low and high concentrations) had a negligible impact on the morphology and chemical composition of corrosion products.
- At both pH 5.5 and 6.2, the presence of Mg^{2+} seems to increase the corrosion rate during the active corrosion period. The reason for this observation is not completed understood. Appendix IV provides the results of electrochemical experiments performed to investigate role of Mg^{2+} (and Ca^{2+}) in CO_2 corrosion before formation of corrosion products (Fe_3C and $FeCO_3$).
- At pH 5.5, the presence of high concentration of Mg^{2+} (4,200 ppm) hindered nucleation of $FeCO_3$ and promoted the formation of a thicker Fe_3C layer (compared to its baseline condition) leading to occasional rupture and/or detachment from the steel surface at the early stage of corrosion process. Preferential corrosion was observed at such locations but did not qualify as localized corrosion since the pitting ratio <2. The localized corrosion did not sustain due to precipitation of a protective $FeCO_3$ within the pits.

CHAPTER 8: CO_2 CORROSION IN ELECTROLYTES WITH THE SIMULTANEOUS PRESENCE OF Ca^{2+} AND Mg^{2+}

As mentioned in the introduction, Mg^{2+} and Ca^{2+} are simultaneously observed in oilfield brines. Now that the effect of Mg^{2+} and Ca^{2+} has been studied separately, it is relevant to study the effect of these ions concurrently. In the current experimental scenario, the solution is saturated with $CaCO_3$ (Ca^{2+} 6000 ppm) and under saturated with respect to $MgCO_3$ (with addition of 857 ppm Mg^{2+} as the $MgCl_2$ salt).

8.1 Methodology and Test Matrix

The experimental condition presented in Table 13 was employed to conduct experiments in the simultaneous presence of Ca^{2+} and Mg^{2+}. The solution was saturated with respect to $CaCO_3$ and undersaturated with respect to $MgCO_3$. An excess amount of granular $CaCO_3$, as a solid powder, was present at the beginning of the experiments (to make the solution with respect to $CaCO_3$). Mg^{2+}, with mass ratio of Ca^{2+}/Mg^{2+} =7, was added to the system using $MgCl_2$ salt; such a ratio mirrors brine analyses [11]. In the conducted experimental conditions, the [Ca^{2+}] was ~6000 ppm and the [Mg^{2+}] was ~857 ppm. The solution preparation procedure was consistent with the previous experiments.

Table 13. Experimental condition to study the effect of simultaneous presence of [Mg^{2+}] and [Ca^{2+}] on CO_2 corrosion at pH 5.5

Parameter	Description	
Temperature	80°C	
pCO_2	0.53 bar	
pH	5.5	
Electrolyte	Baseline	Ca^{2+}/Mg^{2+}=7 (mass ratio)
	1 wt.% NaCl + $NaHCO_3$ + $NaClO_4$ (Ionic Strength≈0.6 M)	0.85 wt.% NaCl + $CaCO_3$ + $MgCl_2$ (Ionic Strength≈0.6 M)
[Mg^{2+}]	0	857 ppm, $S_{MgCO_3 \approx 0.14}$
[Ca^{2+}]	0	6,000 ppm, $S_{CaCO_3 \approx 1}$
S_{FeCO_3}	0 to 10	
Dissolved O_2	<5 ppb	
Experiment Duration	7 days	

8.2 Results and Discussion

The trend of LPR corrosion rate over time with different water chemistry (baseline, $CaCO_3$-saturated, $MgCO_3$-saturated, simultaneous presence of Ca^{2+} and Mg^{2+}) at pH 5.5 is presented in Figure 96. It is obvious that the presence of Mg^{2+} (yellow line) has increased the general corrosion rate in an electrolyte saturated with $CaCO_3$ (dark blue line). Cumulative corrosion rates at day 2, 4 and 7 exposure times to different solutions obtained by the WL method is provided in Figure 97. While the LPR method is informational for trend of corrosion rate over time, the WL method provided more accurate results. WL results show that corrosion in the presence of 4,200 ppm Mg^{2+} is higher than the other scenarios at each measuring point. Indeed, the addition of 857 ppm Mg^{2+} to a $CaCO_3$-saturated solution (yellow line) clearly has increased the corrosion rate compared to a $CaCO_3$-saturated solution (dark blue line). A comparison of OCP over

time, obtained from mild steel exposure to different solutions, is provided in Figure 98. Note that for the solution saturated with $CaCO_3$ (dark blue), higher OCP values were achieved at the end of the experiment. This observation indicates that the corrosion products offered more protection compared to the other experiments in the pseudo-passivation region. The better protectiveness of corrosion products in the presence of Ca^{2+} at pH 5.5 is also reflected in the lower cumulative corrosion rate obtained by WL compared to the other experimental scenarios (see Figure 97).

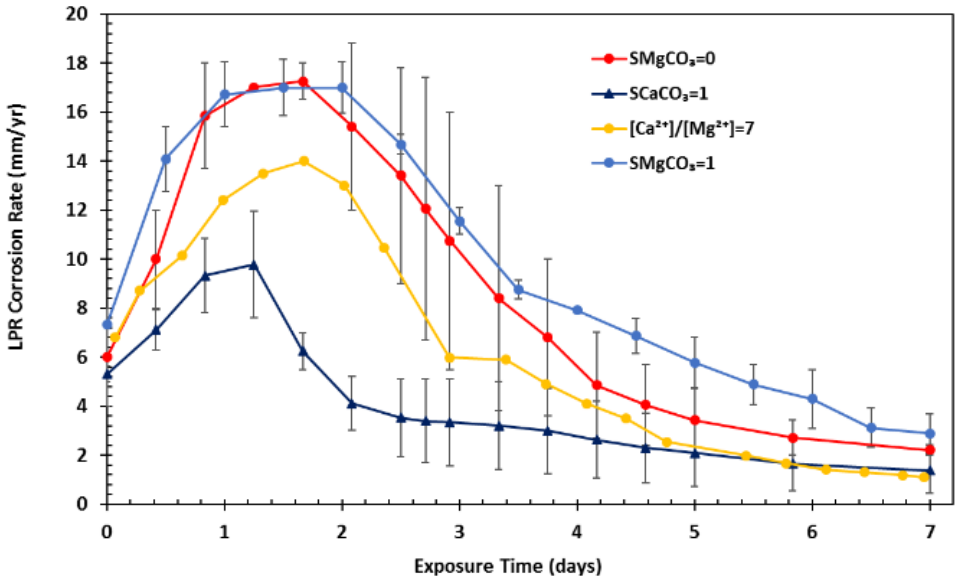

Figure 96. Trend of corrosion rate obtained by LPR over time at 80˚C, pCO_2 0.53 bar, 0.58 m/s, pH 5.5, ionic strength 0.6M [baseline (red), 6000 ppm Ca^{2+} (dark blue), Ca^{2+}/Mg^{2+}=7 (yellow), and 4200 ppm Mg^{2+} (light blue)]

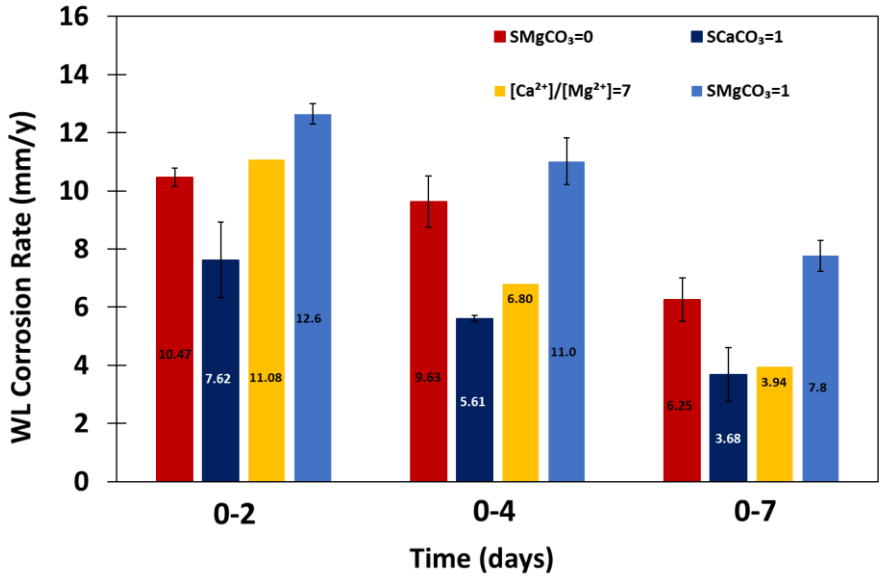

Figure 97. Cumulative corrosion rate obtained by WL over time at 80˚C, pCO_2 0.53 bar, 0.58 m/s, pH 5.5, ionic strength 0.6M [baseline (red), 6000 ppm Ca^{2+} (dark blue), Ca^{2+}/Mg^{2+}=7 (yellow), and 4200 ppm Mg^{2+} (light blue)]

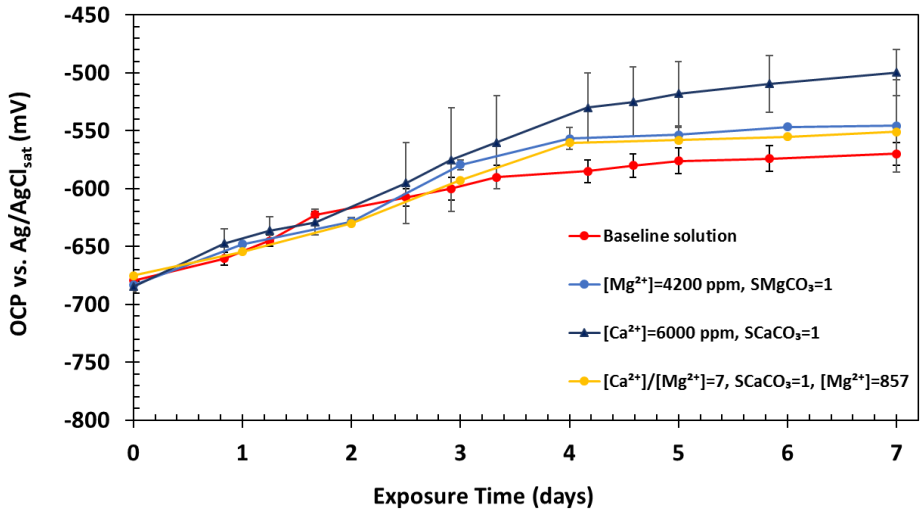

Figure 98. Comparison of OCP over time for UNS G10180 exposed to various solutions at 80˚C, pCO_2 0.53 bar, 0.58 m/s, pH 5.5, ionic strength 0.68 M [baseline (red), 6000 ppm Ca^{2+} (dark blue), Ca^{2+}/Mg^{2+}=7 (yellow), and 4200 ppm Mg^{2+} (light blue)]

8.3 Inhibiting Effect of Mg^{2+} on Carbonate Precipitation

SEM and EDS analysis revealed that a lesser quantity of carbonates was precipitated on top of the Fe_3C layers for electrolytes that had a simultaneous presence of Mg^{2+} and Ca^{2+}, compared to a solution solely saturated with $CaCO_3$. It seems that the presence of Mg^{2+} has decreased precipitation of carbonate crystals. Figure 99 illustrates SEM/EDS data, for comparison, for two solutions: (a) $Ca^{2+}/Mg^{2+}=7$, $SCaCO_3=1$ (b) $Ca^{2+}= 6000$ ppm, $SCaCO_3=1$. Additionally, the inhibiting effect of Mg^{2+} on $FeCO_3$ nucleation and precipitation (within Fe_3C pores) was speculated for experiments with high concentration of Mg^{2+} at the early stage of corrosion process, see section 7.2.3. Such observation of the inhibiting effect of Mg^{2+} on carbonate nucleation/formation are also reported by other researchers [94-96].

Profilometry of specimens were performed by IFM techniques, after removing the corrosion products. No localized corrosion was detected on the specimens' surface.

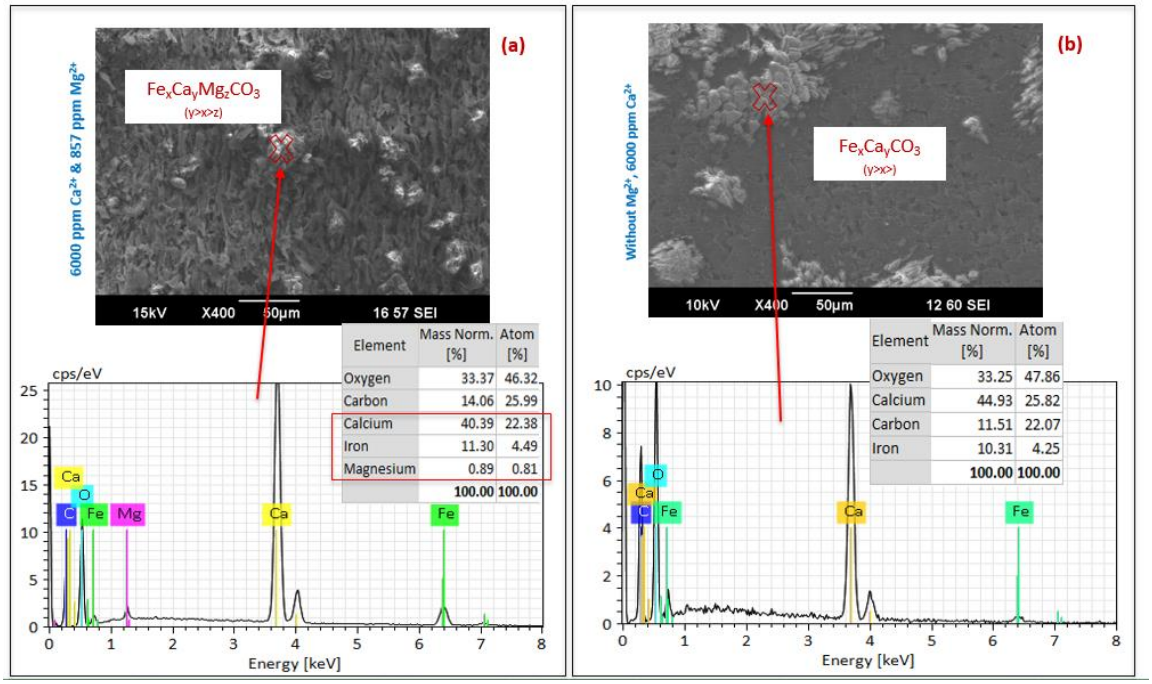

Figure 99. Comparison of SEM/EDS results for two solutions at 80˚C, pCO_2 0.53 bar, 0.58 m/s, pH 5.5, ionic strength 0.68 M [(a); Ca^{2+}/Mg^{2+}=7, $SCaCO_3$=1 and (b) Ca^{2+}= 6000 ppm, $SCaCO_3$=1]

Figure 100 shows EDS line scan analysis of a cross-sectioned specimen after 7 days of exposure to an electrolyte saturated with $CaCO_3$ in the presence of 857 ppm Mg^{2+}. This analysis revealed that a mixed solid solution of $Fe_xCa_yMg_zCO_3$ (x>y, trace z) is formed as the outer layer whereas the inner layer was essentially pure $FeCO_3$. Formation of a pure $FeCO_3$ as the inner layer of corrosion products was also observed in experiments with solely Ca^{2+} or Mg^{2+}; see chapter 6 and chapter 7 of this manuscript, respectively.

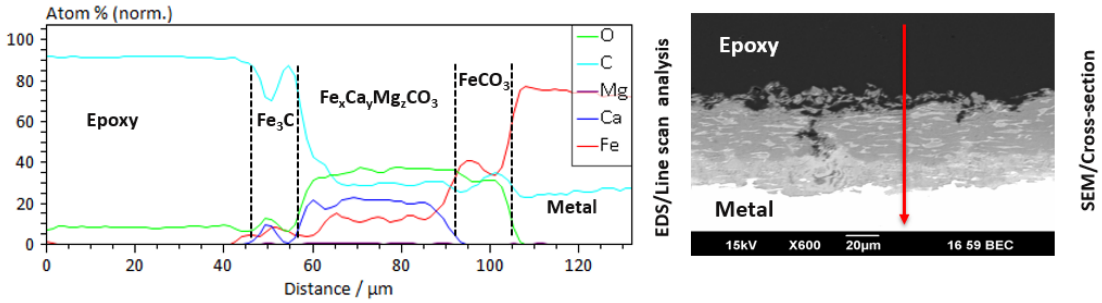

Figure 100. EDS line scan analysis of the surface layers developed on a specimen after 7 days of exposure to a $CaCO_3$-saturated electrolyte with 857 ppm Mg^{2+} at 80˚C, pCO_2 0.53 bar, 0.58 m/s, pH 5.5, ionic strength 0.6M

8.4 Summary

- The presence of Mg^{2+} reduced precipitation of carbonate on the steel surface compared with experiments solely contained Ca^{2+}.
- The presence of Mg^{2+} increased the general corrosion rate at the early stage of the corrosion process. However, the final CR with and without Mg^{2+} was essentially identical.
- No localized corrosion was observed in the presence of Mg^{2+} and Ca^{2+} with Ca^{2+}/Mg^{2+} = 7 (mass ratio).

CHAPTER 9: CONCLUSIONS

The following main conclusions are drawn from the conducted experiments for different scenarios.

- The $CaCO_3$ and $MgCO_3$ saturation degree of the electrolyte, $[Ca^{2+}]$ and $[Mg^{2+}]$, and bulk pH are crucial parameters in studying the effect of Ca^{2+} and Mg^{2+} on CO_2 corrosion. Ignoring the influence of such parameter(s) is one of the main reasons for the existing discrepancies in the available literature on this topic.
- The development of Fe_3C on the carbon steel surface played a critical role in precipitation of corrosion products. The mole fraction of Ca and Mg in the surface corrosion products mainly depended on calcium and magnesium concentration in bulk solution.
- The protective behavior of the surface layers was mainly due to the formation of $FeCO_3$ adjacent to the steel surface (inner layer) rather than the outer layer corrosion product/scale ($Fe_xCa_yMg_zCO_3$, $x+y+z=1$) in the presence of Ca^{2+} and/or Mg^{2+} in the electrolyte. However, the presence of the outer layers facilitated $FeCO_3$ precipitation and enhanced its protectiveness by acting as a mass transfer barrier for Fe^{2+} outwards from the steel and H^+ towards the steel.
- Although $CaCO_3$ is isomorphous with $FeCO_3$, $CaCO_3$ scale was not protective against further corrosion.

- No localized corrosion was observed in the presence of Ca^{2+} and/or $CaCO_3$ scale (if uniform surface coverage is conferred). Patchy precipitation of $CaCO_3$ scale could lead to localized corrosion.
- Unlike $CaCO_3$, formation of $MgCO_3$ was not possible in the current experimental condition due its slow precipitation kinetics.
- The presence of Mg^{2+} in test electrolytes increased the corrosion rate during the active corrosion period while possibly hindering precipitation of $FeCO_3$, compared to Ca^{2+}-containing electrolytes.
- A high concentration of Mg^{2+} (4,200 ppm) at pH 5.5 promoted formation of a thicker Fe_3C layer, compared to its baseline condition, leading to its occasional rupture and/or detachment from the steel surface. Preferential corrosion was observed at such locations but did not qualify as localized corrosion.

CHAPTER 10: FUTURE WORK

Based on the experimental results and conclusions drawn from the current research, the following areas can be further investigated in future studies related to this topic.

- The experiments reported on herein were performed in controlled water chemistry and well-defined mass transfer conditions using a glass cell setup with limited maximum operation pressure (1 bar), temperature (80°C upper limit) and flow velocity. Investigating the effect of Ca^{2+} and Mg^{2+} with higher partial pressures of CO_2, increased temperatures, and more aggressive flow velocities, resembling oilfield conditions, will add more understanding to this topic. Kinetics of corrosion product/scale precipitation and corrosion mechanisms would be different at such conditions. Consequently, autoclave experiments and/or flow loops such as the Thin Channel Flow Cell (TCFC), with application of ion-exchange resins to help controlling water chemistry, are recommended.
- Investigation of the effect of Ca^{2+} and Mg^{2+} and their associated carbonate scales in H_2S environments since the H_2S corrosion mechanism and its potential corrosion products are different from those of CO_2 corrosion. Therefore, an appropriate test scenario would be to study corrosion in the concurrent presence of H_2S and CO_2 with brines containing Ca^{2+} and/or Mg^{2+}, as observed in oilfields.

- Investigate the precipitation kinetics of $FeCO_3$ in the presence of Ca^{2+} and Mg^{2+} with an Electrochemical Quartz Crystal Microbalance (EQCM). This requires the availability of a reliable technique to measure the concentration of Ca^{2+} and Mg^{2+} in the bulk solution over a short time (in scale of minutes).
- Although, short-term electrochemical experiments were performed to understand the influence of Ca^{2+} and Mg^{2+} on the electrochemical behavior of mild steel in CO_2 environment (at the initial stage of corrosion process), a more rigorous electrochemical study is needed for a better understanding of this situation.

REFERENCES

[1] M. B. Kermani and D. Harrop, “The Impact of Corrosion on Oil and Gas Industry,” *SPE Prod. Facil.*, vol. 11, no. 03, pp. 186–190, 1996.

[2] M. Kermani and A. Morshed, “Carbon Dioxide Corrosion in Oil and Gas Production-A Compendium,” *Corrosion*, vol. 59, no. 8, pp. 659–683, 2003.

[3] G. Koch, J. Varney, N. Thompson, O. Moghissi, M. Gould, and J. Payer, “International measures of prevention, application, and economics of corrosion technologies study,” NACE International IMPACT Report, 2016.

[4] R. R. Fessler, “Pipeline Corrosion,” U.S. Department of Transportation Pipeline and Hazardous Materials Safety Administration, Office of Pipeline Safety, Report DTRS56-02-D-70036, 2008.

[5] M. Orazem, *Underground Pipeline Corrosion*. Elsevier, 2014.

[6] H. Mansoori, R. Mirzaee, F. Esmaeilzadeh, A. Vojood, and A. Soltan Dowrani, “Pitting Corrosion Failure Analysis of a Wet Gas Pipeline,” *Eng. Fail. Anal.*, vol. 82, pp. 16–25, 2017.

[7] J. E. Oddo, M. B. Tomson, and others, “Why Scale Forms in the Oil Field and Methods to Predict It,” *SPE Prod. Facil.*, vol. 9, pp. 47–54, 1994.

[8] H. Mansoori, D. Mowla, F. Esmaeelzadeh, and A. H. Mohammadi, “Case Study: Production Benefits from Increasing C-Values,” *Oil Gas J.*, vol. 111, no. 6, pp. 64–69, 2013.

[9] S. Nesic, “Key Issues Related to Modelling of Internal Corrosion of Oil and Gas Pipelines – A Review,” *Corros. Sci.*, vol. 49, no. 12, pp. 4308–4338, 2007.

[10] M. Salman, H. Qabazard, and M. Moshfeghian, “Water Scaling Case Studies in a Kuwaiti Oil Field,” *J. Pet. Sci. Eng.*, vol. 55, no. 1, pp. 48–55, 2007.

[11] P. E. Dresel and A. W. Rose, “Chemistry and Origin of Oil and Gas Well Brines in Western Pennsylvania,” The Pennsylvania State University, Open-File Report OFOG 10–01.0, 2010.

[12] L. Chai and A. Navrotsky, “Synthesis, Characterization, and Energetics of Solid Solution along the Dolomite-Ankerite Join, and Implications for the Stability of Ordered $CaFe(CO_3)_2$,” *Am. Mineral.*, vol. 81, no. 9–10, pp. 1141–1147, 2015.

[13] T. Zoltai and J. H. Stout, *Mineralogy: concepts and principles*. Burgess Publishing Company, 1984.

[14] M. Nordsveen, S. Nesic, R. Nyborg, and A. Stangeland, “A Mechanistic Model for Carbon Dioxide Corrosion of Mild Steel in the Presence of Protective Iron Carbonate Films—Part 1: Theory and Verification,” *Corrosion*, vol. 59, no. 5, pp. 443–456, 2003.

[15] H. Mansoori, R. Mirzaee, A. H. Mohammadi, and F. Esmaeelzadeh, "Acid Washes, Oxygenate Scavengers Work Against Gas Gathering Failures," *Oil Gas J.*, vol. 111, no. 7, pp. 106–111, 2013.

[16] D. L. Graver, L. E. Newton, and R. H. Hausler, *CO_2 Corrosion in Oil and Gas Production: Selected Papers, Abstracts, and References*. NACE International, 1984.

[17] C. De Waard and D. E. Milliams, "Carbonic Acid Corrosion of Steel," *Corrosion*, vol. 31, no. 5, pp. 177–181, 1975.

[18] Y. Zheng, B. Brown, and S. Nesic, "Electrochemical Study and Modeling of H_2S Corrosion of Mild Steel," Corrosion, vol. 70, no. 4, pp. 351–365, 2013.

[19] R. Nyborg, "Overview of CO_2 Corrosion Models for Wells and Pipelines," in *NACE International*, Paper no. 2233, 2002.

[20] A. Kahyarian, M. Achour, and S. Nesic, "CO_2 Corrosion of Mild Steel," in *Trends in Oil and Gas Corrosion Research and Technologies*, Elsevier, pp. 149-190, 2017.

[21] T. Tanupabrungsun, "Thermodynamics and Kinetics of Carbon Dioxide Corrosion of Mild Steel at Elevated Temperatures," Ph.D. Dissertation, Ohio University, 2012.

[22] A. Kahyarian, M. Singer, and S. Nesic, "Modeling of Uniform CO_2 Corrosion of Mild Steel in Gas Transportation Systems: A Review," *J. Nat. Gas Sci. Eng.*, vol. 29, pp. 530–549, 2016.

[23] J. O. Bockris, D. Drazic, and A. R. Despic, "The Electrode Kinetics of the Deposition and Dissolution of Iron," *Electrochimica Acta*, vol. 4, no. 2, pp. 325–361, 1961.

[24] D. M. Dražić and C. S. Hao, "The Anodic Dissolution Process on Active Iron in Alkaline Solutions," *Electrochimica Acta*, vol. 27, no. 10, pp. 1409–1415, 1982.

[25] M. Keddam, "Anodic dissolution," in *Corrosion Mechanisms in Theory and Practice*, 3rd Edit., CRC Press, pp. 149–215, 2011.

[26] R. Nyborg, "CO_2 Corrosion Models for Oil and Gas Production Systems," in *NACE International*, Paper no. 10371, 2010.

[27] G. Ogundele and W. White, "Observations on the Influences of Dissolved Hydrocarbon Gases and Variable Water Chemistries on Corrosion of an API L80 Steel," *Corrosion*, vol. 43, no. 11, pp. 665–673, 1987.

[28] S. Nesic, J. Postlethwaite, and S. Olsen, "An Electrochemical Model for Prediction of Corrosion of Mild Steel in Aqueous Carbon Dioxide Solutions," *Corrosion*, vol. 52, no. 4, pp. 280–294, 1996.

[29] T. Tran, B. Brown, and S. Nesic, "Corrosion of Mild Steel in an Aqueous CO_2 Environment–Basic Electrochemical Mechanisms Revisited," in *NACE International*, Paper no. 5671, 2015.

[30] A. Kahyarian, "Mechanism and Prediction of Mild Steel Corrosion in Aqueous Solutions Containing Carboxylic Acids, Carbon Dioxide, and Hydrogen Sulfide," PhD Dissertation, Ohio University, 2018.

[31] M. Gao, X. Pang, and K. Gao, "The Growth Mechanism of CO_2 Corrosion Product films," *Corros. Sci.*, vol. 53, no. 2, pp. 557–568, 2011.

[32] P. Debye and E. Huckle, "Zur Theorie der Electrolyte," *Phys Z*, vol. 9, pp. 185–206, 1923.

[33] C. W. Davies, "Ion Association," *Butterworths*, pp. 37–53, 1962.

[34] K. S. Pitzer, "Ion Interaction Approach: Theory and Data Correlation," *Act. Coeff. Electrolyte Solut.*, pp. 75–154, 1991.

[35] W. Stumm and J. J. Morgan, *Aquatic Chemistry: Chemical Equilibria and Rates in Natural Waters*. John Wiley and Sons, 2012.

[36] W. Sun, S. Nesic, and R. C. Woollam, "The Effect of Temperature and Ionic Strength on Iron Carbonate ($FeCO_3$) Solubility Limit," *Corros. Sci.*, vol. 51, no. 6, pp. 1273–1276, 2009.

[37] L. N. Plummer and E. Busenberg, "The Solubilities of Calcite, Aragonite and Vaterite in CO_2-H_2O Solutions between 0 and 90°C, and an Evaluation of the Aqueous Model for the System $CaCO_3$-CO_2-H_2O," *Geochim. Cosmochim. Acta*, vol. 46, no. 6, pp. 1011–1040, 1982.

[38] P. Bénézeth, G. D. Saldi, J. L. Dandurand, and J. Schott, "Experimental Determination of the Solubility Product of Magnesite at 50 To 200 °C," *Chem. Geol.*, vol. 286, no. 1–2, pp. 21–31, 2011.

[39] J. Kittrick and F. Peryea, "Determination of the Gibbs Free-Energy of Formation of Magnesite by Solubility Methods," *Soil Sci. Soc. Am. J.*, vol. 50, no. 1, pp. 243–247, 1986.

[40] O. S. Pokrovsky, S. V. Golubev, J. Schott, and A. Castillo, "Calcite, Dolomite and Magnesite Dissolution Kinetics in Aqueous Solutions at Acid to Circumneutral pH, 25 to 150°C and 1 to 55 atm pCO_2: New Constraints on CO_2 Sequestration in Sedimentary Basins," *Chem. Geol.*, vol. 265, no. 1–2, pp. 20–32, 2009.

[41] G. X. Zhao, L. Jian-Ping, H. Shi-Ming, and L. U. Xiang-Hong, "Effect of Ca^{2+} and Mg^{2+} on CO_2 Corrosion Behavior of Tube Steel," *J. Iron Steel Res. Int.*, vol. 12, no. 1, pp. 38–42, 2005.

[42] S. N. Esmaeely, D. Young, B. Brown, and S. Nesic, "Effect of Incorporation of Calcium into Iron Carbonate Protective Layers in CO_2 Corrosion of Mild Steel," *Corrosion*, vol. 73, no. 3, pp. 238–246, 2016.

[43] C. Ding, K. Gao, and C. Chen, "Effect of Ca^{2+} on CO_2 Corrosion Properties of X65 Pipeline Steel," *Int. J. Miner. Metall. Mater.*, vol. 16, no. 6, pp. 661–666, 2009.

[44] S. N. Esmaeely, Y.-S. Choi, D. Young, and S. Nesic, "Effect of Calcium on the Formation and Protectiveness of Iron Carbonate Layer in CO_2 Corrosion," *Corrosion*, vol. 69, no. 9, pp. 912–920, 2013.

[45] S. Zhong and A. Mucci, "Calcite and Aragonite Precipitation from Seawater Solutions of Various Salinities: Precipitation Rates and Overgrowth Compositions," *Chem. Geol.*, vol. 78, no. 3, pp. 283–299, 1989.

[46] K. Gao, F. Yu, X. Pang, and G. Zhang, "Mechanical Properties of CO_2 Corrosion Product Scales and Their Relationship to Corrosion Rates," *Corros. Sci.*, vol. 50, no. 10, pp. 2796–2803, 2008.

[47] X. Jiang, Y. G. Zheng, D. R. Qu, and W. Ke, "Effect of Calcium Ions on Pitting Corrosion and Inhibition Performance in CO_2 Corrosion of N80 Steel," *Corros. Sci.*, vol. 48, no. 10, pp. 3091–3108, 2006.

[48] X. Jiang, S. Nesic, B. Kinsella, B. Brown, and D. Young, "Electrochemical Investigation of the Role of Cl^- on Localized Carbon Dioxide Corrosion Behavior of Mild Steel," *Corrosion*, vol. 69, no. 1, pp. 15-24, 2013.

[49] H. Fang, B. Brown, and S. Nesic, "Sodium Chloride Concentration Effects on General CO_2 Corrosion Mechanisms," *Corrosion*, vol. 69, no. 3, pp. 297–302, 2013.

[50] L. M. Tavares, E. M. da Costa, J. J. de O. Andrade, R. Hubler, and B. Huet, "Effect of Calcium Carbonate on Low Carbon Steel Corrosion Behavior in Saline CO_2 High Pressure Environments," *Appl. Surf. Sci.*, vol. 359, pp. 143–152, 2015.

[51] S. Gao, P. Jin, B. Brown, D. Young, S. Nesic, and M. Singer, "Corrosion Behavior of Mild Steel in Sour Environments at Elevated Temperatures," *Corrosion*, vol. 73, no. 8, pp. 915–926, 2017.

[52] S. Bekhrad and M. Javidi, "CO_2 Corrosion Behavior of Calcite-Covered API 5L X52 Carbon Steel in Aqueous Solutions," *J. Mater. Eng. Perform.*, vol. 28, pp. 1057–1066, 2019.

[53] E. Ghanbari and R. S. Lillard, "The Influence of $CaCO_3$ Scale Formation on AC Corrosion Rates of Pipeline Steel Under Cathodic Protection," *Corrosion*, vol. 74, no. 5, pp. 551–565, 2017.

[54] E. Eriksrud and T. Sontvedt, "Effect of Flow on CO_2 Corrosion Rates in Real and Synthetic Formation Waters," *Proc. Symp. CO2 Corros. Oil Gas Ind. NACE*, vol. 1, pp. 20–38, 1984.

[55] Y. Zhang, H. Shaw, R. Farquhar, and R. Dawe, "The Kinetics of Carbonate Scaling-Application for the Prediction of Downhole Carbonate Scaling," *J. Pet. Sci. Eng.*, vol. 29, no. 2, pp. 85–95, 2001.

[56] N. Spanos and P. G. Koutsoukos, "Kinetics of Precipitation of Calcium Carbonate in Alkaline pH at Constant Supersaturation. Spontaneous and Seeded Growth," *J. Phys. Chem. B*, vol. 102, no. 34, pp. 6679–6684, 1998.

[57] S. Nesic, "Effects of Multiphase Flow on Internal CO_2 Corrosion of Mild Steel Pipelines," *Energy Fuels*, vol. 26, no. 7, pp. 4098–4111, 2012.

[58] ASTM G31-72, "Guide for Laboratory Immersion Corrosion Testing of Metals," ASTM International, 2004.

[59] W. B. Fortune and M. G. Mellon, “Determination of iron with o-phenanthroline: a spectrophotometric study,” *Ind. Eng. Chem. Anal. Ed.*, vol. 10, no. 2, pp. 60–64, 1938.

[60] X. Zhong, B. Brown, W. Li, S. Nesic, and M. Singer, “How to Maintain a Stable Solution Chemistry when Simulating CO_2 Corrosion in a Small Volume Laboratory System,” in *NACE International*, Paper No. 7780, 2016.

[61] R. S. Houk, “Mass spectrometry of inductively coupled plasmas,” *Anal. Chem.*, vol. 58, no. 1, pp. 97-105, 1986.

[62] D. C. Silverman, “The Rotating Cylinder Electrode for Examining Velocity-Sensitive Corrosion-A Review,” *Corrosion*, vol. 60, no. 11, pp. 1003–1023, 2004.

[63] H. Saraç, M. A. Patrick, and A. A. Wragg, “Physical properties of the ternary electrolyte potassium ferri-ferrocyanide in aqueous sodium hydroxide solution in the range 10–90 C,” *J. Appl. Electrochem.*, vol. 23, no. 1, pp. 51–55, 1993.

[64] M. Eisenberg, C. W. Tobias, and C. R. Wilke, “Ionic mass transfer and concentration polarization at rotating electrodes,” *J. Electrochem. Soc.*, vol. 101, no. 6, pp. 306–320, 1954.

[65] F. P. Berger and F.-L. Hau, “Mass transfer in turbulent pipe flow measured by the electrochemical method,” *Int. J. Heat Mass Transf.*, vol. 20, no. 11, pp. 1185–1194, 1977.

[66] D. C. Silverman, “Technical Note: On Estimating Conditions for Simulating Velocity-Sensitive Corrosion in the Rotating Cylinder Electrode,” *Corrosion*, vol. 55, no. 12, pp. 1115–1118, 1999.

[67] M. Stern and A. L. Geary, “Electrochemical Polarization I. A Theoretical Analysis of the Shape of Polarization Curves,” *J. Electrochem. Soc.*, vol. 104, no. 1, pp. 56-63, 1957.

[68] Y. Yang, B. Brown, M. E. Gennaro, and B. Molinas, “Mechanical Strength and Removal of a Protective Iron Carbonate Layer Formed on Mild Steel in CO_2 Corrosion,” in *NACE International*, Paper No. 10383, 2010.

[69] F. Madani Sani, B. Brown, Z. Belarbi, and S. Nesic, “An Experimental Investigation on the Effect of Salt Concentration on Uniform CO_2 Corrosion,” in *NACE International*, Paper No.13026, 2019.

[70] M. Di Bonaventura, B. Brown, M. Singer, and S. Nesic, “Effect of Flow and Steel Microstructure on the Formation of Iron Carbonate,” in *NACE International*, Paper No. 11179, 2018.

[71] ASTM G1, “Standard Practice for Preparing, Cleaning, and Evaluating Corrosion Test.” ASTM International, 2011.

[72] M. G. Fontana, *Corrosion Engineering*, 3rd edition. New York: McGraw-Hill Book Company, 1985.

[73] Z. Ma, Y. Yang, B. Brown, S. Nesic, and M. Singer, “Investigation of precipitation kinetics of $FeCO_3$ by EQCM,” *Corros. Sci.*, vol. 141, pp. 195–202, 2018.

[74] S. Ieamsupapong, B. Brown, M. Singer, and S. Nesic, “Effect of Solution pH on Corrosion Product Layer Formation in a Controlled Water Chemistry System,” in *NACE International*, Paper No. 9160, 2017.

[75] S. Nesic, “Carbon Dioxide Corrosion of Mild Steel,” in *Uhlig’s Corrosion Handbook*, vol. 51, John Wiley and Sons, pp. 229–245, 2011.

[76] F. Farelas, B. Brown, S. Nesic, and others, “Iron carbide and its influence on the formation of protective iron carbonate in CO_2 corrosion of mild steel,” in *NACE International*, Paper No. 2291, 2013.

[77] K. Videm, “The influence of pH and concentration of bicarbonate and ferrous ions on the CO_2 corrosion of carbon steels,” in *NACE International*, Paper No. 83, 1993.

[78] J. Han, S. Nesic, Y. Yang, and B. Brown, “Spontaneous passivation observations during scale formation on mild steel in CO_2 brines,” *Electrochimica Acta*, vol. 56, no. 15, pp. 5396–5404, 2011.

[79] J. M. Olivo, B. Brown, S. Nesic, and others, “Modeling of Corrosion Mechanisms in the Presence of Quaternary Ammonium Chloride and Imidazoline Corrosion Inhibitors,” in *NACE*, Paper No. 7406, 2016.

[80] T. Zoltai and J. H. Stout, *Mineralogy: concepts and principles*. Burgess Pub. Co., 1984.

[81] H. A. Alsaiari, A. Kan, M. Tomson, and others, “Effect of Calcium and Iron (II) Ions on the Precipitation of Calcium Carbonate and Ferrous Carbonate,” *SPE J.*, vol. 15, no. 02, pp. 294–300, 2010.

[82] E. T. Urbansky, “Perchlorate Chemistry: Implications for Analysis and Remediation,” *Bioremediation J.*, vol. 2, no. 2, pp. 81–95, 1998.

[83] H. Y. Ma, C. Yang, G. Y. Li, W. J. Guo, S. H. Chen, and J. L. Luo, “Influence of Nitrate and Chloride Ions on the Corrosion of Iron,” *Corrosion*, vol. 59, no. 12, pp. 1112–1119, 2003.

[84] Z. Xia, K.-C. Chou, and Z. Szklarska-Smialowska, “Pitting Corrosion of Carbon Steel in CO2-Containing NaCl Brine,” *Corrosion*, vol. 45, no. 8, pp. 636–642, 1989.

[85] M. Ergun and A. Y. Turan, “Pitting potential and protection potential of carbon steel for chloride ion and the effectiveness of different inhibiting anions,” *Corros. Sci.*, vol. 32, no. 10, pp. 1137–1142, 1991.

[86] N. G. Smart and J. O. Bockris, “Effect of Water Activity on Corrosion,” *Corrosion*, vol. 48, no. 4, pp. 277–280, 1992.

[87] E. McCafferty and N. Hackerman, “Kinetics of Iron Corrosion in Concentrated Acidic Chloride Solutions,” *J. Electrochem. Soc.*, vol. 119, no. 8, pp. 999–1009, 1972.

[88] N. A. Darwish, F. Hilbert, W. J. Lorenz, and H. Rosswag, "The influence of chloride ions on the kinetics of iron dissolution," *Electrochimica Acta*, vol. 18, no. 6, pp. 421–425, 1973.

[89] Z. Duan and D. Li, "Coupled phase and aqueous species equilibrium of the H_2O–CO_2–NaCl–$CaCO_2$ system from 0 to 250 °C, 1 to 1000 bar with NaCl concentrations up to saturation of halite," *Geochim. Cosmochim. Acta*, vol. 72, no. 20, pp. 5128–5145, 2008.

[90] J. L. Crolet, N. Thevenot, and S. Nesic, "Role of conductive corrosion products in the protectiveness of corrosion layers," *Corrosion*, vol. 54, no. 3, pp. 194–203, 1998.

[91] C. A. Palacios and J. R. Shadley, "Characteristics of corrosion scales on steels in a CO_2-saturated NaCl brine," *Corrosion*, vol. 47, no. 2, pp. 122–127, 1991.

[92] S. Ieamsupapong, "Mechanisms of Iron Carbonate Formation on Mild Steel in Controlled Water Chemistry Conditions," PhD Dissertation, Ohio University, 2016.

[93] R. Barker, D. Burkle, T. Charpentier, H. Thompson, and A. Neville, "A review of iron carbonate ($FeCO_3$) formation in the oil and gas industry," *Corros. Sci.*, vol. 142, pp. 312–341, 2018.

[94] S.-H. Lin and S. C. Dexter, "Effects of Temperature and Magnesium Ions on Calcareous Deposition," *Corrosion*, vol. 44, no. 9, pp. 615–622, . 1988.

[95] M. Hänchen, V. Prigiobbe, R. Baciocchi, and M. Mazzotti, "Precipitation in the Mg-carbonate system-effects of temperature and CO_2 pressure," *Chem. Eng. Sci.*, vol. 63, no. 4, pp. 1012–1028, 2008.

[96] D. C. Golden, D. W. Ming, C. S. Schwandt, R. V. Morris, S. V. Yang, and G. E. Lofgren, "An experimental study on kinetically-driven precipitation of calcium-magnesium-iron carbonates from solution: Implications for the low-temperature formation of carbonates in martian meteorite Allan Hills 84001," *Meteorit. Planet. Sci.*, vol. 35, no. 3, pp. 457–465, 2000.

[97] A. R. West, *Solid state chemistry and its applications*. John Wiley and Sons, 2014.

[98] P. M. Davidson, G. H. Symmes, B. A. Cohen, R. J. Reeder, and D. H. Lindsley, "Synthesis of the new compound $CaFe(CO_3)_2$ and experimental constraints on the $(Ca,Fe)CO_3$ join," *Geochim. Cosmochim. Acta*, vol. 57, no. 23–24, pp. 5105–5109, 1993.

[99] M. E. Orazem and B. Tribollet, *Electrochemical Impedance Spectroscopy*. John Wiley and Sons, 2017.

[100] Z. Zeng, R. S. Lillard, and H. Cong, "Effect of salt concentration on the corrosion behavior of carbon steel in CO_2 environment," *Corrosion*, vol. 72, no. 6, pp. 805–823, 2016.

[101] G. A. Zhang and Y. F. Cheng, "Corrosion of X65 steel in CO_2-saturated oilfield formation water in the absence and presence of acetic acid," *Corros. Sci.*, vol. 51, no. 8, pp. 1589–1595, 2009.

[102] G. A. Zhang and Y. F. Cheng, "On the fundamentals of electrochemical corrosion of X65 steel in CO2-containing formation water in the presence of acetic acid in petroleum production," *Corros. Sci.*, vol. 51, no. 1, pp. 87–94, 2009.

[103] P. Li, T. C. Tan, and J. Y. Lee, "Impedance spectra of the anodic dissolution of mild steel in sulfuric acid," *Corros. Sci.*, vol. 38, no. 11, pp. 1935–1955, 1996.

[104] F. Farelas, M. Galicia, B. Brown, S. Nesic, and H. Castaneda, "Evolution of dissolution processes at the interface of carbon steel corroding in a CO_2 environment studied by EIS," *Corros. Sci.*, vol. 52, no. 2, pp. 509–517, 2010.

[105] D. K. Nordstrom *et al.*, "Revised Chemical Equilibrium Data for Major Water—Mineral Reactions and Their Limitations," in *Chemical Modeling of Aqueous Systems II*, vol. 416, 0 vols., American Chemical Society, pp. 398–413, 1990.

APPENDIX I: XRD DATA PROCESSING

An X-ray diffractometer was used for identification of the phases present on the steel substrate along with determination of the molar fraction of Ca into the lattice of solid solutions ($Fe_xCa_yCO_3$, x+y=1). Figure 101 illustrates the Bravais lattice corresponding to the hexagonal crystal structure of $FeCO_3$, $CaCO_3$, and $Fe_xCa_yCO_3$. As mentioned in the introduction section, such carbonate crystals are isostructural and categorized as “calcite-type”.

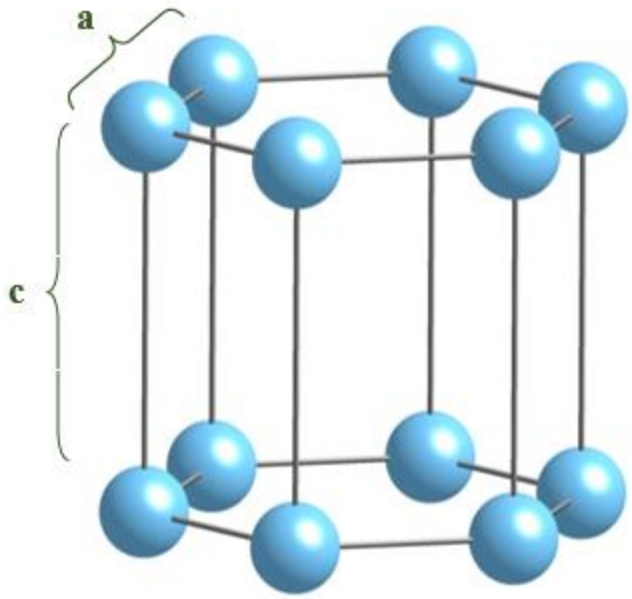

Figure 101. Bravais lattice of a hexagonal unit cell for $FeCO_3$, $CaCO_3$, and $Fe_xCa_yCO_3$ (x+y=1) [42]

The unit cell parameters shown in Figure 101 (“a” and “c”) can be calculated using equation (44). In which, “d” (d-spacing) is calculated from Bragg’s law expressed

in equation (45) and *h*, *k*, and *l* are Miller indices corresponding to lattice planes [97]. The mole fraction of Ca in the $Fe_xCa_yCO_3$ was determined based on the d-spacing of the main peak for $FeCO_3$ located at the (104) inter-planar d-spacing.

$$\frac{1}{d^2} = \frac{4}{3}\left(\frac{h^2+hk+k^2}{a^2}\right) + \frac{l^2}{c^2} \qquad \text{Equation 44}$$

$$d = \frac{n\lambda}{2sin\theta} \qquad \text{Equation 45}$$

Davidson, *et al.,* [98] and Chai*, et al.,* [12] synthesized $Fe_xCa_yCO_3$ and proposed a linear behavior for incorporation of Ca in the mixed solid solution structure *versus* the unit cell parameters (either "a" or "c"). Using this methodology, mole fraction of Ca ("y") in the solid solution can be found from the plotted "y" value *versus* either of the unit cell parameters ("a" or "c"). The plotted "y" values *versus* unit cell parameter "c" for an $FeCO_3$ (brown triangle) and $CaCO_3$ phase (red triangle) is shown in Figure 102, extracted from the literature data [12]. Indeed, the calculated "c" for the current experimental condition and the corresponding "y" values are indicated on Figure 102 for experiments conducted with $CaCO_3$-saturated solution at different $[Ca^{2+}]$ and pH. The accuracy of the calculated data (green circles) are acceptable since they are in accordance with the literature data (blue squares).

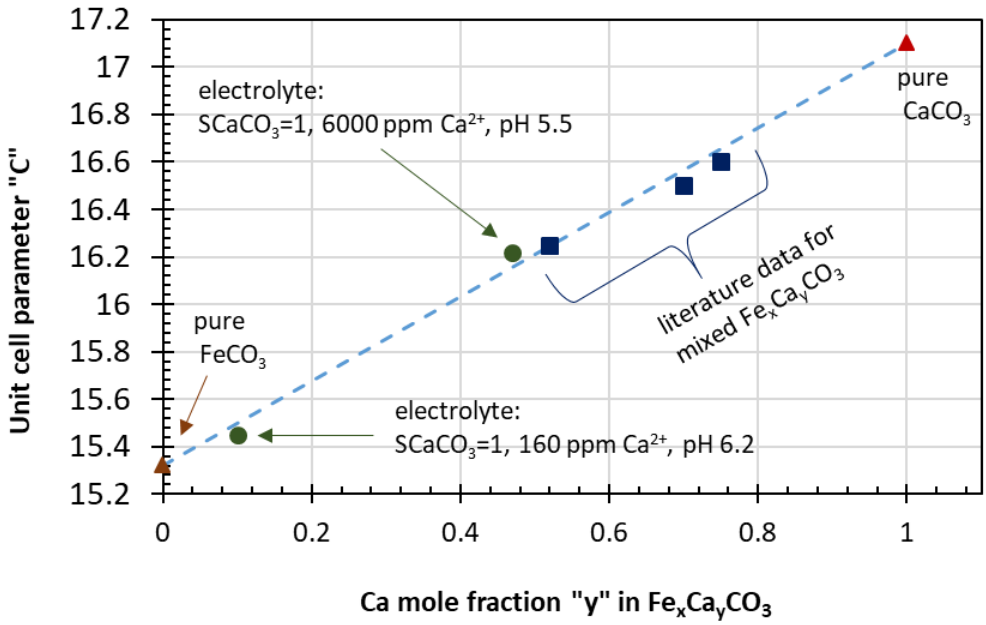

Figure 102. Unit cell parameter "c" versus the Ca mole fraction in the lattice of mixed $Fe_xCa_yCO_3$ for the $CaCO_3$-saturated solutions with 160 and 6000 ppm dissolved Ca^{2+} at pH 6.2 and 5.5, respectively

APPENDIX II: EFFECT OF NON-IDEALITY ON $FeCO_3$ SATURATION CALCULATION

The non-ideality of the solution should be considered when calculating S_{FeCO_3}. However, the highest ionic strength used for the current research was 0.6 M that would influence the solution to deviate slightly from an ideal behavior. Therefore, it was decided to use a $K_{sp,FeCO_3}$ proposed by Sun, *et al.*, for calculation of S_{FeCO_3} and generating relevant graphs, e.g., Figure 37, as many corrosion literature has used this method. This correlation, Equation 15, is a function of temperature and ionic strength as expressed in section 2.1.2 [36]. The ionic strength term in Equation 15 is aimed to cover the non-ideality of the solution. Therefore, concentration of ferrous ions (Fe^{2+}) and carbonate ions (CO_3^{2-}) were used, instead of activity of such ions, for calculation of S_{FeCO_3} as shown Equation 17.

In this appendix, the effect of non-ideality is considered in the solution water chemistry to show how much it influences the S_{FeCO_3} calculation in the experimental conditions throughout this research. Therefore, unlike, Equation 17, activity of ferrous ions ($a_{Fe^{2+}}$) and activity of carbonate ions ($a_{CO_3^{2-}}$) were used as shown in Equation 46. For calculation of $K_{sp,FeCO_3}$, a model proposed by Nordstrom, *et al.*, was used [105] which is only temperature dependent as shown in Equation 47.

$$S_{FeCO_3} = \frac{a_{Fe^{2+}} * a_{CO_3^{2-}}}{K_{sp,FeCO_3}} \qquad \text{Equation 46}$$

$$logK_{sp,FeCO_3} = -59.2385 - 0.041377 * T_k - \frac{2.1963}{T_k} + 24.5724 * LogT_k$$ Equation 47

In order to calculate activity of relevant ions in Equation 46, activity coefficients are needed based on Equation 13 as explained in section 2.1.2.

The relevant activity coefficients were calculated using semi-empirical models described in Table 14 based on the validity of the model in different ionic strengths.

Table 14. List of semi-empirical activity coefficient model and their validity depending on ionic strength of solution

Model	**Equation**	**Validity** (ionic strength range)
Debye-Huckel	$log\,\gamma_i = -Az_i^2\sqrt{I}$	$I < 10^{-2.3}\ M$
Extended Debye-Huckel	$log\,\gamma_i = -Az_i^2(\frac{\sqrt{I}}{1+\mathrm{Ba_i}\sqrt{I}})$	$I < 0.1\ M$
Davies	$log\,\gamma_i = -Az_i^2(\frac{\sqrt{I}}{1+\sqrt{I}} - 0.3 * I\ )$	$I \leq 0.5\ M$
Truesdell-Jones (WATEQ Debye-Huckel)	$log\,\gamma_i = -Az_i^2(\frac{\sqrt{I}}{1+\mathrm{Ba_i^0}\sqrt{I}} + \mathrm{b_i} * I\ )$	$I < 1\ M$
$A = 1.82 \times 10^6(\varepsilon T)^{-3/2}$ $B = 50.3 \times 10^6(\varepsilon T)^{-1/2}$		
For standard conditions (25°C) $A = 0.5085\ \mathrm{M}^{-1/2}$ $B = 3.281\ \mathrm{M}^{-1/2}\ nm^{-1}$		

By considering non-ideality of solution, new graphs are generated and compared with the previous approach. The two main pHs (6.2 and 5.5) and ionic strengths (0.18 M and 0.6 M) were used throughout this manuscript are utilized to compare saturation level of iron carbonate (S_{FeCO_3}) at different ferrous ion concentration ([Fe^{2+}]). Considering Table 14, Davies activity coefficient were used for 0.18 M ionic strength and Truesdell-Jones activity coefficient were used for 0.6 M ionic strength. Consequently, Equation 17 and Equation 46 employed to calculate S_{FeCO_3}, using concentration and activity of relevant ions, respectively. Additionally, the Geochemist's Workbench® simulation package in conjunction with PHREEQC database was used to cross-check the water chemistry calculations. Figure 103 and Figure 104 show comparison of the results of the two approaches (Equation 17 and Equation 46) along with GWB simulation results at different pHs and ionic strengths. Based on these graphs, a lower S_{FeCO_3} was achieved when considering non-ideality of the solution (using Equation 46 and GWB package) for both simulation scenarios. However, the results are in the same order of magnitude in these experimental conditions. It should be mentioned that the S_{FeCO_3} graphs generated throughout this manuscript using Equation 17 would not influence the interpretation of the results nor the final conclusions. However, considering non-ideality of solution gives a more accurate graph for S_{FeCO_3} over the course of experiments. It is worth mentioning that using different activity models (e.g., pitzer *versus* phreeqc) would probably affect the simulation results.

The maximum [Fe^{2+}] generated during experiments at pH 6.2 and 5.5 was ~14-18 ppm and 250-350 ppm, respectively. As mentioned earlier, a considerable body of literature have used Sun, *et al.*, model for calculation of S_{FeCO_3}.

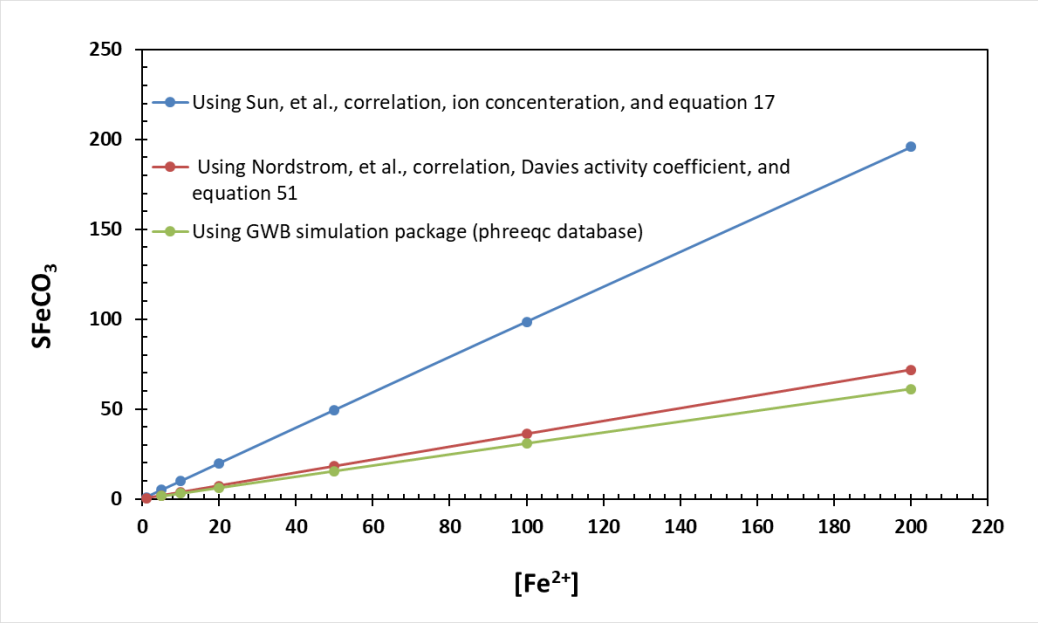

Figure 103. Effect of non-ideality: comparison of iron carbonate saturation (S_{FeCO_3}) calculation using Equation 17, Equation 51, and GWB simulation package at 80°C, pCO_2 0.53 bar, bulk solution pH 6.2, 0.18 M ionic strength

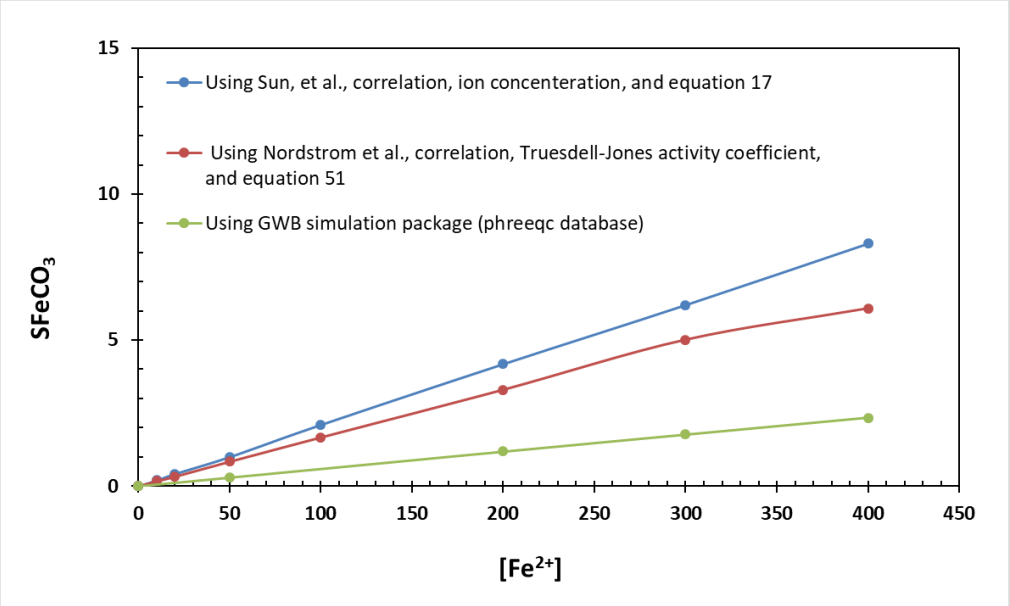

Figure 104. Effect of non-ideality: comparison of iron carbonate saturation (S_{FeCO_3}) calculation using Equation 17, Equation 51, and GWB simulation at 80°C, pCO_2 0.53 bar, bulk solution pH 5.5, 0.60 M ionic strength

During this research, for the experiments with presence of Ca^{2+} ion (Chapter 6) and Mg^{2+} ion (Chapter 7), the solution was saturated with respect to $CaCO_3$ ($S_{CaCO_3} = 1$) and $MgCO_3$ ($S_{MgCO_3} = 1$) over the course of experiment. However, in Chapter 8, with simultaneous presence of Ca^{2+} and Mg^{2+}, the solution was saturated with respect to $CaCO_3$ ($S_{CaCO_3} = 1$) and the initial saturation level with respect to $MgCO_3$ was ~0.14. The saturation level of $MgCO_3$ was calculated considering the non-ideality of solution by using Table 14. Additionally, the water chemistry simulation by GWB and phreeqc activity model showed similar saturation level for $MgCO_3$ at the abovementioned condition.

APPENDIX III: EIS DATA INTERPRETATION

As mentioned in the Section 5.3, EIS measurement (AC impedance) was performed before each LPR measurement to correct the LPR polarization resistance by deducting the solution resistance gained by the impedance signatures. Additionally, EIS data provided an insight into the evolution of corrosion mechanism occurring at the steel surface over long-term experiments. In general, EIS spectra were in accordance with the corrosion mechanism discussed in chapter 6 to 8 based on LPR, OCP, WL, and surface characterization. In this section, two examples of such EIS data are provided and interpreted for experiments conducted at pH 5.5 with and without presence of Ca^{2+} based on conditions provided in Table 7.

EIS data in the absence of Ca^{2+}:

Figure 105 shows LPR corrosion rate and OCP trend over time for a baseline experiment conducted at pH 5.5. A thorough explanation is provided in Section 6.1.2 regarding such graphs. However, it is provided here to facilitate interpretation of EIS data. Corrosion rate can be divided in three stages chronologically based on Figure 105 and the overall EIS spectra provided in Figure 106, Figure 107, and Figure 108 (Nyquist plots, and Bode diagrams, respectively):

1) Active corrosion rate up to approximately 30 hours of exposure (development of Fe_3C skeleton and adsorption of intermediate product).
2) Almost stable corrosion rate approximately from 30 to 60 hours of exposure (achievement of favorable water chemistry for $FeCO_3$ nucleation within Fe_3C pores compared to bulk solution).

3) Decreasing corrosion rate (pseudo-passivation region) approximately from 60 hours of exposure to the end of experiment (precipitation and further growth of $FeCO_3$).

Each of such corrosion periods are discussed separately based on EIS spectra.

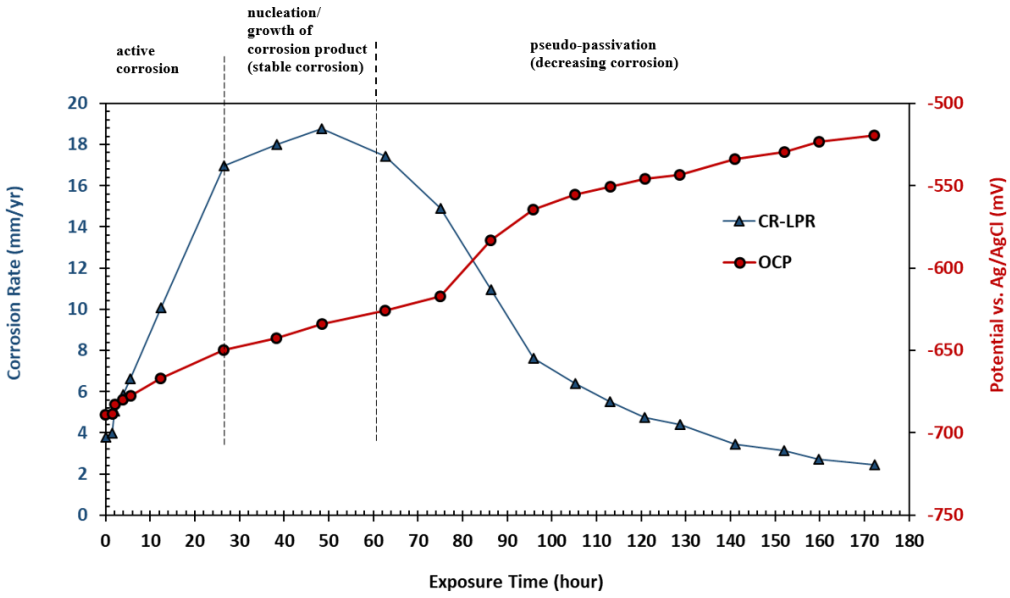

Figure 105. LPR corrosion rate and OCP variation over time for a baseline experiment ($S_{CaCO_3} = 0$) conducted at 80°C, pCO_2 0.53 bar, bulk solution pH 5.5, 0.60 M ionic strength, and 20 rpm

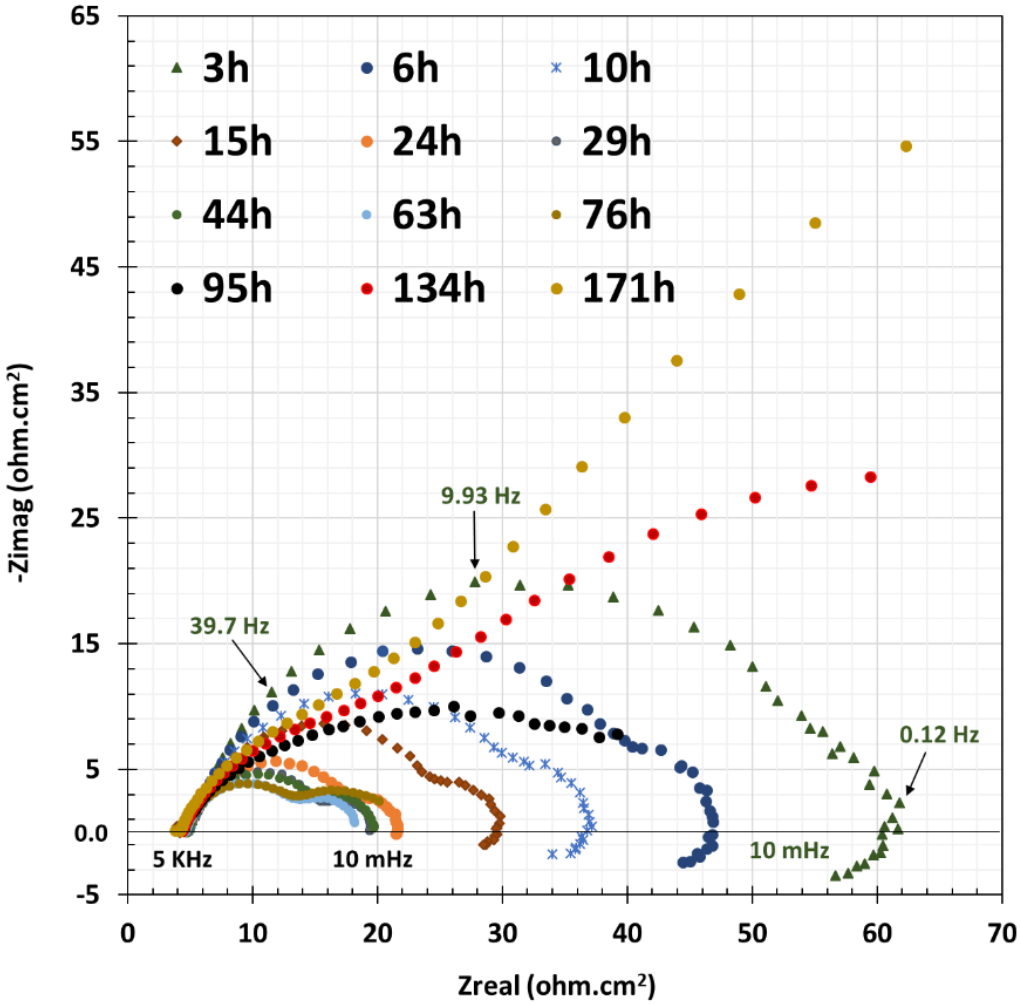

Figure 106. Nyquist plot. EIS spectra obtained over time from a baseline experiment ($S_{CaCO_3} = 0$) conducted at OCP at 80°C, pCO2 0.53 bar, bulk solution pH 5.5, 0.60 M ionic strength, and 20 rpm

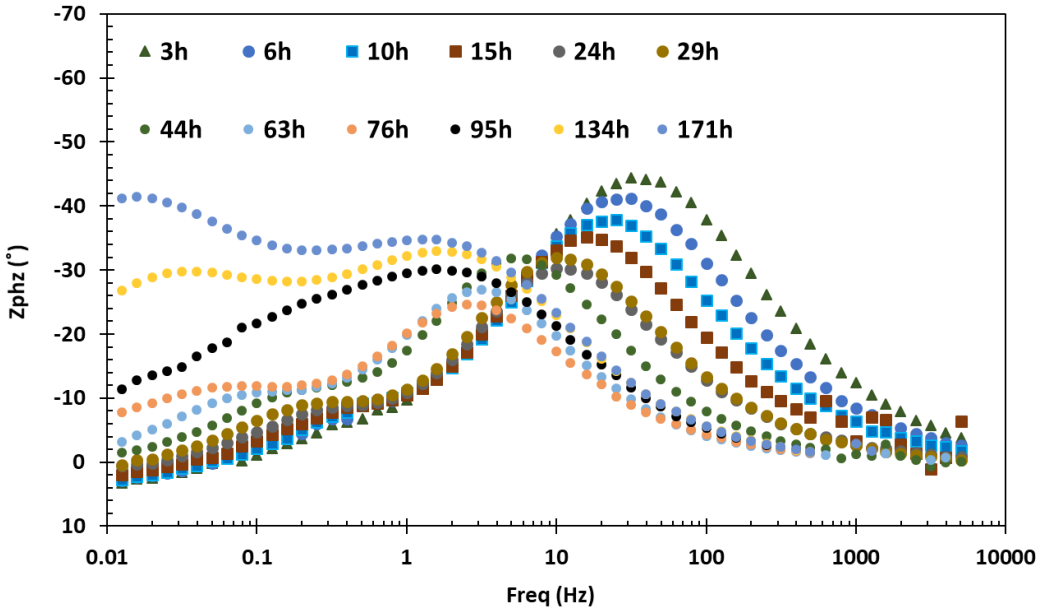

Figure 107. Phase angle. EIS spectra obtained over time from a baseline experiment ($S_{CaCO_3} = 0$) conducted at 80°C, pCO_2 0.53 bar, bulk solution pH 5.5, 0.60 M ionic strength, and 20 rpm

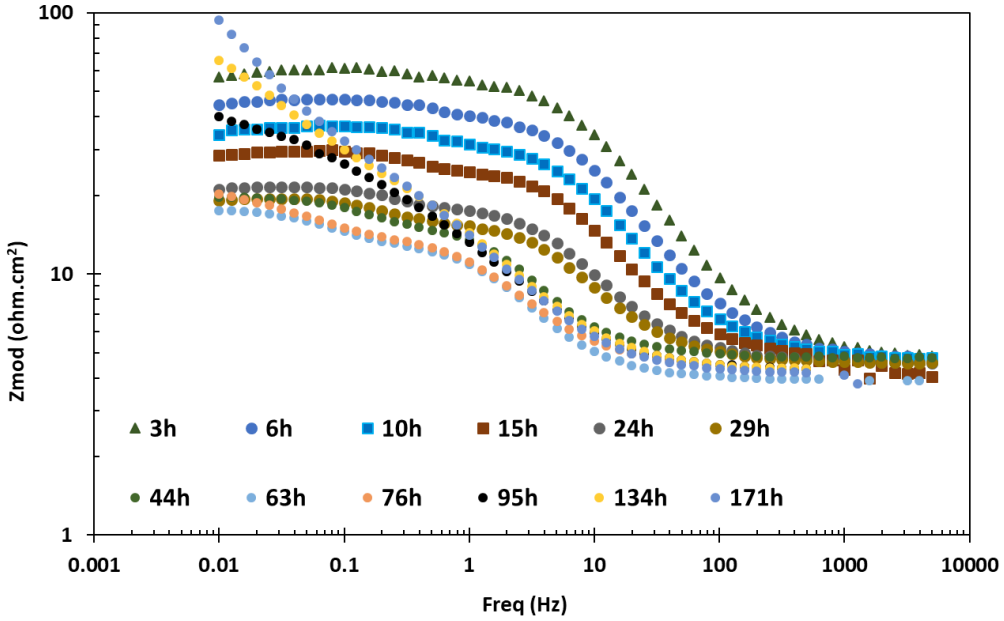

Figure 108. Impedance modulus. EIS spectra obtained over time from a baseline experiment ($S_{CaCO_3} = 0$) conducted at 80°C, pCO_2 0.53 bar, bulk solution pH 5.5, 0.60 M ionic strength, and 20 rpm

Active corrosion period:

Figure 109(a) shows the Nyquist plot evolution in the first 30 hours of exposure. Three time constants can be identified in this period. Two depressed capacitive semicircles in high (HF) and medium (MF) frequencies and an inductive loop in the low frequency (LF) were observed. Figure 109(b) shows normalization of the data provided in Figure 109(a) based on Equation (46) and Equation (47) to eliminate the effect of solution resistance [99].

$$Normalized\ Z_{real} = \frac{Z_{real} - R_{sol.}}{Z_{real,max} - R_{sol.}} \qquad \text{Equation 48}$$

$$Normalized\ -Z_{img.} = \frac{Z_{img.} - R_{sol.}}{Z_{img,max} - R_{sol.}} \qquad \text{Equation 49}$$

Although the magnitude of the overall impedance is different for Nyquist plots, the same corrosion mechanism is taking place in this period as the normalized graphs, presented in Figure 109(b), almost overlapped each other. In Figure 109(a), the capacitive semicircle in HF can be related to the resistance of charge-transfer reactions and it is inversely proportional to the corrosion rate [100]. The second capacitive semicircle in MF is related to development of Fe_3C skeleton which is left behind due to the preferential corrosion of α-Fe phase. The shape of such semicircles is more recognizable with respect to time since more Fe_3C is exposing due to active corrosion in this period. Indeed, the size of both semicircles are decreasing over time and this is reflected in an increasing corrosion rate as can be seen by LPR data in Figure 105.

The presence of an inductive loop in CO_2 corrosion environment is usually associated with an adsorbed intermediate product according to the following reactions [101, 102]:

$$Fe + H_2O \leftrightarrow FeOH_{ads} + H^+ + e^- \qquad \text{Equation 50}$$

$$FeOH_{ads} \rightarrow FeOH^+_{sol} + e^- \qquad \text{Equation 51}$$

$$FeOH^+_{sol} + H^+ \leftrightarrow Fe^{2+}_{sol} + H_2O \qquad \text{Equation 52}$$

As can be seen from Figure 109(a), the magnitude of the inductive loop is decreasing with time as more Fe_3C is exposed on the steel substrate resulted in accelerating hydrogen reduction. The development of semi-conductive Fe_3C provided more favorable site for the adsorption step [103]. As a result, reaction (48) is accelerated and no longer controls the corrosion mechanism [104]. This behavior is manifested in the disappearance of inductive loop over time.

Figure 109(c) and Figure 109(d) show the Bode phase and Bode modulus diagrams, respectively. The three time constants in the phase angle diagram are exhibited as peaks. The peak related to the capacitance of double layer at HF-MF is more obvious compare to the two other peaks. The effect of exposure time on the Bode diagrams can be seen form Figure 109(c) and Figure 109(d). In the impedance modulus diagrams, the HF indicate the solution resistance which are almost unchanged over time. However, the overall impedance in LF is decreasing over time (from 3 h to 29 h). Such data is in accordance with Nyquist plots.

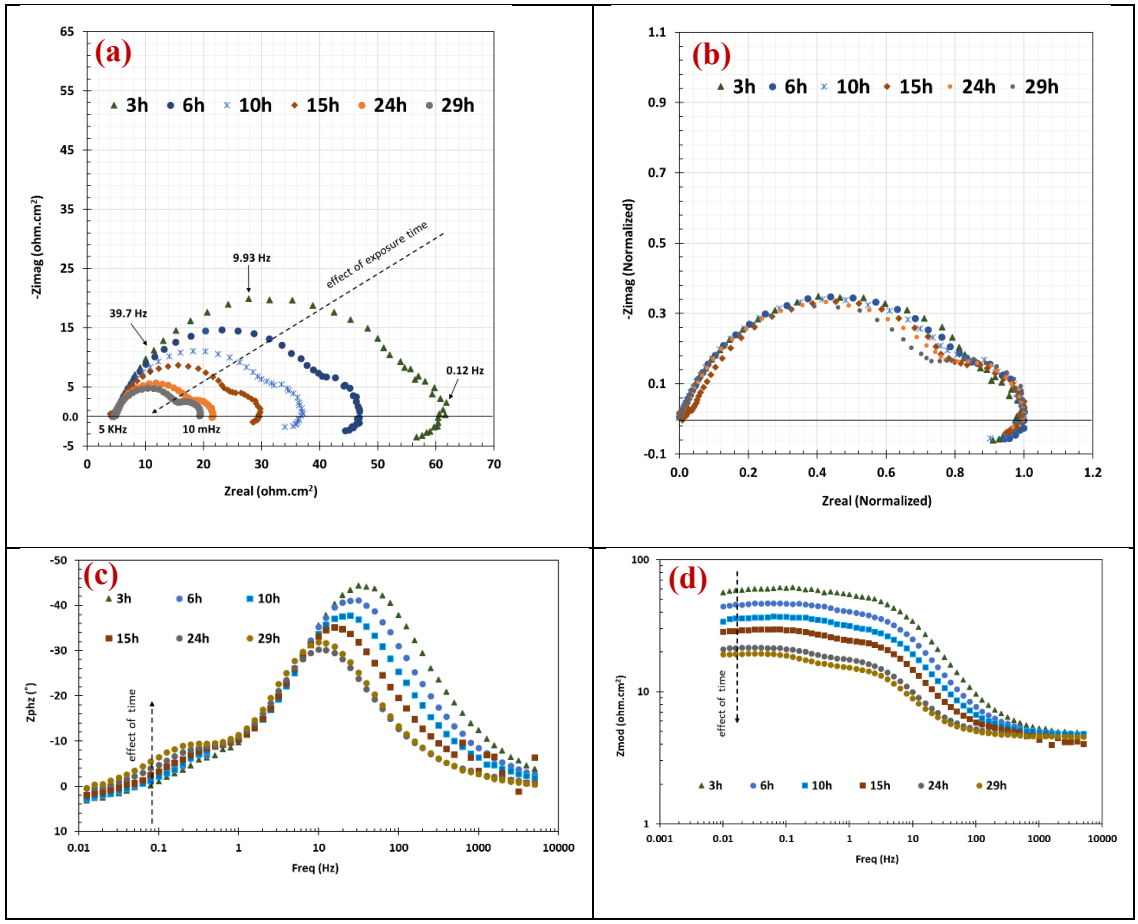

Figure 109. EIS results obtained from active corrosion period of a baseline experiment ($S_{CaCO_3} = 0$) conducted at 80°C, pCO_2 0.53 bar, bulk solution pH 5.5, 0.60 M ionic strength, and 20 rpm: (a) Nyquist plots (b) normalized Nyquist plots (c) phase angle, and (d) impedance modulus

Nucleation/growth period:

At this period, the corrosion rate is almost stable approximately from 30 to 60 hours of exposure. This behavior could be related to the higher pH achieved within the pores of Fe_3C at the steel surface compare to the bulk pH of 5.5. Therefore, the corrosion rate is not in active mode based on the water chemistry achieved at the steel surface (high pH). At this time period, the nucleation of $FeCO_3$ is thermodynamically possible

regardless to the bulk water chemistry as explained in section 6.2.1. However, there seems to be an induction time for precipitation of $FeCO_3$ at this period since the magnitude of the Nyquist plots, provided in Figure 110(a), are almost unchanged from 30 to 60 hours of exposure. Based on Figure 110(a), two time constants exhibited as depressed capacitive semicircles are obvious in such impedance signatures. As explained earlier, the inductive loop is not present at this corrosion period anymore where a considerable thickness of Fe_3C layer is already present (see cross-section specimens in Figure 41). Indeed, the normalization of Nyquist plots in Figure 110(b) indicates that such EIS data are identical and the same mechanism is taking place at this period. The two time constants observed in the Nyquist plots are also recognizable in the phase angle diagram and impedance modulus diagram in Figure 110(c) and Figure 110(d).

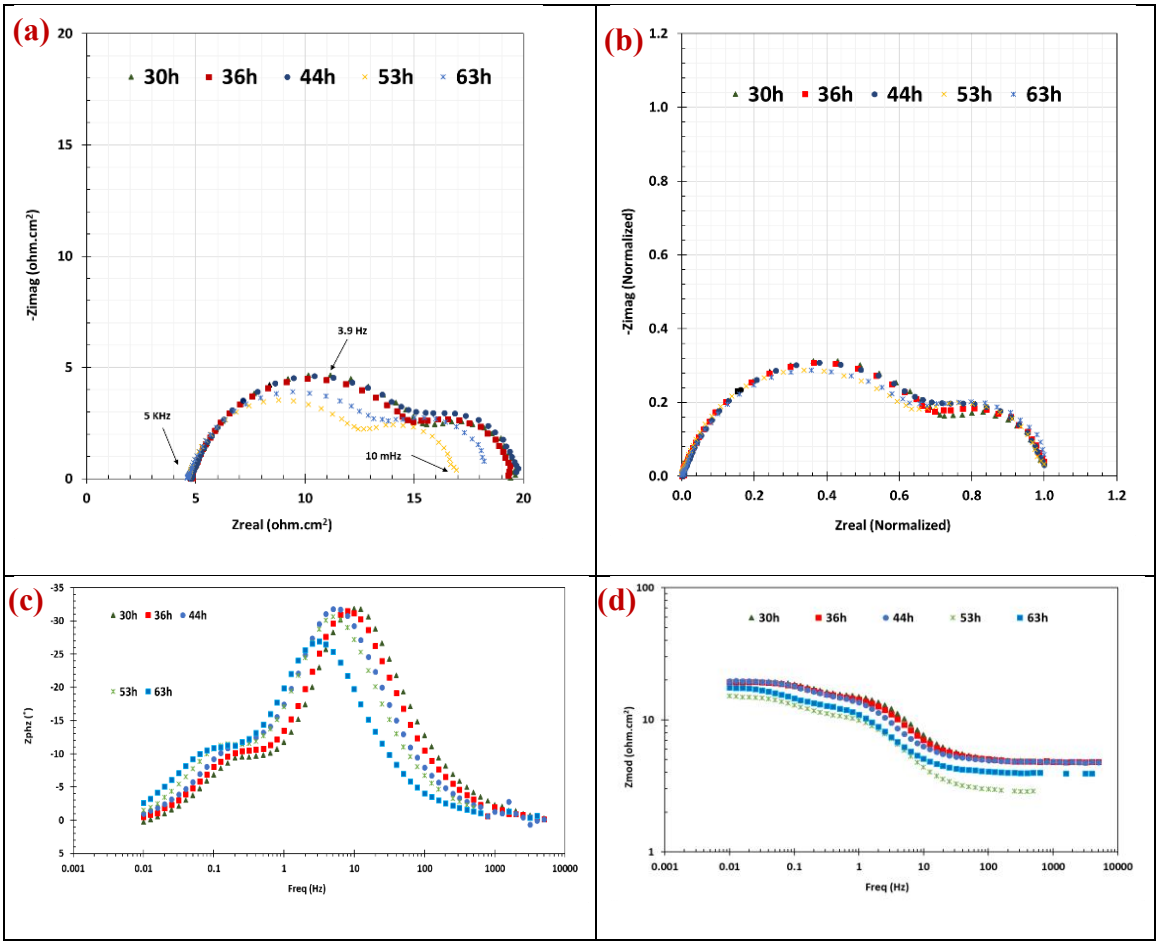

Figure 110. EIS results obtained from stable corrosion period of a baseline experiment ($S_{CaCO_3} = 0$) conducted at 80°C, pCO_2 0.53 bar, bulk solution pH 5.5, 0.60 M ionic strength, and 20 rpm: (a) Nyquist plots (b) normalized Nyquist plots (c) phase angle, and (d) impedance modulus

Pseudo-passivation period:

This period roughly lasts form 63 h of exposure to the end of experiment. At this stage, $FeCO_3$ grows over time and precipitates within the pores of Fe_3C offering a more protective corrosion product layer. Based on the Nyquist plots provided in Figure 111(a) and Figure 111(b) [zoomed in], the diameter of the second semicircle becomes significantly greater than the diameter of the first semicircle over time. This behavior is

due to precipitation of $FeCO_3$ and protecting the steel from further corrosion. The shape of the second semicircle is not complete in Figure 111(a); however, it could have been completed/captured if the EIS measurement had been conducted in a lower frequency (lower than 10 mHz). It should be noted that unlike the two previous corrosion periods, normalization of Nyquist data was not possible since the diameter of the uncompleted capacitive semicircles were unknown. The Bode diagrams provided in Figure 111(c) and Figure 111(d) clearly show presence of two slopes, indicating there are two time constants at this period. The effect of time on the EIS spectra is more obvious compared to the two previous corrosion periods because of the precipitation and growth of $FeCO_3$ and change of corrosion mechanism. Indeed, the overall Bode diagrams provided in Figure 111(c) and Figure 111(d) clearly show the transition of impedance signature after 63 h of exposure when $FeCO_3$ precipitation and growth happens. The trend of EIS spectra reverses at this moment, more obviously in LF (see data points from 76 h to the end of experiment in Figure 111(c) and Figure 111(d)).

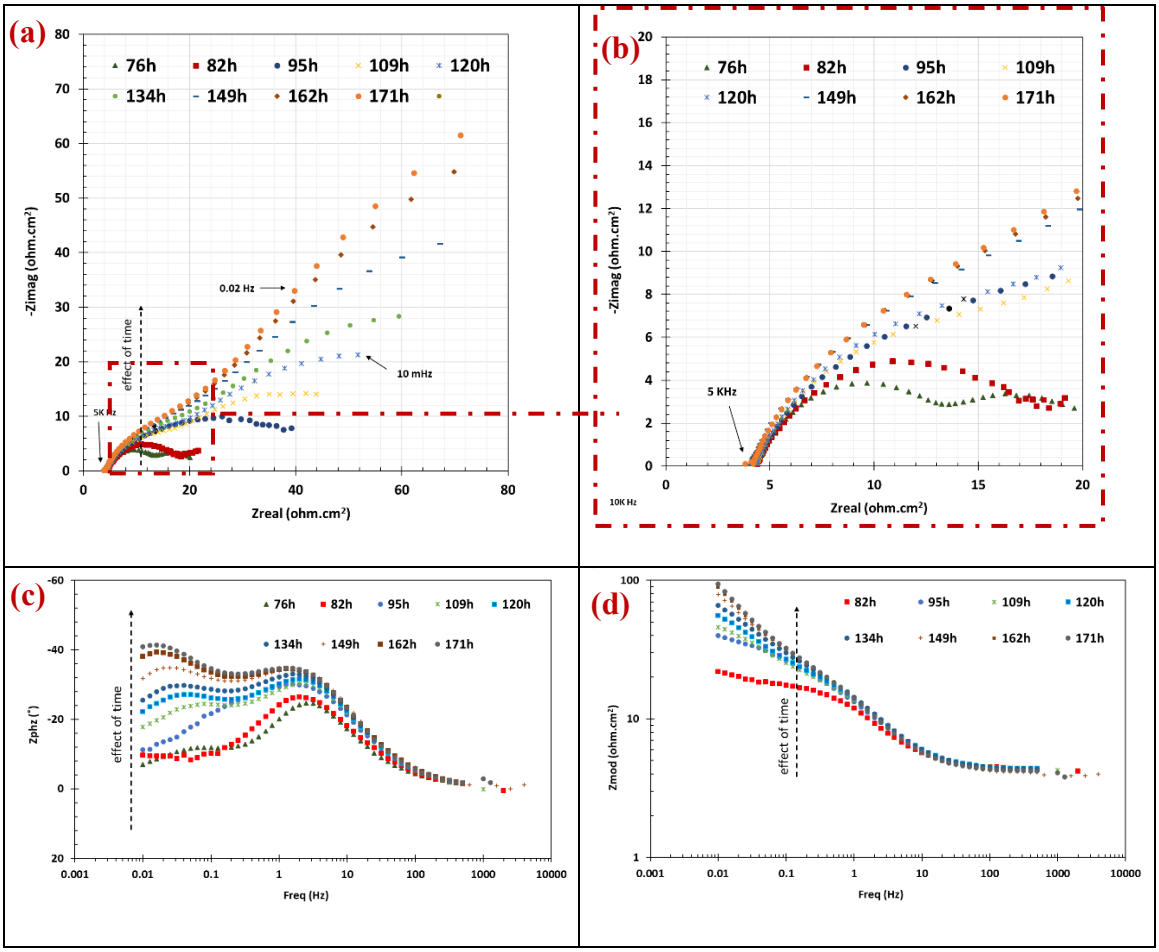

Figure 111. EIS results obtained from decreasing corrosion period of a baseline experiment ($S_{CaCO_3} = 0$) conducted at 80°C, pCO_2 0.53 bar, bulk solution pH 5.5, 0.60 M ionic strength, and 20 rpm: (a) and (b) Nyquist plots, (c) phase angle, and (d) impedance modulus

EIS data in the presence Ca^{2+}:

In this section, EIS measurements in the presence of 6000 ppm Ca^{2+} **($S_{CaCO_3} = 1$)** at pH 5.5 (based on experimental conditions obtainable in Table 7) are presented and interpreted. Figure 112 is provided for a better understanding of the effect of Ca^{2+} on the corrosion rate and open circuit potential over time. Similarly to the baseline experiments,

the EIS spectra can be chronologically categorized in three stages (active, nucleation/growth, and pseudo-passivation) based on Figure 112 and the overall EIS data provided in Figure 113 (Nyquist plots, and Bode diagrams). However, the timeline of corrosion periods, corrosion rate, and amplitude of the EIS signatures are different in the presence of 6000 ppm Ca^{2+} **(**$S_{CaCO_3} = 1$**)** when compared to the experiments without presence of Ca^{2+}. Such differences are also reflected in LPR and OCP trends (see Figure 105 and Figure 112). In presence of 6000 ppm Ca^{2+} **(**$S_{CaCO_3} = 1$**),** the active corrosion and nucleation/growth periods were shorter. Consequently, the decreasing corrosion period happened earlier compared to the experiment without presence of Ca^{2+}. Such EIS findings are in accordance with the mechanism described in Section 6.1.2.3. The EIS measurements in presence of Ca^{2+} related to the three corrosion stages are discussed separately.

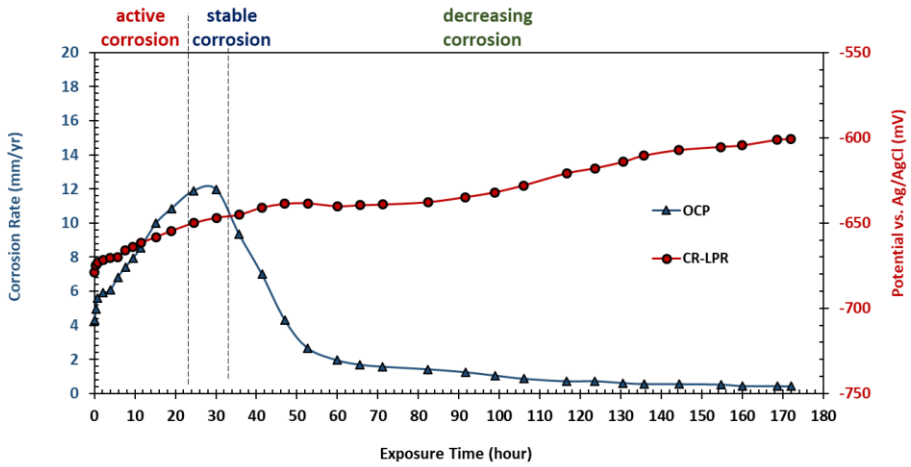

Figure 112. LPR corrosion rate and OCP variation over time for an experiment with presence of 6000 ppm Ca^{2+} ($S_{CaCO_3} = 1$) conducted at 80°C, pCO_2 0.53 bar, bulk solution pH 5.5, 0.60 M ionic strength, and 20 rpm

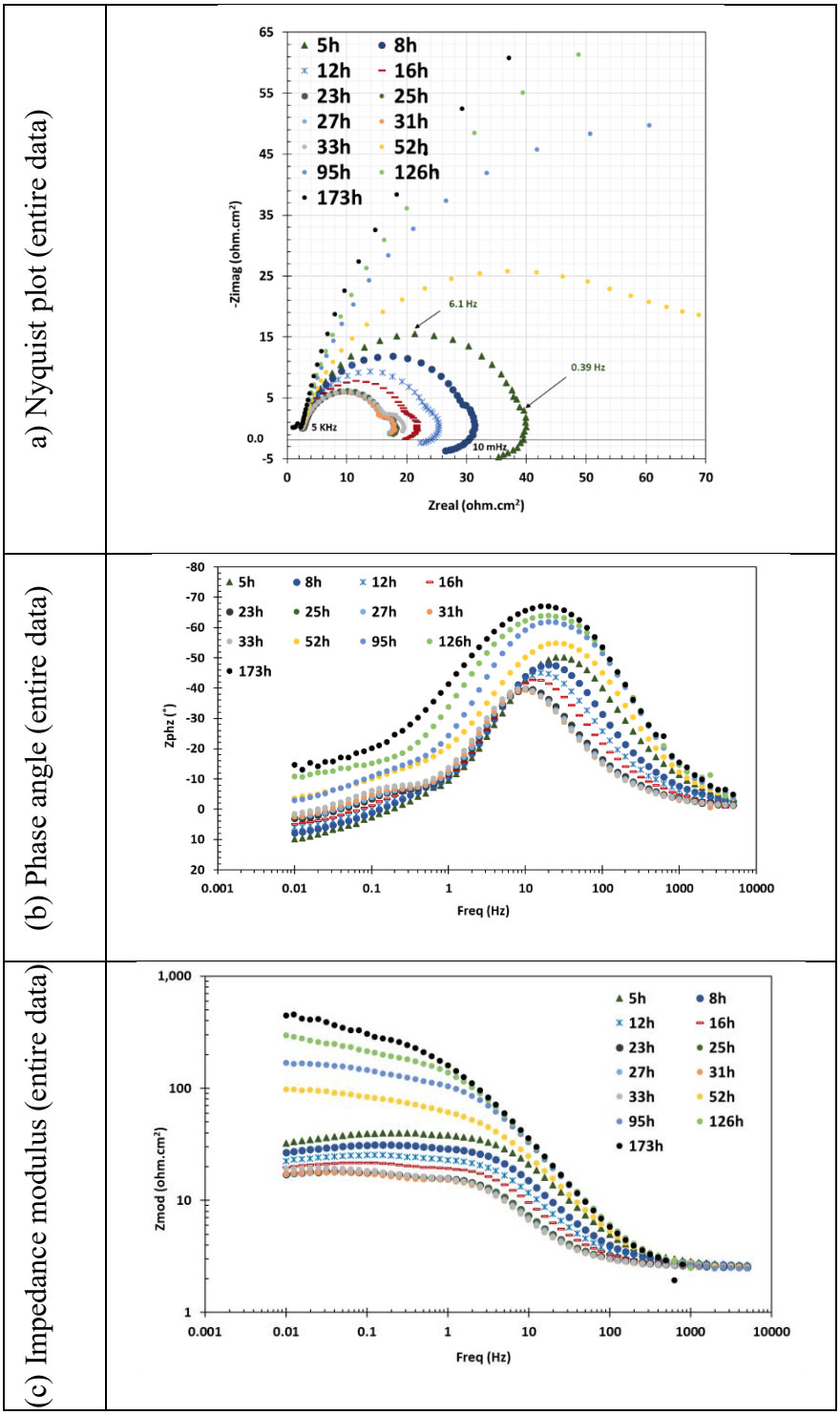

Figure 113. EIS spectra obtained over time from an experiment with presence of 6000 ppm Ca^{2+} ($S_{CaCO_3} = 1$) conducted at 80°C, pCO_2 0.53 bar, bulk solution pH 5.5, 0.60 M ionic strength, and 20 rpm: Nyquist plot (a), phase angle (b), and Impedance modulus (c)

Active corrosion period:

The EIS data related to the active corrosion period in presence of Ca^{2+} are presented in Figure 114. Similarly to the baseline experiment, the Nyquist plots provided in Figure 114(a) show the existence of two capacitive semicircles in MF-HF and one inductive loop in LF. However, the magnitude of impedance signatures and time period are different in presence of 6000 ppm Ca^{2+} compared to those of the baseline experiment. This is essentially related to nucleation and precipitation of $CaCO_3$ within Fe_3C pores which happened much earlier than $FeCO_3$ (for a thorough explanation please see section 6.1.2.3). This resulted in reduction of active surface area and corrosion rate.

The effect of exposure time on Nyquist plots and Bode diagrams is indicated on Figure 114. The same interpretations discussed for the baseline experiment are valid for EIS data provided in Figure 114(b, c, and d). Likewise, the inductive loops in the Nyquist plots are shrinking over time. However, they are not disappearing completely at the end of active corrosion period and their presence are extended into the nucleation/growth period. This could be attributed to the thinner Fe_3C layer achieved in presence of Ca^{2+}.

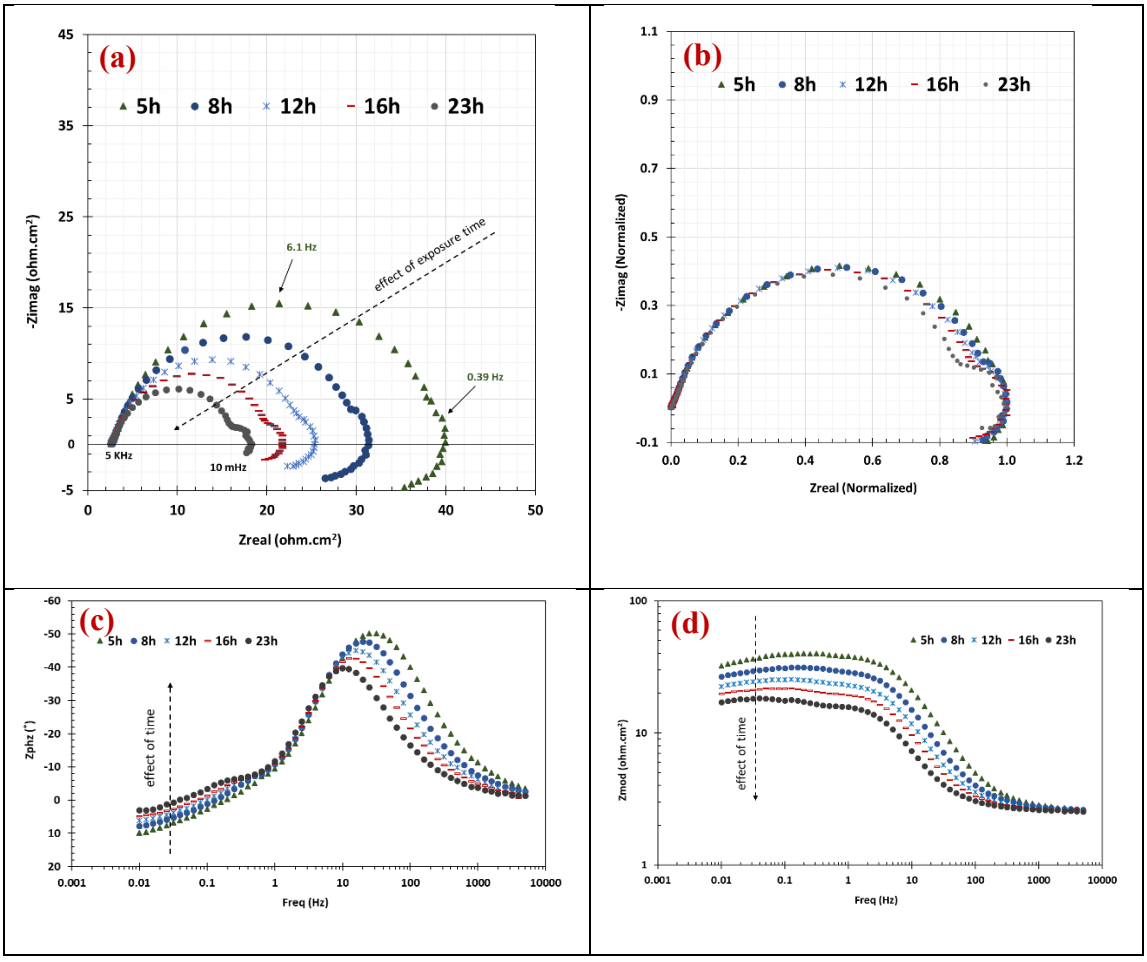

Figure 114. EIS results obtained from active corrosion period of an experiment with presence of 6000 ppm Ca^{2+} ($S_{CaCO_3} = 1$) conducted at 80°C, pCO_2 0.53 bar, bulk solution pH 5.5, 0.60 M ionic strength, and 20 rpm: (a) Nyquist plots (b) normalized Nyquist plots (c) phase angle, and (d) impedance modulus

Nucleation/growth period:

This nucleation/growth period in presence of Ca^{2+} approximately started from 25 h and ended at 31 h of exposure which is much shorter than the same period for the baseline experiment. The main reason is that precipitation of unprotective $CaCO_3$ acted as a mass transfer barrier for Fe^{2+} transport from the steel surface towards the bulk

solution and therefore $FeCO_3$ became supersaturated earlier than in the experiment without presence of $CaCO_3$. In general, in the presence of $Ca^{2+}/CaCO_3$, a smaller thickness of Fe_3C is required to achieve a favorable water chemistry for nucleation/precipitation of protective $FeCO_3$. In this corrosion period, the EIS spectra are almost identical as can be seen from Figure 115. As mentioned earlier, the inductive loops are weakly present at this period. However, they completely disappear in the pseudo-passivation period where precipitation of $FeCO_3$ starts resulting in a drop of corrosion rate. The presence of two slopes in HF-MF and one small slope in LF (related to the weak inductive loops) are obvious from phase angle and modulus diagram in Figure 115(c) and Figure 115(c), respectively.

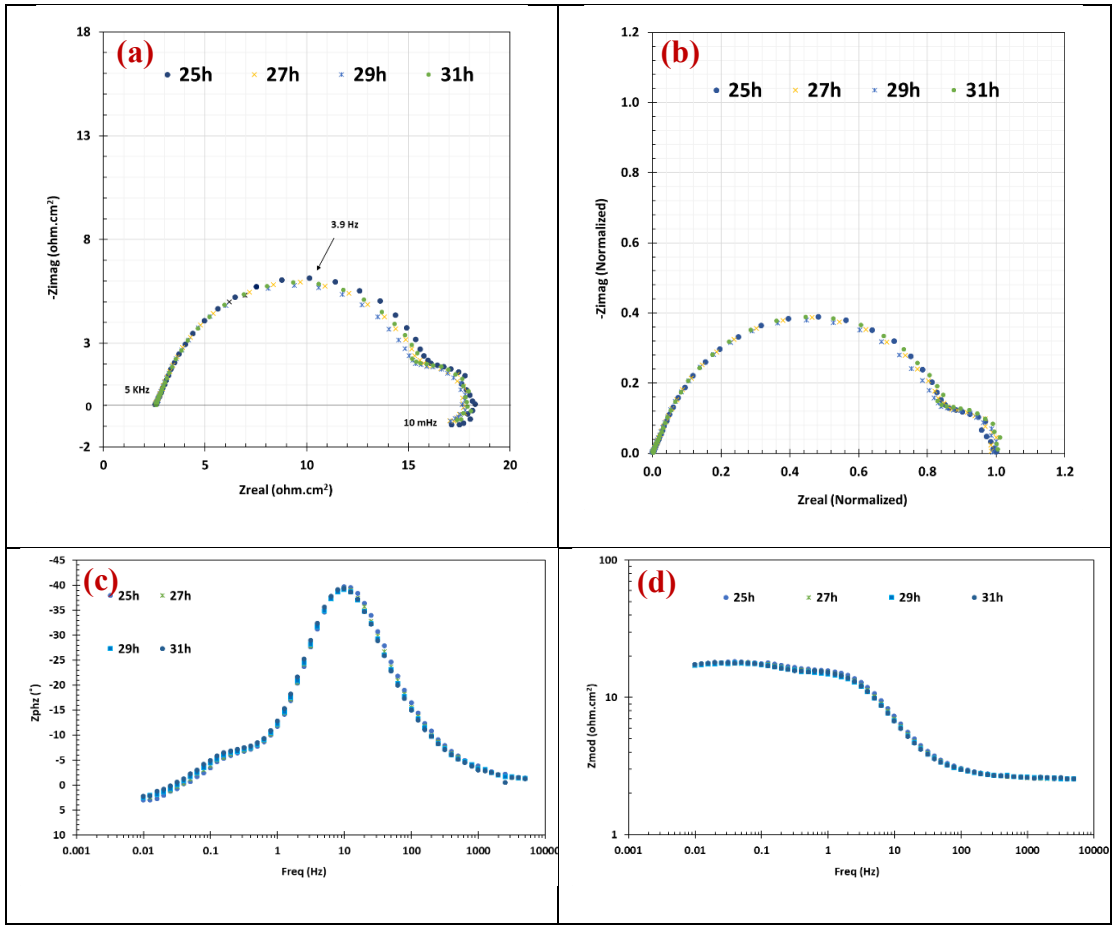

Figure 115. EIS results obtained from stable corrosion period of an experiment with presence of 6000 ppm Ca^{2+} ($S_{CaCO_3} = 1$) conducted at 80°C, pCO_2 0.53 bar, bulk solution pH 5.5, 0.60 M ionic strength, and 20 rpm: (a) Nyquist plots (b) normalized Nyquist plots (c) phase angle, and (d) impedance modulus

Pseudo-passivation period:

This period starts much earlier (roughly at 31 h) than the experiment without Ca^{2+} (roughly at 60h). Two incomplete semicircles are present in the Nyquist plots provided in Figure 116 (a and b). The effect of exposure time on Nyquist plots and Bode diagrams is indicted on Figure 116(a, c, d). The corrosion products offered a better protection at the end of experiment with presence of 6000 ppm Ca^{2+}. This can be seen from the EIS

modulus diagrams in Figure 116(d) and Figure 111(d) with higher impedance modulus in presence of Ca^{2+}. Consequently, the final LPR corrosion rate with and without presence of Ca^{2+} are 0.41 mm/y and 2.46 mm/y, respectively (see Figure 112 and Figure 105).

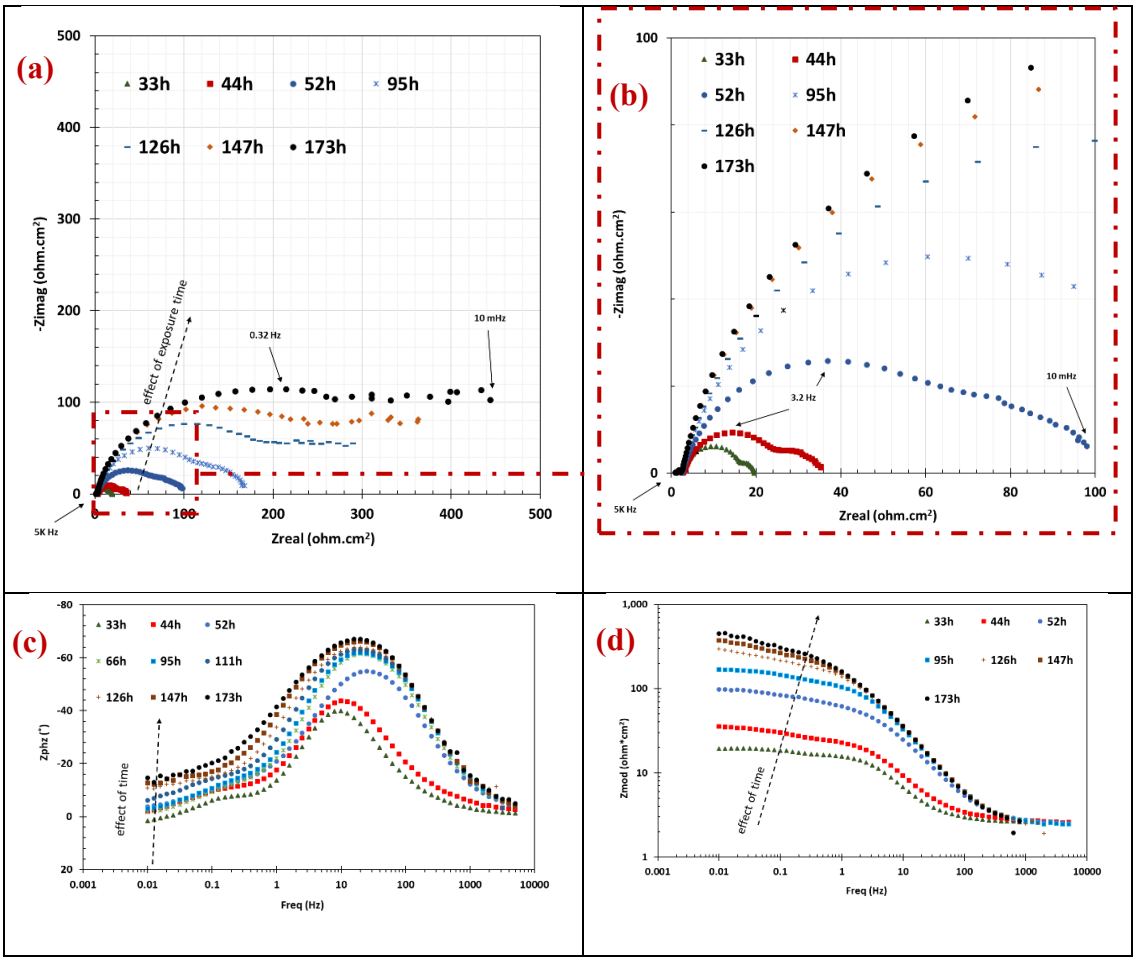

Figure 116. EIS results obtained from decreasing corrosion period of an experiment with presence of 6000 ppm Ca^{2+} ($S_{CaCO_3} = 1$) conducted at 80°C, pCO_2 0.53 bar, bulk solution pH 5.5, 0.60 M ionic strength, and 20 rpm: (a) and (b) Nyquist plots, (c) phase angle, and (d) impedance modulus

Table 15 shows the timeline of the three detected corrosion periods and final LPR corrosion rates with and without presence of 6000 ppm Ca^{2+}. Indeed, Table 16 compares the response of Nyquist plots in different corrosion periods for experiments with and without presence of 6000 ppm Ca^{2+}.

Table 15. Comparison of timeline for corrosion periods and final LPR corrosion with and without presence of 6000 ppm Ca^{2+}

Experiment	**Approximate timeline for corrosion rate**			**Final LPR corrosion rate (7 days)**
	active	Nucleation/growth	Pseudo-passivation	
Without Ca^{2+}	0-30 h	30-60 h	60 h-end	2.46 mm/y
With Ca^{2+}	0-25 h	25-31 h	31 h-end	0.41 mm/y

Table 16. Comparison of EIS Nyquist response in different corrosion periods for experiments with and without presence of 6000 ppm Ca^{2+}

Experiment	**EIS Nyquist Response**		
	active	Nucleation/growth	Pseudo-passivation
Without Ca^{2+}	2 capacitive semicircles + one inductive loop (LF)	2 capacitive semicircles	2 incomplete capacitive semicircles
With Ca^{2+}	2 capacitive semicircles + one inductive loop (LF)	2 capacitive semicircles + one inductive loop (LF)	2 incomplete capacitive semicircles

APPENDIX IV: ELECTROCHEMICAL INVESTIGATION ON THE INFLUENCE OF Ca^{2+} AND Mg^{2+} ON CO_2 CORROSION OF MILD STEEL IN SCALE FREE CONDITIONS

Experiments presented in Chapter 7 and Chapter 8 suggested that LPR corrosion rate initially increased in presence of Mg^{2+} while it was not apparently the case for electrolytes containing Ca^{2+} (Chapter 6). A series of experiments were conducted to investigate the effect of Ca^{2+} and Mg^{2+} ions on electrochemical behavior of CO_2 corrosion of mild steel at the initial stages of the corrosion process (without any interference from corrosion product formation). A rotating electrode was employed to conduct LPR, EIS, and anodic/cathodic sweep measurements at 40°C, pCO_2 0.93 bar, ionic strength of 0.77 M and equimolar concentrations of Ca^{2+} and Mg^{2+} (0.2 M) as shown in Table 17. The experimental procedure follows what is described in Chapter 4, except for using a rotating electrode. The anodic sweep measurement was the final step of the experimental sequence since the steel surface would be significantly altered after that experiment. Similar measurements were performed for a blank solution at the same conditions and ionic strength to serve as baseline and help distinguish the effect of Ca^{2+} and Mg^{2+}. All the experiments were repeated two times to assure reproducibility of the results. OCP measurements were conducted prior to each electrochemical measurement to make sure that the system was in stable condition (OCP measurement typically took less than 8 minutes). The potentiodynamic (anodic and cathodic) sweeps and LPR was corrected using the solution resistance obtained by EIS. Potentiodynamic sweeps were conducted by polarizing the working electrode from the OCP to the cathodic and anodic

region at a scan rate of 0.5 and 1 mV/s (for LPR and EIS measurement details please see Chapter 5.3). UNS G10180 specimens exposed to CO_2 environment are potentially subject to development of Fe_3C and $FeCO_3$. However, due to a relatively short-term exposure before each electrochemical measurement and the low experimental temperature of 40°C (which reduces kinetic of reactions), the possible interference of Fe_3C and $FeCO_3$ layer on the measurements was minimized. Additionally, in some cases, if the OCP after each experiment did not return to the previous experiments (due to potential development of Fe_3C and/or $FeCO_3$), the working electrode was removed from the solution and re-polished.

Table 17. Test matrix for conducting electrochemical measurements in presence of equimolar Mg^{2+} and Ca^{2+}

Parameter	**Description**		
Temperature	40°C		
pCO_2	0.93 bar		
pH	4.64 (adj. by $NaHCO_3$)		
Electrolyte	Baseline	Ca^{2+} - containing	Mg^{2+} - containing
	4.5 wt% NaCl	1 wt% NaCl + $CaCl_2$	1 wt% NaCl + $MgCl_2$
$[Mg^{2+}]$	0	0	0.2 M
$[Ca^{2+}]$	0	0.2 M	0
strength Ionic	0.77		
Dissolved O_2	<5 ppb		
Electrochemical technique	OCP, LPR, Potentiodynamic sweep, EIS		

Table 18 shows the average values of two separate experiments for ionic strength, initial and adjusted pH, LPR CR, and OCP. Although, all the solutions had the same ionic strength, the initial pH of the three solution was slightly different possibly due to

different nature of the dissolved ions and their effect on hydrogen ion activity. The initial autogenous pH of the Ca^{2+}-containing electrolyte, pH 4.64, was selected as the bench mark and the pH of other solutions were adjusted to this value using $NaHCO_3$ salt before immersion of the working electrode. As Table 18 indicates, the LPR CR was higher in presence of Ca^{2+} and Mg^{2+} with the highest value (4.12 mm/y) belonging to solution contains 0.2 M of Mg^{2+}.

Table 18. Mean value of ionic strength, pH, LPR CR, and OCP for three different solutions

Solution	Ionic Strength	Initial pH	Adj. pH with $NaHCO_3$	CR (mm/y)	OCP (mV)
Blank (NaCl)	0.77	3.89	4.64	0.64	-681.50
0.2M [Mg^{2+}] (source $MgCl_2$)	0.77	4.50	4.64	4.12	-709.50
0.2M [Ca^{2+}] (source $CaCl_2$)	0.77	4.64	-	2.50	-690.50

The Nyquist plots and Bode diagrams collected during EIS measurements are presented in Figure 117, Figure 118, and Figure 119, respectively. The Nyquist plots in Figure 117 indicate presence of a depressed capacitive semicircle and an inductive loop in the low frequency region for all the solutions. However, the magnitude of the overall impedance for the solution containing Mg^{2+} is lower than for the Ca^{2+}-containing solution and the blank solution. This observation had been captured accordingly from LPR experiments where the specimens exposed to the Mg^{2+}-containing solution had shown the highest corrosion rate (lowest polarization resistance). The modulus and phase angle diagram (Figure 118 and Figure 119) are in accord with the observations from LPR and Nyquist plots.

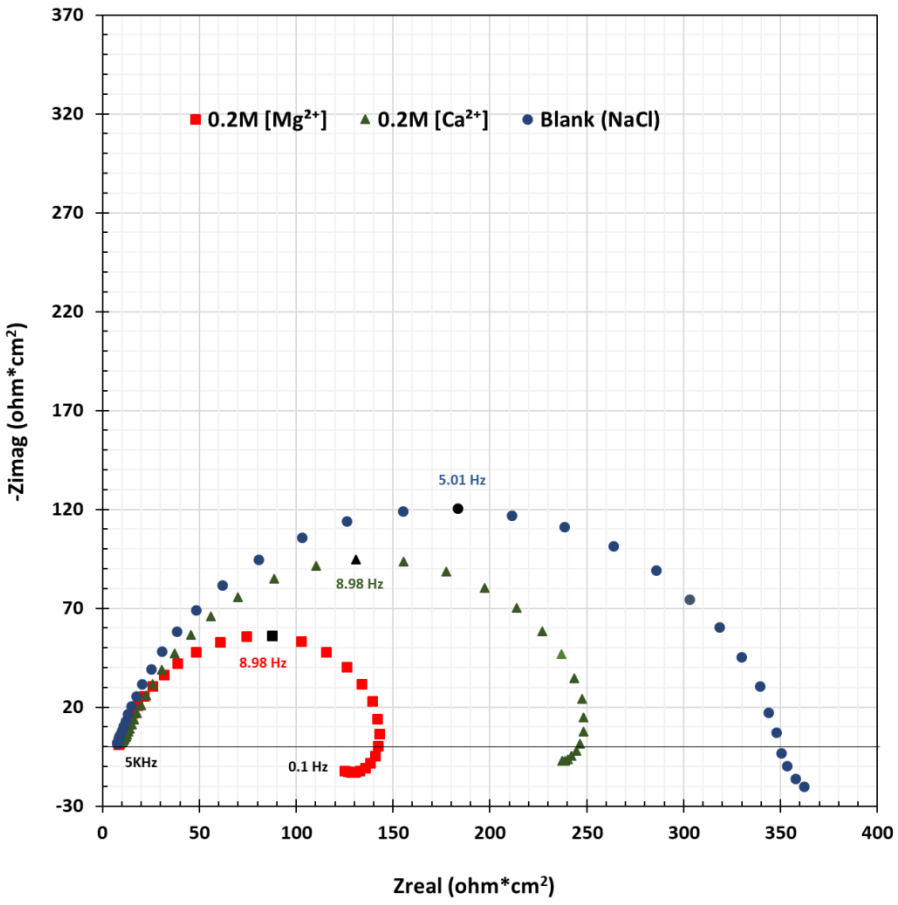

Figure 117. Nyquist plots obtained from a blank, Ca^{2+}-containing, and Mg^{2+}-containing solution at 40°C, pCO_2 0.93 bar, bulk solution pH 4.64, 0.77 M ionic strength, and 1500 rpm

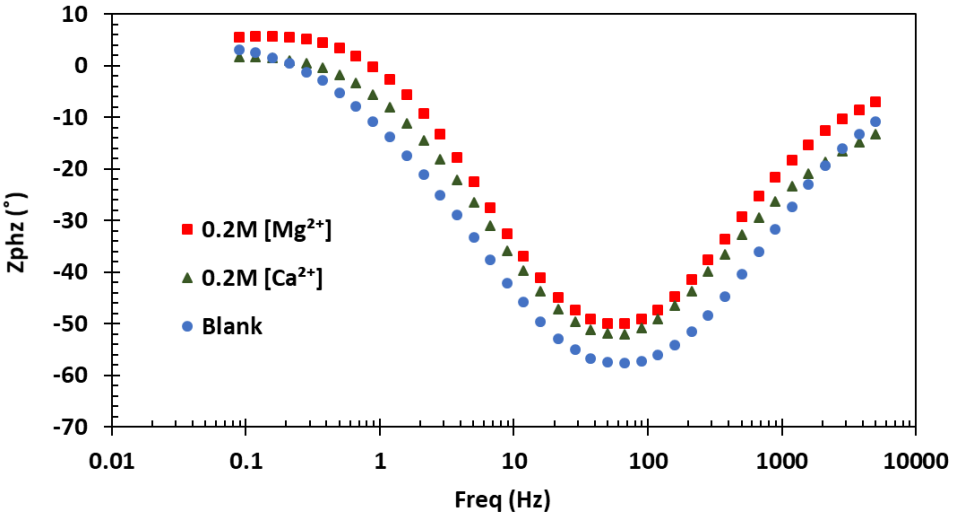

Figure 118. Phase angle diagrams obtained from a blank, Ca^{2+}-containing, and Mg^{2+}-containing solution at 40°C, pCO_2 0.93 bar, bulk solution pH 4.64, 0.77 M ionic strength, and 1500 rpm

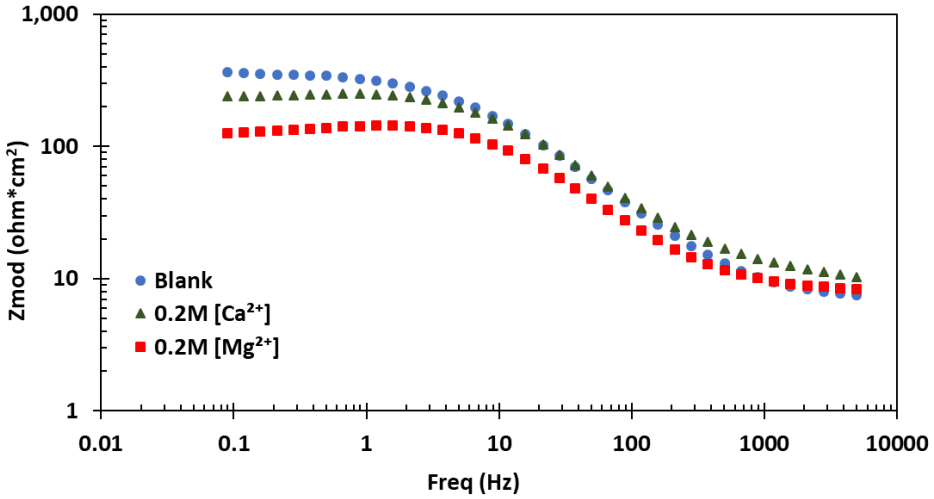

Figure 119. Impedance modulus diagrams obtained from a blank, Ca^{2+}-containing, and Mg^{2+}-containing solution at 40°C, pCO_2 0.93 bar, bulk solution pH 4.64, 0.77 M ionic strength, and 1500 rpm

EIS spectra and LPR CR suggested that mild steel CO_2 corrosion behavior is different in presence of Ca^{2+} and Mg^{2+} ions. However, potentiodynamic sweeps

conducted at the same conditions for the three solutions did not show any significant differences in charge transfer zone as illustrated in Figure 120. To cross-check this finding, additional potentiodynamic sweeps at other conditions were performed. For instance, Figure 121 and Figure 122 show potentiodynamic polarizations of mild steel exposed to CO_2 environment in presence of Ca^{2+}/Mg^{2+} and only Mg^{2+} at 80°C and ~1°C (using an ice bath), respectively. The lower temperature in the latter experiment, was selected for a better observation of the charge transfer zone by lowering kinetics of electrochemical reactions. However, such polarizations suggest that Ca^{2+} and Mg^{2+} do not influence the charge transfer behavior of the main cathodic reaction. Another observation was that at more negative potentials, $CaCO_3$ scale precipitated on the steel surface for Ca^{2+}-containing solution, resulting in a lower current density. this phenomenon is shown in Figure 121. $MgCO_3$ did not precipitate on the steel surface for the Mg^{2+}-containing solution at similar protentional due to its slow precipitation kinetics.

It seems rigorous experiments are needed to investigate the true effect of Ca^{2+} and Mg^{2+} on electrochemical reactions involved in CO_2 environment.

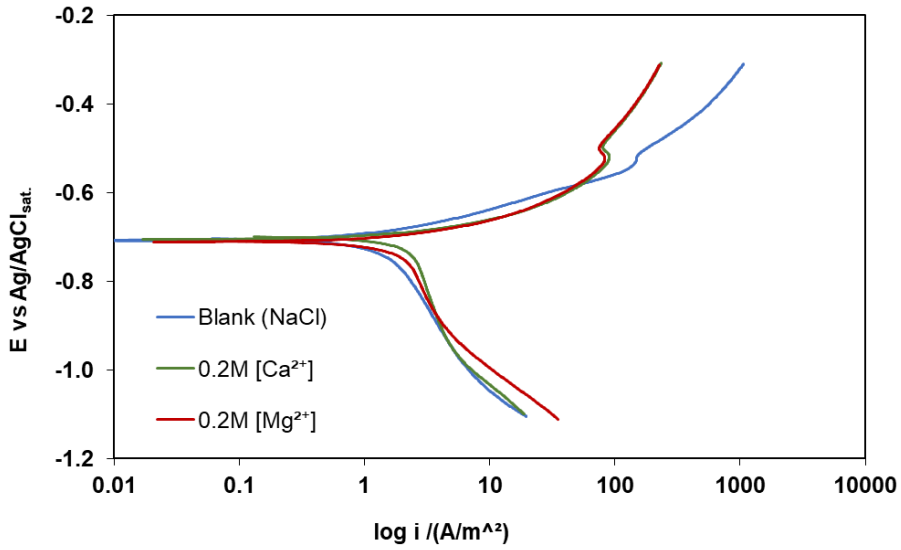

Figure 120. Potentiodynamic polarization of mild steel in presence of a blank, Ca^{2+}-containing, and Mg^{2+}-containing solution at 40°C, pCO_2 0.93 bar, bulk solution pH 4.64, 0.77 M ionic strength, and 1500 rpm

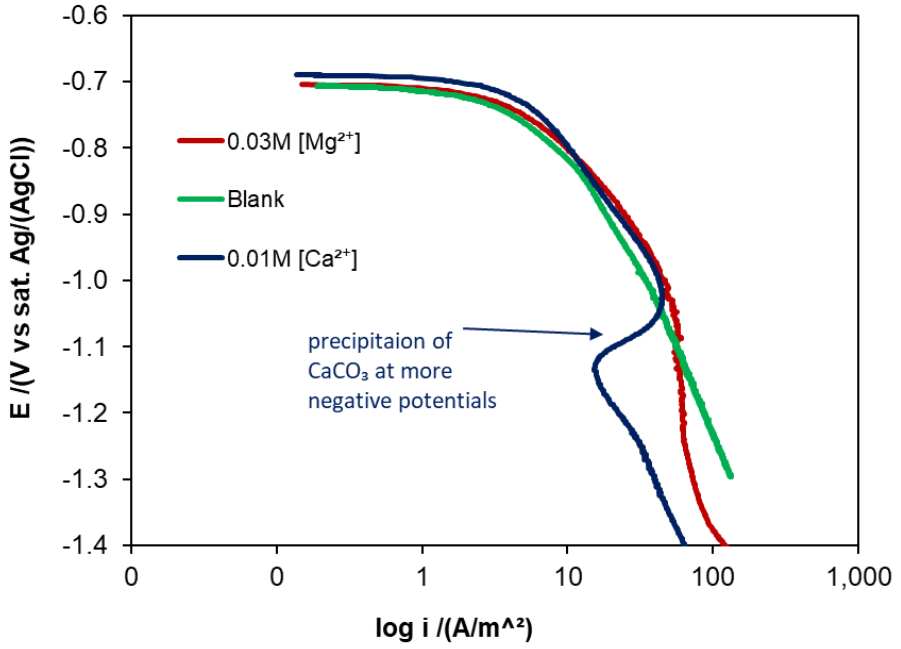

Figure 121. Cathodic polarization of mild steel in presence of a blank, Ca^{2+}-containing, and Mg^{2+}-containing solution at 80°C, pCO_2 0.53 bar, bulk solution pH 6.2, and 250 rpm

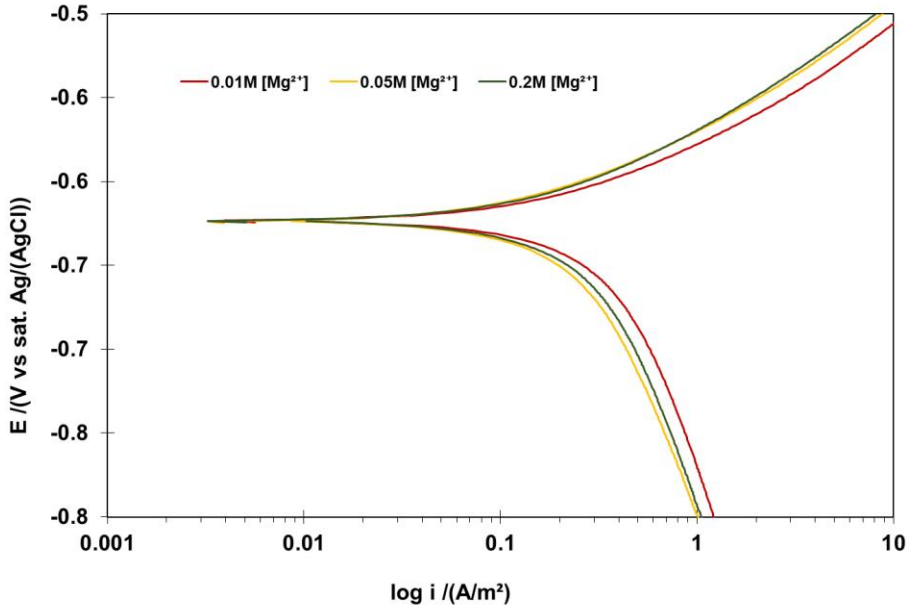

Figure 122. Cathodic polarization of mild steel in presence of different concentration of Mg^{2+} (0.01, 0.05, and 0.2 M) at 1°C, pCO_2 0.99 bar, bulk solution pH 4.23, ionic strength 0.2M to 0.77M, and 2000 rpm

Thesis and Dissertation Services